

Abstract

Sustainable Production of Water and Energy with Osmotically-Driven Membrane Processes and Ion- Exchange Membrane Processes

Ngai Yin Yip

2014

The world population of the 21st century is facing an increasingly challenging energy landscape and declining water quality and availability, further compounded by a rapidly expanding global population against the backdrop of climate change. To meet the challenges of the water-energy nexus in a sustainable manner, existing methods need to be advanced and new technologies developed. Osmotically-driven and ion-exchange membrane processes are two classes of emerging technologies that can offer cost-effective and environmentally sensible solutions to alleviate the pressure on our water and energy demands. The objective of this thesis is to advance forward osmosis (FO), pressure retarded osmosis (PRO), and reverse electrodialysis (RED) for the sustainable production of water and energy.

A main hindrance restricting the progress of osmotically-driven membrane processes, FO and PRO, is the absence of adequate membranes. This work demonstrates the fabrication of thin-film composite polyamide FO membranes that can attain high water flux and PRO membranes capable of achieving power density of 10 W/m^2 , twice the

benchmark of 5 W/m^2 for PRO with natural salinity gradients to be cost-effective. A membrane fabrication platform based on mechanistic understanding of the influence of membrane transport and structural parameters on process performance was developed. The morphology and microstructure of the porous support layer, and hydraulic permeability and salt selectivity of the polyamide active layer were specifically tailored by thoughtful control of the fabrication and modification conditions.

The Gibbs free energy from the mixing of river water with seawater can potentially be harnessed for clean and renewable energy production. This work analyzed the thermodynamics of PRO power generation and determined that energy efficiencies of up to $\sim 91\%$ can theoretically be attained. The intrinsic limitations and practical constraints in PRO were identified and discussed. Using a tenth of the annual global river water discharge of $37,000 \text{ km}^3$ for PRO could potentially produce electricity for over half a billion people, ascertaining natural salinity gradients to be a sizeable renewable source that can contribute to diversifying our energy portfolio.

However, fouling of the membrane support layer can diminish the PRO productivity by detrimentally increasing the hydraulic resistance. Analysis of the water flux behavior and methodical characterization of the membrane properties shed light on the fouling mechanism and revealed the active-support layer interface to play a crucial role during fouling. A brief osmotic backwash was shown to be effective in cleaning the membrane and achieving substantial performance recovery.

Reverse electrodialysis (RED) is an ion-exchange membrane process that can also extract useful work from salinity gradients. This dissertation research examined the energy efficiency and power density of RED and identified a tradeoff relation between

the two performance parameters. Energy efficiency of ~33-44% can be obtained with technologically-available membranes, but the low power densities of $< 1 \text{ W/m}^2$ is likely to be impede the realization of the process. To further advance RED as a salinity energy conversion method, ion-exchange membrane technology and stack design need to be advanced beyond their current limitations.

When analyzed with simulated existing state-of-the-art membranes, PRO exhibited greater energy efficiencies (54–56%) and significantly higher power densities ($2.4\text{--}38 \text{ W/m}^2$) than RED (18–38% and $0.77\text{--}1.2 \text{ W/m}^2$). The drawback of RED is especially pronounced at large salinity gradients, where the high solution concentrations overwhelm the Donnan exclusion effect and detrimentally diminish the ion exchange membrane permselectivity. Additionally, the inherent different in driving force utilization (osmotic pressure difference for PRO and Nernst potential for RED) restricts RED from exploiting larger salinity gradients to enhance performance. Overall, PRO is found to be the more favorable membrane-based technology for accessing salinity energy.

This work presents pioneering advances for forward osmosis and pressure retarded osmosis membrane development. The fundamental studies of the osmotically-driven membrane processes and ion-exchange membrane processes yielded significant findings that enhanced our mechanistic and thermodynamic understanding of the technologies. The important insights can serve to inform the realization of the emerging membrane-based technologies for the sustainable production of water and energy. The implications of the thesis are potentially far-reaching and are anticipated to shape the discussion on FO, PRO, and RED.

**Sustainable Production of Water and Energy with Osmotically-Driven
Membrane Processes and Ion-Exchange Membrane Processes**

A Dissertation

Presented to the Faculty of the Graduate School

of

Yale University

in Candidacy for the Degree of

Doctor of Philosophy

by

Ngai Yin Yip

Dissertation Director: Menachem Elimelech

December, 2014

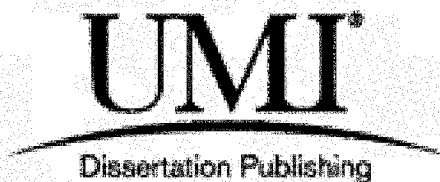
UMI Number: 3582181

All rights reserved

INFORMATION TO ALL USERS

The quality of this reproduction is dependent upon the quality of the copy submitted.

In the unlikely event that the author did not send a complete manuscript and there are missing pages, these will be noted. Also, if material had to be removed, a note will indicate the deletion.

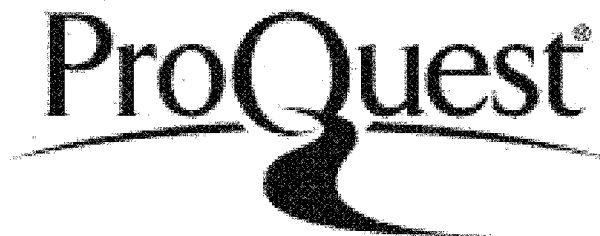


UMI 3582181

Published by ProQuest LLC 2015. Copyright in the Dissertation held by the Author.

Microform Edition © ProQuest LLC.

All rights reserved. This work is protected against unauthorized copying under Title 17, United States Code.



ProQuest LLC
789 East Eisenhower Parkway
P.O. Box 1346
Ann Arbor, MI 48106-1346

© 2014 by Ngai Yin Yip

All rights reserved

Acknowledgements

“It isn't the mountains ahead to climb that wear you out; it's the pebble in your shoe.”

— Muhammad Ali

Pursuing a Ph.D. is like an arduous journey over many mountains and across many rivers. Foremost, my deepest gratitude to Dr. Meny Elimelech for his faith and belief in me, and his invaluable direction and continuous guidance in steering me on track. Whenever I was ready to set my pack down and settle, he will always find words of encouragement to motivate me to push on to higher levels.

To my past and present committee members, Dr. Bill Mitch, Dr. Chinedum Osuji, and Dr. Jaehong Kim, I am also indebted to their generosity with advice and time. I am forever grateful to the Environment and Water Industry Development Council of Singapore for sponsoring my fellowship.

I was most fortunate to be surrounded by brilliant postdocs, students, and collaborators who are simply a joy to work with. Though we are all on our own expedition, it has been a tremendously enriching experience to walk alongside each of you and I hope our paths cross again in the future.

To my friends in New Haven who have, in countless times, lent me their shoulder to balance on as I pick the pebble from my shoe. I thank each and every one of you for smelling the roses with me.

I thank my family who has always been supportive of my endeavors and, last but not least, Lindsay who has been the light in my darkest of times and the warmth in my coldest of nights.

TABLE OF CONTENTS

Thesis Abstract	i	
Title Page	iv	
Acknowledgement	vi	
List of Figures	xiv	
List of Tables	xviii	
Chapter 1	Introduction	1
	1.1 Motivation	2
	1.2 Objectives and Scope of the Dissertation	6
	1.3 Thesis Organization	7
	1.4 Key Contributions	10
	1.5 References.....	13
Chapter 2	Principles of Osmotically-Driven Membrane Processes and Ion Exchange Membrane Processes	15
	2.1 Introduction	17
	2.2 Forward Osmosis	18
	2.3 Pressure Retarded Osmosis	24
	2.4 Reverse Electrodialysis	29
	2.5 References	34
Chapter 3	High Performance Thin-Film Composite Forward Osmosis Membrane	40
	3.1 Introduction	42
	3.2 Materials and Methods	44

	Materials and Chemicals	
	Casting of Polysulfone Support	
	Interfacial Polymerization of TFC Membrane	
	SEM Imaging and Thickness Measurement of Membrane	
	Testing Membrane Performance in FO Mode	
	Determination of Pure Water Permeability and Salt Rejection	
	Determination of FO Membrane Structural Parameters	
3.3	Results and Discussion	49
	Membrane Microstructure and Morphology	
	Performance of TFC-FO Membrane	
	TFC-FO Membrane Structural Parameters	
	Membrane Performance and Chemical Stability with Ammonium Bicarbonate Draw Solution	
3.4	Implications for FO Membrane Development	59
3.5	References	61
Chapter 4	Thin-Film Composite Pressure Retarded Osmosis Membranes for Sustainable Power Generation from Salinity Gradients	63
4.1	Introduction	65
4.2	Theory	68
	Water and Salt Fluxes Across the Active Layer	
	Mass Transfer in the Porous Support Layer	
	Mass Transfer in the External Concentration Polarization Layer	
	Water Flux in PRO with ICP, ECP, and Salt Permeation Effects	
4.3	Materials and Methods	72
	Chemicals and Materials	
	Polysulfone Porous Support Fabrication	
	Polyamide Active Layer Fabrication	
	Active Layer Modification	
	Determination of Membrane Water Permeability and Channel Mass Transfer Coefficient	
	Determination of Membrane Solute Permeability and Structural Parameter	

	Determination of Membrane Performance in PRO Mode	
	Prediction of PRO Water Flux and Power Density	
4.4	Results and Discussion	78
	Validation of the PRO Water Flux Model	
	Membrane Characteristics	
	Water Flux and Projected Power Density of Hand-Cast TFC-PRO Membranes	
	PRO Power Density Depends on Support and Active Layer Membrane Properties	
	Balancing Membrane Permeability-Selectivity to Maximize PRO Performance	
4.5	Implications for Osmotic Power Generation	89
4.6	References	90
Chapter 5	Performance Limiting Effects in Power Generation from Salinity Gradients by Pressure Retarded Osmosis	93
5.1	Introduction	95
5.2	Materials and Methods	98
	Materials and Chemicals	
	Polyamide Active Layer Modification	
	Determination of Membrane Water and Salt Permeabilities	
5.3	Results and Discussion	100
	Membranes are Bounded by Permeability-Selectivity Tradeoff	
	Correlation between Membrane Water and Salt Permeabilities	
	Phenomena Governing Water Flux and Power Density in PRO	
	Influence of Membrane Properties on Peak Power Density	
	Losses in Power Density due to Performance Limiting Effects	
	Influence of Hydrodynamic Conditions on Peak Power Density	
5.4	Implications for Renewable Energy from Salinity Gradients	122
5.5	References	124

Chapter 6	Thermodynamic and Energy Efficiency Analysis of Power Generation from Natural Salinity Gradients by Pressure Retarded Osmosis	127
	6.1 Introduction	129
	6.2 Energy of Mixing	131
	Mixing Releases Free Energy	
	Energy Change of Mixing for Strong Electrolyte Solutions	
	ΔG_{mix} for Ideal Solutions	
	6.3 Reversible Thermodynamic Model of Pressure Retarded Osmosis	136
	Pressure Retarded Osmosis Model	
	Reversible Thermodynamic PRO Process	
	Theoretical Maximum Extractable Work is Equal to the Gibbs Energy of Mixing	
	6.4 Energy Efficiency of Pressure Retarded Osmosis	142
	Extractable Work in a Constant-Pressure PRO Process	
	Entropic Loss and Unutilized Energy	
	Thermodynamic Efficiency of PRO Work Extraction	
	Practical Constraints in PRO Operation	
	6.5 Implications for PRO Energy Production	150
	6.6 References	153
Chapter 7	Influence of Natural Organic Matter Fouling and Osmotic Backwash on Pressure Retarded Osmosis Energy Production from Natural Salinity Gradients	156
	7.1 Introduction	158
	7.2 Materials and Methods	160
	Materials and Chemicals	
	Thin-film Composite Pressure Retarded Osmosis Membrane Fabrication	
	Membrane Characterization	
	Membrane Fouling Protocol	
	Osmotic Backwash	
	Power Density Projection	
	7.3 Results and Discussion	166
	Fabricated Membrane Transport and Structural Parameters	

	NOM Fouling of Membrane Support Layer Substantially Reduces Water Flux	
	Water Flux Behavior Indicates Three Phases During Support Layer Fouling	
	Initial Foulant Deposition at Active-Support Layer Interface Drastically Lowers Membrane Permeability	
	Osmotic Backwash Partially Reverses Fouling	
	Impact of NOM Fouling and Osmotic Backwash on Projected Membrane Power Density	
7.4	Implications for Power Generation	183
7.5	References	185
Chapter 8	Thermodynamic, Energy Efficiency, and Power Density Analysis of Reverse Electrodialysis Power Generation with Natural Salinity Gradients	189
8.1	Introduction	191
8.2	Reversible Thermodynamic Model of Reverse Electrodialysis	193
	Reverse Electrodialysis Model	
	Reversible Thermodynamic RED Process	
	Theoretical Maximum Extractable Work is Equal to the Gibbs Energy of Mixing	
8.3	Energy Efficiency of Reverse Electrodialysis	200
	Internal Resistances in RED Power Generation Circuit	
	Work Extraction with Constant-Resistance External Load	
	Maximum Power Density in Practical RED Operation	
	Energy Conversion Efficiency	
	Losses due to Stack Resistance	
8.4	Influence of Membrane Selectivity on Energy Efficiency	209
	Selectivity Imperfections of Ion Exchange Membranes	
	Uncontrolled Mixing Decreases Extractable Work	
	Imperfect Selectivity Reduces RED Power Generation Efficiency	
8.5	Power Density Analysis	216
	Power Density of Perfect and Imperfect Membrane Selectivity	
	Enhancing Power Density by Energy Efficiency Trade-off	

	Influence of Intermembrane Distance and Membrane Resistance on Power Density	
8.6	Implications for Natural Salinity Gradient Power Generation	223
8.7	References	226
Chapter 9	Comparison of Energy Efficiency and Power Density in Pressure Retarded Osmosis and Reverse Electrodialysis.....	230
9.1	Introduction	232
9.2	Energy Production from Salinity Gradients	234
	Pressure Retarded Osmosis	
	Reverse Electrodialysis	
	Natural, Anthropogenic, and Engineered Salinity Gradients	
9.3	Significant PRO and RED Membrane Properties	240
	Structural Parameter and Mass Transport Coefficient of PRO Membranes	
	PRO Membrane Selectivity–Permeability Tradeoff	
	RED Membrane Ionic Permselectivity–Conductivity Tradeoff	
	Effect of Solution Concentration and Intermembrane Distance	
9.4	Salinity Energy Production Performance Parameters	244
	Membrane Power Density	
	Energy Extraction Efficiency	
	Practical Operation of PRO and RED	
9.5	Energy Extraction Efficiency	247
	Efficiency, Entropy Production, and Unutilized Energy	
	Higher Efficiency is Attainable in PRO than RED	
	Selective Membranes Yield Greater Efficiencies	
9.6	Membrane Power Density	253
	Higher Power Density Obtained with Less Resistive Membranes	
	PRO Better Utilizes Salinity Gradient to Realize Greater Power Densities	
9.7	Implications	257
9.8	References	260

Chapter 10	Conclusions	264
	10.1 Summary	265
	10.2 Novel Contributions	267
	10.3 Implications and Future Directions	271
	10.4 References	275

LIST OF FIGURES

Chapter 1

1.1	Global distribution of water scarcity index	3
1.2	Development of primary energy sources from 1950 to 2008, and projected pathways for 2030 and 2050	4
1.3	Interactive pathways between water, energy, and food/ feed/ fiber, against the backdrop of climate change	5

Chapter 2

2.1	Schematics of reverse osmosis, forward osmosis, and pressure retarded osmosis	18
2.2	Representative plot of water flux across a semipermeable membrane as a function of the applied hydraulic pressure difference	19
2.3	A) Schematic of the Green Machine and B) landfill leachate treatment pilot plant using FO membranes	20
2.4	A) Schematic of the ammonia-carbon dioxide desalination system and B) FO membrane brine contactor pilot system treating shale gas produced water	21
2.5	SEM micrographs of A) commercial thin-film composite polyamide RO membrane and B) commercial integrally- skinned asymmetric cellulose triacetate FO membrane	23
2.6	Schematic of a “osmotic salination energy converter”	25
2.7	A) Seawater-river water PRO demonstration plant in Tofte, Norway and B) schematic of PRO power generation utilizing natural salinity gradients	26
2.8	Timeline of membrane power densities demonstrated experimentally with seawater-river water	28
2.9	Schematic of electrodialysis and reverse electrodialysis	30
2.10	A) Artist impression of a seawater-river water RED power generation plant and B) 50 kW RED pilot plant at the Afsluitdijk in the Netherlands	32

Chapter 3		
3.1	SEM micrographs displaying the structure of a TFC-FO membrane at the A) top and B) bottom surface	50
3.2	SEM micrographs of the cross-section of a TFC-FO membrane A) including PET non-woven fabric and B) a magnified view near the active layer	51
3.3	Comparison of (A) FO water flux and (B) salt rejection between TFC-FO membranes and commercial membranes	54
3.4	Experimental TFC-FO membrane water flux over a range of osmotic pressure differences	56
3.5	SEM cross-sectional micrographs of A) commercial HTI-CTA membrane and B) TFC-RO membrane after removing the PET non-woven fabric	57
 Chapter 4		
4.1	Schematic representation of the salt concentration profile across a thin-film composite membrane in PRO mode at steady state	68
4.2	SEM micrographs of a TFC-PRO membrane with PET fabric layer removed: A) cross-section, B) magnified view of the polyamide active layer surface, and C) magnified view of the skin layer at the top of the PSf porous support	79
4.3	Plots of modeled water flux and power density as a function of applied hydraulic pressure	83
 Chapter 5		
5.1	Correlation between water/NaCl permeability-selectivity and membrane permeability to water	104
5.2	Log-log plot of water and salt permeability coefficients of TFC polyamide membranes subjected to chlorine-alkaline modification	106
5.3	Representative plots of water flux and power density as a function of applied hydraulic pressure	110
5.4	Peak power density as a function of active layer water and salt permeabilities and support layer structural parameter	113
5.5	Losses in W_{peak} due to the individual effect of the performance limiting phenomena: A) ECP, B) ICP, and C) reverse draw salt flux	118

5.6	Maximum peak power density achievable as a function of mass transfer coefficient in the ECP boundary layer	121
 Chapter 6		
6.1	Gibbs free energy of mixing, per unit volume of the river or brackish water, as a function of the relative mixing ratio	134
6.2	Schematics of a pressure retarded osmosis process	137
6.3	A) Representative plot of $\Delta\pi$ as a function of ΔV and B) representative plot of the maximum amount of work that can be extracted in a constant-pressure PRO process	140
6.4	Specific maximum extractable work, frictional losses, and unutilized energy in a constant-pressure PRO process as a function of ϕ for A) river water and B) brackish water	145
6.5	Representative plot of the amount of work that can be extracted in an actual constant-pressure PRO process	149
 Chapter 7		
7.1	Water fluxes of hand-cast TFC-PRO membrane as a function of the cumulative permeate volume in the baseline, fouling, and cleaned membrane experiments	168
7.2	Schematic representation of the water flux and reverse draw solute flux across a thin-film composite membrane in PRO operating in counter-current flow	169
7.3	Representative images of the active and support layer of a hand-cast TFC membrane at various experimental stages	171
7.4	Water flux as a function of the cumulative permeate volume per unit active area of TFC-PRO membrane.....	172
7.5	Water flux and projected membrane power density of the hand-cast TFC-PRO membranes after SRNOM fouling and after osmotic backwash	181
 Chapter 8		
8.1	A) Conceptual schematic of a reverse electrodialysis salinity battery and B) schematic of one RED cell	194
8.2	A) Representative plot of the voltage across the one-cell RED as a function of the moles of salt that permeated and B) representative plot of the useful work extractable	197

8.3	A) Extractable work per unit volume of the LC solution, B) energy conversion efficiency, and C) overall membrane power density of RED energy production, as a function of ϕ	207
8.4	A) Extractable work per unit volume of the LC solution and B) the percentage of Gibbs free energy of mixing that is not extractable due to selectivity imperfections, as a function of ϕ	215
8.5	Overall membrane power density and energy conversion efficiency for seawater-river water RED power generation	220

Chapter 9

9.1	Schematic of A) pressure retarded osmosis (PRO) and B) reverse electrodialysis (RED)	235
9.2	Representative plots of useful work, W , frictional/resistive losses, uncontrolled mixing losses, and unutilized energy for A) PRO and B) RED	248
9.3	Efficiency of work extraction, percent of energy expended to drive water or ion flux, percent of energy lost to uncontrolled mixing, and portion of unutilized energy for PRO and RED	251
9.4	Membrane power density and efficiency of work extraction for PRO and RED at 0.6 M, 1.2 M, and 4.0 M NaCl high concentration (HC) solution concentrations	252
9.5	A) Osmotic pressure difference, $\Delta\pi$, as a function of the fraction of water permeated from the low concentration (LC) solution, and B) electromotive force, ξ_{emf} , as a function of the moles of salt permeated per unit volume of the high concentration (HC) solution	256

LIST OF TABLES

Chapter 3		
3.1	Measured water flux, salt rejection, and calculated structural parameter for TFC-FO membranes	55
Chapter 4		
4.1	Membrane characteristic parameters and modeled peak power densities for all TFC-PRO membranes fabricated	81
Chapter 5		
5.1	Chlorine and alkaline treatment conditions on commercial TFC polyamide RO membrane and the resultant water permeability coefficient, salt rejection, and NaCl permeability coefficient	101
Chapter 7		
7.1	Characteristic transport properties and structural parameter of the fabricated membranes before the organic fouling experiment, after SRNOM fouling, and after osmotic backwash	167
Chapter 9		
9.1	Properties of current high performance membranes analyzed (thin-film composite polyamide membranes for PRO and ion exchange membranes for RED)	241

Chapter 1:

Introduction

1.1 MOTIVATION

Addressing our water and energy problems is most pressing priorities for the 21st century [1, 2]. This urgency is echoed by the National Academy of Engineering's Grand Challenges, with water- and energy-related issues polling in at four out of the top five spots [3]. Water is not just a fluid that quenches our thirst; it is essential for our existence and is as fundamental as the right to live. In July 2010, the United Nation General Assembly declares "the right to safe and clean drinking water and sanitation as a human right that is essential for the full enjoyment of life and all human rights. [4]" Regrettably, water poverty and its associated problems are prevalent: 1.2 billion people lack access to safe drinking water, 2.6 billion have little or no sanitation, and annual fatalities from water-borne diseases number in the millions [5].

Figure 1.1 shows the water stressed regions in the world [6]. Approximately 35% of the world's population is living in water stressed areas. From the geographical distribution, it is evident that developed countries are not spared from the water crisis. Results of a recent study indicates that nearly 80% of the global population is under high incident threat when a broadened criteria defined by human water security and biodiversity was adopted [7]. The need to tackle our water threat is immediate: in its Millennium Development Goals, the World Health Organization targets to "halve the proportion of people without sustainable access to safe drinking water and basic sanitation" by 2015 [8]. To address the world's daunting water challenges, it is imperative to improve water resource management, implement more effective water policies, and advance the science and technology of water production and purification [9, 10].

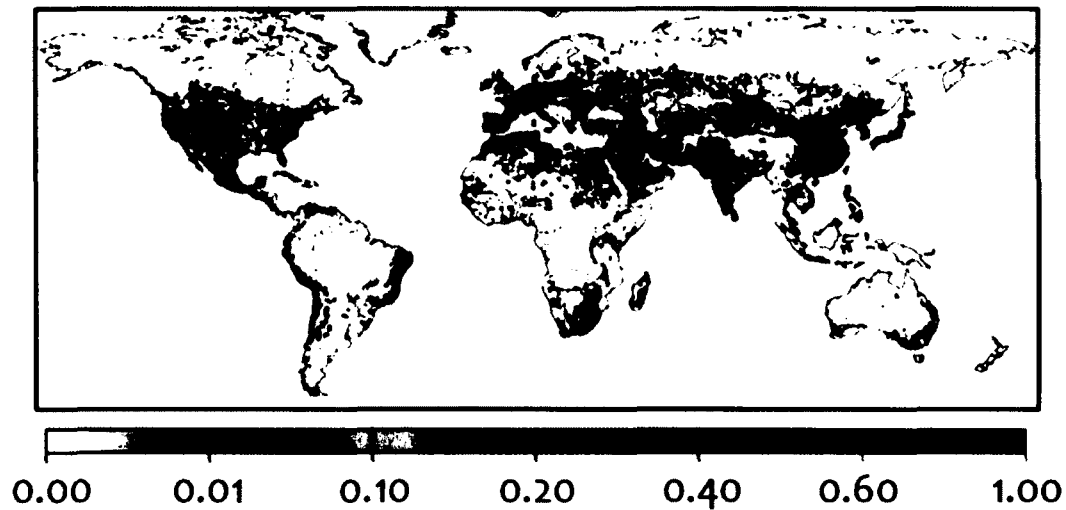


Figure 1.1. Global distribution of water scarcity index, defined as the fraction of renewable freshwater resource withdrawn for consumption by all sectors [6]. A region is considered highly water stressed if the index is higher than 0.4. Approximately 2.4 billion people are currently living in highly water-stressed areas.

Equally as pressing is the need to address the world's energy problems. Current global energy demand far exceeds our capacity for sustainable production. Figure 1.2 shows the breakdown of our primary energy till present, and the projected pathways for sustainability [11]. Prolonged reliance on fossil fuels, which provide the bulk of our present energy, is untenable because of the emission of greenhouse gases and air pollutants [12]. Recent progress in environmentally-benign energy technologies and carbon capture and sequestration methods has been encouraging. However, to realize the transition to a sustainable energy future, further efforts are necessary to advance existing alternative energy production technologies and overcome the current technical limitations [13]. At the same time, additional sustainable sources that are presently overlooked need to be explored and rigorously pursued to diversify our energy portfolio.

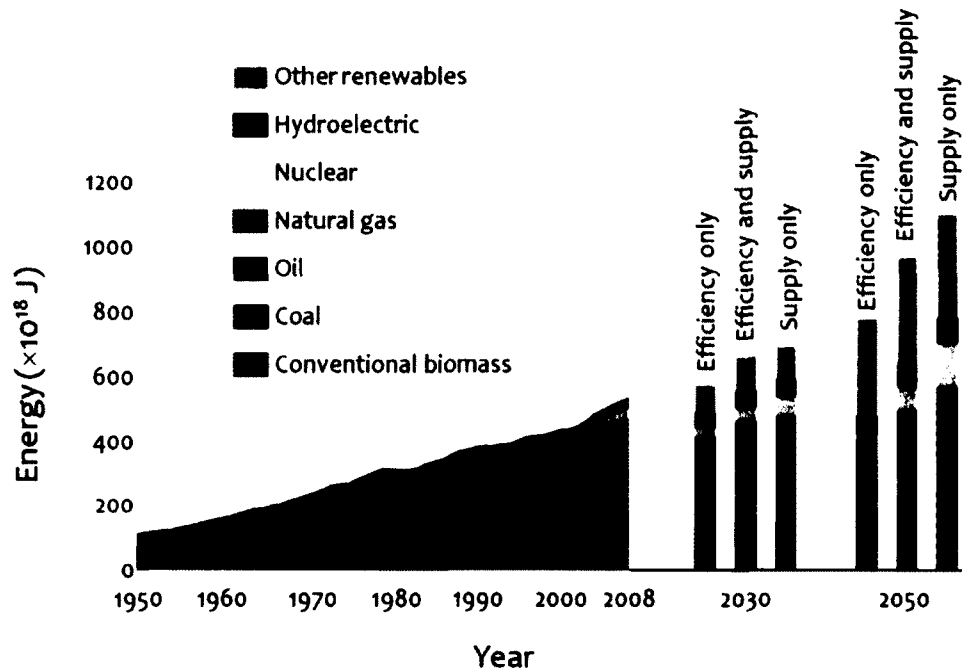


Figure 1.2. Development of primary energy sources from 1950 to 2008. Three illustrative projected pathways for the years 2030 and 2050 are included, representing different strategic approaches to meet our future energy demands. Note that “other renewable” are only a barely visible fraction of the energy breakdown in 2008. Adapted from Global Energy Assessment [11].

The rapidly expanding global population and an accelerating increase in the standard of living for a growing middle class exert further mounting strain on our water and energy demand [13-15]. Energy and water are inextricably and reciprocally linked: the production of energy requires significant amounts of water and produces substantial quantity of wastewater that needs treatment, while the production, purification, transport, and distribution of water, and the treatment and disposal of wastewater are equally dependent upon an affordable energy supply. In their recent publications, both the United Nations and the World Bank have identified the interlocking relation between water and energy for strategic actions [16, 17].

Water and energy are also intricately connected to food [18]. The production, refrigeration, transportation, and processing of food, feed, and fiber consumes energy and water. At the same time, bioenergy and food production competes directly for arable land and water. To further compound to these problems, climate change threatens to exacerbate the global water, energy, and food challenges [7, 13, 14, 17, 19-22]. The water-energy-food nexus, against the backdrop of climate change, is illustrated in Figure 1.3 [19]. In order to meet the challenges of the nexus in a sustainable manner, existing methods need to be advanced and new technologies developed.

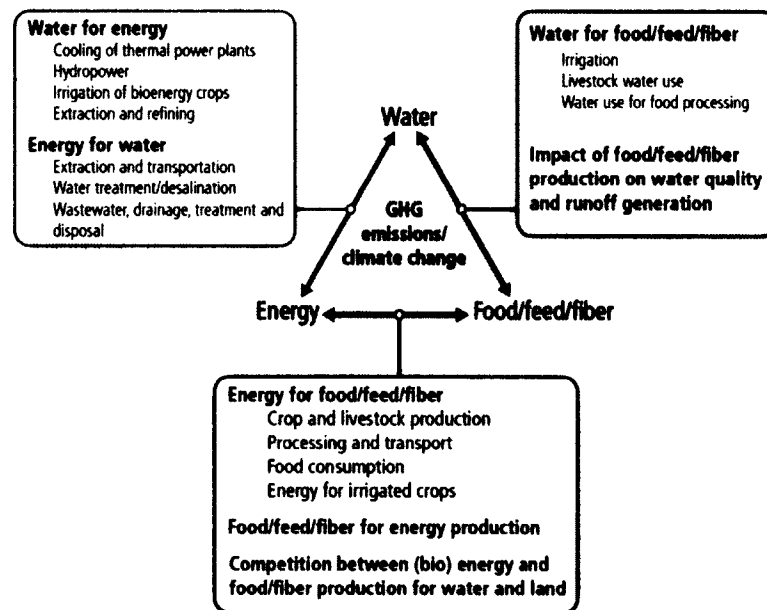


Figure 1.3. Chart illustrating the interactive pathways between water, energy, and food/feed/ fiber, against the backdrop of climate change. Adapted from IPCC 5th Assessment Report [19].

Membrane-based technologies can offer cost-effective and environmentally sensible solutions to alleviate the pressure on our water and energy demands. The advantage of membrane-based processes is succinctly demonstrated by reverse osmosis seawater desalination: the substantially lower energy requirement of reverse osmosis compared to

the alternative thermal distillation enabled the membrane process to gradually establish itself as the leading desalination technology [23, 24]. Emerging membrane technologies have the same benefits as their conventional counterparts. Furthermore, the novel technologies can possess additional competitive advantages that allow them to access applications that are beyond the reach of traditional membrane processes. Hence, emerging membrane-based technologies holds promise to meet some of our water and energy challenges [9, 25].

1.2 OBJECTIVES AND SCOPE OF THE THESIS

The overarching goal of the proposed research is to advance emerging membrane-based technologies — forward osmosis (FO), pressure retarded osmosis (PRO), and reverse electrodialysis (RED) — for the sustainable production of water and energy. The work strategically focuses on answering the most urgent questions at the core of each technology and rigorously tackling the principal challenges. It adopts a fundamentals-grounded approach to evaluate the thermodynamic and kinetic potential of the processes, and achieve robust mechanistic understanding of FO, PRO, and RED. The gleaned insights can be utilized to guide membrane and process development.

The specific targets of this thesis are:

- i. Demonstrate the fabrication of thin-film composite polymeric membranes capable of attaining high performance in osmotically-driven membrane processes, FO and PRO.

- ii. Analyze the performance limiting phenomena in PRO energy production and elucidate their intricate relationship with membrane transport and structural properties.
- iii. Examine the impact of organic fouling in PRO power generation, shed light on the fouling mechanism, and devise effective cleaning techniques that are environmentally-benign.
- iv. Assess the efficiency attainable with pressure retarded osmosis and reverse electro dialysis in salinity gradient power generation, and identify the theoretical upper bounds as constrained by thermodynamic laws.
- v. Compare and highlight the relative merits and drawbacks of salinity energy conversion to useful work using PRO and RED, and relate the comparative advantages to the intrinsic working principles of the technology.

While the studies carried out in thesis are, by no means, definitive and conclusive, they aim to enhance the scientific community's understanding and contribute to making strides towards realization of the technologies.

1.3 THESIS ORGANIZATION

The thesis begins with an introduction of the novel membrane-based technologies studied here: forward osmosis, pressure retarded osmosis, and reverse electro dialysis. In Chapter 2, the basic working principles of the three processes are briefly presented and the chief characteristic distinguishing them from conventional membrane processes are underscored. The chapter highlights the potential environmental applications and

discusses the anticipated challenges. This background chapter lays the scientific foundation of the thesis work and aims to serve as a primer for the subsequent chapters.

Chapters 3 and 4 focus on advancing FO and PRO membranes. The limitations of currently available membranes in osmotically-driven membrane processes (i.e., FO and PRO) are analyzed and the key influencing parameters identified. A membrane fabrication platform, guided by knowledge acquired from the analysis, is presented. By judicious control of the fabrication conditions in the non-solvent induced phase separation step of casting the membrane support layer, and thoughtful modification of membrane selective layer via chemical post-treatment, the study demonstrates hand-cast thin-film composite membranes that can overcome the technical limitations plaguing current commercial membranes.

Chapter 5 delves deeper into factors influencing the membrane power density: a key performance parameter in PRO. Earlier in Chapter 4, a mass transport model incorporating all performance limiting phenomena was formulated to derive the governing equations for water and salt fluxes in pressure retarded osmosis. The complete equations enabled the accurate prediction of flux behavior and, hence, power density performance. Through methodical analysis of the performance limiting effects, the study sheds light on the role of membrane transport and structural properties. The prospect of PRO power generation with natural salinity gradients is critically assessed by determining the potential power density attainable with membranes that are within our technological reach. Technical gaps hindering further advancement of PRO energy production are identified and discussed.

Chapter 6 approaches PRO salinity gradient power generation from thermodynamic and energy efficiency perspectives. The Gibbs free energy of mixing released when fresh river water flows into the oceans represents the theoretical energy that can be harnessed in a hypothetical reversible thermodynamic process. Actual PRO is irreversible because of inevitable entropy production and, hence, have lower practical efficiencies. To obtain a more accurate assessment of pressure retarded osmosis power generation, we apply thermodynamic concepts to evaluate the intrinsic energy efficiency and project the global potential of sustainable energy production from the controlled mixing of river water and seawater. The same approach is employed in Chapter 8 to assess RED power generation from salinity gradients.

Chapter 7 turns the focus towards the implications of using natural waters for PRO power generation. The presence of ubiquitous natural organic matter (NOM) in river water is anticipated to cause membrane fouling and negatively affect process productivity. Here, a methodical study of organic fouling in PRO is carried out to elucidate the fouling mechanism and quantify the corresponding performance decline. The potential of a quick chemical-free osmotic backwash technique is explored and the effectiveness in recovering performance is investigated.

Chapter 8 moves on to reverse electrodialysis power generation, where a critical assessment of the energy efficiency and power density inherent to the technology is presented. The efficiency of converting salinity energy into useful work and the membrane power density are two primary performance indicators that determine the cost-effectiveness of salinity energy production. This chapter simultaneously analyzes the efficiency and power density achievable with technologically-available ion exchange

membranes to obtain a better grasp of the feasibility of RED energy production with natural salinity gradients.

The preceding studies on pressure retarded osmosis and reverse electro dialysis culminates in a direct performance comparison in Chapter 9. The energy efficiency and power density of PRO and RED achievable with existing state-of-the-art membranes are analyzed. The capabilities and limitations of the technologies are identified and related to characteristic working principle governing the process. The prospects of PRO and RED power generation from natural, anthropogenic, and engineered salinity gradients are examined and discussed.

Lastly, Chapter 10 summarizes the thesis' main findings and details the salient contributions. The concluding remarks discuss the implications of these findings within the broader context of sustainable water and energy production, and offer perspectives on the future directions of forward osmosis, pressure retarded osmosis, and reverse electro dialysis.

1.4 KEY CONTRIBUTIONS

This section briefly describes the broad impacts of this dissertation research, while the detailed contributions are presented in the concluding chapter. In summary, **this work surmounted a major hurdle that was impeding the advancement of osmotically-driven membrane processes** by demonstrating the fabrication of thin-film composite membranes capable of achieving unprecedented high performance in forward osmosis and pressure retarded osmosis. **The membrane fabrication and modification platform described here can serve to guide future membrane development efforts.**

The mass transport model presented in this thesis enabled a more **mechanistic understanding of the role of membrane properties on PRO power density**. The finding was extended to show that the optimum power density is obtained with the appropriate balance of transport and structural properties. Hand-cast membranes with such tailored properties exhibited **power densities in excess of 10 W/m², over twice the benchmark of 5 W/m² estimated for PRO power generation with natural salinity gradients to be cost-effective**. Thermodynamic analysis of constant-pressure PRO revealed that the process can **potentially attain energy efficiencies up to 91.1% with river water and seawater**.

The exceptional thermodynamics and kinetics (energy extraction efficiency and power density, respectively) of PRO bodes well for the advancement of sustainable power generation with natural salinity gradients. However, **membrane fouling is anticipated to deduct up to 25% from the useful work in PRO energy production** with river water and seawater, as demonstrated in one of the dissertation's studies. Hence, fouling is likely to be the main challenge and the development of fouling mitigation strategies will be pivotal to realize the potential of salinity energy production with PRO. An expedient, chemical-free osmotic backwash cleaning method proposed in this work was shown to **effectively recover around half of the performance lost to membrane fouling**.

Reverse electrodialysis is the main competitor to PRO in extracting energy from salinity gradients. This thesis analyzed the potential performance of RED with technologically-available high performance ion exchange membranes and showed that **the energy efficiency is ~39%, while power density of ~0.6 W/m² can be obtained**.

The study indicates that, to reap the most reward in power density enhancement, the focal point of **development efforts should center on the membrane conductivity and the channel design of membrane stacks.**

The thesis then further showed that, compared to RED, PRO is better at converting salinity energy to useful work over a range of concentration differences. For natural, anthropogenic, and engineered salinity gradients, **PRO can achieve greater energy efficiency of (54–56%) and higher power densities (2.4–38 W/m²),** two key performance metrics, than RED (18–38% and 0.77–1.2 W/m²). The study further highlighted an **intrinsic inability of RED to take advantage of larger salinity gradients** that is attributed to a characteristic limitation of the Nernst potential.

1.5 REFERENCES

- [1] Smalley, R. E., Future Global Energy Prosperity: The Terawatt Challenge. *MRS Bulletin* **2005**, *30* (06), 412-417.
- [2] McGinnis, R. L. Elimelech, M., Global Challenges in Energy and Water Supply: The Promise of Engineered Osmosis. *Environmental Science & Technology* **2008**, *42* (23), 8625-8629.
- [3] <http://www.engineeringchallenges.org/> (Accessed on: 22 April, 2014).
- [4] General Assembly, *Resolution 64/292*, The United Nations **2010**.
- [5] Montgomery, M. A. Elimelech, M., Water and sanitation in developing countries: Including health in the equation. *Environmental Science & Technology* **2007**, *41* (1), 17-24.
- [6] Oki, T. Kanae, S., Global Hydrological Cycles and World Water Resources. *Science* **2006**, *313* (5790), 1068-1072.
- [7] Vorosmarty, C. J.; McIntyre, P. B.; Gessner, M. O.; Dudgeon, D.; Prusevich, A.; Green, P.; Glidden, S.; Bunn, S. E.; Sullivan, C. A.; Liermann, C. R. Davies, P. M., Global threats to human water security and river biodiversity. *Nature* **2010**, *467* (7315), 555-561.
- [8] <http://www.un.org/millenniumgoals/> (Accessed on: 23 April, 2014).
- [9] Shannon, M. A.; Bohn, P. W.; Elimelech, M.; Georgiadis, J. G.; Marinas, B. J. Mayes, A. M., Science and technology for water purification in the coming decades. *Nature* **2008**, *452* (7185), 301-310.
- [10] Elimelech, M., Special Paper: The global challenge for adequate and safe water. *Journal of Water Supply: Research & Technology-AQUA* **2006**, *55* (1), 3-10.
- [11] Global Energy Assessment, Toward a Sustainable Future. Cambridge University Press, Cambridge, UK and New York, NY, USA and the International Institute for Applied Systems Analysis, Laxenburg, Austria, **2012**.
- [12] Evans, A.; Strezov, V. Evans, T. J., Assessment of sustainability indicators for renewable energy technologies. *Renewable and Sustainable Energy Reviews* **2009**, *13* (5), 1082-1088.
- [13] Chu, S. Majumdar, A., Opportunities and challenges for a sustainable energy future. *Nature* **2012**, *488* (7411), 294-303.
- [14] Vorosmarty, C. J.; Green, P.; Salisbury, J. Lammers, R. B., Global Water Resources: Vulnerability from Climate Change and Population Growth. *Science* **2000**, *289* (5477), 284-288.
- [15] Gleick, P. H., Water Use. *Annual Review of Environment and Resources* **2003**, *28* (1), 275-314.
- [16] Miletto, M. Ünver, O. C., Richard, *World Water Development Report - Water and Energy*, The United Nations World Water Assessment Programme **2014**.
- [17] Rodriguez, D. J.; Delgado, A.; DeLaquil, P. Sohns, A., *Thirsty Energy: Securing Energy in a Water-Constrained World*, The World Bank, **2013**.
- [18] Godfray, H. C. J.; Beddington, J. R.; Crute, I. R.; Haddad, L.; Lawrence, D.; Muir, J. F.; Pretty, J.; Robinson, S.; Thomas, S. M. Toulmin, C., Food Security: The Challenge of Feeding 9 Billion People. *Science* **2010**, *327* (5967), 812-818.

-
- [19] Field, C. B.; Barros, V.; Mach, K.; Mastrandrea, M. Intergovernmental Panel on Climate Change (IPCC) 5th Assessment Report Working Group II., *Climate Change 2014: Impacts, Adaptation, and Vulnerability*. 2014.
- [20] Lobell, D. B.; Burke, M. B.; Tebaldi, C.; Mastrandrea, M. D.; Falcon, W. P. Naylor, R. L., Prioritizing Climate Change Adaptation Needs for Food Security in 2030. *Science* **2008**, *319* (5863), 607-610.
- [21] Schmidhuber, J. Tubiello, F. N., Global food security under climate change. *Proceedings of the National Academy of Sciences* **2007**, *104* (50), 19703-19708.
- [22] Barnett, T. P.; Adam, J. C. Lettenmaier, D. P., Potential impacts of a warming climate on water availability in snow-dominated regions. *Nature* **2005**, *438* (7066), 303-309.
- [23] Elimelech, M. Phillip, W. A., The Future of Seawater Desalination: Energy, Technology, and the Environment. *Science* **2011**, *333* (6043), 712-717.
- [24] Fritzmann, C.; Lowenberg, J.; Wintgens, T. Melin, T., State-of-the-art of reverse osmosis desalination. *Desalination* **2007**, *216* (1-3), 1-76.
- [25] Logan, B. E. Elimelech, M., Membrane-based processes for sustainable power generation using water. *Nature* **2012**, *488* (7411), 313-319.

Chapter 2:

Principles of Osmotically-Driven Membrane Processes and Ion Exchange Membrane Processes

CHAPTER ABSTRACT

Forward osmosis (FO), pressure retarded osmosis (PRO), and reverse electrodialysis (RED) are emerging membrane-based technologies that can address our water and energy challenges. FO separation utilizes an osmotic gradient to drive the permeation of water across a semipermeable membrane. FO can potentially be applied to desalinate seawater and hypersaline feed streams, treat and reclaim wastewater, and dewater algae broth for biofuel production, with reduced energy requirement. PRO is the power generation analog of FO and can produce energy from the controlled mixing of a concentrated and a dilute solution by utilizing the osmotic pressure difference between the solutions. PRO can potentially harness energy from natural and anthropogenic salinity gradients, or convert low-grade heat from, for example, industrial waste heat or low-temperature geothermal sources, to electricity. RED is another emerging technology that can convert salinity energy to useful work. In RED, ion exchange membranes allow the selective permeation of counter ions from the high concentration solution to the low concentration solution, and the ionic current is then converted to an electric current. To further advance FO, PRO, and RED towards actual implementation, membranes capable of attaining high performance need to be developed. In addition, membrane fouling is anticipated to be a critical problem for all three processes and further studies are necessary to attain a more comprehensive understanding of the fouling phenomena to guide the formulation of effective mitigation strategies.

2.1 INTRODUCTION

Membrane processes possess several advantages over other separation methods. These advantages include being relatively less energy intensive, exhibiting higher selectivity, requiring only mild conditions for separation, and having a large selection of membrane materials with tunable properties to further customize for specific tasks [1]. Additionally, the membranes can be packaged into efficient, economical, and high surface-area modules, enabling straightforward scale-up of industrial processes with a relatively low areal footprint requirement [1, 2]. As a result, conventional pressure-driven membrane processes, such as reverse osmosis, nanofiltration, ultrafiltration, and microfiltration, are employed in a wide range of aqueous separation applications, e.g., water and wastewater treatment [3], desalination [4, 5], food and dairy industry [6, 7], petrochemical separations [8], and filtration of pharmaceutical solutions [9]. A recent market report estimates that the global combined membrane demand (both aqueous and gas separation) was valued at ~US\$15.6 billion in 2012 and is anticipated to grow by 8% annually to reach US\$25 billion by 2018 [10].

Emerging and novel membrane processes, likewise, possess the above-mentioned benefits. Additionally, these novel membrane technologies can potentially be used in applications that are beyond the reach of traditional membrane processes, thus broadening the membrane market. Forward osmosis (FO), one such emerging technology, belongs to the class of osmotically-driven membrane processes (ODMPs) that utilize an osmotic pressure difference, rather than a hydraulic pressure difference, as the driving force. The versatility of membranes also allows for their application in unconventional, non-separation processes, as succinctly demonstrated by pressure

retarded osmosis (PRO), another ODMF, and reverse electrodialysis (RED). Instead of performing separations, PRO and RED membranes convert the Gibbs free energy into useful work through the controlled mixing of salinity gradients. In this chapter FO, PRO, and RED are introduced, their potential applications are highlighted, and the challenges for each technology are discussed.

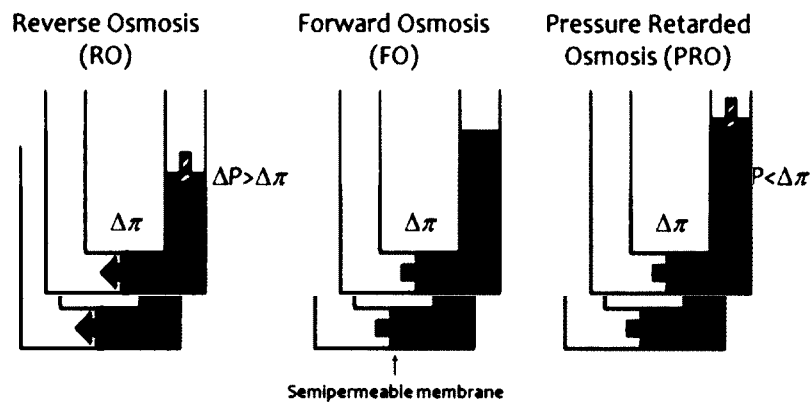


Figure 2.1. Schematics of RO, FO, and PRO, with the arrows indicating the direction of water flow. In RO, the hydraulic pressure difference exceeds the osmotic pressure of the high concentration solution and water diffuses against the osmotic gradient to the low concentration solution. For FO, there is no hydraulic pressure difference and water diffuses to the more saline side of the membrane. In PRO, water still diffuses to the HC solution as the hydraulic pressure applied is less than the osmotic pressure difference, although at an impeded rate.

2.2 FORWARD OSMOSIS

Working Principles. In reverse osmosis (RO), an example of a conventional pressure-driven membrane process, an external hydraulic pressure is applied to the aqueous feed stream (e.g., seawater) to drive the permeation of water across a membrane (Figure 2.1). Because the membrane is selectively permeable to water but retains salts and other dissolved solutes, the product is, hence, pure water. Forward osmosis (FO) employs the same semipermeable membrane but, in contrast, uses a more concentrated “draw”

solution to produce an osmotic gradient that drives water flux from the “feed” solution (Figure 2.1). In other words, FO utilizes an osmotic pressure difference as the driving force, while RO uses a hydraulic pressure difference.

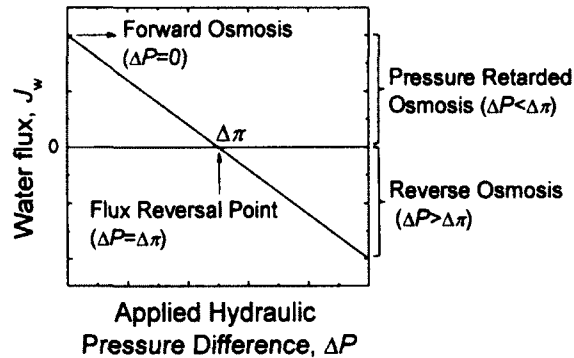


Figure 2.2. Representative plot of water flux across a semipermeable membrane as a function of the applied hydraulic pressure difference. FO occurs when the hydraulic pressure difference is zero, while PRO takes place when the ΔP greater than zero but less than the osmotic pressure difference. If ΔP is exactly equal $\Delta\pi$, there is no water flux. Further increasing ΔP to exceed $\Delta\pi$ results in RO.

The demarcation between the pressure- and osmotically-driven membrane processes is graphically represented in Figure 2.2, which shows water flux as a function of the applied hydraulic pressure. Operating with $\Delta P > \Delta\pi$ yields RO, while FO corresponds to the vertical axis intercept (i.e., $\Delta P = 0$). The general equation governing water flux, J_w , in pressure- and osmotically-driven membrane processes is

$$J_w = A(\Delta\pi_m - \Delta P) \quad (2.1)$$

where A is the water permeability coefficient, an intrinsic property of the membrane, $\Delta\pi_m$ is the osmotic pressure difference across the membrane, and ΔP is the hydraulic pressure difference between the high and low concentration solutions. In FO, ΔP is zero and the flux water is the product of the membrane hydraulic permeability coefficient, A , and the osmotic pressure difference, $\Delta\pi_m$. When ΔP exceeds $\Delta\pi_m$, the direction of water

flux is inverted (eq 2.1) and water permeates against the osmotic gradient to the low concentration side, hence osmosis is *reversed*.

Applications. The principles of forward osmosis is employed is hydration bags, where a highly concentrated sugar solution draws water from contaminated point sources through a semipermeable membrane [11]. Because the process requires no energy input, hydration packs are ideal for scenarios where access to power is restricted, such as for military use or deployment in disaster relief scenarios. Additionally, FO has promising applications in wastewater reclamation [12-14], industrial wastewater treatment [11, 15], osmotic membrane bioreactors [16, 17], and liquid food processing [18, 19]. Recently, FO was successfully applied to treat oil and gas wastewater, saving nearly a million gallons of water (3800 m^3) per well application [20]. The treatment method, termed “Green Machine”, uses common table salt (NaCl) as the draw salt and a schematic is shown in Figure 2.3A. Using the same draw salt, FO was employed in another pilot system to treat landfill leachate up to 94-96% recovery (Figure 2.3B), i.e., ~95% of the water was drawn out from the leachate stream to concentrate it 20-fold [20].

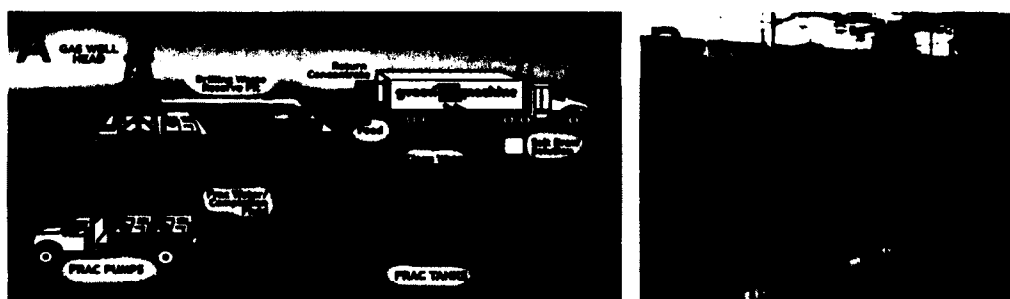


Figure 2.3. A) Schematic of the Green Machine that utilizes FO to treat oil and gas wastewater (image from www.htiwater.com) and B) FO membrane modules used in a pilot plant to treat landfill leachate [20].

The draw solute for the high concentration solution can be an inorganic salt (e.g., NaCl, MgCl_2) or saccharides, as in most of the abovementioned potential applications

[21]. Alternatively, a stimulus-sensitive draw solution can be employed as the high concentration stream, where an external stimulus (such as heat or a magnetic field) is utilized to reconstitute the diluted draw stream [22, 23]. The use of low-temperature heat (<80 °C) to regenerate the draw solution is particularly attractive from an economic perspective, given the relative abundance of industrial waste heat and low-grade geothermal energy sources that are currently unutilized [24]. Several thermal-sensitive draw solutions have been proposed for potential application to FO [23, 25, 26], with thermolytic draw solutions of ammonia-carbon dioxide being the most extensively studied [27-29].

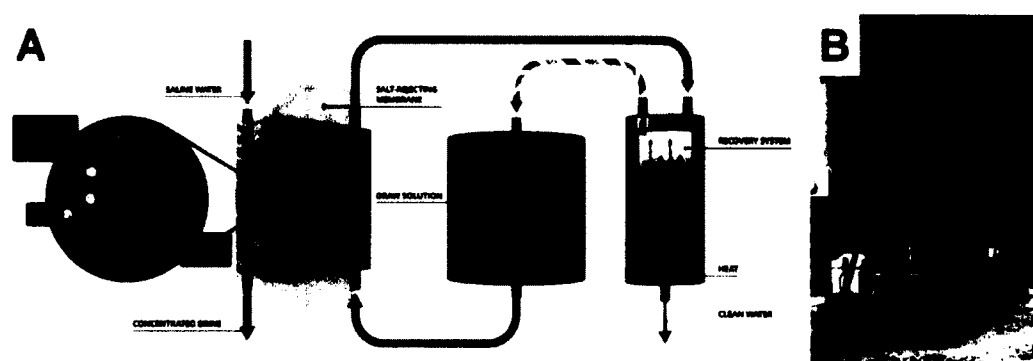


Figure 2.4. A) Schematic of the ammonia-carbon dioxide desalination system. A concentrated solution of $\text{NH}_3\text{-CO}_2$ draws water from the saline feed stream. The diluted $\text{NH}_3\text{-CO}_2$ solution is sent to a recovery stage where low-grade heat is used to regenerate the draw solution and produce fresh water (image from www.oasyswater.com). B) FO membrane brine contactor pilot system treating shale gas produced water, concentrating the feed stream from ~73 g/L to 180 g/L TDS [30].

In a novel FO desalination process, a concentrated draw solution of ammonia-carbon dioxide is used to draw water from a saline feed solution (e.g., seawater or brine) [27]. The diluted draw solution is then fed to a distillation column where low-grade heat is used to strip the dissolved gases, thus producing fresh water (Figure 2.4A). Therefore, the FO desalination process taps into widely available and relatively inexpensive low-

temperature heat sources to desalinate saline streams, achieving an energy advantage over conventional desalination processes that requires electricity or high-temperature heat. Another prominent advantage is that FO can treat hypersaline feed streams (Figure 2.4B) that cannot be desalinated by reverse osmosis and thermal distillation, such as produced water from hydraulic fracturing operations that typically contain 70-250 g/L total dissolved solids (TDS) [30].

Forward osmosis can also be hybridized with other technologies to achieve an even greater range of applications. For instance, an integrated FO-RO membrane system is proposed to potentially lower the energy requirement of seawater desalination [31]. Other studies demonstrated the potential extraction of phosphorus, an important agricultural resource, from wastewater using FO coupled with membrane distillation, another novel membrane technology [32, 33]. Osmotic dilution applications that do not require the draw solution to be regenerated have also been investigated [34]. For example, vastly abundant seawater can be used as the draw solution for broth dewatering in the production of algae biofuels. In another osmotic dilution application, concentrated fertilizer solutions are employed to draw irrigational water from brackish sources, thus reducing the demand on fresh water.

Challenges. Despite the promising potential, forward osmosis has only made limited progress beyond conceptualization. One of the main reasons for the hindered development is the lack of an adequate membrane tailored for FO. Current state-of-the-art thin-film composite polyamide RO membranes (Figure 2.5A) perform poorly in FO as the support layer, designed to withstand the high operating pressures in reverse osmosis, gives rise to severe internal concentration polarization (ICP) *within* the membrane which

drastically reduces the driving force for water flux [35, 36]. Commercial integrally-skinned membranes made from cellulose triacetate (CTA) were specifically designed to suppress ICP (Figure 2.5B), but have relatively low pure water permeability and salt rejection that is intrinsic to the membrane class [27]. Additionally, the asymmetric CTA membranes degrade when exposed to alkaline or acidic solutions [2]. The narrow range of operable pH and the inferior permeability-selectivity acutely limit the productivity and potential applications of the CTA membranes. As such, the development of high performance membranes for FO is imperative to the progress of the technology.

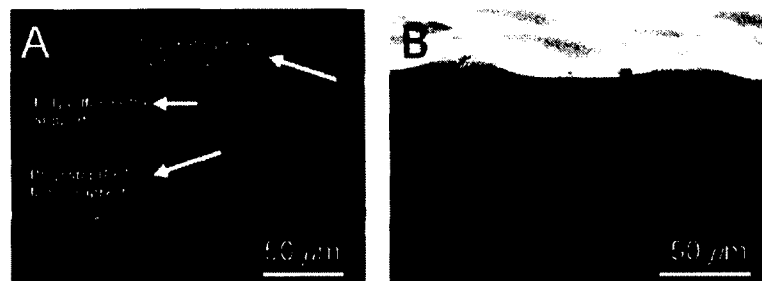


Figure 2.5. Scanning electron microscopy (SEM) micrographs of A) commercial thin-film composite polyamide reverse osmosis membrane [27] and B) commercial integrally-skinned asymmetric cellulose triacetate forward osmosis membrane [37].

Apart from membrane development, draw solutions that are able to generate high osmotic pressures, are benign (both environmental- and health-wise), can be readily reconstituted, does not permeate membranes easily, and are relative inexpensive need to be further advanced to realize the potential of forward osmosis [21]. Fouling, an important phenomenon plaguing conventional pressure-driven membrane processes by reducing water flux productivity, deteriorating permeate quality, increasing energy consumption and treatment cost, as well as shortening membrane life span [38], is anticipated to afflict forward osmosis as well. However fundamental differences from RO fouling are expected in FO as applied hydraulic pressure is absent [39-42]. Further

investigations are necessary to elucidate the FO fouling mechanism and formulate effective fouling mitigations strategies.

2.3 PRESSURE RETARDED OSMOSIS

Working Principles. Pressure retarded osmosis (PRO), similar to forward osmosis, utilizes a net osmotic pressure difference to drive water permeation. Therefore, both PRO and FO are osmotically-driven membrane processes. In PRO, the high concentration draw solution is pressurized, but applied hydraulic pressure difference is less than the osmotic pressure difference across the membrane and, therefore, water still permeates from the more dilute feed solution into the draw side (Figure 2.1). However, the applied hydraulic pressure difference subtracts from the osmotic driving force (i.e., $\Delta\pi - \Delta P$) and, hence, the water flux is *retarded* (eq 2.1).

PRO is represented in Figure 2.2 for $0 < \Delta P < \Delta\pi$. The permeating water increases the draw solution volume and, hence, work is done by the expansion of the pressurized draw solution. The water flux falls correspondingly with increasing applied pressure and reaches zero (flux reversal point) as ΔP approaches the osmotic pressure difference across the membrane (Figure 2.2). Further increasing the hydraulic pressure reverses the water flux direction and the process transits to reverse osmosis, consuming energy to carry out separation. Hence, PRO is the opposite of RO and the energy production analog of forward osmosis, converting the chemical energy between two solutions of different concentration, or “salinity energy”, to useful work.

The Gibbs free energy of mixing represents the theoretical maximum energy that can be extracted when two solutions of different concentrations are combined [43]:

$$-\frac{\Delta G_{\text{mix}, \nu_{\text{LC}}}}{\nu R_g T} \approx \frac{c_{\text{M}}}{\phi} \ln c_{\text{M}} - c_{\text{LC}} \ln c_{\text{LC}} - \frac{(1-\phi)}{\phi} c_{\text{HC}} \ln c_{\text{HC}} \quad (2.2)$$

where $\Delta G_{\text{mix}, \nu_{\text{LC}}}$ is the energy per unit volume of the low concentration (LC) solution, ν is the number of ions each electrolyte molecule dissociates into, R_g is the gas constant, T is the absolute temperature, and c is the molar salt concentration of the resultant mixture, low concentration solution, and high concentration (HC) solution (denoted by subscripts M, LC, and HC, respectively). The LC solution volumetric fraction, ϕ , is the ratio of LC solution volume to the volume of both the LC and HC solution. Figure 2.6 shows an early drawing of a rudimentary contraption to harness the salinity energy between fresh river water and salty seawater for power generation [44].

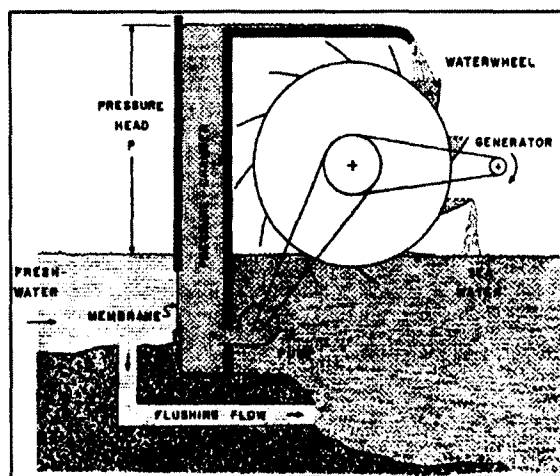


Figure 2.6. Schematic of a “osmotic salination energy converter”, a rudimentary generator to extract power from the natural flow of freshwater into the sea [44].

Applications. The power generating capability enables PRO to be employed for energy production applications. The osmotic pressure difference between fresh river water and seawater is ~ 27 bar, corresponding to the hydraulic head of a ~ 270 m waterfall. Taking seawater to be 0.6 M NaCl and river water to be 1.5 mM NaCl, the Gibbs free energy of mixing released when a cubic meter of river water mixes with an infinite

amount of seawater is ~ 0.81 kWh, or 2.9 kJ/L (eq 2.2). The annual global river discharge is an enormous $\sim 37,300$ km³ [45]. Therefore, natural salinity gradients (i.e., the mixing of seawater and river water) represent a currently untapped source that can potentially contribute to our renewable energy portfolio.

In 2009, the world's first natural salinity gradient PRO power plant was inaugurated in Norway, demonstrating the potential viability of the process (Figure 2.7A) [46]. In this modern version, a hydroturbine is used to extract work from the expanding draw solution volume (Figure 2.7B), rather than an antiquated water wheel as depicted in Figure 2.6. The perennial availability of fresh water estuaries flow indicates that PRO systems will not suffer from the intermittency problems that plague some of the other renewable energy generation methods.

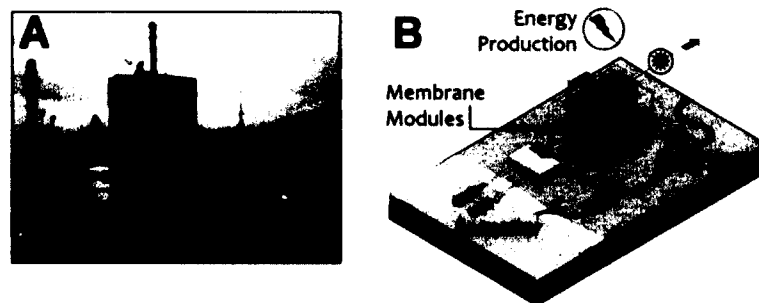


Figure 2.7. A) Seawater-river water PRO demonstration plant in Tofte, Norway (image from www.statkraft.com). B) Schematic of PRO power generation utilizing seawater as the high concentration draw solution and river water as the low concentration feed solution (adapted from ref. [47]).

Apart from seawater, PRO can utilize other hypersaline streams such as water from the Great Salt Lakes in Utah, USA, or the Dead Sea on the border of Israel and Jordan for the draw solution, thereby producing more energy from the controlled mixing process [47-49]. Alternatively, PRO can use anthropogenic waste streams, for example pairing concentrated brine from desalination plants with effluent from wastewater treatment

plants [50-52]. The benefits achieved here is twofold: the power generated in PRO offsets the net energy requirement for desalination and the wastewater is dewatered for easier handling and treatment.

A closed-loop version of PRO, the osmotic heat engine (OHE), has also been proposed [47, 53, 54]. This process employs engineered solutions and uses low-grade heat to power the separation of the draw and feed solution, hence, regenerating the salinity gradient. For example, the draw solution can be a thermolytic salt such as ammonia-carbon dioxide [54, 55], or a highly concentrated solution of an inorganic salt that can be reconstituted by membrane distillation [47, 53], an emerging membrane technology that utilizes low-temperature heat to drive separation. Therefore the OHE, in essence, converts low-grade industrial waste heat and low-temperature geothermal sources that would otherwise be discarded into useable electricity.

Challenges. Similar to FO, the lack of suitable membranes is a major impediment to the advancement of PRO power generation from salinity gradients. Power density, defined as the power produced per unit membrane area, quantifies the rate of salinity energy conversion to useful work. A high power density is desired to reduce capital cost associated with membrane modules. For instance, doubling the power density would halve the membrane area required to generate the same power. Feasibility studies showed that implementation of PRO power generation hinges on the membrane power density [56-58]. In particular, the power density needs to be greater than 5 W/m^2 for seawater-river water PRO power generation to be cost-effective [59].

However, commercially available thin-film composite polyamide RO membranes and integrally-skinned cellulose acetate membranes discussed earlier in the Forward Osmosis

section both yielded power densities considerably lower than the 5 W/m^2 benchmark, with the Norwegian PRO demonstration plant generating less than 0.5 W/m^2 using the asymmetric cellulose acetate membranes [46, 56, 60]. Figure 2.8 summarizes the PRO power densities demonstrated experimentally with model seawater-river water over the past four decades (horizontal line denotes the 5 W/m^2 target). Unlike FO membranes, PRO membranes are subjected to an applied hydraulic pressure and, therefore, have the additional requirement of adequate mechanical robustness [61]. This requisite is especially crucial when hypersaline draw solutions are used, as a greater hydraulic pressure is applied to match the higher draw solution osmotic pressure. To realize PRO power generation, membranes capable of attaining high power densities while possessing sufficient mechanical strength need to be developed.

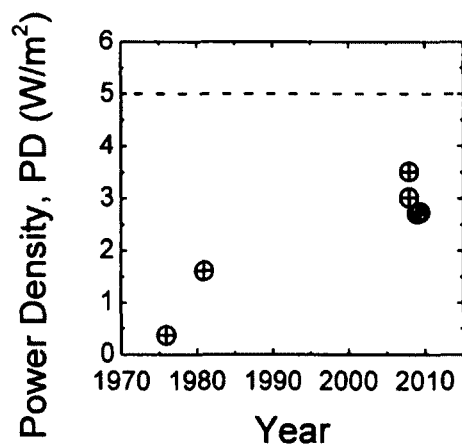


Figure 2.8. Timeline of power densities demonstrated experimentally with model seawater as the draw solution and model river water as the feed solution in coupon-sized membranes. Horizontal dashed blue line indicates the 5 W/m^2 benchmark necessary for cost-effective power generation with natural salinity gradients. Plot adapted from ref. [46].

Previous studies to gauge the potential of sustainable power generation from natural salinity gradients employed the Gibbs free energy of mixing [62-64]. However, the free

energy of mixing represents the theoretical maximum energy that is available for useful work by an ideal reversible thermodynamic process. Hence, the potential estimated by the studies circumscribe the theoretical upper bound of the energy available but does not signify the energy that can actually be realized in a practical PRO unit operation. To obtain a more accurate grasp on the intrinsic efficiency and accessible energy from salinity gradients, more in-depth analyses that incorporate thermodynamic limitations and practical constraints are needed.

Fouling, which is caused by the accumulation of colloidal and particulate matter (colloidal fouling), organic macromolecules (organic fouling), sparingly soluble inorganic compounds (scaling), and microorganisms (biofouling) on the membranes, is a key issue restricting the efficient performance of pressure-driven membrane processes [2]. The ubiquitous nature of the foulants alludes that PRO will similarly face fouling issues that will hamper process efficiency. However in PRO, as foulants are brought into the membrane support layer by water permeation, fouling will occur uncharacteristically *within* the membrane, rather than typically *on* the membrane surface [40, 41, 65]. This unique circumstance sets PRO apart from conventional fouling and warrants further investigations.

2.4 REVERSE ELECTRODIALYSIS

Working Principles. Reverse osmosis, forward osmosis, and pressure retarded osmosis all utilize membranes that are selectively permeable to water and reject solutes. On the other hand, reverse electrodialysis employs charged ion exchange membranes (IEMs) that are selectively permeable to counter ions while retaining co-ions and water. Hence,

the transport mechanism of RED is fundamentally different from FO and PRO. RED is the power generation analog of electrodialysis (ED) separation, just as PRO is to RO.

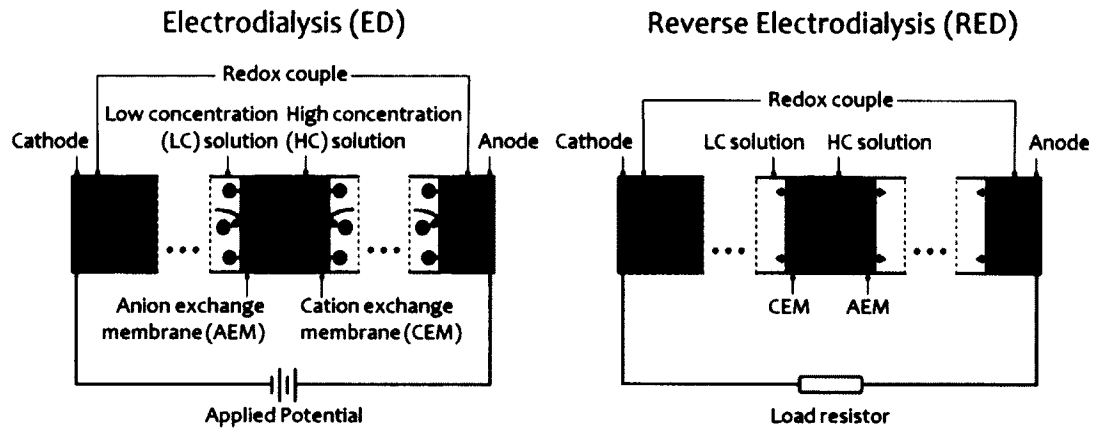


Figure 2.9. Schematics of ED and RED, with the arrows indicating the direction of cation (+) and anion (-) permeation. Repeating pairs of negatively charged cation exchange membranes and positively charged anion exchange membranes selectively allow the permeation of oppositely charged counter ions (cations and anions, respectively), while rejecting co-ions. Note that only one ion exchange membrane pair and the end electrodes are shown. In ED, separation is achieved by applying a voltage to drive the permeation of ions against the ion concentration gradient, i.e., from the low concentration (LC) solution to the high concentration (HC) solution. Conversely, the concentration gradient drives the transport of ions from the HC solution to the LC solution in RED, producing a Nernst potential. A reversible redox couple is circulated at the end electrodes to convert the ionic current to an electric current and work is done by the external load resistor.

For both ED and RED, repeating pairs of cation exchange membranes (CEM) and anion exchange membranes (AEM) alternate between high concentration (HC) and low concentration (LC) solutions (Figure 2.9). The ion concentration difference between the HC and LC solution produces a Nernst potential, ξ_{Nernst} , across the stack:

$$\xi_{\text{Nernst}} = \frac{NR_g T}{zF} \ln \frac{c_{\text{HC}}}{c_{\text{LC}}} \quad (2.3)$$

where N is the number of repeating cells, R_g is the gas constant, T is the absolute temperature, z is the ion valence, and F is the Faraday constant. The molar salt concentration, c , of the high and low concentration solutions are denoted by the subscripts HC and LC, respectively.

In ED, an external voltage in excess of the Nernst potential is applied across the stack to drive the transport of ions against the concentration gradient. The ions permeate from the LC solution into the HC solution, thereby achieving separation. Conversely in RED, the direction of ion flux is reversed; the concentration difference drives the permeation of ions from the HC solution, across the IEMs, and into the LC solution. A reversible redox couple is circulated at the end electrodes to convert the ionic current to an electric current, and useful work is done by the external load resistor. For an ohmic system, the governing equation for ion flux, i , in ED and RED is:

$$i = \frac{1}{ASR_{\text{stack}}} (\xi_{\text{Nernst}} - \xi_{\text{ext}}) \quad (2.4)$$

where ASR_{stack} is the area specific resistance of the stack (defined as the product of stack resistance and effective stack area) and ξ_{ext} is the voltage of the applied external potential (ED) or potential difference across the external resistor (RED). Note that both the RED ion flux equation (eq 2.4) and the PRO water flux equation (eq 2.1) take on the same general form: $1/ASR_{\text{stack}}$, ξ_{Nernst} , and ξ_{ext} are analogous to A , $\Delta\pi_m$, and, ΔP , respectively.

RED is similar to PRO as both processes convert salinity energy into useful work, albeit by different means: salinity energy is directly converted to electricity with RED, while electrical energy is produced indirectly in PRO through the mechanical work of the expanding draw solution volume. In addition, while both processes are membrane-based, the transport phenomenon of RED principally differs from PRO: water permeates across

salt-rejecting membranes in PRO whereas ions are transport across charged membranes in RED. Therefore, PRO and RED are anticipated to possess advantages and limitations characteristic to the technologies.

Applications. RED has been proposed to harness the Gibbs free energy of mixing from natural salinity gradients (Figure 2.10A) [66-68], from hypersaline streams of natural or anthropogenic origin [47, 69, 70], and in closed-looped osmotic heat engines [71]. In October 2013, a 50 kW pilot plant was inaugurated in the Netherlands at the Afsluitdijk to demonstrate power generation from the controlled mixing of seawater and river water (Figure 2.10B) [72]. Alternatively, instead of generating electricity, the end electrodes of can be designed to carry out electrolysis, such as the production of hydrogen fuel [73]. Several systems integrating RED with other processes have also been proposed. For instance, RED can be combined with capacitive electrodes to achieve synergistic benefits [74, 75], while microbial fuel cells coupled with RED have been shown to exhibit enhanced productivity [76, 77]. These microbial reverse electro dialysis fuel cells can further incorporate thermolytic solutions, such as ammonia-carbon dioxide, to convert waste heat to electricity or hydrogen [78, 79].

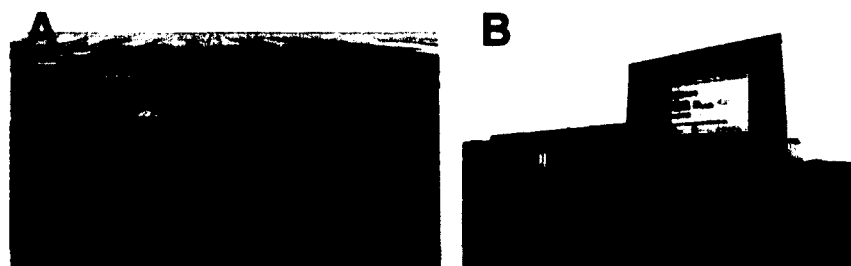


Figure 2.10. A) Artist impression of a seawater-river water RED power generation plant. The inputs streams are “zout” and “zoet” (salty and sweet in English, respectively), and the output stream is “brak” (brackish). B) 50 kW RED pilot plant at the Afsluitdijk in the Netherlands. Images from <http://www.utwente.nl>.

Challenges. Similar to PRO, membrane power density is vital in determining the economical feasibility of RED power generation [80-82]. Membrane properties and stack design are the chief factors that determine the electrical resistance of RED membrane stacks which, in turn, affects the power density. The ionic conductivity of current commercially available ion exchange membranes are relatively high and contributes significantly to the internal resistance of the RED stack, giving rise to relatively low power densities [83-85]. Furthermore, because the electrolyte conductivity is proportional to the salt concentration [86], the low concentration solution drastically elevates the area specific resistance of the RED stack and detrimentally diminishes the power density performance [84, 87, 88]. To improve the membrane power density to cost-effective levels, the RED stack design needs to be enhanced to mitigate the effects of the LC solution resistance and ion exchange membranes with high conductivity need to be developed. Furthermore, the market price of ion exchange membranes is considerably greater than salt rejecting RO membranes. Therefore, for salinity energy sources that are accessible by both PRO and RED, the capital cost associated with membranes is tilted in favor of the more economical PRO.

Fouling is an important performance limiting phenomenon in ED separation [89-92]. The ubiquitous nature of foulant indicates that membrane fouling will also likely be a crucial issue for RED power generation with natural feed streams. Preliminary fouling studies, indeed, point to performance decline in a seawater-river water RED system [93]. Further investigations will be necessary to better understand the fouling mechanisms, develop fouling resistance membranes, and devise effective fouling mitigation strategies.

2.5 REFERENCES

- [1] Mulder, M., Basic principles of membrane technology. 2nd ed.; Kluwer Academic, Dordrecht ; Boston, 1996; p 564 p.
- [2] Baker, R. W., Membrane technology and applications. 3rd ed.; John Wiley & Sons, Chichester, West Sussex ; Hoboken, 2012; p xiv, 575 p.
- [3] Van Der Bruggen, B.; Vandecasteele, C.; Van Gestel, T.; Doyen, W. Leysen, R., A review of pressure-driven membrane processes in wastewater treatment and drinking water production. *Environmental Progress* **2003**, *22* (1), 46-56.
- [4] Matsuura, T., Progress in membrane science and technology for seawater desalination — a review. *Desalination* **2001**, *134* (1–3), 47-54.
- [5] Elimelech, M. Phillip, W. A., The Future of Seawater Desalination: Energy, Technology, and the Environment. *Science* **2011**, *333* (6043), 712-717.
- [6] Daufin, G.; Escudier, J. P.; Carrère, H.; Bérot, S.; Fillaudeau, L. Decloux, M., Recent and Emerging Applications of Membrane Processes in the Food and Dairy Industry. *Food and Bioproducts Processing* **2001**, *79* (2), 89-102.
- [7] Girard, B.; Fukumoto, L. R. Sefa Koseoglu, S., Membrane Processing of Fruit Juices and Beverages: A Review. *Critical Reviews in Biotechnology* **2000**, *20* (2), 109-175.
- [8] Takht Ravanchi, M.; Kaghazchi, T. Kargari, A., Application of membrane separation processes in petrochemical industry: a review. *Desalination* **2009**, *235* (1–3), 199-244.
- [9] McKinnon, B. Avis, K., Membrane filtration of pharmaceutical solutions. *American Journal of Health-System Pharmacy* **1993**, *50* (9), 1921-1936.
- [10] *Market Report: Global Membrane Technology Market*, Acmite Market Intelligence **March, 2013**.
- [11] Cath, T. Y.; Childress, A. E. Elimelech, M., Forward osmosis: Principles, applications, and recent developments. *Journal of Membrane Science* **2006**, *281* (1–2), 70-87.
- [12] Cath, T. Y.; Adams, D. Childress, A. E., Membrane contactor processes for wastewater reclamation in space: II. Combined direct osmosis, osmotic distillation, and membrane distillation for treatment of metabolic wastewater. *Journal of Membrane Science* **2005**, *257* (1–2), 111-119.
- [13] Cath, T. Y.; Gormly, S.; Beaudry, E. G.; Flynn, M. T.; Adams, V. D. Childress, A. E., Membrane contactor processes for wastewater reclamation in space: Part I. Direct osmotic concentration as pretreatment for reverse osmosis. *Journal of Membrane Science* **2005**, *257* (1–2), 85-98.
- [14] Cartinella, J. L.; Cath, T. Y.; Flynn, M. T.; Miller, G. C.; Hunter, K. W. Childress, A. E., Removal of Natural Steroid Hormones from Wastewater Using Membrane Contactor Processes. *Environmental Science & Technology* **2006**, *40* (23), 7381-7386.
- [15] Holloway, R. W.; Childress, A. E.; Dennett, K. E. Cath, T. Y., Forward osmosis for concentration of anaerobic digester centrate. *Water Research* **2007**, *41* (17), 4005-4014.
- [16] Achilli, A.; Cath, T. Y.; Marchand, E. A. Childress, A. E., The forward osmosis membrane bioreactor: A low fouling alternative to MBR processes. *Desalination* **2009**, *239* (1–3), 10-21.

- [17] Cornelissen, E. R.; Harmsen, D.; Beerendonk, E. F.; Qin, J. J.; Oo, H.; de Korte, K. F. Kappelhof, J. W. M. N., The innovative Osmotic Membrane Bioreactor (OMBR) for reuse of wastewater. *Water Science & Technology* **2011**, *63* (8), 1557-1565.
- [18] Garcia-Castello, E. M.; McCutcheon, J. R. Elimelech, M., Performance evaluation of sucrose concentration using forward osmosis. *Journal of Membrane Science* **2009**, *338* (1–2), 61-66.
- [19] Jiao, B.; Cassano, A. Drioli, E., Recent advances on membrane processes for the concentration of fruit juices: a review. *Journal of Food Engineering* **2004**, *63* (3), 303-324.
- [20] Coday, B. D.; Xu, P.; Beaudry, E. G.; Herron, J.; Lampi, K.; Hancock, N. T. Cath, T. Y., The sweet spot of forward osmosis: Treatment of produced water, drilling wastewater, and other complex and difficult liquid streams. *Desalination* **2014**, *333* (1), 23-35.
- [21] Achilli, A.; Cath, T. Y. Childress, A. E., Selection of inorganic-based draw solutions for forward osmosis applications. *Journal of Membrane Science* **2010**, *364* (1–2), 233-241.
- [22] Stone, M. L.; Rae, C.; Stewart, F. F. Wilson, A. D., Switchable polarity solvents as draw solutes for forward osmosis. *Desalination* **2013**, *312*, 124-129.
- [23] Liu, Z.; Bai, H.; Lee, J. Sun, D. D., A low-energy forward osmosis process to produce drinking water. *Energy & Environmental Science* **2011**, *4* (7), 2582-2585.
- [24] Hendricks, T. Choate, W. T., Engineering scoping study of thermoelectric generator systems for industrial waste heat recovery. *US Department of Energy* **2006**, *20*, 6.
- [25] Li, D.; Zhang, X.; Yao, J.; Simon, G. P. Wang, H., Stimuli-responsive polymer hydrogels as a new class of draw agent for forward osmosis desalination. *Chemical Communications* **2011**, *47* (6), 1710-1712.
- [26] Mok, Y.; Nakayama, D.; Noh, M.; Jang, S.; Kim, T. Lee, Y., Circulatory osmotic desalination driven by a mild temperature gradient based on lower critical solution temperature (LCST) phase transition materials. *Physical Chemistry Chemical Physics* **2013**, *15* (44), 19510-19517.
- [27] McCutcheon, J. R.; McGinnis, R. L. Elimelech, M., A novel ammonia–carbon dioxide forward (direct) osmosis desalination process. *Desalination* **2005**, *174* (1), 1-11.
- [28] McCutcheon, J. R.; McGinnis, R. L. Elimelech, M., Desalination by ammonia–carbon dioxide forward osmosis: Influence of draw and feed solution concentrations on process performance. *Journal of Membrane Science* **2006**, *278* (1–2), 114-123.
- [29] Yong, J. S.; Phillip, W. A. Elimelech, M., Reverse Permeation of Weak Electrolyte Draw Solutes in Forward Osmosis. *Industrial & Engineering Chemistry Research* **2012**, *51* (41), 13463-13472.
- [30] McGinnis, R. L.; Hancock, N. T.; Nowosielski-Slepowron, M. S. McGurgan, G. D., Pilot demonstration of the NH₃/CO₂ forward osmosis desalination process on high salinity brines. *Desalination* **2013**, *312*, 67-74.
- [31] Shaffer, D. L.; Yip, N. Y.; Gilron, J. Elimelech, M., Seawater desalination for agriculture by integrated forward and reverse osmosis: Improved product water quality for potentially less energy. *Journal of Membrane Science* **2012**, *415–416*, 1-8.
- [32] Xie, M.; Nghiem, L. D.; Price, W. E. Elimelech, M., A Forward Osmosis–Membrane Distillation Hybrid Process for Direct Sewer Mining: System Performance and Limitations. *Environmental Science & Technology* **2013**, *47* (23), 13486-13493.

- [33] Xie, M.; Nghiem, L. D.; Price, W. E. Elimelech, M., Toward Resource Recovery from Wastewater: Extraction of Phosphorus from Digested Sludge Using a Hybrid Forward Osmosis–Membrane Distillation Process. *Environmental Science & Technology Letters* **2014**, *1* (2), 191-195.
- [34] Hoover, L. A.; Phillip, W. A.; Tiraferri, A.; Yip, N. Y. Elimelech, M., Forward with Osmosis: Emerging Applications for Greater Sustainability. *Environmental Science & Technology* **2011**, *45* (23), 9824-9830.
- [35] Gray, G. T.; McCutcheon, J. R. Elimelech, M., Internal concentration polarization in forward osmosis: role of membrane orientation. *Desalination* **2006**, *197* (1-3), 1-8.
- [36] McCutcheon, J. R. Elimelech, M., Influence of concentrative and dilutive internal concentration polarization on flux behavior in forward osmosis. *Journal of Membrane Science* **2006**, *284* (1-2), 237-247.
- [37] Yip, N. Y.; Tiraferri, A.; Phillip, W. A.; Schiffman, J. D. Elimelech, M., High Performance Thin-Film Composite Forward Osmosis Membrane. *Environmental Science & Technology* **2010**, *44* (10), 3812-3818.
- [38] Bartels, C. R.; Wilf, M.; Andes, K. Iong, J., Design considerations for wastewater treatment by reverse osmosis. *Water Science and Technology* **2005**, *51* (6-7), 473-482.
- [39] Liu, Y. Mi, B., Combined fouling of forward osmosis membranes: Synergistic foulant interaction and direct observation of fouling layer formation. *Journal of Membrane Science* **2012**, *407–408*, 136-144.
- [40] Mi, B. Elimelech, M., Chemical and physical aspects of organic fouling of forward osmosis membranes. *Journal of Membrane Science* **2008**, *320* (1–2), 292-302.
- [41] Mi, B. Elimelech, M., Organic fouling of forward osmosis membranes: Fouling reversibility and cleaning without chemical reagents. *Journal of Membrane Science* **2010**, *348* (1–2), 337-345.
- [42] Mi, B. Elimelech, M., Gypsum Scaling and Cleaning in Forward Osmosis: Measurements and Mechanisms. *Environmental Science & Technology* **2010**, *44* (6), 2022-2028.
- [43] Yip, N. Y. Elimelech, M., Thermodynamic and Energy Efficiency Analysis of Power Generation from Natural Salinity Gradients by Pressure Retarded Osmosis. *Environmental Science & Technology* **2012**, *46* (9), 5230-5239.
- [44] Norman, R. S., Water Salination: A Source of Energy. *Science* **1974**, *186* (4161), 350-352.
- [45] Dai, A. Trenberth, K. E., Estimates of freshwater discharge from continents: Latitudinal and seasonal variations. *Journal of Hydrometeorology* **2002**, *3* (6), 660-687.
- [46] Achilli, A. Childress, A. E., Pressure retarded osmosis: From the vision of Sidney Loeb to the first prototype installation - Review. *Desalination* **2010**, *261* (3), 205-211.
- [47] Logan, B. E. Elimelech, M., Membrane-based processes for sustainable power generation using water. *Nature* **2012**, *488* (7411), 313-319.
- [48] Loeb, S., Energy production at the Dead Sea by pressure-retarded osmosis: challenge or chimera? *Desalination* **1998**, *120* (3), 247-262.
- [49] Loeb, S., One hundred and thirty benign and renewable megawatts from Great Salt Lake? The possibilities of hydroelectric power by pressure-retarded osmosis. *Desalination* **2001**, *141* (1), 85-91.
- [50] Kurihara, M. Hanakawa, M., Mega-ton Water System: Japanese national research and development project on seawater desalination and wastewater reclamation. *Desalination* **2013**, *308*, 131-137.

- [51] Prante, J. L.; Ruskowitz, J. A.; Childress, A. E. Achilli, A., RO-PRO desalination: An integrated low-energy approach to seawater desalination. *Applied Energy* **2014**, *120*, 104-114.
- [52] Saito, K.; Irie, M.; Zaitso, S.; Sakai, H.; Hayashi, H. Tanioka, A., Power generation with salinity gradient by pressure retarded osmosis using concentrated brine from SWRO system and treated sewage as pure water. *Desalination and Water Treatment* **2012**, *41* (1-3), 114-121.
- [53] Lin, S.; Yip, N. Y.; Cath, T. Y.; Osuji, C. O. Elimelech, M., Hybrid Pressure Retarded Osmosis - Membrane Distillation System for Power Generation from Low-Grade Heat: Thermodynamic Analysis and Energy Efficiency. *Environmental Science & Technology* **2014**.
- [54] McGinnis, R. L.; McCutcheon, J. R. Elimelech, M., A novel ammonia-carbon dioxide osmotic heat engine for power generation. *Journal of Membrane Science* **2007**, *305* (1-2), 13-19.
- [55] McGinnis, R. L. Elimelech, M., Global Challenges in Energy and Water Supply: The Promise of Engineered Osmosis. *Environmental Science & Technology* **2008**, *42* (23), 8625-8629.
- [56] Lee, K. L.; Baker, R. W. Lonsdale, H. K., Membranes for Power-Generation by Pressure-Retarded Osmosis. *Journal of Membrane Science* **1981**, *8* (2), 141-171.
- [57] Gerstandt, K.; Peinemann, K. V.; Skilhagen, S. E.; Thorsen, T. Holt, T., Membrane processes in energy supply for an osmotic power plant. *Desalination* **2008**, *224* (1-3), 64-70.
- [58] Skilhagen, S. E.; Dugstad, J. E. Aaberg, R. J., Osmotic power — power production based on the osmotic pressure difference between waters with varying salt gradients. *Desalination* **2008**, *220* (1-3), 476-482.
- [59] Skilhagen, S. E., Osmotic power - a new, renewable energy source. *Desalination and Water Treatment* **2010**, *15* (1-3), 271-278.
- [60] Brekke, G. The Statkraft Prototype Plant. <http://osmosis-summit.event123.no/programsummit2010.cfm> (Accessed on: 16 April, 2014).
- [61] Achilli, A.; Cath, T. Y. Childress, A. E., Power generation with pressure retarded osmosis: An experimental and theoretical investigation. *Journal of Membrane Science* **2009**, *343* (1-2), 42-52.
- [62] La Mantia, F.; Pasta, M.; Deshazer, H. D.; Logan, B. E. Cui, Y., Batteries for Efficient Energy Extraction from a Water Salinity Difference. *Nano Letters* **2011**, *11* (4), 1810-1813.
- [63] Nijmeijer, K. Metz, S., Chapter 5: Salinity Gradient Energy. In *Sustainability Science and Engineering*, Isabel, C. E. Andrea, I. S., Eds. Elsevier: 2010; Vol. Volume 2, pp 95-139.
- [64] Thorsen, T. Holt, T., The potential for power production from salinity gradients by pressure retarded osmosis. *Journal of Membrane Science* **2009**, *335* (1-2), 103-110.
- [65] Thelin, W. R.; Sivertsen, E.; Holt, T. Brekke, G., Natural organic matter fouling in pressure retarded osmosis. *Journal of Membrane Science* **2013**, *438* (0), 46-56.
- [66] Lacey, R. E., Energy by reverse electrodialysis. *Ocean Engineering* **1980**, *7* (1), 1-47.
- [67] Post, J. W.; Hamelers, H. V. M. Buisman, C. J. N., Energy Recovery from Controlled Mixing Salt and Fresh Water with a Reverse Electrodialysis System. *Environmental Science & Technology* **2008**, *42* (15), 5785-5790.

- [68] Weinstein, J. N. Leitz, F. B., Electric Power from Differences in Salinity: The Dialytic Battery. *Science* **1976**, *191* (4227), 557-559.
- [69] Daniilidis, A.; Vermaas, D. A.; Herber, R. Nijmeijer, K., Experimentally obtainable energy from mixing river water, seawater or brines with reverse electro dialysis. *Renewable Energy* **2014**, *64* (0), 123-131.
- [70] Tedesco, M.; Cipollina, A.; Tamburini, A.; van Baak, W. Micale, G., Modelling the Reverse ElectroDialysis process with seawater and concentrated brines. *Desalination and Water Treatment* **2012**, *49* (1-3), 404-424.
- [71] Luo, X.; Cao, X.; Mo, Y.; Xiao, K.; Zhang, X.; Liang, P. Huang, X., Power generation by coupling reverse electro dialysis and ammonium bicarbonate: Implication for recovery of waste heat. *Electrochemistry Communications* **2012**, *19* (0), 25-28.
- [72] wetsus News. <http://www.wetsus.nl/home/wetsus-news/> (Accessed on: 16 April, 2014).
- [73] Hatzell, M. C.; Ivanov, I.; D. Cusick, R.; Zhu, X. Logan, B. E., Comparison of hydrogen production and electrical power generation for energy capture in closed-loop ammonium bicarbonate reverse electro dialysis systems. *Physical Chemistry Chemical Physics* **2014**, *16* (4), 1632-1638.
- [74] Sales, B. B.; Saakes, M.; Post, J. W.; Buisman, C. J. N.; Biesheuvel, P. M. Hamelers, H. V. M., Direct Power Production from a Water Salinity Difference in a Membrane-Modified Supercapacitor Flow Cell. *Environmental Science & Technology* **2010**, *44* (14), 5661-5665.
- [75] Vermaas, D. A.; Bajracharya, S.; Sales, B. B.; Saakes, M.; Hamelers, B. Nijmeijer, K., Clean energy generation using capacitive electrodes in reverse electro dialysis. *Energy & Environmental Science* **2013**, *6* (2), 643-651.
- [76] Kim, Y. Logan, B. E., Microbial Reverse Electro dialysis Cells for Synergistically Enhanced Power Production. *Environmental Science & Technology* **2011**, *45* (13), 5834-5839.
- [77] Kim, Y. Logan, B. E., Hydrogen production from inexhaustible supplies of fresh and salt water using microbial reverse-electro dialysis electrolysis cells. *Proceedings of the National Academy of Sciences* **2011**, *108* (39), 16176-16181.
- [78] Cusick, R. D.; Kim, Y. Logan, B. E., Energy Capture from Thermolytic Solutions in Microbial Reverse-Electro dialysis Cells. *Science* **2012**, *335* (6075), 1474-1477.
- [79] Nam, J.-Y.; Cusick, R. D.; Kim, Y. Logan, B. E., Hydrogen Generation in Microbial Reverse-Electro dialysis Electrolysis Cells Using a Heat-Regenerated Salt Solution. *Environmental Science & Technology* **2012**, *46* (9), 5240-5246.
- [80] Daniilidis, A.; Herber, R. Vermaas, D. A., Upscale potential and financial feasibility of a reverse electro dialysis power plant. *Applied Energy* **2014**, *119* (0), 257-265.
- [81] Długolecki, P.; Gambier, A.; Nijmeijer, K. Wessling, M., Practical Potential of Reverse Electro dialysis As Process for Sustainable Energy Generation. *Environmental Science & Technology* **2009**, *43* (17), 6888-6894.
- [82] Post, J. W.; Goeting, C. H.; Valk, J.; Goinga, S.; Veerman, J.; Hamelers, H. V. M. Hack, P. J. F. M., Towards implementation of reverse electro dialysis for power generation from salinity gradients. *Desalination and Water Treatment* **2010**, *16* (1-3), 182-193.

-
- [83] Długołęcki, P.; Nijmeijer, K.; Metz, S. Wessling, M., Current status of ion exchange membranes for power generation from salinity gradients. *Journal of Membrane Science* **2008**, *319* (1–2), 214-222.
- [84] Veerman, J.; de Jong, R. M.; Saakes, M.; Metz, S. J. Harmsen, G. J., Reverse electro dialysis: Comparison of six commercial membrane pairs on the thermodynamic efficiency and power density. *Journal of Membrane Science* **2009**, *343* (1–2), 7-15.
- [85] Güler, E.; Elizen, R.; Vermaas, D. A.; Saakes, M. Nijmeijer, K., Performance-determining membrane properties in reverse electro dialysis. *Journal of Membrane Science* **2013**, *446* (0), 266-276.
- [86] Robinson, R. A. Stokes, R. H., Electrolyte solutions. 2nd rev. ed.; Dover Publications, Mineola, NY, **2002**; p xv, 571 p.
- [87] Vermaas, D. A.; Guler, E.; Saakes, M. Nijmeijer, K., Theoretical power density from salinity gradients using reverse electro dialysis. *Energy Procedia* **2012**, *20* (0), 170-184.
- [88] Vermaas, D. A.; Saakes, M. Nijmeijer, K., Doubled Power Density from Salinity Gradients at Reduced Intermembrane Distance. *Environmental Science & Technology* **2011**, *45* (16), 7089-7095.
- [89] Korngold, E.; de Körösy, F.; Rahav, R. Taboch, M. F., Fouling of anionselective membranes in electro dialysis. *Desalination* **1970**, *8* (2), 195-220.
- [90] Lindstrand, V.; Sundström, G. Jönsson, A.-S., Fouling of electro dialysis membranes by organic substances. *Desalination* **2000**, *128* (1), 91-102.
- [91] Lindstrand, V.; Jönsson, A.-S. Sundström, G., Organic fouling of electro dialysis membranes with and without applied voltage. *Desalination* **2000**, *130* (1), 73-84.
- [92] Bazinet, L. Araya-Farias, M., Effect of calcium and carbonate concentrations on cationic membrane fouling during electro dialysis. *Journal of Colloid and Interface Science* **2005**, *281* (1), 188-196.
- [93] Vermaas, D. A.; Kunteng, D.; Saakes, M. Nijmeijer, K., Fouling in reverse electro dialysis under natural conditions. *Water Research* **2013**, *47* (3), 1289-1298.

Chapter 3:

High Performance Thin-Film Composite Forward Osmosis Membrane

CHAPTER ABSTRACT

Recent studies show that osmotically-driven membrane processes may be a viable technology for desalination, water and wastewater treatment, and power generation. However, the absence of a membrane designed for such processes is a significant obstacle hindering further advancements of this technology. This chapter presents the development of a high performance thin-film composite membrane for forward osmosis applications. The membrane consists of a selective polyamide active layer formed by interfacial polymerization on top of a polysulfone support layer fabricated by phase separation onto a thin (40 μm) polyester non-woven fabric. By careful selection of the polysulfone casting solution (i.e., polymer concentration and solvent composition) and tailoring the casting process, we produced a support layer with a mix of finger-like and sponge-like morphologies that give significantly enhanced membrane performance. The structure and performance of the new thin-film composite forward osmosis membrane are compared with those of commercial membranes. Using a 1.5 M NaCl draw solution and a pure water feed, the fabricated membranes produced water fluxes exceeding $18 \text{ Lm}^{-2}\text{h}^{-1}$, while consistently maintaining observed salt rejection greater than 97%. The high water flux of the fabricated thin-film composite forward osmosis membranes was directly related to the thickness, porosity, tortuosity, and pore structure of the polysulfone support layer. Furthermore, membrane performance did not degrade after prolonged exposure to an ammonium bicarbonate draw solution.

3.1 INTRODUCTION

Osmotically-driven membrane processes have the potential to sustainably produce clean drinking water or electric power. These membrane-based technologies exploit the natural phenomenon of osmosis, which occurs when two solutions of differing concentration are placed on opposite sides of a semi-permeable membrane. The generated osmotic pressure difference drives the permeation of water across the membrane from the dilute solution to the concentrated solution, while the selective property of the membrane retains the solutes in their respective solutions. Engineered osmosis relies on the appropriate selection of the concentrated draw solution. More energy efficient processes can be realized when the separation of draw solute from water requires less energy than the separation of water from contaminants dissolved in the dilute feed solution.

Forward osmosis (FO) is a subset of osmotically-driven membrane processes, which has promising applications in seawater desalination [1, 2], wastewater reclamation [3-5], industrial wastewater treatment [2, 6], osmotic membrane bioreactors [7], and liquid food processing [2, 8, 9]. For example, in a novel FO desalination process, a concentrated draw solution of ammonia-carbon dioxide is used to draw water from a saline feed solution. The diluted draw solution is then fed to a distillation column where low-grade heat is used to remove the dissolved gases, thus producing fresh water [10].

Despite the potential to address key issues surrounding global water and energy demands, osmotically-driven membrane processes have yet to progress significantly beyond conceptualization. The major obstacle to advancing this technology is the lack of an adequate membrane. A membrane designed for an osmotically-driven process should reject dissolved solutes, produce high permeate water fluxes, be compatible with the

selected draw solution, and withstand the mechanical stresses generated by the operating conditions. Existing commercial membranes lack one or more of the above mentioned characteristics, inhibiting their use in osmotically-driven membrane processes. Commercial FO membranes are made from cellulose triacetate (CTA) which degrades when exposed to an ammonium bicarbonate draw solution [11]. Additionally, cellulose acetate membranes have relatively low pure water permeability and salt rejection, which limits their use for desalination. On the other hand, conventional thin-film composite (TFC) reverse osmosis (RO) membranes exhibit high salt rejection and satisfy the chemical stability and mechanical strength requirements. However, TFC membranes yield very poor permeate water fluxes in FO because they are designed for pressure-driven membrane processes, such as RO [12].

TFC-RO membranes fail in FO operation because the thick and dense support layers, necessary to withstand large hydraulic pressures, result in internal concentration polarization (ICP). ICP adversely affects the performance of all asymmetric membranes in FO, with the effects being exacerbated for TFC-RO membranes due to their thick and dense porous support. The porous support layer acts as a diffusive boundary layer, which severely reduces the osmotic pressure difference across the active layer [13]. Because this boundary layer is unperturbed by stirring [13, 14], modifying the support layers is essential to minimize the performance-limiting effects of ICP that currently hinder TFC membranes [10]. Prior studies have demonstrated, through both experiments and modeling, that the additional resistance to mass transfer of this boundary layer is proportional to the support layer thickness and tortuosity, and inversely proportional to the support layer porosity [14-16]. Therefore, the ideal support layers for FO membranes

to enhance performance would be very thin, highly porous, and provide a direct path from the draw solution to the active surface of the membrane.

In this work, we demonstrate the fabrication of a TFC membrane tailored for FO operation. Innovative modifications made to the membrane casting procedure, as well as the resultant effects of these changes on the microstructure of the membranes are described. Salt rejection and water flux of the newly fabricated TFC-FO membranes are compared to commercially available RO and FO membranes. These performance results are linked to the membrane structural properties. Finally, the chemical stability of the TFC-FO membrane in a concentrated ammonium bicarbonate solution is demonstrated, indicating potential application in the ammonia-carbon dioxide FO process. This study aims to demonstrate the ability to fabricate membranes with a structure adapted to FO processes, thus providing a basis for further developments of osmotically-driven membranes.

3.2 MATERIALS AND METHODS

Materials and Chemicals. Polysulfone (PSf) beads (M_n : 22,000 Da), 1-methyl-2-pyrrolidinone (NMP, anhydrous, 99.5%), *N,N*-dimethylformamide (DMF, anhydrous, 99.8%), 1,3-phenylenediamine (MPD, >99%), and 1,3,5-benzenetricarbonyl trichloride (TMC, 98%) were used as received (Sigma-Aldrich, St. Louis, MO). TMC was dispersed in Isopar-G, a proprietary non-polar organic solvent (Univar, Redmond, WA). For the membrane performance tests, sodium chloride (NaCl, crystals, ACS reagent) from J.T. Baker (Phillipsburg, NJ) and ammonium bicarbonate (NH_4HCO_3 , powder, certified ACS)

from Fisher Scientific (Pittsburgh, PA) were dissolved in deionized (DI) water obtained from a Milli-Q ultrapure water purification system (Millipore, Billerica, MA).

A commercial polyester non-woven fabric (PET, Grade 3249, Ahlstrom, Helsinki, Finland) was used as a backing layer for the PSf supports. The thin (40 μm) PET fabric had a relatively open structure. Commercial asymmetric cellulose triacetate (HTI-CTA) forward osmosis membranes (Hydration Technology Inc., Albany, OR) and thin-film composite seawater reverse osmosis membranes (TFC-RO, SW30-HR, Dow Chemical Company, Midland, MI) were acquired for comparison. Additionally, the PET fabric layer of some TFC-RO samples was removed according to procedures described in our previous study [12]; these membrane samples are designated as "TFC-RO No PET".

Casting of Polysulfone Support. PSf beads (12 wt%) were dissolved in a mixed solvent system of DMF and NMP, at a ratio of 1:3 DMF:NMP on a weight basis. The solution was stirred at room temperature (23 °C) for 8 h and then stored in a desiccator for at least 15 h prior to casting. The thin, low-density PET fabric was attached to a clean glass plate using laboratory adhesive tape. NMP was applied to wet the fabric and the excess NMP was removed using an air knife. A casting knife (Gardco, Pompano Beach, FL), set at a gate height of 150 μm , was used to spread the PSf solution onto the wetted PET fabric. The whole composite was immediately immersed in a precipitation bath containing 3 wt% NMP in DI water at room temperature to initiate the phase separation. The support membrane was allowed to sit in the precipitation bath for 10 min, at which point it was transferred to a DI water bath for storage until polyamide formation.

Interfacial Polymerization of TFC Membrane. Polyamide TFC membranes were produced by first immersing a hand-cast PSf support membrane in an aqueous solution of

3.4 wt% MPD for 120 s. An air knife was then used to remove the excess MPD solution from the membrane surface. Next, the MPD-saturated support membrane was immersed into the 0.15 wt% TMC in Isopar-G solution for 60 s, resulting in the formation of an ultra-thin polyamide film. The composite membranes were cured in DI water at 95 °C for 120 s, then rinsed with a 200 ppm NaOCl aqueous solution for 120 s, followed by rinsing for 30 s with a 1000 ppm NaHSO₃ aqueous solution, before a final heat curing step at 95 °C for 120 s. The fabricated TFC membranes (TFC-FO) were rinsed thoroughly and stored in DI water at 4 °C. This formulation was adapted from a patent for interfacial polymerization of polyamide active layer on PSf support for TFC-RO membranes [17].

SEM Imaging and Thickness Measurement of Membrane. Micrographs of the membranes were obtained utilizing a Hitachi Ultra-High-Resolution Analytical Field Emission Scanning Electron Microscope (FE-SEM) SU-70. Cross-sections were obtained by flash-freezing the membranes using liquid nitrogen, then cracking the sample. An Emitech SC7620 sputtering machine was used to coat all samples for 15-30 s with gold-platinum. The thickness of the membranes was measured using a digital micrometer (series 293-330, Mitutoyo, Mississauga, Ontario Canada) at 5 different locations for each membrane sample.

Testing Membrane Performance in FO Mode. The experimental crossflow FO system employed is similar to that described in our previous studies [10, 12, 13]. The unit was custom built with channel dimensions of 77 mm long, 26 mm wide, and 3 mm deep on both sides of the membrane. We operated the unit with co-current cross-flows without mesh spacers. The volume of both feed and draw solutions was 2.0 L at the start

of each experimental run. Variable speed gear pumps (Cole-Parmer, Vernon Hills, IL) were used to pump the solutions in closed loops at 1.0 L/min (21.4 cm/s crossflow velocity) and a water bath (Neslab, Newington, NH) maintained the temperature of both the feed and draw solutions at 25 ± 0.5 °C. All membranes were tested in FO mode, with the porous support layer against the draw solution and the active layer against the feed solution.

The experimental protocol to determine water flux is similar to that previously described [10, 18]. A 1.5 M NaCl solution was used for the draw solution and DI water was used as the feed solution. The resulting bulk osmotic pressure difference, $\Delta\pi$, was 76.6 bar (1,110 psi), calculated by a software package from OLI Systems, Inc. (Morris Plains, NJ). After the water flux and temperature stabilized, the flux was taken as the average reading over 1 h. The draw solution concentration is assumed to be constant throughout the experiment, since the volumetric water flux was low relative to the volume of draw solution.

A similar experimental protocol was used to determine membrane performance and chemical stability with an ammonium bicarbonate draw solution (1.5 M NH_4HCO_3). After the initial test, the membrane was stored in 1.5 M NH_4HCO_3 (pH 7.9) at 4 °C for 7 days, removed from the bath, and re-tested. The bath was used to simulate prolonged exposure to high concentrations of NH_4HCO_3 . Storage at low temperature minimized potential growth of microorganisms on the membrane.

Determination of Pure Water Permeability and Salt Rejection. Pure water permeability and salt rejection of the TFC-FO and commercial membranes were evaluated in a laboratory-scale crossflow RO test unit [19]. The effective membrane area

was 20.02 cm², the crossflow velocity was fixed at 21.4 cm/s, and the temperature was constant at 25 ± 0.5 °C. The loaded membrane was first compacted with DI water at an applied pressure, ΔP , of 27.6 bar (400 psi) until the permeate flux reached a steady state (at least 15 h). Pure water flux, J_w , was calculated by dividing the volumetric permeate rate by the membrane area. Salt rejection was characterized by keeping the applied pressure at 27.6 bar (400 psi) and measuring rejection of 50 mM NaCl solution using a calibrated conductivity meter (Oakton Instruments, Vernon Hills, IL).

Intrinsic water permeability, A , was determined by dividing the water flux by the applied pressure, $A = J_w/\Delta P$. Observed NaCl rejection, R , was determined from the difference in bulk feed (c_b) and permeate (c_p) salt concentrations, $R = (1 - c_p)/c_b$. The rejection values for each sample are the average of three different measurements collected over approximately 30 min each. The solute permeability coefficient, B , was determined from [11, 20]:

$$B = J_w \left(\frac{1-R}{R} \right) \exp \left(-\frac{J_w}{k} \right) \quad (3.1)$$

where k , the crossflow cell mass transfer coefficient, is calculated from correlations for this geometry [21].

Determination of FO Membrane Structural Parameters. The support layer resistance to solute diffusion, K , of one TFC-FO membrane was determined using the experimental protocol previously described [13]. Water flux was measured in FO mode with DI water as the feed solution and NaCl draw concentrations of 0.05, 0.1, 0.5, 1.0, and 1.5 M. The resulting flux versus osmotic pressure data was used to calculate the resistance to solute diffusion, K , via fitting to [15]:

$$K = \left(\frac{1}{J_w} \right) \ln \frac{B + A\pi_{D,b}}{B + J_w + A\pi_{F,m}} \quad (3.2)$$

where J_w is the measured water flux, $\pi_{D,b}$ is the bulk osmotic pressure of the draw solution, and $\pi_{F,m}$ is the osmotic pressure at the membrane surface on the feed side (0 bar for DI water feed solution). The resistance to diffusion K can be expressed as the reciprocal of a thin film mass transfer coefficient [14]:

$$K = \frac{t_s \tau}{D\varepsilon} \quad (3.3)$$

where D is the diffusion coefficient of the draw solute, t_s is the support layer thickness, τ the tortuosity, and ε the porosity [13]. We define the membrane structural parameter S :

$$S = KD = \frac{t_s \tau}{\varepsilon} \quad (3.4)$$

which is independent of the draw solution properties, assuming the draw solutes do not swell or plasticize the PSf and PET layers.

3.3 RESULTS AND DISCUSSION

Membrane Microstructure and Morphology. The active surface of the TFC-FO membrane has a uniform ridge-and-valley morphology (Figure 3.1A), which is characteristic of polyamide membranes formed using an interfacial polymerization [22]. The polyamide layer appears continuous, with high salt rejections observed in RO tests, thereby indicating that a functional selective layer was formed. After carefully removing the PET non-woven fabric, the bottom surface of the PSf support layer was imaged, and the distinct, highly porous structure of this surface is shown in Figure 3.1B. Pore

diameters on the bottom surface of the PSf support layer range from 2 to 10 μm ; similar values of 5 to 12 μm are obtained from the cross-sectional SEM micrographs shown in Figure 3.2A. The average thickness of the membranes as measured by micrometer is $95.9 \pm 12.6 \mu\text{m}$. A finger-like morphology spans most of the PSf layer thickness, but the higher magnification micrograph in Figure 3.2B reveals a thin, 1- to 2- μm layer consisting of a dense sponge-like morphology near the top surface. This sponge-like morphology is favorable for the formation of an integral polyamide layer [11]. No change in morphology of the membrane was observed after pressurization in RO experiments.

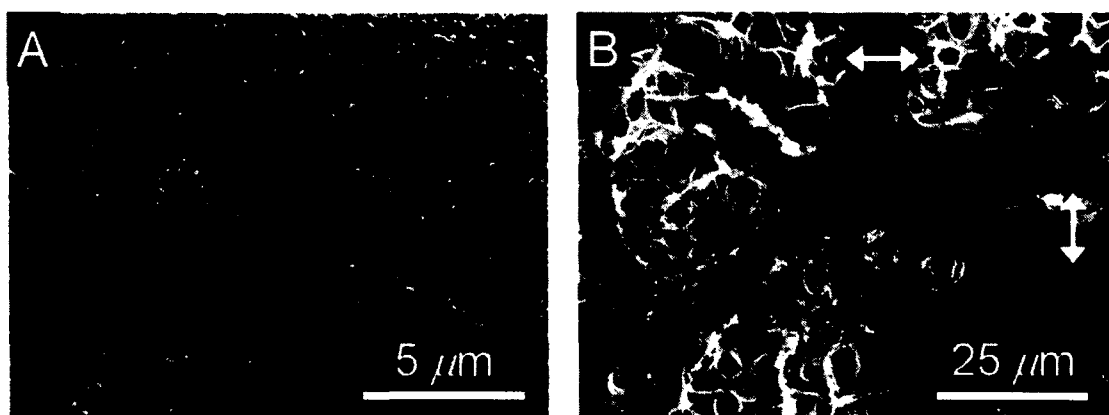


Figure 3.1. SEM micrographs displaying the structure of a TFC-FO membrane (TFC-FO-2) at the A) top surface of the active polyamide layer and B) at the bottom surface of the PSf support layer. The white arrows indicate the areas where the PET fibers and PSf layer were in contact, as evidenced by a visibly lower porosity.

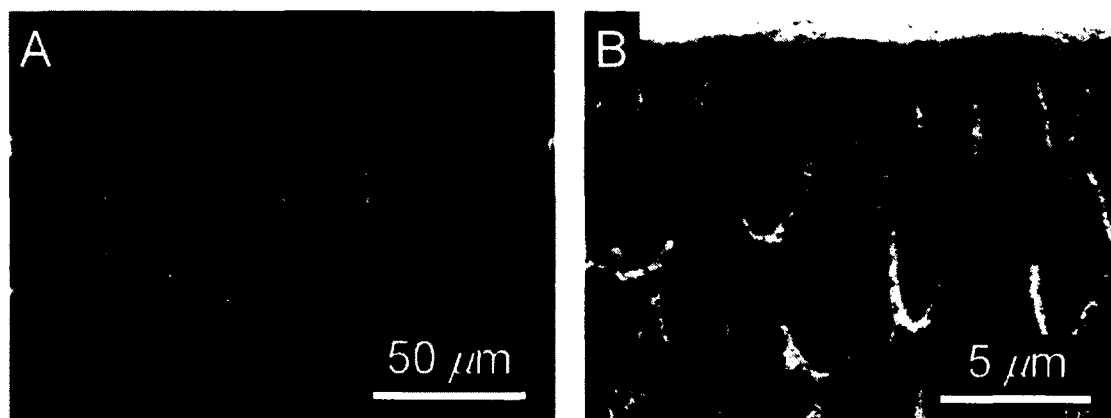


Figure 3.2. SEM micrographs of the cross-section of a TFC-FO membrane (TFC-FO-2) A) including PET non-woven fabric and B) a magnified view of the dense, sponge-like morphology near the active layer. The average total membrane thickness is 95.9 ± 12.6 μm as determined using a digital micrometer.

Producing a PSf support membrane with a thin layer of the sponge-like morphology on top of a finger-like layer is critical to fabricating a robust TFC-FO membrane. The sponge-like layer allows for an integral PA layer to form while the finger-like layer decreases the resistance to mass transfer. This finding is consistent with previous reports on TFC membranes; membranes with a dense support layer were better able to reject dissolved salts, but were hindered by low water fluxes [23].

The use of a mixed solvent system facilitated the formation of the desired microstructure. Immersing the cast thin film of polymer solution into the non-solvent (water) bath results in the non-solvent permeating into the polymer solution. Along with this influx of non-solvent into the polymer solution, there is also an outflux of solvent from the polymer solution to the non-solvent bath. As a result of this exchange, the composition of the polymer film changes until the stability limit of the system is reached, where it phase separates into a polymer-rich and a polymer-poor phase. These two phases eventually form the polymer matrix and pores, respectively. The pore

morphology is determined by the polymer precipitation rate — rapid precipitation produces finger-like pores and slow precipitation produces sponge-like pores [11, 24]. When the influx of non-solvent and the outflux of solvent are nearly equal in magnitude, the net flux is small, and the polymer solution is slowly exposed to the non-solvent. Slowly exposing the polymer to non-solvents results in a slow precipitation rate, and sponge-like pores form. On the other hand, rapid precipitation occurs when the influx of non-solvent dominates the net flux, producing finger-like pores.

NMP, the primary solvent used, permeates into the non-solvent bath more slowly because it is a more favorable solvent for PSf, while the co-solvent DMF, a less favorable solvent for PSf [25], quickly permeates into the non-solvent bath. This difference in exchange rates between NMP and DMF results in rapid and slow precipitation rates, respectively, when pure solvents are used. In the mixed solvent system, the precipitation rate can be tailored by controlling the relative amounts of the two solvents. The addition of DMF to the casting solution slows the permeation of solvent into the non-solvent bath, promoting the formation of the dense sponge layer at the top surface. The NMP increases the precipitation rate, leading to the formation of the underlying finger-like structure [26].

The PSf support layer was cast from a 12 wt% polymer solution. This is lower than polymer concentrations used in the production of conventional TFC-RO membranes, which typically range between 15 and 25 wt% [17, 20]. A lower concentration of polymer in the casting solution facilitates the formation of the finger-like structure and also yields higher porosity in the resultant PSf layer [20]. The benefits of these structural features of the PSf layer for FO operations are discussed below.

Performance of TFC-FO Membrane. Intrinsic water permeability, A , and salt rejection, R , of the TFC-FO membrane were measured in an RO cross-flow cell. Our fabricated TFC-FO membrane had an A value of $1.14 \pm 0.06 \text{ L m}^{-2}\text{h}^{-1}\text{bar}^{-1}$ ($3.18 \pm 0.17 \times 10^{-12} \text{ m s}^{-1}\text{Pa}^{-1}$), comparable to the values measured for the commercial TFC-RO membrane with and without the PET non-woven fabric, $1.28 \pm 0.04 \text{ L m}^{-2}\text{h}^{-1}\text{bar}^{-1}$ ($3.55 \pm 0.10 \times 10^{-12} \text{ m s}^{-1}\text{Pa}^{-1}$) and $1.46 \pm 0.05 \text{ L m}^{-2}\text{h}^{-1}\text{bar}^{-1}$ ($4.06 \pm 0.29 \times 10^{-12} \text{ m s}^{-1}\text{Pa}^{-1}$), respectively. These similar transport parameters are anticipated because both types of TFC membranes use the interfacial polymerization of polyamide to form the selective layer. The HTI-CTA membranes, on the other hand, are asymmetric cellulose acetate-based membranes and have a lower A value of $0.36 \pm 0.11 \text{ L m}^{-2}\text{h}^{-1}\text{bar}^{-1}$ ($0.98 \pm 0.31 \times 10^{-12} \text{ m s}^{-1}\text{Pa}^{-1}$).

FO water fluxes measured using a DI water feed solution and a 1.5 M NaCl draw solution are presented in Figure 3.3A for the various membranes. Water flux values for individual runs with each TFC-FO membrane are summarized in Table 3.1. Our hand-cast TFC-FO membranes exhibited the highest water flux ($18.15 \pm 0.96 \text{ L m}^{-2}\text{h}^{-1}$), nearly twice that achieved by the commercial HTI-CTA membranes ($9.58 \pm 0.11 \text{ L m}^{-2}\text{h}^{-1}$). As anticipated, the TFC-RO membranes with the PET fabric attached performed poorly in FO tests, yielding very low water fluxes ($2.22 \pm 0.22 \text{ L m}^{-2}\text{h}^{-1}$). However, after the PET fabric was removed, performance improved to $7.26 \pm 0.87 \text{ L m}^{-2}\text{h}^{-1}$. Despite having a lower intrinsic water permeability, the better performance of the HTI-CTA membrane over the TFC-RO membrane highlights the paramount significance of the support layer structure in influencing FO water flux [12].

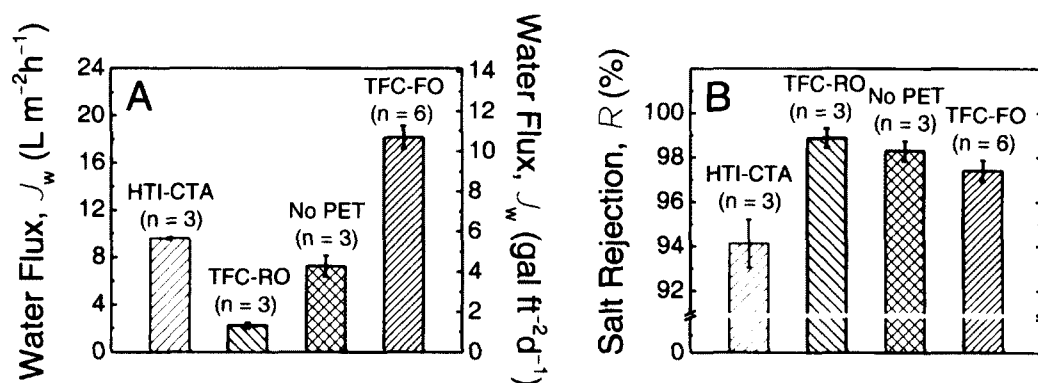


Figure 3.3. Comparison of (A) FO water flux and (B) salt rejection between TFC-FO membranes and commercial membranes: HTI-CTA (FO membrane), TFC-RO (RO membrane), and TFC-RO membrane after removal of the PET non-woven fabric (“No PET”). The number of samples, n , used to obtain average and standard deviation is indicated. Experimental conditions for FO flux were as follows: 1.5 M NaCl draw solution, DI water feed solution, and feed and draw solution temperature of 25 °C. Experimental conditions for salt rejection in RO measurement were as follows: 50 mM NaCl feed solution, 27.6 bar (400 psi) applied pressure, cross-flow of 21.4 cm/s, and temperature of 25 °C.

Figure 3.3B presents the observed salt rejection, R , using a 50 mM NaCl feed at a pressure drop of 27.6 bar (400 psi). The TFC membranes gave average salt rejections higher than those observed for the HTI-CTA membranes, which had an average R of 94.1 ± 1.1 %. This observation is expected because thin-film composite membranes generally have higher salt rejection rates than asymmetric membranes [27]. The TFC-RO membranes had average salt rejections of 98.9 ± 0.4 and 98.3 ± 0.4 %, before and after the PET fabric had been removed, respectively. The similarity between salt rejections before and after fabric removal indicates that peeling off the fabric does not compromise the integrity of the selective skin layer. The TFC-FO membranes developed in this work have an average salt rejection of 97.4 ± 0.5 %, slightly lower than the rejection observed for the commercial TFC-RO membranes. This difference is attributed to human

variability, which occurs as a result of the hand-casting procedure. Characteristic performance values (e.g., A , B , J_w , and R) for the membranes used in this study are tabulated in Table 3.1.

Table 3.1. Summary of measured water flux, J_w , salt rejection, R , and calculated structural parameter, S , for all the TFC-FO membranes tested. The experimental conditions are stated. Temperature for all tests was 25 ± 0.5 °C.

Membrane	Feed solution concentration, c_F (M)	Draw solution concentration, c_D (M)	$^a \Delta\pi$ (bar)	Experimental FO flux, J_w ($L\ m^{-2}h^{-1}$)	Salt rejection, R (%)	Structural parameter, S (μm)
TFC-FO-1	DI water	1.5 M NaCl	76.1	19.51	97.1	431
TFC-FO-2	DI water	1.5 M NaCl	76.1	16.81	98.4	540
TFC-FO-3	DI water	1.5 M NaCl	76.1	17.57	97.5	517
TFC-FO-4	DI water	1.5 M NaCl	76.1	17.95	97.2	482
TFC-FO-5	DI water	1.5 M NaCl	76.1	18.93	97.3	478
TFC-FO-6	DI water	1.5 M NaCl	76.1	18.17	97.1	506
Avg.				18.16	97.41	492
St. Dev.				0.96	0.46	38
TFC-FO-2	DI water	1.5 M NH_4HCO_3	57.0	16.55		
TFC-FO-2	DI water	1.5 M NH_4HCO_3 (after 7 days)	57.0	16.28		

^a Calculated by a software package from OLI Systems, Inc. (Morris Plains, NJ).

TFC-FO Membrane Structural Parameters. Water flux versus osmotic pressure difference for one of our TFC-FO membranes (TFC-FO-2, Table 3.1) is presented in Figure 3.4. Ideally, the curve would be linear, but internal concentration polarization (ICP) causes a non-linear dependence [13]. Minimizing ICP is crucial to the design of a high performance FO membrane [16]. As water permeates across the membrane, diluting the draw solution at the active surface of the membrane, diffusion works to restore the concentration to that of the bulk draw solution. When diffusion is not rapid enough to

keep the solution well-mixed, the effective osmotic pressure, and thus, the water flux, is reduced. Therefore, decreasing ICP relies on reducing the resistance to solute diffusion in the porous support. The diffusion coefficient of the draw solute is fixed, leaving only the structural parameter S (defined earlier in eq 3.4) as a means to reduce ICP. S has units of length and can be thought of as the characteristic distance a solute particle must travel to reach the active layer of the membrane from the bulk draw solution. FO membranes with thinner, more porous, and less tortuous support layers will have smaller values of S and produce higher water fluxes.

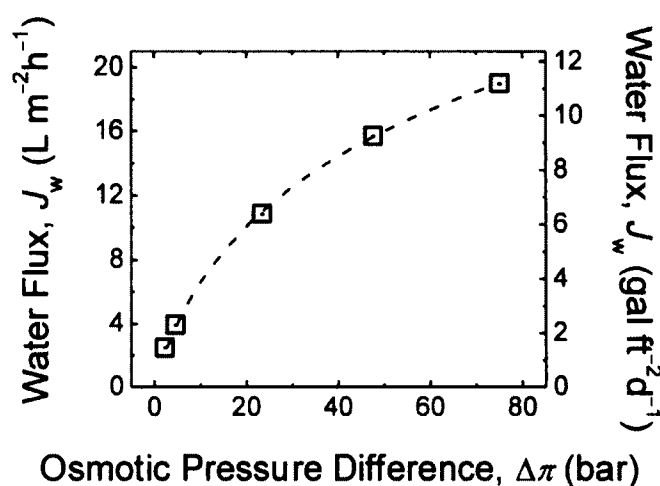


Figure 3.4. Experimental TFC-FO membrane water flux (open square symbols) over a range of osmotic pressure differences (i.e., draw solution osmotic pressure minus feed osmotic pressure) obtained using NaCl. The data points shown correspond to NaCl concentrations of 0.05, 0.1, 0.5, 1, and 1.5 M. Osmotic pressures were calculated from the corresponding salt concentrations using a software package from OLI Systems, Inc. (Morris Plains, NJ). Feed concentration is held constant (DI water) while draw solution concentration is varied. Other experimental conditions were: crossflow rate (feed and draw solution) of 21.4 cm/s and temperature of both feed and draw solutions of 25 °C. Data are fitted using eq 3.2 (dashed line) to obtain value of the resistance to solute transfer, K .

The structural parameter S for our TFC-FO membrane (TFC-FO-2, Table 3.1) is determined by fitting the experimental data in Figure 3.4 to eq 3.2. The dashed line is the curve calculated using a value of $1.61 \times 10^{-9} \text{ m}^2/\text{s}$ for D_{NaCl} [28] and $442 \mu\text{m}$ for S . We also use eq 3.2 to find S for the individual FO membranes using the corresponding measured water flux data (Table 3.1). The average value obtained from these runs, $492 \pm 38 \mu\text{m}$, agrees well with the data, fitting over a range of draw solution concentrations as shown in Figure 3.4. Our calculations also give S values of $595 \pm 114 \mu\text{m}$ for the HTI-CTA membranes, and $9583 \pm 1351 \mu\text{m}$ and $2155 \pm 292 \mu\text{m}$ for the TFC-RO membranes with and without the PET fabric, respectively.

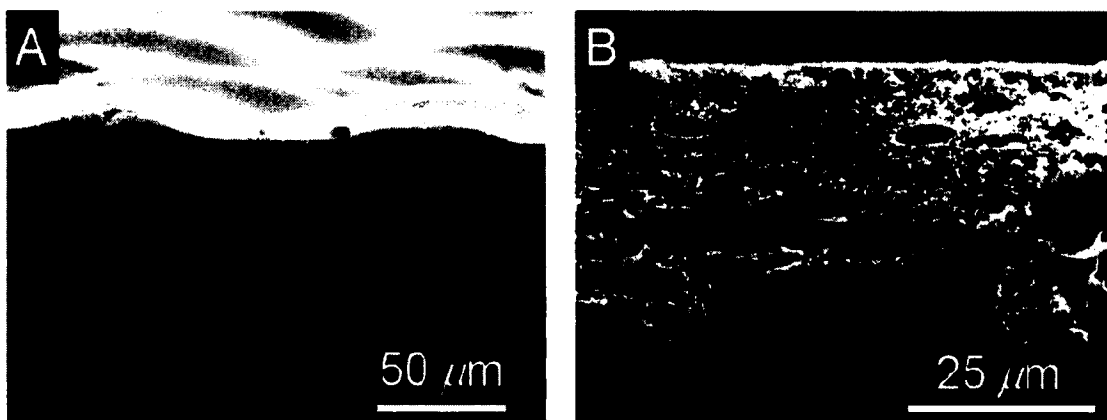


Figure 3.5. SEM micrographs display the cross-section of A) commercial HTI-CTA membrane and B) TFC-RO membrane after removing the PET non-woven fabric. Thickness of the asymmetric membrane was approximately $95 \mu\text{m}$; the TFC-RO membrane was approximately $125 \mu\text{m}$ and $50 \mu\text{m}$, before and after PET removal, respectively, as confirmed using a digital micrometer.

Comparing cross-sectional SEM micrographs of the commercial membranes in Figure 3.5 with those taken of our TFC-FO membranes (Figure 3.2) demonstrates the link between membrane structure and the structural parameter S . Figure 3.5A presents the unique structure of the HTI-CTA cross-section. The SEM micrograph shows what

appears to be a woven mesh embedded in a continuous polymer layer. The overall thickness is approximately $100\ \mu\text{m}$, as confirmed with a micrometer ($94.4 \pm 0.3\ \mu\text{m}$). By embedding the woven mesh within the continuous polymer layer, the need for a thick backing layer is eliminated. However, the membrane appears denser than our TFC-FO membrane, thereby explaining its inferior performance.

The TFC-RO membrane consists of a thin active layer supported by a microporous polymer layer, which is backed by a non-woven fabric (Figure 3.5B). Estimates from micrographs give a microporous polymer support thickness of approximately $50\ \mu\text{m}$ and a nonwoven backing fabric thickness of $75\ \mu\text{m}$. These values are consistent with measurements made using a micrometer: $125.1 \pm 0.7\ \mu\text{m}$ for the entire membrane and $50.6 \pm 2.8\ \mu\text{m}$ for the membrane after removing the non-woven fabric layer. The support layer of the membrane appears to have a sponge-like morphology, which is necessary for RO operations because the finger-like structures or macrovoids can compromise the mechanical integrity [26]. However, unlike RO, FO does not require applied hydraulic pressure, and the higher resistance to mass transfer of the sponge-like microstructure compared to the finger-like microstructure is a hindrance. The significant resistance to mass transfer of the sponge-like morphology is evidenced by the higher calculated S value ($2155 \pm 292\ \mu\text{m}$) for the relatively thin ($50\ \mu\text{m}$) TFC-RO membrane without PET.

Membrane Performance and Chemical Stability with Ammonium Bicarbonate Draw Solution. The HTI-CTA membrane is cellulose-based, precluding its use with the ammonia-carbon dioxide draw solution. Cellulose acetate degrades at exponentially increasing rates when operated outside its stable pH range of 4–6 [11, 29], while our TFC-FO membrane should be stable up to pH 11 because it uses a polyamide chemistry

[30]. We have tested the chemical stability of the TFC-FO membrane by measuring the water flux using a 1.5 M NH_4HCO_3 draw solution (pH 7.9). The observed water flux of $16.55 \text{ L m}^{-2}\text{h}^{-1}$ agrees well with the water flux predicted for an osmotic pressure of 57.0 bar (827 psi) generated by the 1.5 M NH_4HCO_3 draw solution. After this initial test, the membrane was soaked in the 1.5 M ammonium bicarbonate solution for 7 days. Following this exposure, no visual changes were observed and the water flux remained constant ($16.28 \text{ L m}^{-2}\text{h}^{-1}$) demonstrating the chemical stability of our membrane.

3.4 IMPLICATIONS FOR FO MEMBRANE DEVELOPMENT

This work demonstrates the fabrication of a TFC-FO membrane that is chemically stable and is less hindered by internal concentration polarization. Further improvements to TFC-FO membrane performance are possible through tailoring the support membrane structure [31], modifying the support membrane chemistry [12], and optimizing the interfacial polymerization conditions [27]. The membrane structural parameter S shows that by increasing the void fraction and decreasing the thickness and tortuosity, the resistance to mass transfer can be reduced. Decreasing the membrane thickness to $40 \mu\text{m}$, a goal that can be achieved using industrial coating equipment, would improve the structural parameter from $492 \mu\text{m}$ to $205 \mu\text{m}$. Varying the casting conditions can further optimize the microporous support structure [11, 20], decreasing the structural parameter and thereby improving TFC-FO membrane performance. New, more hydrophilic chemistries obtained using a different polymer (e.g., polyethersulfone) or the addition of hydrophilic additives (e.g., polyethylene oxide or poly(4-vinylpyridine)) may also improve FO membrane performance as previous research suggests [12]. Finally, several

different interfacial polymerization chemistries have been used to make membranes. Polyamides remain the standard for desalination, but different chemistries might be well-suited for other osmotically-driven membrane processes [27]. These new TFC-FO membranes may find application in a variety of processes, such as seawater and brackish water desalination, wastewater reclamation and reuse, and energy generation by pressure retarded osmosis [32].

3.5 REFERENCES

- [1] Kravath, R. E. Davis, J. A., Desalination of Sea-Water by Direct Osmosis. *Desalination* **1975**, *16* (2), 151-155.
- [2] Cath, T. Y.; Childress, A. E. Elimelech, M., Forward osmosis: Principles, applications, and recent developments. *Journal of Membrane Science* **2006**, *281* (1-2), 70-87.
- [3] Cath, T. Y.; Gormly, S.; Beaudry, E. G.; Flynn, M. T.; Adams, V. D. Childress, A. E., Membrane contactor processes for wastewater reclamation in space Part I. Direct osmotic concentration as pretreatment for reverse osmosis. *Journal of Membrane Science* **2005**, *257* (1-2), 85-98.
- [4] Cartinella, J. L.; Cath, T. Y.; Flynn, M. T.; Miller, G. C.; Hunter, K. W. Childress, A. E., Removal of natural steroid hormones from wastewater using membrane contactor processes. *Environmental Science & Technology* **2006**, *40* (23), 7381-7386.
- [5] Cath, T. Y.; Adams, D. Childress, A. E., Membrane contactor processes for wastewater reclamation in space II. Combined direct osmosis, osmotic distillation, and membrane distillation for treatment of metabolic wastewater. *Journal of Membrane Science* **2005**, *257* (1-2), 111-119.
- [6] Holloway, R. W.; Childress, A. E.; Dennett, K. E. Cath, T. Y., Forward osmosis for concentration of anaerobic digester centrate. *Water Research* **2007**, *41* (17), 4005-4014.
- [7] Achilli, A.; Cath, T. Y.; Marchand, E. A. Childress, A. E., The forward osmosis membrane bioreactor: A low fouling alternative to MBR processes. *Desalination* **2009**, *239* (1-3), 10-21.
- [8] Jiao, B.; Cassano, A. Drioli, E., Recent advances on membrane processes for the concentration of fruit juices: a review. *Journal of Food Engineering* **2004**, *63* (3), 303-324.
- [9] Garcia-Castello, E. M.; McCutcheon, J. R. Elimelech, M., Performance evaluation of sucrose concentration using forward osmosis. *Journal of Membrane Science* **2009**, *338* (1-2), 61-66.
- [10] McCutcheon, J. R.; McGinnis, R. L. Elimelech, M., A novel ammonia-carbon dioxide forward (direct) osmosis desalination process. *Desalination* **2005**, *174* (1), 1-11.
- [11] Baker, R., Membrane technology and applications. 2nd ed.; Wiley, **2004**; p 552.
- [12] McCutcheon, J. R. Elimelech, M., Influence of membrane support layer hydrophobicity on water flux in osmotically driven membrane processes. *Journal of Membrane Science* **2008**, *318* (1-2), 458-466.
- [13] McCutcheon, J. R. Elimelech, M., Influence of concentrative and dilutive internal concentration polarization on flux behavior in forward osmosis. *Journal of Membrane Science* **2006**, *284* (1-2), 237-247.
- [14] Lee, K. L.; Baker, R. W. Lonsdale, H. K., Membranes for Power-Generation by Pressure-Retarded Osmosis. *Journal of Membrane Science* **1981**, *8* (2), 141-171.
- [15] Loeb, S.; Titelman, L.; Korngold, E. Freiman, J., Effect of porous support fabric on osmosis through a Loeb-Sourirajan type asymmetric membrane. *Journal of Membrane Science* **1997**, *129* (2), 243-249.
- [16] McCutcheon, J. R. Elimelech, M., Modeling water flux in forward osmosis: Implications for improved membrane design. *Aiche Journal* **2007**, *53* (7), 1736-1744.
- [17] Cadotte, J. E. Interfacially synthesized reverse osmosis membrane. US Patent 4277344, **1981**.

- [18] McCutcheon, J. R.; McGinnis, R. L. Elimelech, M., Desalination by ammonia-carbon dioxide forward osmosis: Influence of draw and feed solution concentrations on process performance. *Journal of Membrane Science* **2006**, *278* (1-2), 114-123.
- [19] Ang, W. S. Elimelech, M., Protein (BSA) fouling of reverse osmosis membranes: Implications for wastewater reclamation. *Journal of Membrane Science* **2007**, *296* (1-2), 83-92.
- [20] Mulder, J., Basic principles of membrane technology. 2nd ed.; Springer, **1996**; p 584.
- [21] Hoek, E. M. V.; Kim, A. S. Elimelech, M., Influence of crossflow membrane filter geometry and shear rate on colloidal fouling in reverse osmosis and nanofiltration separations. *Environmental Engineering Science* **2002**, *19* (6), 357-372.
- [22] Ghosh, A. K.; Jeong, B. H.; Huang, X. F. Hoek, E. M. V., Impacts of reaction and curing conditions on polyamide composite reverse osmosis membrane properties. *Journal of Membrane Science* **2008**, *311* (1-2), 34-45.
- [23] Cadotte, J. E. K., R. S.; Sand, J. E.; Petersen, R. J, Improved Porous Supports for Thin-Film Composite Reverse Osmosis Membranes. *Report for Office of Water Research and Technology* **1981**, 51 p.
- [24] Strathmann, H.; Kock, K.; Amar, P. Baker, R. W., Formation Mechanism of Asymmetric Membranes. *Desalination* **1975**, *16* (2), 179-203.
- [25] Hansen, C. M., Hansen solubility parameters : a user's handbook. 2nd ed.; CRC Press, Boca Raton, **2007**; p 519 p.
- [26] vandeWitte, P.; Dijkstra, P. J.; vandenBerg, J. W. A. Feijen, J., Phase separation processes in polymer solutions in relation to membrane formation. *Journal of Membrane Science* **1996**, *117* (1-2), 1-31.
- [27] Petersen, R. J., Composite Reverse-Osmosis and Nanofiltration Membranes. *Journal of Membrane Science* **1993**, *83* (1), 81-150.
- [28] Lobo, V. M. M., Mutual Diffusion-Coefficients in Aqueous-Electrolyte Solutions (Technical Report). *Pure and Applied Chemistry* **1993**, *65* (12), 2614-2640.
- [29] Vos, K. D.; Burris, F. O. Riley, R. L., Kinetic Study of Hydrolysis of Cellulose Acetate in Ph Range of 2-10. *Journal of Applied Polymer Science* **1966**, *10* (5), 825-832.
- [30] Cadotte, J. E.; Petersen, R. J.; Larson, R. E. Erickson, E. E., New Thin-Film Composite Seawater Reverse-Osmosis Membrane. *Desalination* **1980**, *32* (1-3), 25-31.
- [31] Ghosh, A. K. Hoek, E. M. V., Impacts of support membrane structure and chemistry on polyamide-poly sulfone interfacial composite membranes. *Journal of Membrane Science* **2009**, *336* (1-2), 140-148.
- [32] McGinnis, R. L. Elimelech, M., Global Challenges in Energy and Water Supply: The Promise of Engineered Osmosis. *Environmental Science & Technology* **2008**, *42* (23), 8625-8629.

Chapter 4:

Thin-Film Composite Pressure Retarded Osmosis Membranes for Sustainable Power Generation from Salinity Gradients

CHAPTER ABSTRACT

Pressure retarded osmosis has the potential to produce renewable energy from natural salinity gradients. This work presents the fabrication of thin-film composite membranes customized for high performance in pressure retarded osmosis. We also present the development of a theoretical model to predict the water flux in pressure retarded osmosis, from which we can predict the power density that can be achieved by a membrane. The model is the first to incorporate external concentration polarization, a performance limiting phenomenon that becomes significant for high performance membranes. The fabricated membranes consist of a selective polyamide layer formed by interfacial polymerization on top of a polysulfone support layer made by phase separation. The highly porous support layer (structural parameter $S = 349 \mu\text{m}$), which minimizes internal concentration polarization, allows the transport properties of the active layer to be customized to enhance PRO performance. It is shown that a hand-cast membrane that balances permeability and selectivity ($A = 5.81 \text{ L m}^{-2}\text{h}^{-1}\text{bar}^{-1}$, $B = 0.88 \text{ L m}^{-2}\text{h}^{-1}$) is projected to achieve the highest potential peak power density of 10.0 W/m^2 for a river water feed solution and seawater draw solution. The outstanding performance of this membrane is attributed to the high water permeability of the active layer, coupled with a moderate salt permeability and the ability of the support layer to suppress the undesirable accumulation of leaked salt in the porous support. Membranes with greater selectivity (i.e., lower salt permeability, $B = 0.16 \text{ L m}^{-2}\text{h}^{-1}$) suffered from a lower water permeability ($A = 1.74 \text{ L m}^{-2}\text{h}^{-1}\text{bar}^{-1}$) and would yield a lower peak power density of 6.1 W/m^2 , while membranes with a higher permeability and lower selectivity ($A = 7.55 \text{ L$

$\text{m}^{-2}\text{h}^{-1}\text{bar}^{-1}$, $B = 5.45 \text{ L m}^{-2}\text{h}^{-1}$) performed poorly due to severe reverse salt permeation, resulting in a similar projected peak power density of 6.1 W/m^2 .

4.1 INTRODUCTION

Current global energy demand far exceeds our capacity for sustainable production. Prolonged reliance on fossil fuels, which provide the bulk of our energy, is untenable because of the emission of greenhouse gases and air pollutants [1]. Although the development of a broad range of alternative energy technologies is making progress in increasing sustainable energy production, we still depend heavily on fossil fuels to meet our needs. To satisfy the energy requirements of the present and future, existing alternative energy production technologies must be advanced beyond their current limitations [1], and additional sources of sustainable energy must be tapped.

Pressure retarded osmosis (PRO) holds the potential to produce renewable energy from natural and anthropogenic salinity gradients [2]. PRO exploits the osmotic pressure difference that develops when a semi-permeable membrane separates two solutions of different concentrations. As a result of the osmotic pressure difference, water permeates from the dilute “feed solution” into the more concentrated “draw solution”. A hydraulic pressure less than the osmotic pressure difference is applied on the draw solution, and a hydroturbine extracts work from the expanding draw solution volume.

Input streams for PRO are available in both natural and industrial settings. Natural salinity gradients, for example those arising from the mixing of freshwater rivers flowing into oceans, have the potential to produce 1650 TWh/year [3]. Additionally, PRO can use anthropogenic waste streams, such as concentrated brine from a desalination plant [4], as

draw solutions. A closed-loop version of PRO, the osmotic heat engine, has also been proposed. This process uses low grade heat to power the separation and regeneration of its thermolytic draw solution of dissolved ammonia and carbon dioxide gases. The conversion of low grade heat that would otherwise be discarded into useable electricity creates a net benefit [5]. The continuous availability of both natural water resources and anthropogenic waste streams indicates that PRO systems will not suffer from the intermittency problems that plague some other renewable energy generation methods.

Despite its potential, the development of PRO has been hindered by the lack of a suitable membrane. The bulky support layers of reverse osmosis (RO) membranes cause severe internal concentration polarization (ICP), which dramatically reduces water flux [6]. Consequently, these RO membranes achieve only nominal power densities (power produced per membrane area) in PRO operation. A commercial cellulose acetate membrane designed for another osmotically driven membrane process, forward osmosis (FO), experience relatively less ICP due to its specialized support layer [7, 8]. However, the relatively low intrinsic water permeability of the membrane material restricts the power density it can attain. Furthermore, cellulose acetate membranes can operate only within a pH range of 4 to 6 [9, 10], therefore limiting their application.

A PRO pilot plant in Norway that was built to demonstrate the technology used cellulose acetate membranes to generate $< 0.5 \text{ W/m}^2$ [11]. This power density is an order of magnitude lower than the power density of 5 W/m^2 required to make this specific installation commercially viable [12]. To date, no membrane has demonstrated a PRO power density greater than 3.5 W/m^2 using freshwater and seawater [2].

For power generation by PRO to be commercially feasible, the gap in membrane performance must be bridged. We have recently developed a high performance thin-film composite FO membrane [13, 14]. Through control of the fabrication parameters, the support layer was tailored to decrease ICP, thereby increasing water flux. Like FO, PRO requires a membrane that minimizes ICP. However, a key difference between the two processes affords us the opportunity to further customize the active layer. FO is a separation process and requires a highly selective membrane, while PRO exploits the controlled mixing of solutions to generate energy and therefore only needs enough salt rejection to maintain the osmotic driving force [6]. The constraint of high selectivity that limits water flux in FO through the selectivity-permeability trade-off [15] is therefore partially relaxed for PRO membranes, and an additional degree of freedom exists in PRO membrane design.

This study demonstrates the fabrication of a customized thin-film composite membrane that has the potential to achieve a high power density in PRO. Hand-cast thin-film composite PRO membranes with a range of water and salt permeabilities were prepared. Membrane performance was evaluated in PRO configuration using a model seawater draw solution paired with river or brackish water feed solutions. The influence of membrane properties on power density in PRO systems is analyzed and discussed. This experimental and theoretical work aims to provide basic criteria in the design of customized PRO membranes for sustainable power generation by establishing the influence of membrane characteristics on PRO performance.

4.2 THEORY

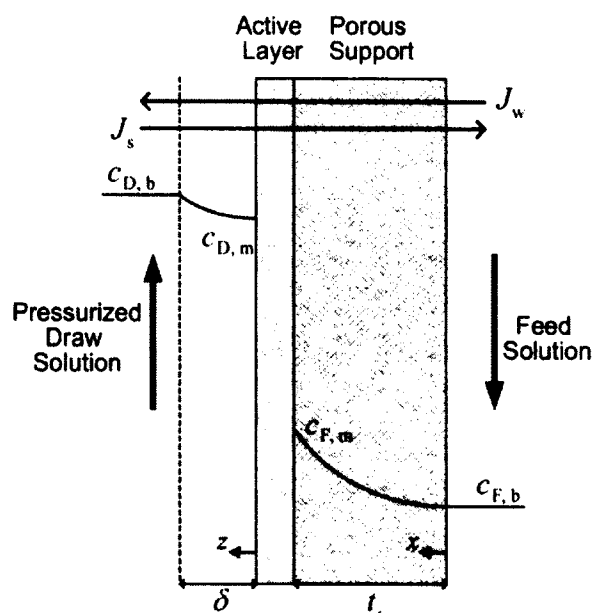


Figure 4.1. A schematic representation of the salt concentration profile across a thin-film composite membrane in PRO mode at steady state. The feed and draw solutions are introduced to the membrane in crossflow. Dilutive external concentration polarization occurs in the mass transfer boundary layer of the draw solution, reducing the local concentration at the active layer from $c_{D,b}$ to $c_{D,m}$. Concentrative internal concentration polarization takes place within the porous support, increasing the local concentration at the active-support interface from $c_{F,b}$ to $c_{F,m}$. Concentrative ECP in the feed solution is assumed to be negligible. The pressurized draw solution creates a hydraulic pressure drop across the membrane, ΔP , which is lower than the osmotic pressure difference across the membrane.

A schematic of the salt concentration profile across a thin-film composite membrane operating in PRO mode (i.e., active layer facing the draw solution) is shown in Figure 4.1. Due to the detrimental effects of internal concentration polarization (ICP) within the porous support, salt permeation across the membrane, and external concentration polarization (ECP) in the draw solution, the osmotic driving force is lower than the osmotic pressure difference between the bulk draw and feed solutions. Earlier studies to derive the PRO water flux equation did not take ECP into account [6, 8]. ECP can be

significant for high performance PRO membranes having low membrane structural parameters and high water fluxes. In this section we present the derivation of the complete water flux equation for PRO taking into consideration all the above-mentioned effects.

Water and Salt Fluxes Across the Active Layer. Water flux, J_w , across the membrane is given by [9]

$$J_w = A(\Delta\pi_m - \Delta P) \quad (4.1)$$

where A is the intrinsic water permeability coefficient of the membrane, $\Delta\pi_m$ is the effective osmotic pressure across the active layer, and ΔP is the applied hydraulic pressure difference across the membrane. Salt permeates across the membrane in the opposite direction of the water flux, from the more concentrated draw solution into the feed solution. The reverse salt flux, J_s , is described by [6, 16]

$$J_s = B(c_{D,m} - c_{F,m}) \quad (4.2)$$

where B is the salt permeability coefficient of the membrane active layer and $c_{D,m}$ and $c_{F,m}$ are the solute concentrations in solution at the active layer interface on the draw and feed sides, respectively.

Mass Transfer in the Porous Support Layer. As water permeates across the membrane, the feed solutes are selectively retained by the semi-permeable active layer and build up within the porous support, resulting in ICP. Diffusion works to restore this local concentration to the bulk feed solution concentration, but is hindered by the porous support which acts as an unstirred boundary layer. The salt flux across the porous support is the sum of the diffusive component, driven by the salt concentration gradient,

and the convective component, arising from the bulk flow of water through the membrane [6]:

$$J_s = D^s \frac{dc(x)}{dx} - J_w c(x) \quad (4.3)$$

where D^s is the effective diffusion coefficient of the draw solute in the porous support. It can be related to the bulk diffusion coefficient, D , by accounting for the porosity, ε , and tortuosity, τ , of the support layer, i.e., $D^s = D\varepsilon/\tau$ [16].

At steady-state, the salt fluxes across the active (eq 4.2) and support (eq 4.3) layers are equal:

$$D^s \frac{dc(x)}{dx} - J_w c(x) = B(c_{D,m} - c_{F,m}) \quad (4.4)$$

Integrating eq 4.4 across the support layer thickness, from the porous layer-feed solution interface, $x = 0$, where the salt concentration is $c_{F,b}$, to the porous layer-active layer interface, $x = t_s$, where the salt concentration is $c_{F,m}$ (Figure 4.1), yields

$$c_{F,m} = c_{F,b} \exp\left(\frac{J_w S}{D}\right) + \frac{B}{J_w} (c_{D,m} - c_{F,m}) \left[\exp\left(\frac{J_w S}{D}\right) - 1 \right] \quad (4.5)$$

where $S = t_s \tau / \varepsilon$ is the support layer structural parameter [13]. Note that in the above analysis we do not consider ECP in the feed solution because the support layer thickness is relatively large, thereby dominating concentration polarization.

Eq 4.5 indicates that the salt concentration at the active-support interface, $c_{F,m}$, is the sum of two terms. The effect of concentrative ICP is described by the first term on the right-hand side, where the bulk feed solution concentration is magnified by a factor of $\exp(J_w S / D)$. The second term accounts for the increase in salt concentration at the

membrane interface due to the reverse permeation of draw solution salt into the porous support.

Mass Transfer in the External Concentration Polarization Layer. As water permeates across the membrane, it dilutes the draw solution at the active layer, resulting in ECP. Similar to ICP, the salt flux within this ECP boundary layer comprises diffusive and convective components [9]:

$$J_s = D \frac{dc(z)}{dz} - J_w c(z) \quad (4.6)$$

At steady-state, the salt flux within the ECP boundary layer (eq 4.6) is equal to the salt flux across the active layer (eq 4.2). Integrating the resulting equation across the ECP boundary layer from the active layer, $z = 0$, where the salt concentration is $c_{D,m}$, to the bulk draw solution, $z = \delta$, where the salt concentration is $c_{D,b}$, yields

$$c_{D,m} = c_{D,b} \exp\left(-\frac{J_w}{k}\right) - \frac{B}{J_w} (c_{D,m} - c_{F,m}) \left[1 - \exp\left(-\frac{J_w}{k}\right)\right] \quad (4.7)$$

where $k = D/\delta$ is the boundary layer mass transfer coefficient. Inspecting eq 4.7 reveals that $c_{D,m}$ is dependent on two terms. The first term describes the bulk draw concentration, $c_{D,b}$, corrected for ECP by the factor $\exp(-J_w/k)$, while the second term represents the loss in solute concentration due to salt leakage across the active layer.

Water Flux in PRO with ICP, ECP, and Salt Permeation Effects. Both $c_{D,m}$ and $c_{F,m}$ are local interfacial concentrations on either side of the active layer interface and therefore are not experimentally accessible. To circumvent this, we subtract eq 4.5 from eq 4.7 and rearrange to obtain

$$c_{D,m} - c_{F,m} = \frac{c_{D,b} \exp\left(-\frac{J_w}{k}\right) - c_{F,b} \exp\left(\frac{J_w S}{D}\right)}{1 + \frac{B}{J_w} \left[\exp\left(\frac{J_w S}{D}\right) - \exp\left(-\frac{J_w}{k}\right) \right]} \quad (4.8)$$

Next, we assume the osmotic pressure is linearly proportional to the salt concentration, i.e., the van't Hoff equation is applicable. Hence, the effective osmotic driving force, $\Delta\pi_m$, is proportional to $\Delta c_m = c_{D,m} - c_{F,m}$ (eq 4.8). Substituting $\Delta\pi_m$ into eq 4.1 yields an expression for the water flux in PRO:

$$J_w = A \left\{ \frac{\pi_{D,b} \exp\left(-\frac{J_w}{k}\right) - \pi_{F,b} \exp\left(\frac{J_w S}{D}\right)}{1 + \frac{B}{J_w} \left[\exp\left(\frac{J_w S}{D}\right) - \exp\left(-\frac{J_w}{k}\right) \right]} - \Delta P \right\} \quad (4.9)$$

This equation utilizes experimentally accessible parameters and incorporates the performance limiting phenomena of ICP and ECP as well as salt leakage across the membrane.

4.3 MATERIALS AND METHODS

Chemicals and Materials. All chemicals used were analytical grade. Polysulfone (PSf) beads (M_n : 22,000 Da), *N-N*-dimethylformamide (DMF, anhydrous, 99.8%), 1,3-phenylenediamine (MPD, >99%), and 1,3,5-benzenetricarbonyl trichloride (TMC, 98%) were used as received (Sigma-Aldrich, St. Louis, MO). TMC was dissolved in Isopar-G, a proprietary non-polar organic solvent (Univar, Redmond, WA). A thin (40 μm), open structure polyester non-woven fabric (PET, Grade 3249, Ahlstrom, Helsinki, Finland) was used as a backing layer for the PSf supports.

Polysulfone Porous Support Fabrication. The thin, porous support layer was fabricated by non-solvent induced phase separation of PSf on the PET, following the procedure outlined in our previous publications [13, 14]. PSf (9 wt%) was dissolved in DMF by stirring at room temperature (23 °C) for 8 h and then stored in a desiccator for at least 15 h prior to casting. The thin, low-density PET fabric was attached to a clean glass plate using laboratory adhesive tape and then wet with DMF. Any excess solvent that pooled on the surface of the fabric was carefully removed using laboratory wipes. The PSf solution was drawn down the PET fabric using a casting knife (Gardco, Pompano Beach, FL) with an adjustable gate height fixed at 250 μm (~10 mils). The whole composite was immediately immersed in a precipitation bath containing 3 wt % DMF in DI water at room temperature to initiate phase separation [9, 17]. The support membrane remained in the precipitation bath for 10 min before being transferred to a DI water bath for storage prior to polyamide (PA) formation.

Polyamide Active Layer Fabrication. The PA active layer was formed on top of the hand-cast PSf support layers via interfacial polymerization [13, 14]. The hand-cast support was immersed in a 3.4 wt % aqueous MPD solution for 120 s, and an air knife was used to remove the excess solution from the membrane surface. Next, the MPD-saturated support membrane was immersed in a 0.15 wt % TMC in Isopar-G solution for 60 s to form the ultra-thin PA layer. The composite membrane was then sequentially cured in DI water at 95 °C for 120 s, rinsed with a 200 ppm sodium hypochlorite (NaOCl) aqueous solution for 120 s, soaked in a 1000 ppm sodium bisulfite (NaHSO_3) aqueous solution for 30 s, and lastly subjected to a second wet curing step at 95 °C for 120 s. The fabricated TFC membranes were rinsed thoroughly and stored in DI water at 4 °C.

Active Layer Modification. Exposure of the PA active layer to chlorine alters its structure and morphology, resulting in increased water permeability and decreased selectivity (or salt rejection) of the membrane [18, 19]. By careful control of the reaction parameters, water and salt permeabilities of the membrane active layer can be tailored [20]. Post-treatment was carried out to produce three batches of TFC-PRO membranes with varying active layer transport properties. The first batch of membranes was not subjected to any post-treatment and designated “LP” for its relatively lower water and salt permeabilities. The second batch was immersed in 1000 ppm NaOCl aqueous solution adjusted to pH 7.0 for 60 min, and then transferred to a 0.1 M NaOH aqueous solution for 16 h; this batch was designated as “MP” for its medium water and salt permeabilities. The third batch was treated in 2000 ppm NaOCl at pH 7.0 for 120 min before being soaked in 0.1 M NaOH for 62 h; this batch was designated as “HP” for its high water and salt permeabilities. The post-treated membranes were rinsed thoroughly and stored in DI water at 4 °C.

Determination of Membrane Water Permeability and Channel Mass Transfer Coefficient. Intrinsic water permeability of the TFC-PRO membranes was evaluated in a laboratory-scale crossflow RO test unit, as described in our previous work [21]. The average, k , calculated from eq 4.9, for the crossflow cell was $38.5 \pm 20.5 \mu\text{m/s}$ ($138.6 \pm 73.9 \text{ L m}^{-2}\text{h}^{-1}$). The relatively large standard deviation is attributed to experimental errors in the measurement of membrane parameters that propagate through the calculation of k .

Determination of Membrane Solute Permeability and Structural Parameter. Solute permeability and support layer structural parameter of the membranes were

determined in an experimental crossflow FO system described in our previous studies [13, 22]. The custom built cell has an effective membrane area of 20.02 cm². Variable speed gear pumps (Cole-Parmer, Vernon Hills, IL) were used to co-currently circulate the solutions in closed loops at a crossflow velocity of 21.4 cm/s. No mesh feed spacers were used. A water bath (Neslab, Newington, NH) kept the temperature of both feed and draw solutions constant at 25 ± 0.5 °C. All characterization tests were conducted with the membrane in FO configuration, i.e., porous support layer facing a 0.5 M NaCl draw solution and active layer facing a DI water feed solution.

The protocols to measure water and reverse salt flux were adapted from our previous publication [16]. After equilibrating the FO system, the bypass valves were closed to channel the draw and feed solutions to the membrane cell, and data recording was initiated. Water flux was determined by monitoring the rate of change in weight of the draw solution, and the NaCl concentration in the feed was measured at 3 min intervals with a calibrated conductivity meter (Oakton Instruments, Vernon Hills, IL). Once water flux had stabilized, concentration data was logged for another 30 min (i.e., 10 data points).

Solute permeability and support layer structural parameter can be determined from the water flux and reverse salt permeation measurements. Consider a species mass balance on NaCl in the feed solution

$$c_{F,b} (V_{F_0} - J_w A_m t) = c_{F,b_0} V_{F_0} + J_s A_m t \quad (4.10)$$

where $c_{F,b}$ is the bulk feed solute concentration, V_{F_0} is the initial volume of the feed solution, J_w is the measured water flux, A_m is the membrane area, t is the time elapsed, and C_{F,b_0} is the initial NaCl concentration. Reverse salt flux, J_s , is driven by the difference in salt concentration across the membrane. Since the feed solution is DI water,

J_s is the product of draw (NaCl) concentration at the active layer interface and salt permeability coefficient, B . The former is approximated by accounting for dilutive internal concentration polarization (ICP) of the bulk draw solution through the factor $\exp(-J_w S/D)$:

$$J_s = Bc_{D,b} \exp\left(-\frac{J_w S}{D}\right) \quad (4.11)$$

where $c_{D,b}$ is the bulk concentration of the draw (NaCl), S is the structural parameter of the support layer, and D is the diffusion coefficient of the draw solute. The structural parameter is obtained from [23]

$$S = \left(\frac{D}{J_w}\right) \ln\left(\frac{B + A\pi_{D,b}}{B + J_w}\right) \quad (4.12)$$

where $\pi_{D,b}$ is the osmotic pressure of the bulk draw solution. Substitution of eqs 4.11 and 4.12 into eq 4.10 yields:

$$c_{F,b} = \frac{c_{F,b_0} V_{F_0} + Bc_{D,b} \left(\frac{B + J_w}{B + A\pi_{D,b}}\right) A_m t}{(V_{F_0} - J_w A_m t)} \quad (4.13)$$

The membrane water permeability, A , is determined from the RO test, and c_{F,b_0} , V_{F_0} , $c_{D,b}$, $\pi_{D,b}$, and A_m are known experimental parameters. The solute permeability coefficient, B , and membrane structural parameter, S , can be calculated using eqs 4.12 and 4.13 by fitting feed concentration data as a function of time together with the measured J_w .

Determination of Membrane Performance in PRO Mode. One fabricated membrane from each batch (LP#1, MP#1, and HP#1) was tested in the FO system with the model seawater draw solution for PRO water flux performance at zero applied

hydraulic pressure. Experimental runs were conducted with river and brackish water feed solutions to simulate scenarios with different input streams. The membranes were oriented in PRO configuration (i.e., with the active layer facing the draw solution). Mesh spacers were employed in the draw channel to improve mixing, and both draw and feed stream flow rates were maintained at 1.0 L/min (21.4 cm/s crossflow velocity in feed channel) in co-current crossflow. The setup was maintained at a constant temperature of 25 ± 0.5 °C. Water flux was measured by monitoring the rate of change in weight of the draw solution, averaged over a 30 min period after it had stabilized.

Prediction of PRO Water Flux and Power Density. The water flux in PRO accounting for dilutive external concentration polarization (ECP) in the draw stream, concentrative ICP, and buildup of leaked draw salts in the porous support layer is described by eq 4.9, derived in the theory section. The power density, W , is defined as the power generated per unit membrane area:

$$W = J_w \Delta P \quad (4.14)$$

With inputs of known membrane characteristic parameters A , B , and S ; solution properties $\pi_{D,b}$, $\pi_{F,b}$, and D ; and mass transfer coefficient k , eq 4.9 can be solved numerically to obtain the theoretical PRO water flux over a range of applied pressures. The corresponding power densities can then be determined with eq 4.14. For predicting performance of the fabricated TFC-PRO membranes with the model seawater draw solution, the solute permeability coefficient, diffusion coefficient, and mass transfer coefficient for NaCl were used as approximations for coefficients of the multi-component system. Osmotic pressure of model seawater was calculated by a software package from

OLI Systems, Inc. (Morris Plains, NJ) while osmotic pressures of river and brackish water were determined by the van't Hoff equation.

4.4 RESULTS AND DISCUSSION

Validation of the PRO Water Flux Model. To validate the derived water flux model, a commercial cellulose triacetate (CTA) FO membrane (Hydration Technology Inc., Albany, OR) was tested in a PRO system under a range of applied hydraulic pressures. Characteristic parameters A , B , and S of the CTA membrane based on our recent study [13] were used in conjunction with eqs 4.9 and 4.14 to predict the water flux, J_w , and power density, W , as a function of applied hydraulic pressure, ΔP . The good agreement between actual and predicted water flux values validates the derived model (results not shown). Therefore, eqs 4.9 and 4.14 can be utilized to adequately project the peak power densities achievable by our fabricated TFC-PRO membranes by extrapolating from the experimental PRO water flux at no applied hydraulic pressure.

Membrane Characteristics. Representative scanning electron microscope (SEM) micrographs of the hand-cast TFC-PRO membrane are presented in Figure 4.2. Figure 4.2A shows a cross-sectional micrograph of a TFC-PRO membrane, demonstrating that large finger-like macrovoids ($\sim 10 \mu\text{m}$ width) span almost the entire support layer thickness. A close inspection of Figure 4.2A reveals that a less porous sponge-like morphology is present in the top skin portion of the PSf support (Figure 4.2C). Previous studies demonstrated that this specific structure is capable of minimizing the detrimental effects of ICP while allowing the formation of a polyamide layer that possesses high water permeability and salt rejection properties [13, 14].



Figure 4.2. SEM micrographs of a TFC-PRO membrane with PET fabric layer removed: A) cross-section with a finger-like macrovoid structure extending across the entire PSf support layer; B) magnified view of the polyamide active layer surface; and C) magnified view of the skin layer at the top of the PSf porous support with dense, sponge-like morphology. The magnified views are representative images and do not correspond to the actual locations on the center micrograph.

The values of the structural parameter S (349 ± 35 m, averaged over all 9 membranes), calculated from FO experiments (Table 4.1), verify the high porosity and low tortuosity of the hand-cast support layer. The 3 different membrane formulations — LP, MP and HP — had comparable S values, which is expected because the same fabrication process was followed for all the support layers. Furthermore, these values are consistent with previous experiments [14] and confirm the ability of this particular support structure to minimize ICP.

A thin, sponge-like skin layer forming on top of a layer containing macrovoids indicates that the two layers undergo different formation pathways during the phase separation process [14, 24]. Because the solvent of the casting solution is DMF, which has a relatively low heat of mixing with the non-solvent (water) [25], when the polymer solution is plunged into the non-solvent bath, the ratio of solvent outflux to water influx is high. This results in the top portion of the polymer film beginning to gel before the initiation of phase separation, thereby producing a dense sponge-like skin layer near the

top of the support layer (Figure 4.2C) [17, 26]. As the phase separation process progresses, the relatively low viscosity of the 9 wt% polymer solution allows for the rapid influx of non-solvent (i.e., rapid demixing conditions), resulting in the phase separation front moving faster than the gelation front [27]. The rapid demixing conditions, coupled with the higher concentration of polymer-poor regions [28], promote the formation of macrovoids that span most of the support layer thickness (Figure 4.2A) [29]. Additionally, pre-wetting the PET fabric with DMF facilitated the formation of macrovoids that remain open at the PSf-PET interface, which is critical to minimizing ICP [14].

Figure 4.2B presents an SEM micrograph of the TFC-PRO membrane active layer. The image shows a visually uniform ridge-and-valley morphology, which is typical of polyamide thin films formed by interfacial polymerization [30]. The resulting TFC-PRO membranes have an average water permeability coefficient, A , of $1.63 \pm 0.18 \text{ L m}^{-2}\text{h}^{-1}\text{bar}^{-1}$ and an average salt (NaCl) permeability coefficient, B , of $0.11 \pm 0.04 \text{ L m}^{-2}\text{h}^{-1}$. We designate these membranes LP for “low permeability” in Table 4.1. These values of the A and B permeability coefficients are consistent with those for previous hand-cast thin-film composite polyamide membranes [14, 31, 32].

We modified the transport properties of some membranes through chlorine and alkaline post-treatments of the polyamide thin films. The reactant concentrations, pH, and exposure times were controlled during the active layer modification to enhance the water flux at the expense of some salt retention capabilities [20]. Although the exact reason for these changes is not well understood, several mechanisms have been proposed

to explain the phenomenon, including Orton rearrangement [33], direct aromatic ring chlorination [34], and change in hydrogen bonding behavior [19].

Table 4.1. Summary of membrane characteristic parameters and modeled peak power densities for all TFC-PRO membranes fabricated.

Membrane	^a Intrinsic Water Permeability, A (L m ⁻² h ⁻¹ bar ⁻¹)	^b Solute Permeability Coefficient, B (L m ⁻² h ⁻¹)	^b Structural Parameter, S (μm)	^c Peak Power Density, W_{peak}	
				River Water (W/m ²)	Brackish Water (W/m ²)
LP#1	1.74	0.16	307	6.09	5.29
LP#2	1.42	0.08	355	5.24	4.56
LP#3	1.71	0.09	384	6.03	5.09
avg	1.63	0.11	349	5.79	4.98
st. dev.	0.18	0.04	39	0.47	0.38
MP#1	5.81	0.88	370	10.0	7.69
MP#2	4.08	0.77	332	9.21	7.38
MP#3	3.16	0.61	316	8.37	6.90
avg	4.35	0.76	340	9.21	7.33
st. dev.	1.34	0.14	28	0.84	0.40
HP#1	7.55	5.45	327	6.08	5.16
HP#2	7.35	4.12	336	6.82	5.71
HP#3	7.76	3.86	416	5.78	4.80
avg	7.55	4.48	360	6.23	5.22
st. dev.	0.20	0.85	49	0.54	0.46

^a Determined by permeate flux measurement in RO tests at 17.2 bar (250 psi) with DI water feed solution at 25 °C.

^b Determined by water flux and reverse salt flux measurements in FO tests with 0.5 M NaCl draw solution and DI water feed solution at 25 °C.

^c Calculated using eqs 4.9 and 4.14 with seawater draw solution and river water or brackish water feed solutions at 25 °C.

The membranes were subjected to one of two different post-treatments. The milder process resulted in an approximately 3-fold increase in A to $4.35 \pm 1.34 \text{ L m}^{-2}\text{h}^{-1}\text{bar}^{-1}$ and an increased B of $0.76 \pm 0.14 \text{ L m}^{-2}\text{h}^{-1}$. These samples are designated MP for “medium permeability” (Table 4.1). The stronger treatment produced TFC membranes with significantly higher A and B values of $7.55 \pm 0.20 \text{ L m}^{-2}\text{h}^{-1}\text{bar}^{-1}$ and $4.48 \pm 0.85 \text{ L m}^{-2}\text{h}^{-1}$, respectively (designated HP for “high permeability” in Table 4.1). SEM micrographs of the different active layers indicate a similar ridge-and-valley morphology, with little or no distinguishable difference from the unmodified membrane.

Water Flux and Projected Power Density of Hand-Cast TFC-PRO Membranes.

Experimentally measured water fluxes for our fabricated membranes, LP#1, MP#1, and HP#1, are presented in Figure 4.3. Measurements were made with no applied hydraulic pressure using a model seawater draw solution and both river water and brackish water feed solutions (indicated by open square and circle symbols, respectively). The characteristic membrane parameters, A , B , and S , of the different membranes are displayed above the water flux plots as bar graphs. These characteristic properties are used in conjunction with eqs 4.9 and 4.14 to extrapolate the water flux and power density as a function of applied hydraulic pressure. The solid and dashed lines show the calculated power densities for river water and brackish water feed solutions, respectively. A horizontal dashed line, corresponding to a power density W of 5 W/m^2 , is included as a visual guide in the plots of power density. There is generally good agreement between our experimental data obtained at no applied hydraulic pressure and the theoretical predictions. The water flux J_w is slightly over-predicted for HP#1 due to the variation of the mass transfer coefficient k as previously discussed.

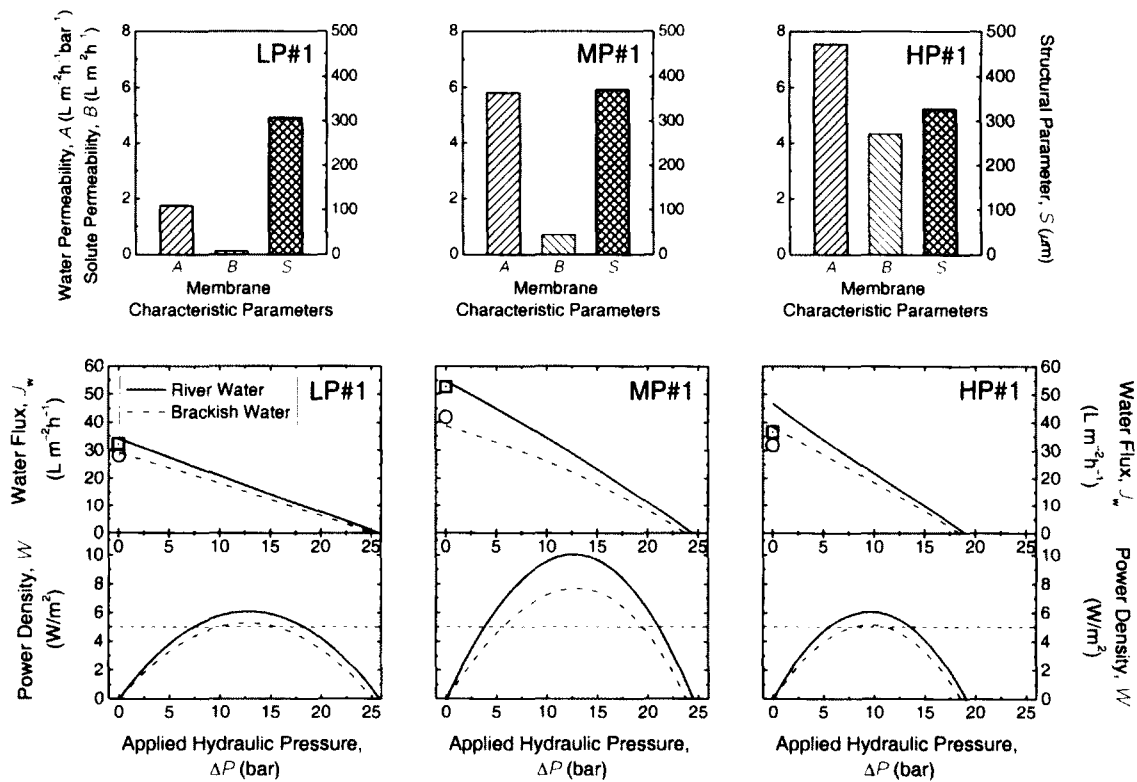


Figure 4.3. Plots of modeled water flux, J_w , and power density, W , (bottom) as a function of applied hydraulic pressure, ΔP , for TFC-PRO LP#1 (left), MP#1 (center), and HP#1 (right) membranes, and their respective characteristic parameters (top): intrinsic water permeability, A , solute permeability coefficient, B , and support layer structural parameter, S . Osmotic pressure of model seawater is 26.14 bar as determined by OLI Stream Analyzer software, and osmotic pressures of model river water and 1,000 ppm TDS brackish water are 0.045 and 0.789 bar respectively, as calculated using the van't Hoff equation. Symbols (open squares and circle symbols) represent measured experimental water fluxes of the membrane with model river water and brackish water as feed solutions, respectively. All experiments and calculations are done for draw and feed solutions at 25 °C.

The power density of the membranes investigated increases with increasing ΔP , until it reaches a maximum value of W_{peak} when the applied hydraulic pressure is approximately half of the osmotic pressure difference across the membrane, i.e., $\Delta P \approx (\pi_D - \pi_F)/2$. The predicted peak power densities of the 9 fabricated TFC-PRO membranes are summarized in Table 4.1. Membranes with different active layer

formulation, i.e., LP, MP, and HP, exhibit different W_{peak} . For example, with a river water feed solution and a seawater draw solution, the values of W_{peak} are 6.09, 10.0, and 6.08 W/m^2 for LP#1, MP#1, and HP#1, respectively. For a brackish water feed solution, the W_{peak} values for LP#1, MP#1, and HP#1 are slightly less, at 5.29, 7.69, and 5.16 W/m^2 , respectively, due to the higher salt concentration of the feed solution. In all cases, the W_{peak} values exceed 5 W/m^2 , and are the highest PRO peak power densities reported to date [2]. The outstanding performance of the TFC-PRO membranes is attributed to the combination of a customized support layer, which minimizes ICP, and an active layer that possesses high water permeability and moderately low salt permeability.

PRO Power Density Depends on Support and Active Layer Membrane Properties. The progress in power generation by PRO has been hindered by the absence of a suitable membrane [2, 6, 35]. Commercial membranes employed in previous studies lacked the right combination of transport properties, thereby limiting the W_{peak} to $< 3.5 \text{ W}/\text{m}^2$ when using a draw solution of approximately seawater concentration [2]. In this section, we discuss the role of the support layer structural parameter as well as active layer transport properties — salt and water permeabilities — in PRO water flux and power density performance.

a. Support Layer Structural Parameter. As water from the feed solution (river or brackish water) permeates across the active layer into the draw solution (seawater), the semi-permeable layer retains salts from the feed solution causing their local concentration within the support layer to increase. The buildup of salt concentration adversely affects PRO performance by increasing the local osmotic pressure of the feed solution, which decreases the effective osmotic driving force, thereby diminishing the water flux [6, 36].

Diffusion works to restore the concentration to that of the bulk feed solution but is limited by the porous support of the membrane which acts as an unstirred boundary layer and determines the extent of internal concentration polarization. The detrimental effect of ICP can be seen by examining the PRO water flux equation, eq 4.9, where the feed solution osmotic pressure $\pi_{f,b}$ is magnified by a factor of $\exp(J_w S/D)$.

The support layer structural parameter S is determined solely by the microstructure of the support membrane, and is defined as $S=t_s \tau/\varepsilon$, where t_s is the support thickness, τ is the tortuosity, and ε is the porosity. S has units of length and can be regarded as the characteristic distance a solute particle must diffuse from the active layer-porous support interface of the membrane to reach the bulk feed solution. When this distance is shorter, diffusion is more effective at restoring the concentration at the interface to that in the bulk feed solution. By thoughtful control of the support layer casting conditions, a membrane with a thin, porous, and non-tortuous support layer was fabricated in this study, which allows for a low S ($349 \pm 35 \mu\text{m}$) to be achieved. The low value of S minimizes the effective thickness of the ICP boundary layer, thereby allowing for higher water flux and power density performance.

b. Active Layer Salt Permeability. ICP is exacerbated by the reverse flux of draw solute [16], whereby the solute permeates from the more concentrated draw solution (seawater) into the feed solution (river or brackish water). The leaked solute accumulates in the porous support and further increases the interfacial osmotic pressure, producing an additional reduction of the osmotic driving force. The negative effects of this coupling between reverse salt permeation and ICP is reflected in the denominator of eq 4.9, where the osmotic pressure difference across the membrane is reduced by a factor of

$1+B/J_w[\exp(J_w S/D)-\exp(-J_w/k)]$. To mitigate this adverse effect, the membrane salt permeability, B , needs to be minimized. Although the PRO requirements for salt rejection are relaxed compared to FO systems, sufficient retention is necessary to keep an adequate osmotic driving force.

Both B and S need to be low to reduce the negative effect of reverse salt flux. A membrane with a large structural parameter will have its performance severely limited by the effects of the reverse solute flux, even if it has a relatively low solute permeability [6]. For example, commercial RO membranes have thick and dense support layers with large S on the order of 10,000 μm [13], and hence suffer from severe ICP effects [13, 22]. The effect of reverse salt permeation coupled with severe ICP is evident in PRO when the feed solution used is DI water. Despite the absence of solute from the feed stream, i.e., $\pi_{f,b}=0$, and a relatively low salt permeability B , any small amount of salt leaked over from the draw solution builds up within the porous support due to severely hindered diffusion. The detrimental effect of this increased leaked salt concentration on water flux is readily seen by examining eq 4.9. Due to the large S , the exponential ICP term, $\exp(J_w S/D)$, overwhelms the relatively small B and the ECP term, $\exp(-J_w/k)$, which ranges between zero and one. The large ICP term dominates the denominator expression, meaning that ICP markedly reduces the osmotic driving force across the membrane, which leads to a severely diminished water flux. Along with the low S parameter of the support layer, the TFC-PRO membranes fabricated in our study also have low values of B to adequately suppress reverse salt flux.

c. Active Layer Water Permeability. The driving force for water flux is the difference between the effective osmotic pressure, which accounts for the effects of concentration

polarization, and the applied hydraulic pressure. Water flux in PRO is equal to the driving force multiplied by the membrane intrinsic water permeability, A , as stated in eq 4.9. The commercial CTA FO membrane investigated in a previous PRO study yielded a modest W_{peak} of $\sim 2.7 \text{ W/m}^2$ despite having both a relatively low S of $\sim 678 \mu\text{m}$ and a low B of $0.40 \text{ L m}^{-2}\text{h}^{-1}$ [7]. Because asymmetric cellulose triacetate membranes have inherently lower A values ($0.67 \text{ L m}^{-2}\text{h}^{-1}\text{bar}^{-1}$ [7]) when compared to TFC membranes (e.g., A values summarized in Table 4.1), their performance is limited [13, 22]. During the fabrication of our TFC-PRO membranes, the support and active layers were formed in separate steps, allowing the properties of the two layers to be tailored almost independently of each other. By careful fabrication and modification of the membrane active layer, our TFC-PRO membranes were able to achieve higher water permeabilities with a moderate decline in salt retention capabilities. This active layer combined with the thin, porous support layer results in a higher water flux and power density.

Balancing Membrane Permeability-Selectivity to Maximize PRO Performance.

As the membranes become more permeable to water, i.e., LP→MP→HP, a corresponding increase in J_w and W_{peak} was not always observed. The 3 membrane formulations have comparable values of S and hence experience a similar degree of ICP. Despite HP#1 having the highest A , its achievable W_{peak} was significantly lower than the less permeable MP#1. This observation can be attributed to the substantially higher solute permeability of HP#1, which leads to more reverse salt permeation. The higher A of HP#1 ($\sim 30\%$ greater than MP#1) was accompanied by a disproportionate increase in B (over 6 times greater than MP#1). Consequently, the adverse effect of reverse salt permeation coupled

with ICP is severely amplified, overwhelming the benefit of higher water permeability. Therefore, the resulting water flux and power density are markedly reduced.

In order to maximize PRO performance, the membrane active layer should have a high A and a low B . However, progress toward this ideal situation is limited by the permeability-selectivity tradeoff that governs current separation membranes [37, 38], including polyamide TFC membranes [15, 28, 30], where an increase in water permeability is accompanied by an increase in salt permeation. Increasing the value of A up to a certain point benefits the PRO process because it allows for a higher water flux, after which the corresponding increase in B will result in the PRO productivity being hindered by the reverse permeation of draw solute. Therefore, to maximize the peak power density that can be achieved by a membrane in PRO, the active layer needs to be designed by balancing the tradeoff between permeability and selectivity.

Balancing the tradeoff between permeability and selectivity of PRO membranes will depend on the specific support layer structural parameter. The low S value of our fabricated membranes is essential to take advantage of more permeable but less selective active layers. The membranes are able to tolerate greater increases in B than membranes with a larger S value (e.g. commercial RO membranes) because the low S enables fast diffusion to keep the solution within the support sufficiently mixed, thereby mitigating the detrimental effect of reverse salt permeation. Hence, we are able to exploit the higher A and achieve a significantly higher W_{peak} .

4.5 IMPLICATIONS FOR OSMOTIC POWER GENERATION

The membranes developed in this work demonstrate the potential to produce high power densities in PRO with natural salinity gradients in excess of the goal of 5 W/m^2 necessary to produce osmotic power cost-effectively [12]. Important considerations for the design of future high performance PRO membranes are highlighted in this study. The experimental and simulated results illustrate that the PRO performance of a membrane can be maximized when the active layer transport properties are tailored to the support layer. For a particular support layer structural parameter S , the active layer permeabilities can be optimized to achieve the highest W_{peak} by balancing the benefit of a higher water permeability with the drawback of greater reverse salt leakage. A thin and porous support layer is crucial to exploiting a highly permeable but less selective active layer. By reducing ICP, a lower S value increases the membrane tolerance for the reverse permeation of salt, which enables the membrane to attain a greater W_{peak} .

River water is a precious resource, due to its lower concentration of dissolved solids, and hence brackish water may be a more feasible feed stream for a PRO plant to produce energy. The extrapolated performance for our highest performing membrane suggests that brackish water could be utilized as feed solution to produce a peak power density of 7.69 W/m^2 at an applied pressure near 13 bar. Alternatively, the same system could be operated at a lower applied hydraulic pressure of 5.6 bar, and still meet the proposed goal of 5 W/m^2 . This ability to operate at a reduced hydraulic pressure allows for greater flexibility when balancing the need to produce a thin porous support layer with one that can reliably withstand the mechanical stresses generated during operation.

4.6 REFERENCES

- [1] Evans, A.; Strezov, V. Evans, T. J., Assessment of sustainability indicators for renewable energy technologies. *Renewable & Sustainable Energy Reviews* **2009**, *13* (5), 1082-1088.
- [2] Achilli, A. Childress, A. E., Pressure retarded osmosis: From the vision of Sidney Loeb to the first prototype installation - Review. *Desalination* **2010**, *261* (3), 205-211.
- [3] Thorsen, T. Holt, T., The potential for power production from salinity gradients by pressure retarded osmosis. *Journal of Membrane Science* **2009**, *335* (1-2), 103-110.
- [4] Loeb, S., Production of Energy from Concentrated Brines by Pressure-Retarded Osmosis .1. Preliminary Technical and Economic Correlations. *Journal of Membrane Science* **1976**, *1* (1), 49-63.
- [5] McGinnis, R. L.; McCutcheon, J. R. Elimelech, M., A novel ammonia-carbon dioxide osmotic heat engine for power generation. *Journal of Membrane Science* **2007**, *305* (1-2), 13-19.
- [6] Lee, K. L.; Baker, R. W. Lonsdale, H. K., Membranes for Power-Generation by Pressure-Retarded Osmosis. *Journal of Membrane Science* **1981**, *8* (2), 141-171.
- [7] Achilli, A.; Cath, T. Y. Childress, A. E., Power generation with pressure retarded osmosis: An experimental and theoretical investigation. *Journal of Membrane Science* **2009**, *343* (1-2), 42-52.
- [8] Xu, Y.; Peng, X. Y.; Tang, C. Y. Y.; Fu, Q. S. A. Nie, S. Z., Effect of draw solution concentration and operating conditions on forward osmosis and pressure retarded osmosis performance in a spiral wound module. *Journal of Membrane Science* **2010**, *348* (1-2), 298-309.
- [9] Baker, R. W., Membrane technology and applications. 2nd ed.; J. Wiley, Chichester ; New York, **2004**; p x, 538 p.
- [10] Vos, K. D.; Burris, F. O. Riley, R. L., Kinetic Study of Hydrolysis of Cellulose Acetate in pH Range of 2-10. *Journal of Applied Polymer Science* **1966**, *10* (5), 825-&.
- [11] Brekke, G. The Statkraft Prototype Plant. <http://osmosis-summit.event123.no/programsummit2010.cfm> (Accessed on: 16 April, 2014).
- [12] Skilhagen, S. E., Osmotic power - a new, renewable energy source. *Desalination and Water Treatment* **2010**, *15* (1-3), 271-278.
- [13] Yip, N. Y.; Tiraferri, A.; Phillip, W. A.; Schiffman, J. D. Elimelech, M., High Performance Thin-Film Composite Forward Osmosis Membrane. *Environmental Science & Technology* **2010**, *44* (10), 3812-3818.
- [14] Tiraferri, A.; Yip, N. Y.; Phillip, W. A.; Schiffman, J. D. Elimelech, M., Relating Performance of Thin-Film Composite Forward Osmosis Membranes to Support Layer Formation and Structure. *Journal of Membrane Science* **2011**, *367* (1-2), 340-352.
- [15] Geise, G. M.; Park, H. B.; Sagle, A. C.; Freeman, B. D. McGrath, J. E., Water permeability and water/salt selectivity tradeoff in polymers for desalination. *Journal of Membrane Science* **2011**, *369* (1-2), 130-138.
- [16] Phillip, W. A.; Yong, J. S. Elimelech, M., Reverse Draw Solute Permeation in Forward Osmosis: Modeling and Experiments. *Environmental Science & Technology* **2010**, *44* (13), 5170-5176.

- [17] van de Witte, P.; Dijkstra, P. J.; van den Berg, J. W. A. Feijen, J., Phase separation processes in polymer solutions in relation to membrane formation. *Journal of Membrane Science* **1996**, *117* (1-2), 1-31.
- [18] Glater, J.; Zachariah, M. R.; Mccray, S. B. Mccutchan, J. W., Reverse-Osmosis Membrane Sensitivity to Ozone and Halogen Disinfectants. *Desalination* **1983**, *48* (1), 1-16.
- [19] Kwon, Y. N. Leckie, J. O., Hypochlorite degradation of crosslinked polyamide membranes - II. Changes in hydrogen bonding behavior and performance. *Journal of Membrane Science* **2006**, *282* (1-2), 456-464.
- [20] Jons, S. D.; Stutts, K. J.; Ferritto, M. S. Mickols, W. E. Treatment of composite polyamide membrane to improve performance. 5876602, **1999**.
- [21] Ang, W. S. Elimelech, M., Protein (BSA) fouling of reverse osmosis membranes: Implications for wastewater reclamation. *Journal of Membrane Science* **2007**, *296* (1-2), 83-92.
- [22] McCutcheon, J. R.; McGinnis, R. L. Elimelech, M., A novel ammonia-carbon dioxide forward (direct) osmosis desalination process. *Desalination* **2005**, *174* (1), 1-11.
- [23] Cath, T. Y.; Childress, A. E. Elimelech, M., Forward osmosis: Principles, applications, and recent developments. *Journal of Membrane Science* **2006**, *281* (1-2), 70-87.
- [24] Wijmans, J. G.; Kant, J.; Mulder, M. H. V. Smolders, C. A., Phase-Separation Phenomena in Solutions of Polysulfone in Mixtures of a Solvent and a Nonsolvent - Relationship with Membrane Formation. *Polymer* **1985**, *26* (10), 1539-1545.
- [25] Yanagishita, H.; Nakane, T. Yoshitome, H., Selection Criteria for Solvent and Gelation Medium in the Phase Inversion Process. *Journal of Membrane Science* **1994**, *89* (3), 215-221.
- [26] Mulder, M. H. V.; Hendrikman, J. O.; Wijmans, J. G. Smolders, C. A., A Rationale for the Preparation of Asymmetric Pervaporation Membranes. *Journal of Applied Polymer Science* **1985**, *30* (7), 2805-2820.
- [27] McKelvey, S. A. Koros, W. J., Phase separation, vitrification, and the manifestation of macrovoids in polymeric asymmetric membranes. *Journal of Membrane Science* **1996**, *112* (1), 29-39.
- [28] Mulder, M., Basic principles of membrane technology. 2nd ed.; Kluwer Academic, Dordrecht ; Boston, **1996**; p 564 p.
- [29] Smolders, C. A.; Reuvers, A. J.; Boom, R. M. Wienk, I. M., Microstructures in Phase-Inversion Membranes .1. Formation of Macrovoids. *Journal of Membrane Science* **1992**, *73* (2-3), 259-275.
- [30] Petersen, R. J., Composite Reverse-Osmosis and Nanofiltration Membranes. *Journal of Membrane Science* **1993**, *83* (1), 81-150.
- [31] Ghosh, A. K. Hoek, E. M. V., Impacts of support membrane structure and chemistry on polyamide-polysulfone interfacial composite membranes. *Journal of Membrane Science* **2009**, *336* (1-2), 140-148.
- [32] Lind, M. L.; Ghosh, A. K.; Jawor, A.; Huang, X. F.; Hou, W.; Yang, Y. Hoek, E. M. V., Influence of Zeolite Crystal Size on Zeolite-Polyamide Thin Film Nanocomposite Membranes. *Langmuir* **2009**, *25* (17), 10139-10145.
- [33] Kawaguchi, T. Tamura, H., Chlorine-Resistant Membrane for Reverse-Osmosis .1. Correlation between Chemical Structures and Chlorine Resistance of Polyamides. *Journal of Applied Polymer Science* **1984**, *29* (11), 3359-3367.

-
- [34] Glater, J. Zachariah, M. R., A Mechanistic Study of Halogen Interaction with Polyamide Reverse-Osmosis Membranes. *ACS Symposium Series* **1985**, *281*, 345-358.
- [35] Mehta, G. D. Loeb, S., Internal Polarization in the Porous Substructure of a Semipermeable Membrane under Pressure-Retarded Osmosis. *Journal of Membrane Science* **1978**, *4* (2), 261-265.
- [36] Loeb, S.; Titelman, L.; Korngold, E. Freiman, J., Effect of porous support fabric on osmosis through a Loeb-Sourirajan type asymmetric membrane. *Journal of Membrane Science* **1997**, *129* (2), 243-249.
- [37] Robeson, L. M., Correlation of Separation Factor Versus Permeability for Polymeric Membranes. *Journal of Membrane Science* **1991**, *62* (2), 165-185.
- [38] Mehta, A. Zydney, A. L., Permeability and selectivity analysis for ultrafiltration membranes. *Journal of Membrane Science* **2005**, *249* (1-2), 245-249.

Chapter 5:

**Performance Limiting Effects in
Power Generation from Salinity
Gradients by Pressure Retarded
Osmosis**

CHAPTER ABSTRACT

Pressure retarded osmosis has the potential to utilize the free energy of mixing when fresh river water flows into the sea for clean and renewable power generation. Here, we present a systematic investigation of the performance limiting phenomena in pressure retarded osmosis — external concentration polarization, internal concentration polarization, and reverse draw salt flux — and offer insights on the design criteria of a high performance pressure retarded osmosis power generation system. Thin-film composite polyamide membranes were chemically modified to produce a range of membrane transport properties, and the water and salt permeabilities were characterized to determine the underlying permeability-selectivity tradeoff relationship. We show that power density is constrained by the tradeoff between permeability and selectivity of the membrane active layer. This behavior is attributed to the opposing influence of the beneficial effect of membrane water permeability and the detrimental impact of reverse salt flux coupled with internal concentration polarization. Our analysis reveals the intricate influence of active and support layer properties on power density and demonstrates that membrane performance is maximized by tailoring the water and salt permeabilities to the structural parameters. An analytical parameter that quantifies the relative influence of each performance limiting phenomena is employed to identify the dominant effect restricting productivity. External concentration polarization is shown to be the main factor limiting performance at high power densities. Enhancement of the hydrodynamic flow conditions in the membrane feed channel reduces external concentration polarization and thus, yields improved power density. However, doing so will also incur additional operating costs due to the accompanying hydraulic pressure

loss. This study demonstrates that by thoughtful selection of the membrane properties and hydrodynamic conditions, the detrimental effects that limit productivity in a pressure retarded osmosis power generation process can be methodically minimized to achieve high performance.

5.1 INTRODUCTION

Developing clean and renewable energy sources is one of the greatest global challenges of our time. The continued dependence on fossil fuels to meet our growing energy demands is unsustainable due to its finite availability and the emission of greenhouse gases and air pollutants. Although the advancement of a broad range of alternative energy technologies has increased sustainable production, we still rely substantially on fossil fuels for our current energy consumption [1]. To realize sustainable energy production for the present and future, intensive research and development is needed to overcome the deficiencies that limit existing alternative energy approaches and produce novel technological options [1].

Natural salinity gradients have been identified as a potential source of renewable energy [2]. When two solutions of different concentration are mixed, the Gibbs free energy of mixing is released. The approximately 0.61 kWh (2.2 MJ) of energy dissipated when 1 m³ of fresh river water flows into the sea can potentially be harvested for power production [3]. A recent study estimates the global renewable energy from natural salinity gradients could reach 2 TW, or ~13% of the current world energy consumption, if the energy of mixing from all rivers flowing into the ocean was harnessed [3].

Pressure retarded osmosis (PRO) is one of the methods proposed to tap this source of renewable energy [4, 5]. PRO utilizes the osmotic pressure difference that develops when a semi-permeable membrane separates two solutions of different concentration, to drive the permeation of water from the dilute “feed solution” into the more concentrated “draw solution.” A hydraulic pressure less than the osmotic pressure difference is applied to the draw solution, thereby “retarding” water flux across the membrane, and a hydroturbine extracts work from the expanding draw solution volume. PRO can also use anthropogenic waste streams, such as concentrated brine from a desalination plant [6], as a draw solution. A closed-loop version of PRO, the osmotic heat engine, uses a thermolytic draw solution of ammonia and carbon dioxide to convert waste thermal energy into useful electrical energy [7].

Progress in PRO power generation, however, has been hindered by the absence of an adequate membrane. Commercial membranes employed in previous studies did not possess the necessary transport and structural properties, and hence achieved only nominal power densities (power produced per membrane area) [8, 9]. A PRO pilot plant in Norway, built to demonstrate power production from natural salinity gradients, generated less than 0.5 W/m^2 using asymmetric cellulose acetate membranes [10]. This power density is an order of magnitude lower than the power density of 5 W/m^2 required for this specific installation to be commercially viable [11]. Similarly, previous studies with commercial membranes demonstrated low PRO power densities of $<3.5 \text{ W/m}^2$ using a draw solution with a concentration approximately equal to that of seawater [12].

Several groups have recently demonstrated membranes capable of high performance in osmotically-driven membrane processes [13-17]. In our previous work, we presented

the fabrication of thin-film composite (TFC) membranes customized for high performance in PRO [18]. The membranes consist of a selective polyamide layer formed by interfacial polymerization on top of a polysulfone support layer made by phase separation. The phase separation fabrication conditions were selected to produce a thin and highly porous support layer that minimizes internal concentration polarization (ICP) and, at the same time, facilitates the formation of an integral polyamide active layer [16]. The polyamide layer was subjected to a chlorine-alkaline post-treatment in order to tune the water and salt permeabilities. Using a river water feed solution and a seawater draw solution, a power density of $\sim 10.0 \text{ W/m}^2$ was projected for the prototype PRO-TFC polyamide membrane. The enhanced performance was attributed to the high water permeability of the active layer coupled with a moderate salt permeability and the ability of the support layer to suppress the undesirable accumulation of leaked salt into the porous support [18].

The fabricated membranes in our earlier study demonstrated the dependence of PRO power density on membrane active and support layer properties [18]. The permeability-selectivity tradeoff that governs separation membranes dictates that a more water permeable membrane is also less selective for salt [19-21]. Although a membrane active layer with greater water permeability produces a higher water flux and hence, yields a larger power density, the concomitant decline in selectivity causes a simultaneous increase in reverse salt flux. The greater reverse permeation of draw salt, exacerbated by internal concentration polarization in the membrane support layer, gives rise to a reduction in the osmotic driving force across the membrane [18, 22]. The detrimental effect of ICP-coupled reverse salt flux works against the benefit of a more permeable but

less selective membrane to restrict PRO performance [18]. The findings of the chapter reveal the convoluted influence of membrane properties on the performance limiting effects and the ensuing power density. As such, an understanding of how membrane properties, as well as other operating parameters, affect water flux and power density is crucial for the design of a high performance PRO system.

In this study we provide a systematic investigation of the detrimental effects of the performance limiting phenomena on PRO power generation from natural salinity gradients. Membranes with a range of transport properties were prepared and evaluated to determine the permeability-selectivity tradeoff relationship for thin-film composite polyamide membranes. The influence of membrane properties (specifically, water permeability, salt permeability, and structural parameter) and hydrodynamic conditions on power density performance is analyzed and discussed. We introduce an analytical “Loss Factor” to quantify the dominance of the detrimental effects — external concentration polarization, internal concentration polarization, and reverse salt flux. The role of the membrane properties and hydrodynamic conditions in determining the extent of the performance limiting phenomena is examined to provide insight into their intricate relationship with the resultant power density.

5.2 MATERIALS AND METHODS

Materials and Chemicals. Commercial thin-film composite seawater reverse osmosis membranes (TFC-RO, SW30-HR, Dow Chemical Company, Midland, MI) were acquired for the chlorine–alkaline treatment of the polyamide active layer to produce membranes with a range of water and salt permeabilities. All chemicals used were analytical grade.

To prepare the chlorine reagent for membrane modification, sodium hypochlorite aqueous solution (Sigma Aldrich, St. Louis, MO) was added to deionized (DI) water (Milli-Q, Millipore, Billerica, MA) and adjusted to pH 7.0 by dosing with 6 M hydrochloric acid. The alkaline reagent for the membrane modification was made by diluting 1 M sodium hydroxide (Fisher Scientific, Pittsburgh, PA) in DI water to the concentration of 0.1 M.

Polyamide Active Layer Modification. Exposure of the polyamide active layer to chlorine alters its structure and morphology, resulting in increased water permeability and decreased selectivity (or salt rejection) of the membrane [23-25]. By carefully controlling the reaction parameters, the water and salt permeabilities of the membrane active layer can be tailored [18, 26]. Different degrees of modification were carried out on the commercial TFC-RO membranes in a two-step treatment to produce seven batches of membranes, denoted I through VII, with a range of active layer transport properties. Batch I membranes were not subjected to either treatment step. The membranes of batches II to VII were first immersed in 300, 500, 1000, 1500, 2000, or 3000 ppm NaOCl aqueous solution, respectively, for 60 min. In the second step, membrane batches III through VII were transferred to a 0.1 M NaOH aqueous solution and soaked for 16 h, while batch II membranes were left out of this alkaline-treatment step. The treated membranes were then rinsed thoroughly and stored in DI water at 4 °C. Two membranes were prepared in each batch for a total of 14 membrane samples.

Determination of Membrane Water and Salt Permeabilities. Pure water permeability and salt rejection of the modified TFC-RO membranes were evaluated in a laboratory-scale crossflow RO test unit [27]. The effective membrane area was 20.02

cm², the crossflow velocity was fixed at 21.4 cm/s, and spacers were not employed in the feed channel. The loaded membrane was first compacted with DI water at an applied pressure, ΔP , of 31.0 bar (450 psi) until the permeate flux reached a steady state (at least 15 h). The applied pressure was then lowered to 27.6 bar (400 psi) and the pure water flux, J_w , was calculated by dividing the volumetric permeate rate by the membrane area. Intrinsic water permeability coefficient, A , was determined by dividing the water flux by the applied pressure, $A = J_w/\Delta P$.

Salt rejection was characterized by keeping the applied pressure at 27.6 bar (400 psi) and measuring rejection of 50 mM NaCl solution using a calibrated conductivity meter (Oakton Instruments, Vernon Hills, IL). Observed NaCl rejection, R , was determined from the difference in bulk feed (c_b) and permeate (c_p) salt concentrations, $R = 1 - c_p/c_b$. The rejection values for each sample are the average of three different measurements collected over a ~60 min period. The solute permeability coefficient, B , was determined from [28, 29]:

$$B = J_w \left(\frac{1-R}{R} \right) \exp \left(-\frac{J_w}{k_f} \right) \quad (5.1)$$

where k_f , the crossflow cell mass transfer coefficient, is calculated from correlations for this geometry [30]. The temperature of the system was maintained at 25 ± 0.5 °C throughout the experiment.

5.3 RESULTS AND DISCUSSION

Membranes are Bounded by Permeability-Selectivity Tradeoff. Chlorine-alkaline treatment was carried out on a commercial TFC-SWRO membrane to obtain a range of

active layer transport properties. A summary of the intrinsic water permeability coefficient, A , salt (NaCl) rejection, R , and NaCl permeability coefficient, B , for the resulting membranes is presented in Table 5.1. The concentration of the NaOCl aqueous solution in the chlorination step and the inclusion of a 16-h alkaline immersion step are also indicated in the Table.

Table 5.1. Summary of chlorine and alkaline treatment conditions on commercial TFC polyamide RO membrane and the resultant water permeability coefficient, salt rejection, and NaCl permeability coefficient of the modified active layer.

^a Modification	NaOCl Concentration (ppm)	Alkaline immersion	^b Intrinsic Water Permeability, A ($L\ m^{-2}h^{-1}bar^{-1}$)	^c Salt Rejection, R (%)	^d Solute Permeability Coefficient, B ($L\ m^{-2}h^{-1}$)
I	–	No	1.22 ± 0.06	99.1 ± 0.0	0.10 ± 0.01
II	300	No	2.11 ± 0.28	99.3 ± 0.2	0.16 ± 0.10
III	500	Yes	3.73 ± 0.55	98.5 ± 0.6	0.54 ± 0.08
IV	1,000	Yes	4.37 ± 0.10	97.6 ± 0.9	1.11 ± 0.53
V	1,500	Yes	5.04 ± 0.07	95.2 ± 0.8	1.82 ± 0.42
VI	2,000	Yes	6.71 ± 0.10	89.3 ± 0.3	4.99 ± 0.00
VII	3,000	Yes	7.70 ± 0.34	86.4 ± 2.4	7.67 ± 0.49

^a Two samples were modified and characterized for each treatment condition.

^b Determined by permeate flux measurement in RO tests at 27.6 bar (400 psi) with DI water feed at 25 °C.

^c Determined by conductivity measurements in RO tests at 27.6 bar (400 psi) with 50 mM (2,920 mg/L) NaCl feed solution at 25 °C.

^d Determined from water flux and salt rejection measurements in RO tests at 27.6 bar (400 psi) with 50 mM (2,920 mg/L) NaCl feed solution at 25 °C.

The reactant concentration, solution pH, and exposure times of the chlorine-alkaline treatment were designed to enhance the water permeability of the SWRO polyamide active layer at the expense of some salt rejection capabilities [18, 26]. Although several mechanisms had been proposed to explain the phenomenon, including Orton

rearrangement [31], direct aromatic ring chlorination [32], and increased rotational freedom or flexibility of polymer chains due to the change in hydrogen bonding behavior [24, 33], the exact mechanism for the change in transport properties of the membrane active layer is not yet fully determined.

Seven batches of membranes, denoted I through VII in Table 5.1, were subjected to chlorine-alkaline treatments of increasing strength. Batch I membranes were not modified and have the lowest average water permeability coefficient, A , of $1.22 \text{ L m}^{-2}\text{h}^{-1}\text{bar}^{-1}$ and also the lowest average salt (NaCl) permeability coefficient, B , of $0.10 \text{ L m}^{-2}\text{h}^{-1}$. Membranes of batch VII were exposed to the harshest modification treatment (immersion in a 3000 ppm NaOCl aqueous solution at pH 7.0 for 60 min, followed by a 0.1 M NaOH soak for 16 h) and have the highest average A and B of $7.70 \text{ L m}^{-2}\text{h}^{-1}\text{bar}^{-1}$ and $7.67 \text{ L m}^{-2}\text{h}^{-1}$, respectively, among the batches (Table 5.1). As expected, the average water and salt permeability of the membranes increased from batch I to VII, with increasing strength of chlorine-alkaline treatment. The range of A and B values determined here are consistent with previous studies employing similar modification conditions [18, 26], and are typical of seawater RO, brackish water RO, and tight nanofiltration membranes [34]. The salt rejections, R , of all the membranes were above 86% (Table 5.1), verifying the ability of the active layers to retain salt and hence, maintain an osmotic gradient across the membrane in PRO applications.

An inspection of the A and B trend (Table 5.1) reveals the permeability-selectivity tradeoff that governs TFC polyamide membranes [29, 34, 35], as well as other polymeric membranes [19, 21], where an increase in water permeability is accompanied by a concomitant increase in salt permeation. For the membranes investigated here, an

increase in the water permeability coefficient, A , is generally accompanied by an even larger increase in the salt permeability coefficient, B . This disproportionate decrease in selectivity is more drastic at higher permeabilities. For example, membranes from batch IV have an average A value 3.6 times greater than membranes from batch I, and their average B value is 11.1 times larger. Furthermore, while the average A of membranes from batch VII is 6.3 times that of membranes from batch I, the average B is 77 times greater (Table 5.1).

The productivity of conventional SWRO membranes is constrained by the permeability-selectivity tradeoff. Specifically, the high selectivity required to produce permeate of low solute concentration in a single-pass RO (>99.3% salt rejection [28]) puts an upper limit on the permeability of the membrane for seawater desalination. PRO, on the other hand, exploits the controlled mixing of solutions to generate energy and therefore, only needs enough salt rejection to maintain the osmotic driving force [8]. The constraint of high selectivity is hence partially relaxed for PRO membranes, affording us an additional degree of freedom in customizing the active layer.

Correlation between Membrane Water and Salt Permeabilities. A recent study demonstrated a permeability-selectivity tradeoff for salt-rejecting polymeric membranes [35], similar to that observed in gas separation membranes [19, 20, 36]. Using literature data, an upper bound behavior was observed between the membrane permeability to water, P_w , and the water/salt permeability selectivity, P_w/P_s (where P_s is the membrane permeability to salt), and an empirical relationship was proposed [35]:

$$\frac{P_w}{P_s} = \frac{\lambda}{(P_w)^\beta} \quad (5.2)$$

where λ and β are empirical fitting parameters. The plot of P_w/P_s as a function of P_w in Figure 5.1A shows the permeability-selectivity tradeoff and upper bound behavior.

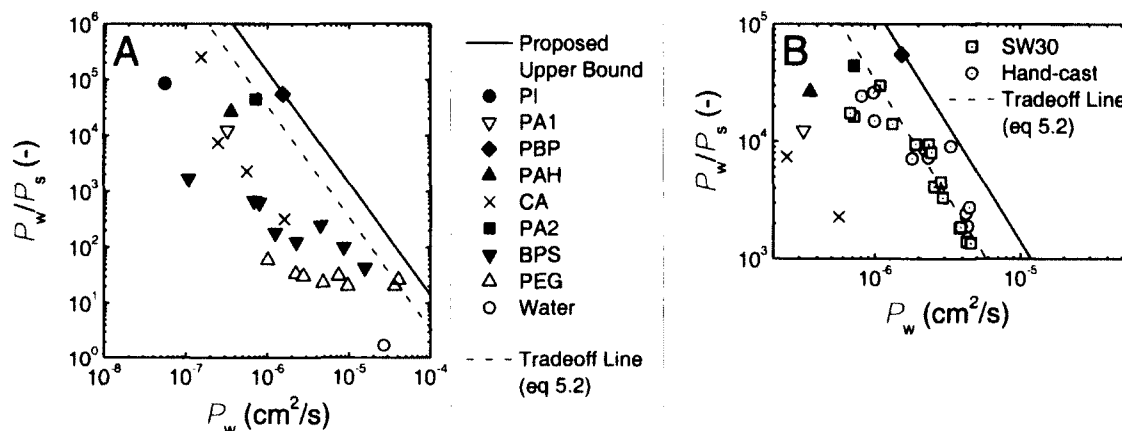


Figure 5.1. Correlation between water/NaCl permeability-selectivity, P_w/P_s , and membrane permeability to water, P_w . (A) Data from Geise et al. [35] for various polymeric materials: PI (polyimide), PA1 (aromatic polyamide), PBP (polybenzimidazolepyrrolone), PAH (polyamide-hydrazide), CA (cellulose acetate), PA2 (aromatic polyamide), BPS (sulfonated poly(arylene ether sulfone)), PEG (crosslinked poly(ethylene glycol)), and pure water. The solid black line represents the proposed upper bound relationship [35] (eq 5.2 with $\lambda = 1.4 \times 10^{-7} \text{ cm}^4/\text{s}^2$ and $\beta = 2$). Dashed red line ($\lambda = 0.37 \times 10^{-7} \text{ cm}^4/\text{s}^2$ and $\beta = 2$) indicates the permeability-selectivity tradeoff for modified polyamide active layers investigated in this study and our recent publication [18]. Empirical fitting parameter λ was determined by fitting the data to eq 5.5 and assuming $L = 150 \text{ nm}$. (B) Experimental data used to determine the tradeoff line (eq 5.2, dashed red line). Green square symbols represent commercial TFC-SWRO membrane, SW30, modified in this study. Blue circle symbols indicate data for post-treated hand cast PRO membranes reported in our recent publication [18].

The membrane permeabilities to water and salt, P_w and P_s , respectively, are intrinsic properties of the active layer material, and can be related to the bulk transport properties of the membrane by [35]:

$$A = \frac{P_w}{L} \frac{M_w}{\rho R_g T} \quad (5.3)$$

$$B = \frac{P_s}{L} \quad (5.4)$$

where A is the membrane water permeability coefficient, L is the thickness of the active layer, M_w is the molar mass of water, ρ is the density of water, R_g is the gas constant, T is the absolute temperature, and B is the membrane salt (NaCl) permeability coefficient. Substitution of eqs 5.3 and 5.4 into eq 5.2 yields an equation linking the water permeability coefficient of the membrane active layer to its salt permeability coefficient through the permeability-selectivity tradeoff relationship presented in Figure 5.1B:

$$B = \frac{L^\beta}{\lambda} \left(\frac{\rho R_g T}{M_w} \right)^{\beta+1} A^{\beta+1} \quad (5.5)$$

The A and B values determined in this study (Table 5.1), together with the permeability data from our recent publication on hand-cast polyamide PRO membranes [18], were fitted to eq 5.5 with L^β/λ as the empirical fitting parameter. In the gas separation tradeoff relationship, the slope of the tradeoff line, β , is proportional to the difference in the squares of the gas molecule diameters [20]. It is hypothesized that β for salt-rejecting membranes takes on a similar fundamental physical meaning, but is currently undetermined [35]. Therefore, we adopted the value of $\beta = 2$ from the permeability-selectivity tradeoff study on salt-rejecting polymeric membranes [35] to perform the fitting.

The experimental data and fitted line are presented in Figure 5.2, with the water and salt permeability coefficients plotted on a log-log scale. For temperature $T = 298$ K, the fitting parameter L^2/λ was calculated to be $6.11 \times 10^{-3} \text{ s}^2/\text{cm}^2$. The plot of P_w/P_s as a function of P_w in Figure 5.1B shows that the TFC polyamide membranes exhibit the permeability-selectivity tradeoff relationship and a similar upper bound behavior

(indicated by the dashed red line, $\lambda = 0.37 \times 10^{-7} \text{ cm}^4/\text{s}^2$). Due to inherent challenges in the accurate measurement of the effective active layer thickness of a polyamide thin-film composite membrane, the thickness values reported in literature falls over a wide range (40 to 300 nm) [34, 35, 37]. As the active layers studied here and in our recent work were modified from seawater reverse osmosis TFC polyamide membranes, an identical polyamide film thickness, L , of 150 nm was assumed to calculate P_w and P_s using eqs 5.3 and 5.4, respectively. The data points generally lie on a slope of ~ 2 over one order of magnitude in P_w . The good agreement between the slope of the experimental results and the assumed value of $\beta = 2$ reinforces the hypothesis that the slope of the tradeoff line represents a yet to be uncovered, fundamental physical principle that governs transport across the active layer [35].

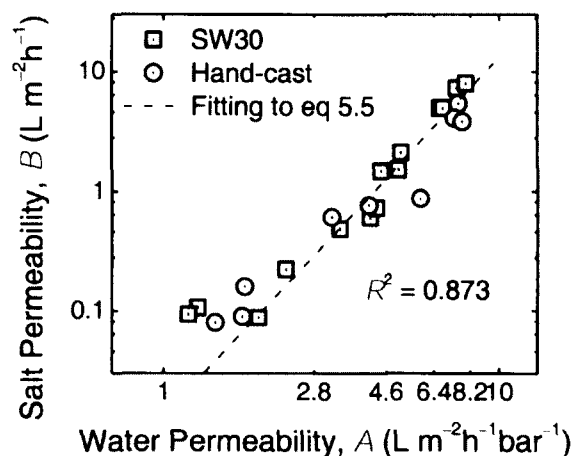


Figure 5.2. Log-log plot of water and salt permeability coefficients of TFC polyamide membranes subjected to chlorine-alkaline modification. Green square symbols indicate commercial SWRO membranes, SW30, modified in this study. Blue circle symbols indicate data for post-treated hand cast TFC polyamide PRO membranes reported in our recent publication [18]. A and B data is fitted to eq 5.5 for $T = 298 \text{ K}$, $M_w = 18 \text{ g/mol}$, and $\beta = 2$. Fitting parameter L^2/λ is determined to be $6.11 \times 10^{-3} \text{ s}^2/\text{cm}^2$.

Our recent study demonstrated that in order to maximize PRO performance, the membrane active layer should be highly permeable to water and highly selective to salt [18]. However, progress toward this ideal situation is limited by the permeability-selectivity tradeoff that governs salt-rejecting membranes, as shown above. Thin-film composite polyamide membranes are widely used in separation and purification applications and are considered state-of-the-art technology salt-rejecting membranes [28, 29, 34, 38]. The empirical relationship between the water and salt permeability coefficient of TFC polyamide membranes (eq 5.5) developed here can serve as a useful tool in the design of membranes for PRO power generation. In the following subsections, we will demonstrate that by balancing the tradeoff between the permeability and selectivity of the membrane active layer, PRO power density performance can be maximized.

Phenomena Governing Water Flux and Power Density in PRO. In osmotically-driven membrane processes, the effective osmotic pressure across the membrane less the applied hydraulic pressure, $\Delta\pi_m - \Delta P$, provides the driving force for water flux. In PRO, $\Delta\pi_m$ is lower than the osmotic pressure difference between the bulk draw and feed solutions (i.e., $\Delta\pi_m < \pi_{D,b} - \pi_{F,b}$) due to the detrimental effects of external concentration polarization (ECP) in the draw solution, internal concentration polarization (ICP) within the porous support, and reverse salt flux, J_s^R , across the membrane.

In our recent study, we presented the development of a model to predict the water flux in PRO. The model incorporates the performance limiting phenomena of ECP, ICP, and reverse permeation of salt [18]:

$$J_w = A(\Delta\pi_m - \Delta P) = A \left\{ \frac{\pi_{D,b} \exp\left(-\frac{J_w}{k}\right) - \pi_{F,b} \exp\left(\frac{J_w S}{D}\right)}{1 + \frac{B}{J_w} \left[\exp\left(\frac{J_w S}{D}\right) - \exp\left(-\frac{J_w}{k}\right) \right]} - \Delta P \right\} \quad (5.6)$$

where $\pi_{D,b}$ and $\pi_{F,b}$ are the osmotic pressures of the bulk draw and feed solution, respectively, k is the ECP mass transfer coefficient, S is the structural parameter of the membrane support layer, and D is the diffusion coefficient of the solute. The power density, W , defined as the power generated per unit membrane area, can be calculated from:

$$W = J_w \Delta P \quad (5.7)$$

Here, we discuss the detrimental influence of the three performance limiting phenomena — ECP, ICP, and reverse salt flux — on PRO performance. Specifically, the effect of each phenomenon on the salt concentration at the membrane interface is examined and related to the resultant water flux performance.

a. External Concentration Polarization. As water permeates across the membrane, it dilutes the draw solution and lowers the salt concentration at the active layer, $c_{D,m}$, resulting in external concentration polarization at the draw solution side. The reduced osmotic pressure at the solution-membrane interface lowers $\Delta\pi_m$ and hence, diminishes the resultant water flux. The effect of dilutive ECP on water flux is reflected in the numerator of the PRO water flux governing equation, eq 5.6, where the osmotic pressure of the draw solution is reduced by a factor of $\exp(-J_w/k)$.

b. Internal Concentration Polarization. As water permeates across the membrane, the feed solutes are selectively retained by the semi-permeable active layer and build up within the porous support. Consequently, the salt concentration at the active-support

layer interface, $c_{F,m}$, increases. Diffusion works to restore this local concentration to the bulk feed solution concentration, $c_{F,b}$, but is hindered by the porous support, which acts as an unstirred boundary layer. The elevated salt concentration within the membrane support layer, termed internal concentration polarization, reduces the effective osmotic pressure across the membrane and therefore, lowers J_w . The detrimental effect of concentrative ICP can be seen by examining the PRO water flux equation (eq 5.6), where the feed solution osmotic pressure $\pi_{F,b}$ is magnified by a factor of $\exp(J_w S/D)$.

c. Reverse Salt Flux. The deleterious effect of ICP is exacerbated by the reverse flux of draw solute, J_s^R , whereby the solute permeates from the more concentrated draw solution into the feed solution side [39]. The leaked solute accumulates in the porous support and further increases the interfacial osmotic pressure, $\pi_{F,m}$. This produces an additional reduction of the osmotic driving force and, consequently, a lower water flux [18, 22]. The negative effect of this coupling between reverse salt permeation and ICP is reflected in the denominator of eq 5.6, where the osmotic pressure difference across the membrane is reduced by a factor of $1 + B/J_w[\exp(J_w S/D) - \exp(-J_w/k)]$. The reverse flux of draw solute also decreases the interfacial osmotic pressure at the draw side of the membrane. However, the net influence of J_s^R on the osmotic pressure difference across the active layer is dominated by the effect in the membrane support layer. This can be validated by applying practical values of S , D , and k , to the denominator of eq 5.6, where the ICP factor, $\exp(J_w S/D)$, which ranges from 1 to ∞ , will typically overwhelm the ECP factor, $\exp(-J_w/k)$, which ranges between zero and one, in the term $\exp(J_w S/D) - \exp(-J_w/k)$.

Representative plots of J_w and W as a function of the applied hydraulic pressure, ΔP , are shown in Figure 5.3. In the ideal case where all three performance limiting phenomena are absent (indicated by the solid grey lines), relatively high PRO water flux (governed by eq 5.6, $\Delta\pi_m = \pi_{D,b} - \pi_{F,b}$) and power density (eq 5.7) can theoretically be attained. However, due to the combined detrimental effects of ECP, ICP, and reverse salt flux, the actual J_w and W are much lower than the hypothetical ideal scenario.

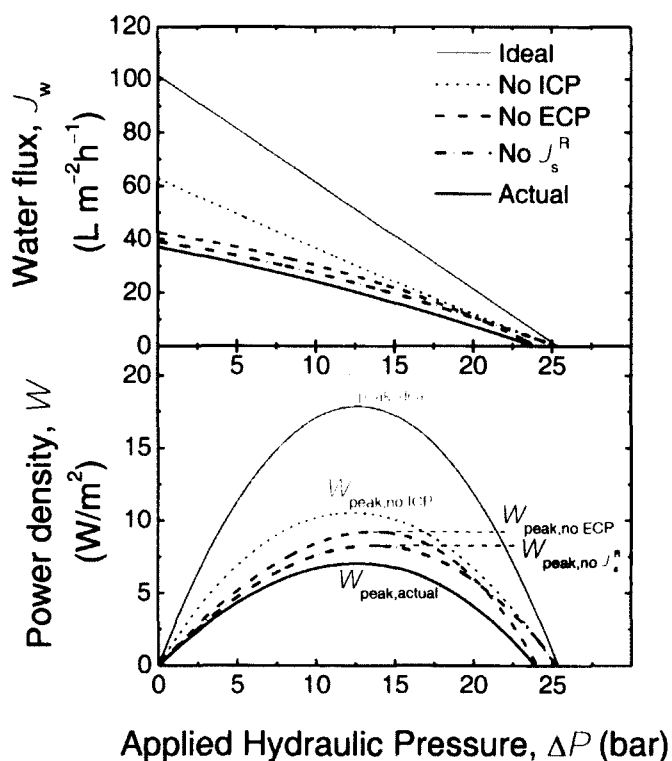


Figure 5.3. Representative plots of water flux (eq 5.6) and power density (eq 5.7) as a function of applied hydraulic pressure, ΔP . Ideal water flux and power density without any detrimental effects (i.e., $\Delta\pi_m = \pi_{D,b} - \pi_{F,b}$) is indicated by the solid grey line, while the solid black line shows the J_w and W for an actual membrane, incorporating all three performance-limiting effects of ECP, ICP and reverse draw salt flux. The water flux and power density of hypothetical cases where there is no ICP (i.e., $\exp(J_w S/D) = 1$), ECP (i.e., $\exp(-J_w/k) = 1$), or reverse salt flux, J_s^R , (i.e., $B/J_w[\exp(J_w S/D) - \exp(-J_w/k)] = 0$) are represented by the dotted red line, dashed blue line, and dot-dashed green line, respectively. J_w and W were calculated using $\pi_{D,b} = 26.14$ bar, $\pi_{F,b} = 0.789$ bar, $A = 4.0$ $L \cdot m^{-2} \cdot h^{-1} \cdot bar^{-1}$, $B = 0.85$ $L \cdot m^{-2} \cdot h^{-1}$, $S = 350$ μm , and $k = 38.5$ $\mu m/s$ (138.6 $L \cdot m^{-2} \cdot h^{-1}$).

To isolate the contribution of each phenomenon to diminishing PRO performance, we consider three hypothetical scenarios where one of the detrimental effects is absent. In Figure 5.3, the dashed blue lines, dotted red lines, and dot-dashed green lines represent the theoretical cases where there is no external concentration polarization, internal concentration polarization, or reverse salt flux, respectively. The water flux values for these three scenarios are determined using eq 5.6. For the case of “No ECP”, the external concentration polarization factor, $\exp(-J_w/k)$, is set to unity. To simulate the “No ICP” condition, we apply an internal concentration polarization factor $\exp(J_w S/D) = 1$ to eq 5.6. For the third hypothetical case where there is no reverse salt flux (i.e., “No J_s^R ”), the denominator of the water flux equation, $1+B/J_w[\exp(J_w S/D)-\exp(-J_w/k)]$, is set to unity. Note that by simultaneously fixing the above three factors to unity in eq 5.6 (i.e., no ECP, ICP, and J_s^R), the ideal water flux and power density (Figure 5.3, solid grey lines) are recovered.

Removing one of the detrimental effects resulted in higher water flux and power density for the three hypothetical cases than the actual scenario (Figure 5.3). Therefore, minimizing the detrimental effects of the performance limiting phenomena would enhance PRO performance. This is quantitatively evident in the PRO water flux (eq 5.6), where J_w can be enhanced by reducing the ICP and reverse salt flux factors, $\exp(J_w S/D)$ and $1+B/J_w[\exp(J_w S/D)-\exp(-J_w/k)]$, respectively, or raising the ECP factor, $\exp(-J_w/k)$. Understanding the parameters affecting each phenomenon will enable an informed approach to suppress the performance limiting effects and guide in the design of a high-performance PRO system. In the following sections, we will look at the role of the membrane and channel flow condition in determining the extent of the performance

limiting phenomena and examine the influence of the parameters on the peak power density.

Influence of Membrane Properties on Peak Power Density. Operating PRO at a high power density will maximize the utilization of membrane area and reduce capital cost requirements [5, 8]. To achieve peak power density, W_{peak} , a hydraulic pressure that is approximately half of the osmotic pressure difference across the membrane is applied (i.e., $\Delta P \approx (\pi_D - \pi_F)/2$, as depicted in Figure 5.3). Recently, we presented the fabrication of thin-film composite membranes capable of producing high W_{peak} [18]. The enhanced performance was attributed to the high water permeability of the active layer, coupled with a moderate salt permeability and the ability of the support layer to suppress the accumulation of leaked salt into the porous support. The findings of the study highlighted the important role of membrane transport and structural properties in determining the achievable W_{peak} .

Figure 5.4 shows a contour plot of the projected W_{peak} as a function of membrane properties A , B , and S . The peak power densities were determined by solving $dW/d\Delta P = 0$ numerically using eqs 5.6 and 5.7. Membrane water permeability is represented on a linear scale on the bottom horizontal axis. As the salt permeability is related to A by the tradeoff relationship (eq 5.5), the corresponding B values are indicated on the top horizontal axis (not to scale). The range of S values, indicated on the log-scale vertical axis, was chosen to represent the structural parameters of TFC polyamide membranes that are commercially available, SWRO membrane ($\sim 10,000 \mu\text{m}$) [17], or TFC polyamide membranes that have been demonstrated in a laboratory setting, including: hollow fiber membranes ($\sim 600\text{-}1,400 \mu\text{m}$) [13], hand-cast flat sheet membranes ($\sim 300\text{-}$

3,000 μm) [16], and nanofiber composite membranes ($\sim 80\text{-}110$ μm) [14]. To simulate power generation from natural salinity gradients, the osmotic pressures of the draw and feed solutions were taken to be $\pi_{\text{D,b}} = 26.14$ bar and $\pi_{\text{F,b}} = 0.045$ bar, to represent seawater and river water, respectively [18]. The mass transfer coefficient in the draw side ECP boundary layer, $k = 38.5$ $\mu\text{m/s}$ (138.6 $\text{L m}^{-2}\text{h}^{-1}$), was based on the experimental value determined in our previous PRO study [18].

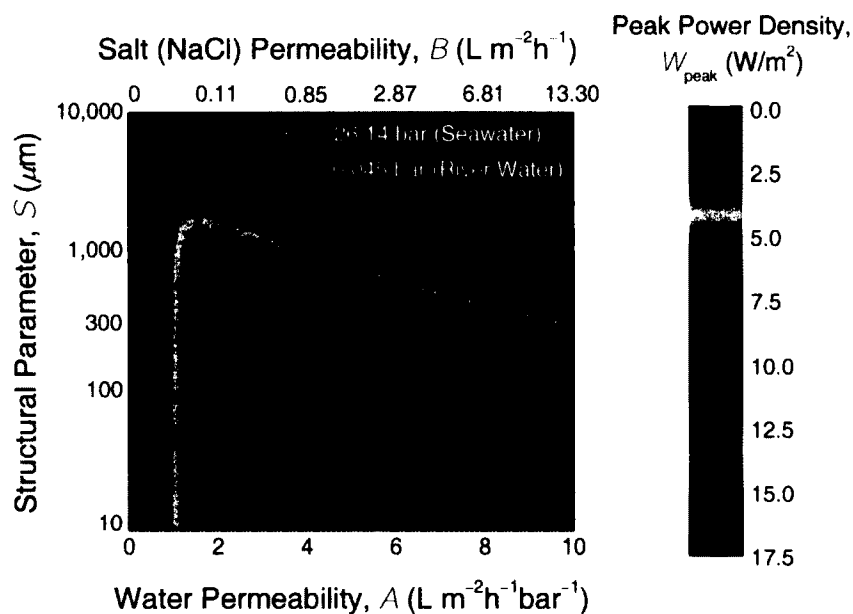


Figure 5.4. Peak power density, W_{peak} , as a function of active layer water and salt permeabilities (bottom and top horizontal axes, respectively) and support layer structural parameter, S (vertical axis). Dotted horizontal line represents a structural parameter of 300 μm , while dashed violet line indicates the active layer properties (values of A and B pair), where peak power density is maximized, $W_{\text{peak,max}}$, for a particular S . Osmotic pressures of the draw and feed solutions are 26.14 and 0.045 bar, respectively, simulating seawater and river water [18]. The ECP mass transfer coefficient used in the calculations is $k = 38.5$ $\mu\text{m/s}$ (138.6 $\text{L m}^{-2}\text{h}^{-1}$).

Water flux in PRO is equal to the osmotic driving force, $\Delta\pi_{\text{m}} - \Delta P$, multiplied by the membrane water permeability coefficient, A , as stated in eq 5.6. As the membrane becomes more permeable to water (i.e., Figure 5.4, left to right), a corresponding increase

in W_{peak} is observed up to a certain point, after which W_{peak} decreases instead. The maximum peak power density, $W_{\text{peak,max}}$, that can be attained for a particular structural parameter (indicated by the dashed violet line) occurs at a specific pair of water and salt permeabilities. For example, W_{peak} reaches a maximum of 9.29 W/m^2 for $S = 300 \text{ }\mu\text{m}$ (dotted horizontal line) when $A = 4.2 \text{ L m}^{-2}\text{h}^{-1}\text{bar}^{-1}$ and $B = 0.99 \text{ L m}^{-2}\text{h}^{-1}$ (intersection with dashed violet line). The drop in W_{peak} at higher membrane permeabilities is attributed to the limiting effect of reverse draw salt flux — the decreased selectivity of the active layer results in greater passage of draw salt into the membrane support layer, thereby diminishing the osmotic driving force. To the left of the dashed violet line, increasing the water permeability benefits the PRO process as it allows for a higher water flux, and hence, W_{peak} increases to a maximum value. Beyond that, the detrimental effect of leaked salt accumulated in the porous support overwhelms any gain from a higher A . Therefore, PRO power density performance is maximized by balancing the tradeoff between the permeability and selectivity of the membrane active layer.

Membranes with a smaller structural parameter achieve maximum W_{peak} at higher active layer permeabilities, as shown by the dashed violet line sloping towards the bottom right in Figure 5.4. The performance limiting effect of reverse salt flux is coupled to ICP in the support layer — a membrane with a lower S minimizes the effect of ICP by facilitating the diffusion of leaked draw solute to the bulk solution, thereby mitigating the negative impact of salt buildup at the membrane interface. The dependence of ICP-coupled reverse salt flux on the support layer structural parameter S can be seen by examining the denominator of the PRO water flux equation, $1+B/J_w[\exp(J_w S/D)-\exp(-J_w/k)]$. Structural parameter $S = t_s \pi/\varepsilon$, where t_s is the support

layer thickness, τ is the tortuosity, and ε is the porosity, characterizes the average distance a solute molecule must travel through the support layer when going from the active layer to the bulk feed solution. Membranes with a lower S value are able to tolerate greater increases in B by enabling better mixing of the solution within the porous support, and hence, reduce the ICP factor, $\exp(J_w S/D)$, to suppress the detrimental effects of salt leakage. This allows the membranes to take greater advantage of more permeable but less selective active layers and achieve a higher $W_{\text{peak,max}}$. Therefore, the optimal combination of active layer permeability and selectivity to achieve the maximum W_{peak} is determined by the support layer structural parameter.

Conventional TFC reverse osmosis membranes have a thick and dense support layer ($S = 10,000 \mu\text{m}$) and hence, can only attain a paltry $W_{\text{peak,max}}$ of 1.09 W/m^2 , even with an optimal active layer ($A = 0.6 \text{ L m}^{-2}\text{h}^{-1}\text{bar}^{-1}$ and $B = 0.003 \text{ L m}^{-2}\text{h}^{-1}$). To meet the target of 5 W/m^2 necessary to produce osmotic power cost-effectively [11], the TFC polyamide membrane will need to possess a structural parameter $< 1,200 \mu\text{m}$, together with balanced active layer transport properties (Figure 5.4, intersection of 5 W/m^2 contour line and dashed violet line). With an S value of $100 \mu\text{m}$, approximately the lowest structural parameter reported in literature for a TFC membrane [14], the projected $W_{\text{peak,max}}$ is 12.5 W/m^2 with a seawater draw solution and river water feed solution. This demonstrates that, while balancing the active layer A and B allows the maximum W_{peak} to be achieved, the magnitude of $W_{\text{peak,max}}$ is constrained by the support layer structural parameter.

In the development of the PRO water flux equation, the negative effect of concentrative external concentration polarization in the feed solution was considered to be negligible [18]. However, as the process approaches the operating regime of high

water fluxes and low S values, this simplifying assumption may no longer hold true as concentrative ECP exerts a more significant influence on limiting J_w and W . As such, although the projected $W_{\text{peak,max}}$ for a very thin and highly porous support layer (e.g., $S = 50 \mu\text{m}$), can reach as high as 14.0 W/m^2 , this value is likely to be an over-prediction, and a more comprehensive model is needed to reflect the impact of concentrative ECP in the feed side on PRO performance. Furthermore, decreasing the thickness and increasing the porosity of the support layer may compromise the ability of a conventional TFC membrane to withstand hydraulic pressure. Membrane mechanical strength, though beyond the scope of this work, should be an important factor to consider in the future development of PRO membranes. Lastly, to simplify the PRO water flux and power density predictions, the permeability coefficient of NaCl salt was used in the model. In an actual PRO process utilizing natural salinity gradients, the draw solution will contain a mixture of ionic species. Therefore, the real power density is likely to deviate slightly from the model predictions.

Losses in Power Density due to Performance Limiting Effects. PRO power density performance is limited by the detrimental effects of ICP, ECP, and reverse salt flux. To isolate the negative contribution of each phenomenon and identify the dominant effect, we consider the hypothetical peak power density, $W_{\text{peak|hyp}}$, of three theoretical scenarios where the effect of one phenomenon is ignored (as described earlier and illustrated in Figure 5.3). Hence, the difference in the peak power density between the hypothetical and the actual case can be attributed to the phenomenon that was intentionally left out. Dividing this difference by $W_{\text{peak|hyp}}$, we obtain an analytical

parameter that we call the loss factor, LF, which describes the individual influence of ICP, ECP, or reverse draw salt flux on power density performance:

$$LF = \frac{W_{\text{peak|hyp}} - W_{\text{peak}}}{W_{\text{peak|hyp}}} = 1 - \frac{W_{\text{peak}}}{W_{\text{peak|hyp}}} \quad (5.8)$$

The loss factors for external concentration polarization (LF_{ECP}), internal concentration polarization (LF_{ICP}), and reverse draw salt flux (LF_{J_r}) were calculated for the earlier W_{peak} analysis (Figure 5.4) and presented in Figures 5.5A through C, respectively. The top and bottom horizontal axes represent the water and salt permeability of the active layer, respectively, the vertical axis indicates the support layer structural parameter, and the dashed violet line demarcates $W_{\text{peak,max}}$. To enable comparison between the three phenomena, a common scale bar is adopted. A high loss factor (approaching 1) signifies a greater influence from the effect, while an LF of zero denotes no detrimental impact from the phenomenon. The analytical loss factors provide useful insights into the phenomena limiting performance in PRO and facilitate a systematic approach to optimize operating parameters for high power density.

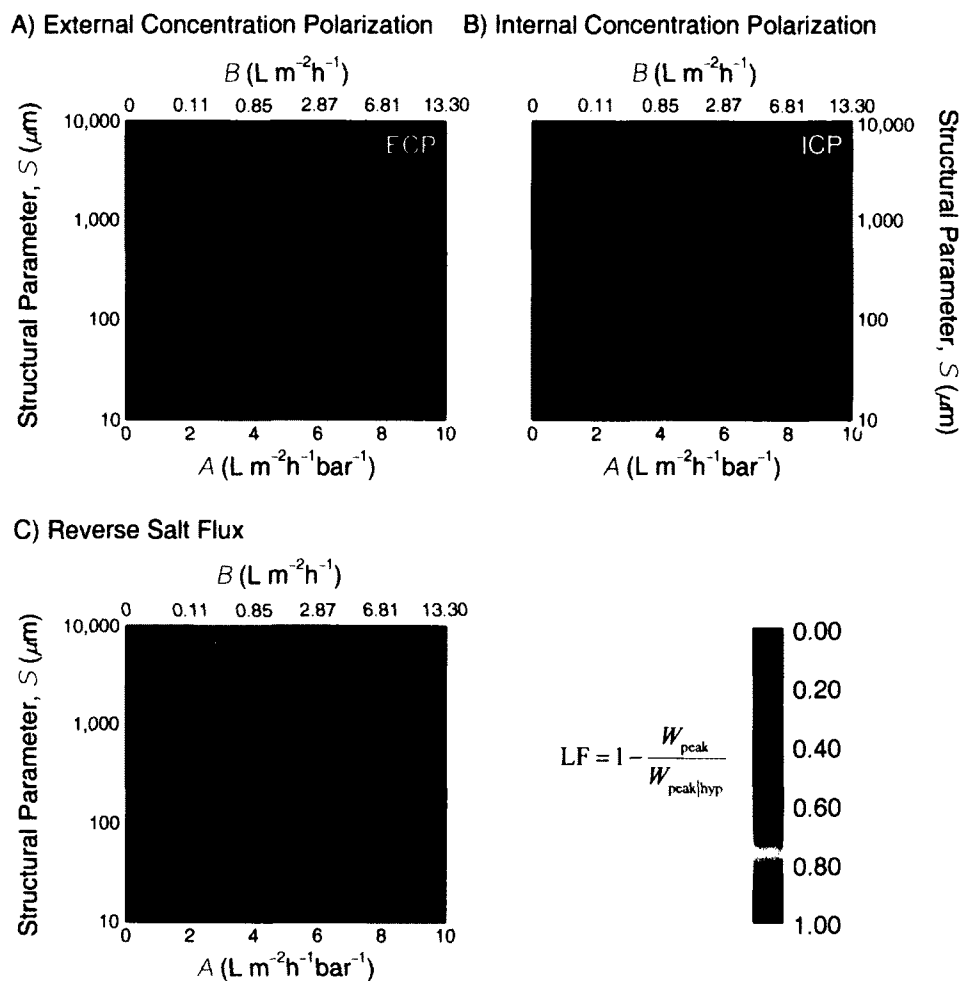


Figure 5.5. Losses in W_{peak} due to the individual effect of the performance limiting phenomena: A) ECP, B) ICP, and C) reverse draw salt flux as a function of active layer water and salt permeabilities (bottom and top horizontal axes, respectively), and the support layer structural parameter, S (vertical axis). Scale bar indicates the loss factor, $1 - W_{peak}/W_{peak|hyp}$ (eq 5.8). Dashed violet line indicates $W_{peak,max}$. Osmotic pressures of the draw and feed solution are 26.14 and 0.045 bar, respectively, simulating seawater and river water [18]. The ECP mass transfer coefficient used in the calculations is $k = 38.5 \mu m/s$ ($138.6 L m^{-2} h^{-1}$).

Internal concentration polarization and reverse salt flux (Figures 5.5B and C, respectively) exhibit similar LF trends for the seawater-river water analysis. This reinforces the coupling between the reverse draw salt flux and ICP, where the leaked solute is hindered by the membrane porous support from mixing with the bulk feed

solution. To the left of $W_{\text{peak,max}}$ (dashed violet line), LF_{ICP} and LF_{J^R} are less than ~ 0.25 , while to the right, both loss factors increase sharply to 0.75 and beyond. This observation is consistent with our earlier discussion, stating that at lower A and B , the PRO process is able to take advantage of an increase in water permeability to realize a higher W_{peak} , while at higher permeabilities, the adverse effect of ICP-coupled reverse salt flux dominates and hence, negates any potential benefits from a larger A .

In actual PRO power generation from salinity gradients, it may be more feasible to utilize input streams of higher salinity as the feed solution, instead of river water with relatively low dissolved solids (~ 80 ppm TDS, $\pi_{\text{f,b}} = 0.045$ bar). The analysis was repeated with a more salty brackish water ($\sim 5,000$ ppm TDS, $\pi_{\text{f,b}} = 3.95$ bar) as the feed solution. Similar trends in LF were generally observed when a more saline feed solution was employed, with the exception of the loss factor for ICP. Compared to river water feed solution, LF_{ICP} was higher at large structural parameters when brackish water was used as the feed solution, signifying a more influential role played by internal concentration polarization.

As water permeates across the membrane, the feed solutes are selectively retained and concentrate within the porous support layer. Hence, the osmotic pressure at the active layer interface is the bulk osmotic pressure of the feed solution multiplied by the ICP factor — $\pi_{\text{f,b}} \exp(J_w S/D)$. Use of a very dilute feed solution reduces the interfacial concentration, thus mitigating the detrimental effect of concentrative ICP. However, when the feed solution contains more salt, internal concentration polarization amplifies the larger $\pi_{\text{f,b}}$, resulting in a considerably higher interfacial osmotic pressure at the feed side. Thus, the driving force for water flux, $\Delta\pi_m$, is drastically lowered, and PRO

performance is diminished. The ICP factor, $\exp(J_w S/D)$, increases exponentially with S . Therefore, a minimized membrane support layer structural parameter is vital to achieve high power density with saline feed solutions.

A comparison of Figure 5.4 with Figure 5.5A shows that the loss factor for external concentration polarization displays a roughly inverse trend to the power density. The extent of ECP is determined by the water flux across the membrane — water permeation dilutes the draw solution at the membrane and hence, reduces the interfacial osmotic pressure. As power density, W , is J_w multiplied by the applied hydraulic pressure, ΔP (eq 5.7), ECP will therefore be more adverse at higher power densities. At large water fluxes and low S values (i.e., bottom right quadrant of Figure 5.5A), LF_{ECP} escalates to >0.40 , suggesting that ECP is the key phenomenon limiting PRO performance at high W . As such, after the membrane transport and structural properties are optimized, the PRO power density performance can be further enhanced by inducing favorable hydrodynamic flow conditions in the draw solution channel to minimize ECP.

Influence of Hydrodynamic Conditions on Peak Power Density. As water permeates across the membrane, the osmotic driving force is reduced due to dilutive external concentration polarization. The extent of ECP is determined by the mass transfer coefficient, k , in the boundary layer. By improving the mixing at the membrane-solution interface through increased crossflow velocity or the use of spacers, the mass transfer coefficient can be enhanced. The detrimental effect of the ECP factor, $\exp(-J_w/k)$, in eq 5.6 is reduced by the higher k value, thus increasing the PRO peak power density performance.

Figure 5.6 shows the projected $W_{\text{peak,max}}$ (dashed violet line, left vertical axis) as a function of the mass transfer coefficient, k . The maximum peak power densities were determined numerically using eqs 5.5, 5.6, and 5.7, and by simultaneously solving for the conditions for peak W (i.e., $dW/d\Delta P = 0$) and maximum W_{peak} (i.e., $dW_{\text{peak}}/dA = 0$). The corresponding water permeability coefficient, A , required to maximize the peak power density is indicated by the solid blue line (right vertical axis). A seawater draw solution ($\pi_{\text{D,b}} = 26.14$ bar) and a river water feed solution ($\pi_{\text{F,b}} = 0.045$ bar) were used to simulate power generation from natural salinity gradients. The structural parameter ($S = 300 \mu\text{m}$) represents a high performance support layer fabricated by the phase inversion technique employed in the manufacture of conventional TFC membrane [16].

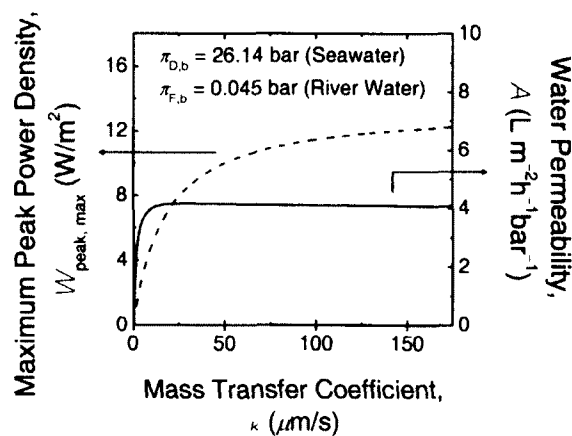


Figure 5.6. Maximum peak power density achievable, $W_{\text{peak,max}}$ (dashed violet line), as a function of mass transfer coefficient, k , in the ECP boundary layer. The corresponding membrane water permeability, A , to achieve this maximum peak power density is indicated by the solid blue line. Membrane porous support structural parameter, S was assigned a value of $300 \mu\text{m}$. Osmotic pressure of the draw and feed solutions is 26.14 bar and 0.045 bar, respectively, to simulate seawater and river water [18].

When the mass transfer coefficient is low, dilutive ECP is significant and PRO power density is low. An increase in k quickly eliminates this inefficiency, translating to rapid gains in $W_{\text{peak,max}}$, as indicated by the initial steep slope of the dashed violet line. At high

J_w , the enhancement in peak power performance diminishes with increasing k , and gradually levels off after $W_{\text{peak,max}} > 12 \text{ W/m}^2$. This behavior is attributed to: i) the growing influence of the other two performance limiting phenomena, ICP and reverse salt flux; and ii) the increased dilutive ECP effect at greater water fluxes, as indicated by J_w in the ECP factor, $\exp(-J_w/k)$. While enhancing the hydrodynamic conditions in the draw side of the membrane channel can increase the power density performance, it would also raise the parasitic hydraulic losses and impose additional pumping cost to the PRO process. Hence, any power density improvements from a higher k would only be worthwhile if they can offset the hydraulic losses to achieve a net gain in overall productivity. Analysis of the relationship between $W_{\text{peak,max}}$ and k , such as the one presented in Figure 5.6, can help guide the design of a cost-efficient PRO system. We note that the balanced water permeability coefficient required to maximize peak power density (i.e., $dW_{\text{peak}}/dA = 0$) is essentially independent of the hydrodynamic conditions for $k > 5 \mu\text{m/s}$, as indicated by the flat portion of the solid blue line.

5.4 IMPLICATIONS FOR RENEWABLE ENERGY FROM SALINITY GRADIENTS

To realize sustainable power generation with natural salinity gradients, the cost-efficiency of PRO and other competing technologies needs to be enhanced. This study demonstrates that the performance of a PRO power generation process can be methodically improved through thoughtful selection of the membrane properties and hydrodynamic conditions to purposefully minimize the performance limiting effects. At the heart of PRO power generation is the semi-permeable membrane, and thus, the

productivity of the process is circumscribed by the membrane properties. Further substantial improvements in performance necessitate membrane development to depart from the conventional thin-film composite polyamide membranes that are currently considered state-of-the-art technology [38, 40]. Examples of next-generation PRO membranes envisioned include: self-supporting selective layers that eliminate ICP by doing away with the need for a porous layer and novel membrane materials with superior transport properties that can shift the permeability-selectivity upper bound further outwards.

5.5 REFERENCES

- [1] Hoffert, M. I.; Caldeira, K.; Benford, G.; Criswell, D. R.; Green, C.; Herzog, H.; Jain, A. K.; Kheshgi, H. S.; Lackner, K. S.; Lewis, J. S.; Lightfoot, H. D.; Manheimer, W.; Mankins, J. C.; Mauel, M. E.; Perkins, L. J.; Schlesinger, M. E.; Volk, T. Wigley, T. M. L., Advanced technology paths to global climate stability: Energy for a greenhouse planet. *Science* **2002**, *298* (5595), 981-987.
- [2] Pattle, R. E., Production of Electric Power by Mixing Fresh and Salt Water in the Hydroelectric Pile. *Nature* **1954**, *174* (4431), 660-660.
- [3] La Mantia, F.; Cui, Y.; Pasta, M.; Deshazer, H. D. Logan, B. E., Batteries for Efficient Energy Extraction from a Water Salinity Difference. *Nano Letters* **2011**, *11* (4), 1810-1813.
- [4] Loeb, S., Osmotic Power-Plants. *Science* **1975**, *189* (4203), 654-655.
- [5] Ramon, G. Z.; Feinberg, B. J. Hoek, E. M. V., Membrane-based production of salinity-gradient power. *Energy & Environmental Science* **2011**, *4* (11), 4423-4434.
- [6] Loeb, S., Production of Energy from Concentrated Brines by Pressure-Retarded Osmosis. I. Preliminary Technical and Economic Correlations. *Journal of Membrane Science* **1976**, *1* (1), 49-63.
- [7] McGinnis, R. L.; McCutcheon, J. R. Elimelech, M., A novel ammonia-carbon dioxide osmotic heat engine for power generation. *Journal of Membrane Science* **2007**, *305* (1-2), 13-19.
- [8] Lee, K. L.; Baker, R. W. Lonsdale, H. K., Membranes for Power-Generation by Pressure-Retarded Osmosis. *Journal of Membrane Science* **1981**, *8* (2), 141-171.
- [9] Achilli, A.; Cath, T. Y. Childress, A. E., Power generation with pressure retarded osmosis: An experimental and theoretical investigation. *Journal of Membrane Science* **2009**, *343* (1-2), 42-52.
- [10] Brekke, G. The Statkraft Prototype Plant. <http://osmosis-summit.event123.no/programsummit2010.cfm> (Accessed on: 16 Apr, 2014).
- [11] Skilhagen, S. E., Osmotic power - a new, renewable energy source. *Desalination and Water Treatment* **2010**, *15* (1-3), 271-278.
- [12] Achilli, A. Childress, A. E., Pressure retarded osmosis: From the vision of Sidney Loeb to the first prototype installation - Review. *Desalination* **2010**, *261* (3), 205-211.
- [13] Wang, R.; Shi, L.; Tang, C. Y. Y.; Chou, S. R.; Qiu, C. Fane, A. G., Characterization of novel forward osmosis hollow fiber membranes. *Journal of Membrane Science* **2010**, *355* (1-2), 158-167.
- [14] Song, X. X.; Liu, Z. Y. Sun, D. D., Nano gives the answer: Breaking the bottleneck of internal concentration polarization with a nanofiber composite forward osmosis membrane for a high water production rate. *Advanced Materials* **2011**, *23* (29), 3256-3260.
- [15] Yang, Q.; Wang, K. Y. Chung, T. S., Dual-Layer Hollow Fibers with Enhanced Flux As Novel Forward Osmosis Membranes for Water Production. *Environmental Science & Technology* **2009**, *43* (8), 2800-2805.
- [16] Tiraferrri, A.; Yip, N. Y.; Phillip, W. A.; Schiffman, J. D. Elimelech, M., Relating Performance of Thin-Film Composite Forward Osmosis Membranes to Support Layer Formation and Structure. *Journal of Membrane Science* **2011**, *367* (1-2), 340-352.

- [17] Yip, N. Y.; Tiraferri, A.; Phillip, W. A.; Schiffman, J. D. Elimelech, M., High Performance Thin-Film Composite Forward Osmosis Membrane. *Environmental Science & Technology* **2010**, *44* (10), 3812-3818.
- [18] Yip, N. Y.; Tiraferri, A.; Phillip, W. A.; Schiffman, J. D.; Hoover, L. A.; Kim, Y. C. Elimelech, M., Thin-Film Composite Pressure Retarded Osmosis Membranes for Sustainable Power Generation from Salinity Gradients. *Environmental Science & Technology* **2011**, *45* (10), 4360-4369.
- [19] Robeson, L. M., Correlation of Separation Factor Versus Permeability for Polymeric Membranes. *Journal of Membrane Science* **1991**, *62* (2), 165-185.
- [20] Freeman, B. D., Basis of permeability/selectivity tradeoff relations in polymeric gas separation membranes. *Macromolecules* **1999**, *32* (2), 375-380.
- [21] Mehta, A. Zydney, A. L., Permeability and selectivity analysis for ultrafiltration membranes. *Journal of Membrane Science* **2005**, *249* (1-2), 245-249.
- [22] Wei, J.; Liu, X.; Qiu, C. Q.; Wang, R. Tang, C. Y. Y., Influence of monomer concentrations on the performance of polyamide-based thin film composite forward osmosis membranes. *Journal of Membrane Science* **2011**, *381* (1-2), 110-117.
- [23] Glater, J.; Zachariah, M. R.; Mccray, S. B. Mccutchan, J. W., Reverse-Osmosis Membrane Sensitivity to Ozone and Halogen Disinfectants. *Desalination* **1983**, *48* (1), 1-16.
- [24] Kwon, Y. N. Leckie, J. O., Hypochlorite degradation of crosslinked polyamide membranes - II. Changes in hydrogen bonding behavior and performance. *Journal of Membrane Science* **2006**, *282* (1-2), 456-464.
- [25] Glater, J.; Hong, S. K. Elimelech, M., The Search for a Chlorine-Resistant Reverse-Osmosis Membrane. *Desalination* **1994**, *95* (3), 325-345.
- [26] Jons, S. D.; Stutts, K. J.; Ferritto, M. S. Mickols, W. E. Treatment of composite polyamide membrane to improve performance. US Patent 5876602, **1999**.
- [27] Ang, W. S. Elimelech, M., Protein (BSA) fouling of reverse osmosis membranes: Implications for wastewater reclamation. *Journal of Membrane Science* **2007**, *296* (1-2), 83-92.
- [28] Baker, R. W., Membrane technology and applications. 2nd ed.; J. Wiley, Chichester ; New York, **2004**; p 538.
- [29] Mulder, M., Basic principles of membrane technology. 2nd ed.; Kluwer Academic, Dordrecht ; Boston, **1996**; p 564.
- [30] Hoek, E. M. V.; Kim, A. S. Elimelech, M., Influence of crossflow membrane filter geometry and shear rate on colloidal fouling in reverse osmosis and nanofiltration separations. *Environmental Engineering Science* **2002**, *19* (6), 357-372.
- [31] Kawaguchi, T. Tamura, H., Chlorine-Resistant Membrane for Reverse-Osmosis .I. Correlation between Chemical Structures and Chlorine Resistance of Polyamides. *Journal of Applied Polymer Science* **1984**, *29* (11), 3359-3367.
- [32] Glater, J. Zachariah, M. R., A Mechanistic Study of Halogen Interaction with Polyamide Reverse-Osmosis Membranes. *ACS Symposium Series* **1985**, *281*, 345-358.

-
- [33] Kwon, Y. N.; Tang, C. Y. Leckie, J. O., Change of chemical composition and hydrogen bonding behavior due to chlorination of crosslinked polyamide membranes. *Journal of Applied Polymer Science* **2008**, *108* (4), 2061-2066.
- [34] Petersen, R. J., Composite Reverse-Osmosis and Nanofiltration Membranes. *Journal of Membrane Science* **1993**, *83* (1), 81-150.
- [35] Geise, G. M.; Park, H. B.; Sagle, A. C.; Freeman, B. D. McGrath, J. E., Water permeability and water/salt selectivity tradeoff in polymers for desalination. *Journal of Membrane Science* **2011**, *369* (1-2), 130-138.
- [36] Robeson, L. M.; Freeman, B. D.; Paul, D. R. Rowe, B. W., An empirical correlation of gas permeability and permselectivity in polymers and its theoretical basis. *Journal of Membrane Science* **2009**, *341* (1-2), 178-185.
- [37] Freger, V., Nanoscale heterogeneity of polyamide membranes formed by interfacial polymerization. *Langmuir* **2003**, *19* (11), 4791-4797.
- [38] Elimelech, M. Phillip, W. A., The Future of Seawater Desalination: Energy, Technology, and the Environment. *Science* **2011**, *333* (6043), 712-717.
- [39] Phillip, W. A.; Yong, J. S. Elimelech, M., Reverse Draw Solute Permeation in Forward Osmosis: Modeling and Experiments. *Environmental Science & Technology* **2010**, *44* (13), 5170-5176.
- [40] Lee, K. P.; Arnot, T. C. Mattia, D., A review of reverse osmosis membrane materials for desalination-Development to date and future potential. *Journal of Membrane Science* **2011**, *370* (1-2), 1-22.

Chapter 6:

**Thermodynamic and Energy
Efficiency Analysis of Power
Generation from Natural Salinity
Gradients by Pressure Retarded
Osmosis**

CHAPTER ABSTRACT

The Gibbs free energy of mixing dissipated when fresh river water flows into the sea can be harnessed for sustainable power generation. Pressure retarded osmosis (PRO) is one of the methods proposed to generate power from natural salinity gradients. In this study, we carry out a thermodynamic and energy efficiency analysis of PRO work extraction. First, we present a reversible thermodynamic model for PRO and verify that the theoretical maximum extractable work in a reversible PRO process is identical to the Gibbs free energy of mixing. Work extraction in an irreversible constant-pressure PRO process is then examined. We derive an expression for the maximum extractable work in a constant-pressure PRO process and show that it is less than the ideal work (i.e., Gibbs free energy of mixing) due to inefficiencies intrinsic to the process. These inherent inefficiencies are attributed to (i) frictional losses required to overcome hydraulic resistance and drive water permeation and (ii) unutilized energy due to the discontinuation of water permeation when the osmotic pressure difference becomes equal to the applied hydraulic pressure. The highest extractable work in constant-pressure PRO with a seawater draw solution and river water feed solution is 0.75 kWh/m^3 while the free energy of mixing is 0.81 kWh/m^3 — a thermodynamic extraction efficiency of 91.1%. Our analysis further reveals that the operational objective to achieve high power density in a practical PRO process is inconsistent with the goal of maximum energy extraction. This study demonstrates thermodynamic and energetic approaches for PRO and offers insights on actual energy accessible for utilization in PRO power generation through salinity gradients.

6.1 INTRODUCTION

The impetus to reduce greenhouse gas emissions and mitigate climate change has invigorated research on alternative power sources [1]. Natural salinity gradients have been identified as a promising source of clean renewable energy. The free energy of mixing that is released when two solutions of different salt concentration are combined can be harnessed for sustainable power production [2]. When fresh river water mixes with the sea, free energy equal to a 270 meter high waterfall is released [3]. The annual global river discharge of $\sim 37,300 \text{ km}^3$ represents an enormous source of renewable energy [4] that can potentially produce an estimated 2 TW of electricity, or 13% of global electricity consumption [5].

Several methods have been proposed to harvest this sustainable energy source, including reverse electrodialysis, [6, 7] mixing entropy batteries, [5] and pressure retarded osmosis (PRO) [8, 9]. In PRO salinity power generation, the osmotic pressure difference across a semipermeable membrane drives the permeation of water from the dilute river water “feed solution” into concentrated seawater “draw solution”. A hydraulic pressure less than the osmotic pressure difference is applied to the draw solution, thereby “retarding” water flux across the membrane, and a hydroturbine extracts work from the expanding draw solution volume. In 2009, the world’s first PRO power plant came into operation in Norway, demonstrating the potential viability of the process [9]. The prospects of cost-effective osmotic power production are further bolstered by the recent development of thin-film composite PRO membranes with transport and structural properties projected to produce high power densities [10-12].

Previous studies on power generation from natural salinity gradients employed the Gibbs free energy of mixing to evaluate the realizable energy [3, 5, 13, 14]. However, the free energy of mixing represents the theoretical maximum energy that is available for useful work by a reversible thermodynamic process and does not take into account the intrinsic thermodynamic inefficiencies. Hence, actual work output will always be less than the theoretical energy available because practical work extraction processes are irreversible in nature and, thus, generate entropy [15-17]. To obtain the actual extractable work — a more applicable and relevant figure — thermodynamic conversion efficiencies have to be incorporated into the energy analysis.

In this study we carry out a thermodynamic and energy efficiency analysis of pressure retarded osmosis. The theoretical maximum extractable work in a PRO process is determined from a reversible thermodynamic model for PRO and compared to the Gibbs free energy of mixing. We then examine the thermodynamic efficiency of work extraction in a practical constant-pressure PRO process using natural salinity gradients. The inherent inefficiencies of frictional losses and unutilized energy imposed by the constant-pressure PRO process are analyzed and discussed. Finally, we look at the practical constraints of an actual PRO process and highlight the implications on energy extraction efficiency. Our analysis of the thermodynamic considerations in the extraction of work from natural salinity gradients provides insights into the energy efficiency intrinsic to the PRO power generation process.

6.2 ENERGY OF MIXING

When two solutions of different compositions are mixed, the Gibbs free energy of mixing is released. In this section we draw upon established thermodynamic concepts [15, 16, 18-20] to present a condensed theoretical background on the energy change of mixing for a binary system of aqueous strong electrolyte solutions.

Mixing Releases Free Energy. Mixing two solutions, A and B, of different composition yields a resultant mixture, M. The difference in the Gibbs free energy between the final mixture (G_M) and initial (G_A and G_B) solutions gives the change in free energy of mixing [15]. The Gibbs free energy of mixing per mole of the system, ΔG_{mix} , is [16]

$$-\Delta G_{\text{mix}} = R_g T \left\{ \left[\sum x_i \ln(\gamma_i x_i) \right]_M - \phi_A \left[\sum x_i \ln(\gamma_i x_i) \right]_A - \phi_B \left[\sum x_i \ln(\gamma_i x_i) \right]_B \right\} \quad (6.1)$$

where x_i is the mole fraction of species i in solution, R_g is the gas constant, and T is the absolute temperature. The activity coefficient, γ_i , is incorporated to account for the behavior of non-ideal solutions, and is a function of the temperature, pressure, and solution composition [16]. ϕ_A and ϕ_B are the ratios of the total moles in solutions A or B, respectively, to the total moles in the system (i.e., $\phi_A + \phi_B = 1$). Here, we adopt the negative convention for the energy of mixing to reflect that energy is released.

An inspection of eq 6.1 reveals that ΔG_{mix} is dependent on the relative proportion of the initial solutions (ϕ_A and ϕ_B) and the composition of the solutions (x_i and, implicitly, γ_i) for a mixing process at constant temperature and pressure. The Gibbs free energy of mixing described in eq 6.1 is applicable for all general mixing processes, [15] and it is equal and opposite in sign to the minimum energy required to separate the mixture M into products A and B [19].

Energy Change of Mixing for Strong Electrolyte Solutions. For a two-component system of aqueous strong electrolyte solutions, the two species are water and a salt that dissociates completely in solution (denoted by subscripts w and s , respectively). For relatively low salt concentration solutions, both the mole fraction of water, x_w , and the activity coefficient, γ_w , can be approximated to unity [18]. Therefore, $\ln(\gamma_w x_w)$ for the initial solutions and final mixture approaches zero in eq 6.1. In this case, the contribution of the salt species to ΔG_{mix} overwhelms the contribution of the water species and the molar Gibbs free energy of mixing (eq 6.1) simplifies to

$$-\frac{\Delta G_{\text{mix}}}{\nu R_g T} \approx [x_s \ln(\gamma_s x_s)]_{\text{M}} - \phi_A [x_s \ln(\gamma_s x_s)]_{\text{A}} - \phi_B [x_s \ln(\gamma_s x_s)]_{\text{B}} \quad (6.2)$$

where ν , the number of ions each electrolyte molecule dissociates into, accounts for the multiple ionic species contribution of the strong electrolyte salt [16].

For practicality and ease of application, the mole fraction and molar mixing energy in eq 6.2 are converted to molar salt concentration and Gibbs free energy of mixing per unit volume, respectively. This is achieved by assuming the volumetric and mole contribution of the salt to the solution is negligible compared to water, and that the volume of the system remains constant in the mixing process ($V_A + V_B = V_M$). Thus, the mole fractions can be approximated to the volumetric fractions. The Gibbs free energy of mixing per unit volume of the resultant mixture, $\Delta G_{\text{mix}, V_M}$, is then

$$-\frac{\Delta G_{\text{mix}, V_M}}{\nu R_g T} \approx c_M \ln(\gamma_{s, M} c_M) - \phi c_A \ln(\gamma_{s, A} c_A) - (1 - \phi) c_B \ln(\gamma_{s, B} c_B) \quad (6.3)$$

where c is the molar salt concentration of the aqueous solutions and ϕ is the ratio of the total moles in solution A to the total moles in the system (i.e., $\phi = \phi_A$ and $1 - \phi = \phi_B$).

Based on the above simplifying assumptions, ϕ is also the volumetric ratio of solution A to the total system volume (i.e., $\phi = V_A / V_M$). An examination of eq 6.3 shows that $\Delta G_{\text{mix}, V_M}$ is solely a function of the salt concentration and mole fraction (or volume fraction) of the initial solutions (c_M is determined by c_A , c_B , and ϕ , while γ is dependent on c).

In power generation from natural salinity gradients, often seawater from the ocean is abundant while fresh water from the estuaries is the limiting resource. As such, expressing the mixing energy per unit volume of the dilute solution would more accurately capture the energy available for extraction. Multiplying eq 6.3 by V_M/V_A ($\approx 1/\phi$) yields the Gibbs free energy of mixing per unit volume of A (the more dilute solution):

$$-\frac{\Delta G_{\text{mix}, V_A}}{\nu R_g T} \approx \frac{c_M}{\phi} \ln(\gamma_{s,M} c_M) - c_A \ln(\gamma_{s,A} c_A) - \frac{(1-\phi)}{\phi} c_B \ln(\gamma_{s,B} c_B) \quad (6.4)$$

Figure 6.1 shows $\Delta G_{\text{mix}, V_A}$, calculated using eq 6.4, for the mixing of a fresh water source with seawater as a function of the mole fraction of the fresh water, ϕ , in 0.1 increments. Fresh waters (dilute solution A) with salinities of 1.5 and 17 mM (~ 88 and ~ 1000 mg/L) NaCl were selected to represent river water (blue square symbols) and brackish water (red circle symbols), respectively [10]. The seawater (concentrated solution B) was taken to be 600 mM (35 g/L) NaCl [10] and the temperature, T , was fixed at 298 K. The activity coefficients of the initial solutions (A and B) and resultant mixture (M) were approximated by linear interpolation.

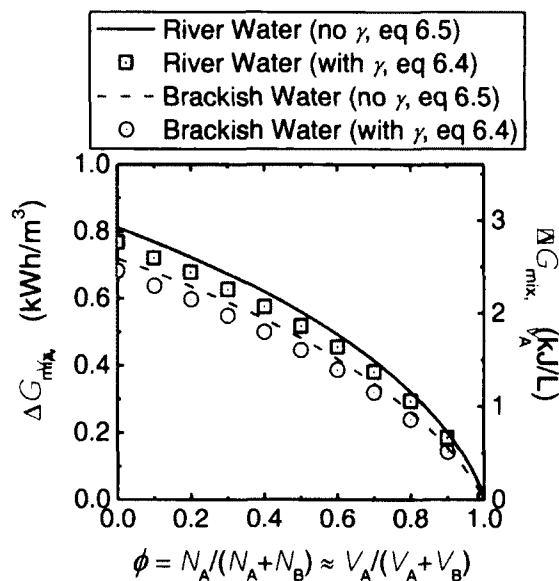


Figure 6.1. Gibbs free energy of mixing, $\Delta G_{\text{mix},\lambda}$, as a function of ϕ . The change in free energy of mixing is expressed as the energy released per unit volume of the river or brackish water. Blue square symbols and red circle symbols indicate $\Delta G_{\text{mix},\lambda}$ calculated with activity coefficients (eq 6.4) for river water and brackish water, respectively. Solid blue line and dashed red line represent $\Delta G_{\text{mix},\lambda}$ determined without γ (eq 6.5) for river water and brackish water, respectively. The calculations were carried out for a temperature of 298 K, and the concentration of seawater was assumed to be 600 mM (35 g/L) NaCl, while the concentrations of river water and brackish water were taken to be 1.5 and 17 mM (88 and 1000 mg/L) NaCl, respectively. For the dilute concentrations considered here, the mole fraction can be approximated to be the volumetric fraction of freshwater.

The highest mixing energy of 0.77 kWh/m^3 (2.76 kJ/L) is achieved for river water when ϕ tends to zero (i.e., an infinitesimal amount of fresh water mixes with an infinitely large volume of seawater). This value of 0.77 kWh/m^3 is similar to the minimum energy to desalinate seawater at 0% recovery [21, 22] (the minor difference between the values is attributed to the slight difference in concentrations and approximations employed for the calculations). This observation is consistent with our understanding of reversible thermodynamics: the separation energy at 0% recovery is equal in magnitude but

opposite in sign to the free energy of mixing at $\phi = 0$. As the mole fraction of the fresh water increases, $\Delta G_{\text{mix}, \nu_A}$ decreases and eventually reaches zero at $\phi = 1$. A similar trend is observed for brackish water, except that at $\phi = 0$, the energy of mixing is 0.68 kWh/m^3 (2.45 kJ/L). This value is lower compared to river water due to the higher initial salt content of brackish water. Note that actual seawater contains a mixed composition of ionic species other than Na^+ and Cl^- [23], and the energy of mixing will, therefore, differ slightly from the above calculated values.

ΔG_{mix} for Ideal Solutions. For the relatively low salt concentrations investigated in this study, the mole fraction of salt (or molar salt concentration) dominates over the salt activity coefficient in the logarithmic term in eq 6.4, i.e., $\ln(\gamma_s x_s) = \ln(\gamma_s) + \ln(x_s) \approx \ln(x_s)$. For example, for a 600 mM NaCl solution, which is representative of seawater, $\ln(x_s) = \ln(0.0107) = -4.54$ is much greater in magnitude than $\ln(\gamma_s) = \ln(0.672) = -0.40$ [18]. To further simplify the analysis, we can neglect the activity coefficients (i.e., assume ideal behavior) and eq 6.4 further reduces to

$$-\frac{\Delta G_{\text{mix}, \nu_A}}{\nu R_g T} \approx \frac{c_M}{\phi} \ln c_M - c_A \ln c_A - \frac{(1-\phi)}{\phi} c_B \ln c_B \quad (6.5)$$

Figure 6.1 shows $\Delta G_{\text{mix}, \nu_A}$, determined using eq 6.5, for the mixing of a river water (solid blue line) and brackish water (dashed red line) with seawater, as a function of ϕ . The concentrations of the fresh water sources and seawater were the same as those used in the previous calculations of $\Delta G_{\text{mix}, \nu_A}$ (i.e., with eq 6.4). The highest mixing energies of 0.81 kWh/m^3 (2.92 kJ/L) and 0.72 kWh/m^3 (2.59 kJ/L) are achieved for river water and brackish water, respectively, when ϕ tends to zero. The free energy of mixing

determined without the activity coefficient, γ , exhibits a similar trend compared to $\Delta G_{\text{mix},V_A}$ with γ (i.e., eq 6.4), except the values are slightly higher. The similar trend and magnitude of the mixing energies between eqs 6.4 and 6.5 reinforces the validity of the simplifying step to ignore the activity coefficients. Although some precision is sacrificed, eq 6.5 offers a great ease of application, compared to eq 6.4, as $\Delta G_{\text{mix},V_A}$ can be determined directly.

The change in Gibbs free energy represents an upper bound on the energy that can be extracted for useful work, regardless of the pathway. However, the second law of thermodynamics stipulates that in actual cases, the useful work extracted is always less than $\Delta G_{\text{mix},V_A}$ due to the production of entropy [15]. The inherent irreversible energy losses in the work extraction processes are analogous to the thermodynamic inefficiencies of separation processes, where the energy consumed to carry out the purification is always greater than the theoretical minimum energy of separation [19]. Therefore, an efficient work extraction process is one that minimizes such thermodynamic inefficiencies and utilizes most of the available energy.

6.3 REVERSIBLE THERMODYNAMIC MODEL OF PRESSURE RETARDED OSMOSIS

In pressure retarded osmosis power generation, a semipermeable membrane separates two solutions of different concentration. The osmotic pressure difference that develops across the membrane drives the permeation of water from the dilute feed solution into the more concentrated draw solution. A hydraulic pressure less than the osmotic pressure difference is applied to the draw solution and a hydroturbine extracts work from the

expanding draw solution volume. In this section, we present a reversible thermodynamic model of PRO and show the derivation of the theoretical maximum extractable work. In the following analyses, a 600 mM NaCl draw solution is used to simulate seawater of ~ 35 g/L TDS, while the salt concentrations of the feed solutions are 1.5 and 17 mM NaCl, to represent river water and brackish water of approximately 88 and 1000 mg/L TDS, respectively [10]. The temperature is 298 K and assumed to remain constant throughout the PRO process.

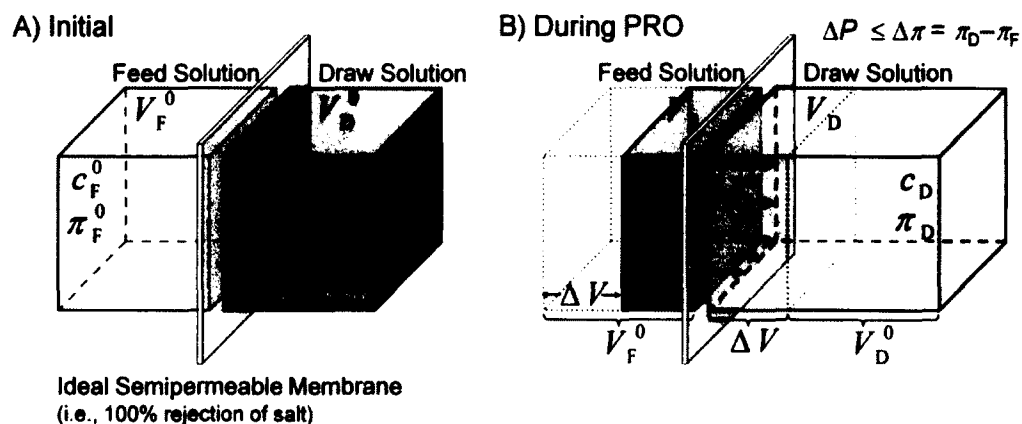


Figure 6.2. Schematics of a pressure retarded osmosis process. The draw and feed solutions are separated by an ideal semipermeable membrane that allows the passage of water while completely rejecting salt. (A) Initially, the higher concentration of the draw solution induces an osmotic pressure difference, $\Delta\pi = \pi_D^0 - \pi_F^0$, across the membrane to provide the driving force for water flux from the feed side to the draw side. (B) During the PRO process, the draw solution is pressurized by an applied hydraulic pressure, ΔP . Due to the cumulative volume of pure water, ΔV , that has permeated across the membrane, the feed solution is concentrated while the draw solution is diluted.

Pressure Retarded Osmosis Model. Figure 6.2 shows the schematics of a PRO process. The dilute feed solution (of initial concentration c_F^0 and volume V_F^0) is separated from the draw solution (of initial concentration c_D^0 and volume V_D^0) by an ideal semipermeable membrane that completely rejects salt (NaCl) while allowing water

to permeate (Figure 6.2A). We assume the van't Hoff relation to be valid (i.e., ideal solutions) for the concentration range considered here. Therefore, the osmotic pressure of the solutions is $\pi = \nu c R_g T$, where c is the molar salt concentration, ν is the number of ionic species each salt molecule dissociates into, R_g is the gas constant, and T is the absolute temperature.

The difference in osmotic pressure drives water flux from the feed to the draw solution, as illustrated in Figure 6.2B. As water permeates across the membrane, it dilutes the draw solution to concentration $c_D = c_D^0 V_D^0 / (V_D^0 + \Delta V)$, where ΔV is the permeate volume. Volume is conserved, based on the earlier assumption that the dilute solutions exhibit ideal behavior, and ΔV is equivalent to the increase in draw solution volume and decrease in feed solution volume. The concentration of the feed solution, hence, increases to $c_F = c_F^0 V_F^0 / (V_F^0 - \Delta V)$ due to the complete rejection of salt by the membrane.

In the absence of an applied hydraulic pressure, water permeation is terminated when the concentrations of the draw and feed solutions equilibrate and the net osmotic driving force vanishes (i.e., $\Delta\pi = 0$). The concentration of the final solutions at this point, denoted by the superscript f , is

$$c_F^f = c_D^f = (1 - \phi) c_D^0 + \phi c_F^0 \equiv c^f \quad (6.6)$$

where $\phi = V_F^0 / (V_D^0 + V_F^0)$ is the ratio of the initial feed solution volume to both initial draw and feed solution volume. Note that ϕ is approximately the mole fraction because we assume the volumetric contribution of salt is negligible compared to water. Hence, ϕ is consistent with the previous definition used to determine the energy of mixing.

The total volume of permeate, ΔV^f , that ultimately passes into the draw solution can be calculated by solving ΔV for $c_D = c_F$:

$$\frac{\Delta V^f}{V_F^0} = \frac{1-\phi}{\phi} \left(\frac{c_D^0}{c^f} - 1 \right) = \left(1 - \frac{c_F^0}{c^f} \right) \quad (6.7)$$

The final total permeate volume divided by the initial feed solution volume (eq 6.7) gives the fraction of V_F^0 that eventually permeates into the draw solution.

Reversible Thermodynamic PRO Process. In the theoretical reversible thermodynamic PRO model, an infinitesimal water flux is maintained throughout the osmosis process. This is achieved by applying a hydraulic pressure, ΔP , negligibly smaller than the osmotic pressure difference, $\Delta\pi$, on the draw solution such that an infinitesimally small volume of pure water permeates across the membrane. The draw solution is diluted very slightly by the minuscule permeate while the concentration of the feed solution increases a little. Hence, the osmotic pressure difference decreases such that $\Delta\pi = \Delta P$. The applied hydraulic pressure is then lowered marginally for another tiny drop of water to permeate across. Based on the van't Hoff relation, the osmotic pressure difference when ΔV has permeated across the membrane is linearly proportional to the concentration difference ($\Delta c = c_D - c_F$):

$$\Delta\pi = \nu R_g T \Delta c = \nu R_g T \left(\frac{V_D^0}{V_D^0 + \Delta V} c_D^0 - \frac{V_F^0}{V_F^0 - \Delta V} c_F^0 \right) \quad (6.8)$$

The process of gradually reducing the applied hydraulic pressure is repeated in infinite small steps to achieve a continuous decrease in ΔP while keeping $\Delta P = \Delta\pi$. At any point during the process, the applied hydraulic pressure can be raised such that ΔP is just slightly higher than $\Delta\pi$. The process is thus “reversed” as an infinitesimally small

volume of pure water permeates back into the feed solution. A representative plot of $\Delta\pi$ as a function of ΔV (eq 6.8) is shown in Figure 6.3A for a seawater draw solution and brackish water feed solution. The volumetric fraction of the feed solution $\phi = 0.4$ and $\nu = 2$ for NaCl. The horizontal axis intercept indicates the final permeate volume, ΔV^f , when the salinity difference reaches zero.

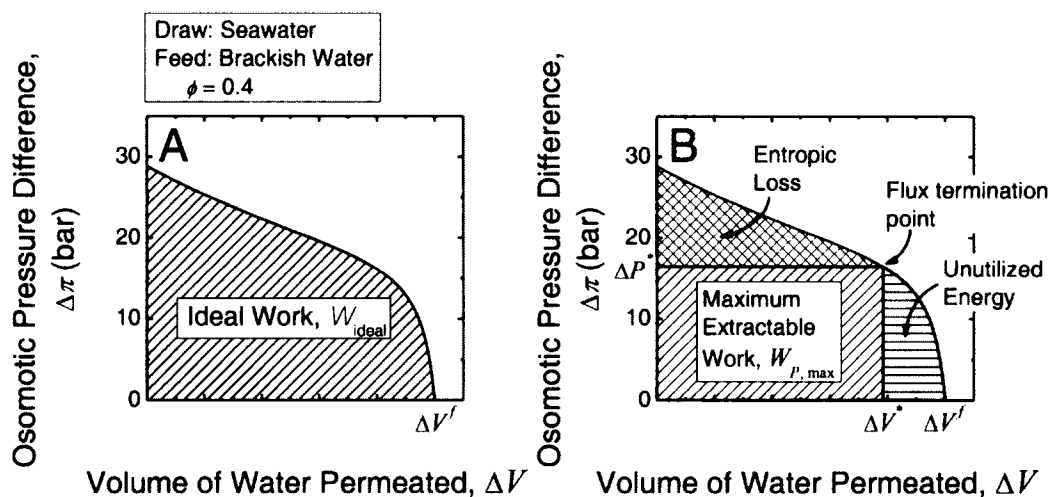


Figure 6.3. A) Representative plot of $\Delta\pi$ as a function of ΔV (eq 6.8), indicated by the solid black line. In a reversible thermodynamic PRO process, ΔP is always equal to $\Delta\pi$ to achieve an infinitesimal water flux; hence, W_{ideal} is equivalent to the area under the pressure-volume curve (eq 6.10). B) Representative plot of the maximum amount of work that can be extracted in a constant-pressure PRO process, $W_{p,max}$. The area of the region marked "Entropic Loss" represents the energy required to overcome the frictional forces as water permeates across the semipermeable membrane. The energy of mixing associated with the remaining volume of water that did not permeate across the membrane ($\Delta V^f - \Delta V^*$) is indicated by the region "Unutilized Energy". In these representative plots, the draw solution is seawater (600 mM or 35 g/L NaCl), the feed solution is brackish water (17 mM or 1000 mg/L NaCl), the volumetric fraction of the feed solution, ϕ , is 0.4, and temperature $T = 298$ K.

Substituting the initial draw solution volume expressed in terms of initial feed solution volume, $V_D^0 = (1 - \phi)V_F^0 / \phi$, into eq 6.8 yields

$$\Delta\pi = \nu R_g T \left(\frac{(1-\phi)c_D^0}{1-\phi \left(1 - \frac{\Delta V}{V_F^0}\right)} - \frac{c_F^0}{1 - \frac{\Delta V}{V_F^0}} \right) \quad (6.9)$$

Thus, using eq 6.9, we can express $\Delta\pi$ in terms of $\Delta V/V_F^0$ — the volumetric fraction of the initial feed solution that has permeated into the draw solution.

Theoretical Maximum Extractable Work is Equal to the Gibbs Energy of Mixing. In a reversible thermodynamic process, no entropy is generated [15]. Therefore, the work done by the expansion in volume of the pressurized draw solution in a reversible PRO process represents the ideal amount of work extractable. Integrating ΔP across the increase in draw solution volume (i.e., ΔV from 0 to ΔV^f) yields the maximum energy available for extraction — the ideal work, W_{ideal} :

$$W_{\text{ideal}} = \int_0^{\Delta V^f} \Delta P d(\Delta V) \quad (6.10)$$

A graphical representation of W_{ideal} is given by the area under the pressure-volume plot as depicted in Figure 6.3A.

As $\Delta P = \Delta\pi$ throughout reversible thermodynamic PRO, we can substitute eq 6.9 into eq 6.10 and solve the integral to arrive at the specific ideal work, W_{ideal,V_F^0} , defined as energy per unit volume of the initial feed solution:

$$-\frac{W_{\text{ideal},V_F^0}}{\nu R_g T} = \frac{c^f}{\phi} \ln c^f - c_F^0 \ln c_F^0 - \frac{(1-\phi)}{\phi} c_D^0 \ln c_D^0 \quad (6.11)$$

The negative sign in eq 6.11 signifies that work is being done by the system. An inspection of eq 6.11 shows that W_{ideal,V_F^0} is determined by the salt concentration, c^0 , and relative proportion, ϕ , of the initial feed and draw solutions. More significantly, by

comparing eq 6.11 with eq 6.5, we see that the theoretical maximum extractable work is equal to the Gibbs free energy of mixing. This is consistent with the principles of thermodynamics — the change in the Gibbs free energy of a system is equivalent to the work done by the system in an ideal reversible thermodynamic process [15, 16]. Figure 6.1, therefore, also represents the ideal work extractable in a reversible PRO process.

6.4 ENERGY EFFICIENCY OF PRESSURE RETARDED

OSMOSIS

Actual processes are not completely reversible in nature due to entropy production. Hence, the amount of energy that can be extracted will always be less than the theoretical maximum energy, W_{ideal} [15]. The second law of thermodynamics, therefore, imposes an upper limit on the efficiency that can be achieved by an actual energy extraction process such as PRO. In this section, we examine the thermodynamic efficiency of PRO power generation with natural salinity gradients, and discuss the inefficiencies intrinsic to the process.

Extractable Work in a Constant-Pressure PRO Process. In an actual PRO process, a constant hydraulic pressure is applied on the draw side, and the permeation of water ceases when $\Delta\pi$ is equal to the constant applied pressure. Therefore, the final total permeate volume is less than ΔV^J and is determined by substituting $\Delta\pi = \Delta P$ into eq 6.8. The work done by a constant-pressure PRO process (denoted by the subscript P) is the product of the applied pressure and the permeate volume:

$$W_p = \Delta P \Delta V = \nu R_g T \left(\frac{V_D^0}{V_D^0 + \Delta V} c_D^0 - \frac{V_F^0}{V_F^0 - \Delta V} c_F^0 \right) \Delta V \quad (6.12)$$

As the final total permeate volume is a function of ΔP , W_P is dependent on the constant hydraulic pressure applied. Keeping the draw side highly pressurized would result in a small ΔV and a corresponding low W_P . Alternatively, a large permeate volume is achieved by maintaining a low ΔP , but the resultant W_P would consequently be small. Work is maximized when the constant-pressure PRO is operated at an optimum applied hydraulic pressure, ΔP^* , and permeate volume, ΔV^* . Solving $dW_P/d\Delta P$ (or $dW_P/d\Delta V$) equals to zero yields

$$\Delta V^* = \frac{\sqrt{c_D^0} - \sqrt{c_F^0}}{\sqrt{c_D^0} + \frac{\phi}{1-\phi}\sqrt{c_F^0}} V_F^0 \quad (6.13)$$

$$\Delta P^* = \nu R_g T \left[(1-\phi)c_D^0 - \phi c_F^0 + (2\phi-1)\sqrt{c_D^0 c_F^0} \right] \quad (6.14)$$

Substituting eqs 6.13 and 6.14 into eq 6.12 gives the maximum extractable work in constant-pressure PRO, $W_{P,\max}$:

$$W_{P,\max} = \Delta P^* \Delta V^* = \nu R_g T (1-\phi) \left(\sqrt{c_D^0} - \sqrt{c_F^0} \right)^2 V_F^0 \quad (6.15)$$

Figure 6.3B illustrates the optimum applied hydraulic pressure difference and permeate volume for a seawater draw solution and brackish water feed solution when $\phi = 0.4$. The maximum extractable work in constant pressure PRO is demarcated by the area of the patterned blue region. Dividing the maximum work by V_F^0 gives the specific $W_{P,\max}$ (energy per unit initial feed solution volume). An examination of eq 6.15 reveals the constant negative slope of the function with respect to ϕ : $W_{P,\max}$ is highest when ϕ is equal to zero, and as ϕ increases to one, the specific $W_{P,\max}$ decreases linearly to zero.

Entropic Loss and Unutilized Energy. Because constant-pressure PRO is not a completely reversible process, $W_{P,\max}$ is less than the ideal amount of work extractable (eq 6.11). During water permeation, the frictional forces between the water molecules and the membrane give rise to hydraulic resistance [24, 25]. To achieve a non-zero water flux across the semipermeable membrane, a portion of the osmotic driving force is expended to overcome the resistance. Entropy is produced when energy is spent to counter the solvent-membrane friction. This energy is, thus, not tapped for useful work and is analogous to the irreversible energy loss in a reverse osmosis desalination process [22, 26]. The energy lost to entropy production is represented as the area of the patterned red region in Figure 6.3B, and is expressed as

$$\text{Entropic Loss} = \int_0^{\Delta V^*} \Delta P d(\Delta V) - \Delta P^* \Delta V^* \quad (6.16)$$

In constant-pressure PRO, the actual permeate volume is smaller than the volume of water that would eventually permeate into an unpressurized draw solution. This is because the permeation of water is terminated when the osmotic pressure difference is equal to the constant applied hydraulic pressure (i.e., interception of horizontal line, ΔP , and $\Delta\pi$ curve in Figure 6.3B), before the feed and draw solutions reach the same concentration. At this point, the net driving force for water flux becomes zero. Hence, the energy of mixing embedded in the “unpermeated” volume ($\Delta V^f - \Delta V^*$) is not extracted for useful work. This “unutilized energy” is indicated as the area of green patterned region in Figure 6.3B, and is described by:

$$\text{Unutilized Energy} = \int_{\Delta V^*}^{\Delta V^f} \Delta P d(\Delta V) \quad (6.17)$$

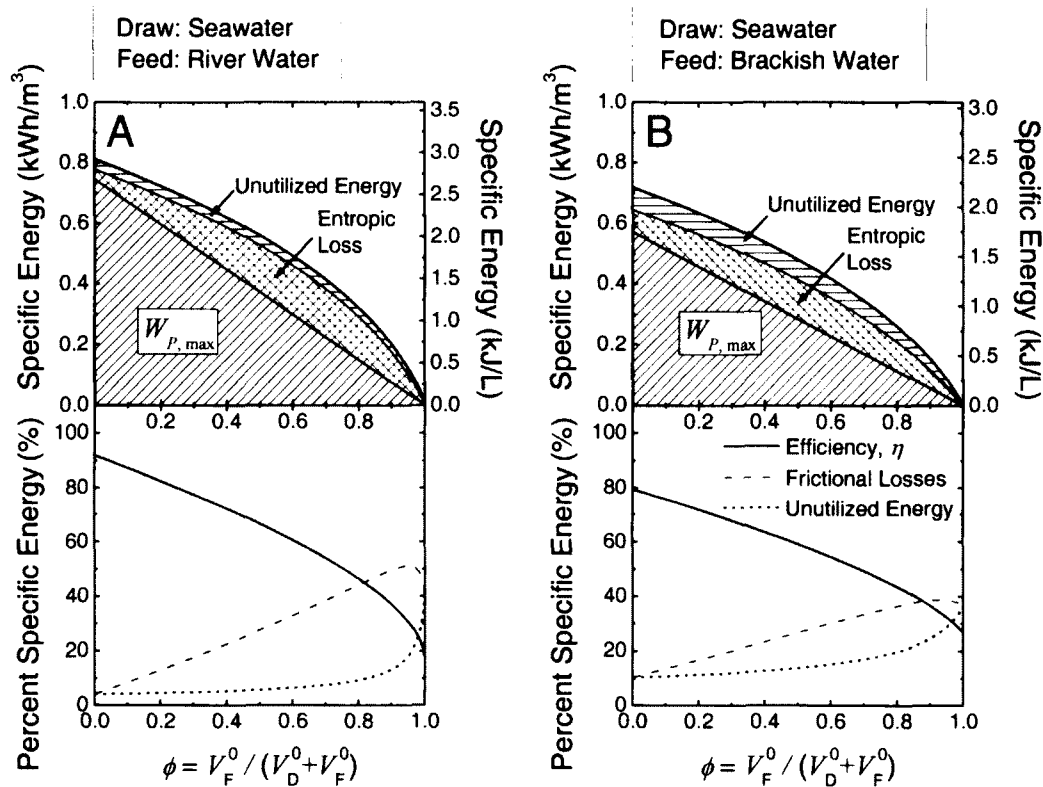


Figure 6.4. Top: Specific maximum extractable work, frictional losses, and unutilized energy in a constant-pressure PRO process as a function of ϕ . Bottom: Efficiency of work extraction (solid blue line) as a function of ϕ . The percent of energy required to overcome the frictional forces as water is driven across the semipermeable membrane (i.e., entropic loss) is indicated by the dashed red line. The dotted green line represents the percent of total energy that is unutilized due to the osmotic pressure difference being smaller than the constant applied hydraulic pressure difference (i.e., $\Delta\pi \leq \Delta P$). A) River water (1.5 mM NaCl) and B) brackish water (17 mM NaCl) are employed as the feed solutions. The draw solution is seawater (600 mM NaCl) and temperature $T = 298$ K.

Thermodynamic Efficiency of PRO Work Extraction. The first law of thermodynamics stipulates that the sum of the useful, dissipated, and remaining energy (maximum extractable work, entropic loss, and unutilized energy, respectively) is equal to the ideal work [15, 16]. Figure 6.4 (top) shows stacked plots of the specific energies as a function of ϕ , for river water (A) and brackish water (B) feed solution. The wedges representing entropic loss and unutilized energy (patterned red and green region,

respectively) are stacked on top of the specific $W_{P,\max}$ (patterned blue region) to yield the specific ideal work, W_{ideal,V_F^0} . Adding up the specific energies in these plots yields the specific Gibbs free energy of mixing, $\Delta G_{\text{mix},V_A}$, indicated in Figure 6.1 (solid blue line and dashed red line for a river water and brackish water feed solution, respectively).

The thermodynamic efficiency of work extraction, η , is defined as the maximum percent of the Gibbs free energy of mixing, or ideal work, that can be extracted in constant-pressure PRO:

$$\eta = \frac{W_{P,\max}}{\Delta G_{\text{mix}}} \times 100\% \quad (6.18)$$

The thermodynamic efficiency is calculated by substituting eqs 6.5 (or 6.11) and 6.15 into eq 6.18. Here, we assume zero energy losses from the PRO system components, such as pumps, pressure exchangers, and hydroturbines. Hence, η represents the thermodynamic limit of work extraction and is a measure of the inefficiencies due to entropy production and unutilized energy that are intrinsic to constant-pressure PRO. An inspection of eqs 6.5 (or 6.11) and 6.15 reveals that η is determined by the initial salt concentrations and relative proportion, ϕ , of the feed and draw solutions. Figure 6.4 (bottom) shows η (solid blue line) for a river water (A) and brackish water (B) feed solution paired with a seawater draw solution. The portion of energy consumed by frictional losses and the unutilized energy of mixing are indicated by the dashed red line and dotted green line, respectively.

For a river water-seawater PRO system, the specific $W_{P,\max}$ is largest at 0.75 kWh/m³ (2.68 kJ/L) when $\phi = 0$, and decreases linearly to zero as ϕ increases to unity (eq 6.15 and Figure 6.4A, top). The thermodynamic efficiency decreases concomitantly from 91.1

to 18.1% (Figure 6.4A, bottom). Therefore, it is energetically desirable to operate constant-pressure PRO at small ϕ values (i.e., small feed solution volume is paired with a large draw solution volume) to simultaneously achieve a high specific $W_{P,\max}$ and η . In an actual crossflow membrane module, ϕ is determined by the volumetric flowrate in the feed and draw channels. Hence, a small ϕ corresponds to a relatively low feed stream flowrate. A similar trend is observed for the brackish water-seawater system (Figure 6.4B): the specific $W_{P,\max}$ and η are highest at 0.57 kWh/m³ (2.06 kJ/L) and 79.4%, respectively, when ϕ approaches zero. The lower salt concentration in the initial river water feed solution, relative to the brackish water, allows a higher specific $W_{P,\max}$ and thermodynamic efficiency to be attained. However, the higher purity of river water also signifies that it is a more precious and desirable resource compared to brackish water. These, and other, factors will need to be considered when selecting the feed solution for PRO power generation with natural salinity gradients.

Practical Constraints in PRO Operation. Membrane power density (power produced per membrane area) is a key factor in determining the economical feasibility of PRO power generation [3, 9, 27]. Operating at a high power density will maximize the utilization of membrane area, thereby reducing capital cost and enhancing cost-effectiveness [3, 9]. To maximize power density, a hydraulic pressure approximately half of the osmotic pressure difference is applied across the membrane, i.e., $\Delta P \approx \frac{1}{2}(\pi_D - \pi_F)$ [10, 27]. However, based on our preceding discussion, the ΔP requirement for maximum power density is incompatible with the condition for achieving maximum extractable work in constant-pressure PRO, $W_{P,\max}$ (eq 6.15). Therefore, when PRO is operated to

maximize power density, the extractable work is not fully accessed (except for $\phi = 0.5$, where both aims are simultaneously realized).

Membrane power density is the product of the PRO water flux and the applied hydraulic pressure [27], while the water flux is proportional to the effective osmotic driving force across the membrane [27, 28]. As PRO progresses, the osmotic driving force ($\Delta\pi - \Delta P$) decreases due to dilution of the draw solution and concentration of the feed solution. Beyond a certain point, the ensuing water flux and power density become too low for cost-effective operation. The practical constraint to sustain an appreciable water flux at all points along the membrane requires the process to be terminated before the effective driving force reaches zero. Hence, the actual permeate volume, ΔV_{actual} , is lower than the total volume that would eventually permeate if the process had proceeded to completion.

A representation of the two operational constraints on work extraction is depicted in Figure 6.5 for a brackish water-seawater PRO system with $\phi = 0.4$. The process is operated at a constant-pressure of $\Delta P_{\text{actual}} = \frac{1}{2}(\pi_{\text{D}}^0 - \pi_{\text{F}}^0) = 14.5$ bar to maximize membrane power density [10, 27]. When the effective osmotic driving force falls below a certain level, the process is discontinued. The actual extractable work, $W_{P,\text{actual}}$, entropic loss, and unutilized energy are represented by the areas of patterned blue, red, and green regions, respectively. To facilitate comparison, the maximum extractable work, $W_{P,\text{max}}$, is indicated by the area within the dashed blue line.

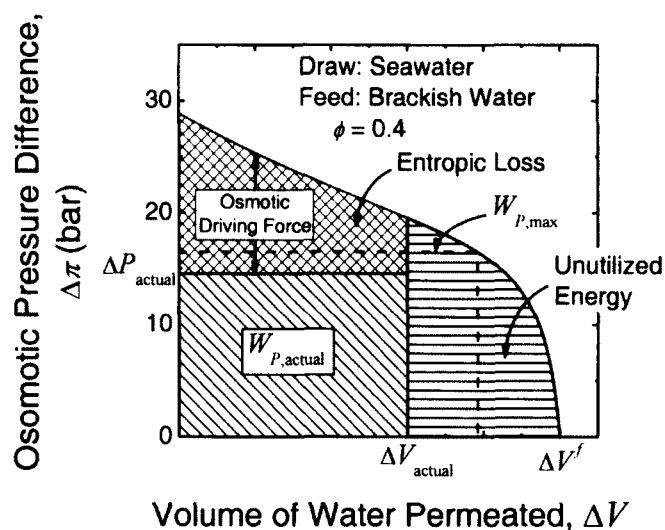


Figure 6.5. Representative plot of the amount of work that can be extracted in an actual constant-pressure PRO process, $W_{P,actual}$. The osmotic pressure difference in excess of the hydraulic pressure (i.e., $\Delta\pi - \Delta P$) provides the driving force for water flux (i.e., to overcome membrane-water friction). In an actual PRO process, the constant applied hydraulic pressure difference is constrained by the operational need to sustain sufficient water flux. Therefore, the actual work that is extracted, represented by the patterned region marked $W_{P,actual}$, is less than the $W_{P,max}$, indicated by area under the dotted blue line. In this representative plot, the draw solution is seawater (600 mM NaCl), the feed solution is brackish water (17 mM NaCl), the volumetric fraction of the feed solution, ϕ , is 0.4, and the temperature $T = 298$ K.

To maximize power density, the required applied hydraulic pressure departs from the optimal ΔP^* and the actual extractable work is lower than $W_{P,max}$. Figure 6.5 shows that more energy is expended to overcome membrane hydraulic resistance and achieve a higher water flux (indicated by the overlapped area of $W_{P,max}$ and entropic loss). That is, work is consumed for entropy production instead. As PRO proceeds, the dwindling water flux causes the membrane power density to diminish and eventually triggers the process to be discontinued. The remaining energy of mixing is unutilized and, therefore, a greater portion of the available energy is not extracted for power generation (area of patterned green region in Figure 6.5).

The operational objectives to maximize and maintain sufficient power density are not aligned with the goal of maximum work extraction. In satisfying the practical power density requirements, the maximum extractable work in constant-pressure PRO is not fully exploited. The actual efficiency of PRO work extraction, $\eta_{\text{actual}} = (W_{P,\text{actual}}/\Delta G_{\text{mix}}) \times 100\%$ is lower than the constant-pressure thermodynamic efficiency, i.e., $\eta_{\text{actual}} < \eta$. Therefore, practical PRO systems will need to balance the two inconsistent objectives of maximizing power density and maximizing extraction efficiency through the operating parameters (applied hydraulic pressure and process termination point).

6.5 IMPLICATIONS FOR PRO ENERGY PRODUCTION

Our recent studies demonstrated the intricate influence of membrane properties on PRO power density performance [10, 11]. The membrane transport and structural parameters relate the bulk osmotic pressure difference and applied hydraulic pressure to the power density [10, 11, 27]. A higher power density can be attained under the same operating conditions by employing high performance membranes — active layer with high water permeability and salt selectivity, coupled with customized support layer that suppresses the detrimental effect of internal concentration polarization [10, 11]. Improved membranes can enable PRO to be operated cost-effectively even when power density is not maximized, i.e., $\Delta P_{\text{actual}} \neq \frac{1}{2}(\pi_{\text{D}} - \pi_{\text{F}})$. Higher performance membranes will also better utilize small osmotic pressure differences to produce relatively higher water fluxes, thereby enabling the generation of adequate power densities even with the dwindled $\Delta\pi$ towards the later phase of the PRO process. As the process is allowed to proceed further, a larger portion of the free energy of mixing is converted to usable work. Therefore, the

innovation of PRO membranes with the desired transport and structural properties can enhance the efficiency of work extraction while maintaining sufficient water flux and power density for cost-effective operation.

Fouling is a key issue affecting productivity in membrane processes as it gives rise to flux decline and shortened membrane life-span [22, 29-31]. To mitigate these detrimental effects, pretreatment of the input streams is typically employed in separation processes, such as reverse osmosis desalination, which incurs an additional energy cost to the overall process [22, 29, 31, 32]. The PRO input feed stream will similarly need to undergo pretreatment to control membrane fouling [33]. Here, brackish water can have an advantage over river water. Brackish waters from groundwater are naturally filtered through the subsurface. Hence, a significant portion of the organic and colloidal matter that cause membrane fouling is naturally removed [34]. Employing brackish groundwater with lower fouling potential, instead of surface river water, can potentially reduce the energy requirement for pretreatment, thus making PRO power generation from salinity gradients more attractive.

Technological advances that are within our reach can address some of the above-mentioned challenges. If the obstacles are adequately overcome, PRO can potentially harvest part of the energy of mixing from the annual global river discharge of $\sim 37,300 \text{ km}^3$ to generate a significant source of clean sustainable energy [4]. For a PRO power plant operated at an actual efficiency $\eta_{\text{actual}} = 60\%$ with a river water feed solution and a seawater draw solution, i.e., $\Delta G_{\text{mix}} = 0.77 \text{ kWh/m}^3$, the specific extractable work will be $\eta_{\text{actual}} \times \Delta G_{\text{mix}} = 0.46 \text{ kWh/m}^3$. Assuming a further 20% is lost from inefficiencies in

PRO system components, 0.37 kWh of useful work can be derived per cubic meter of the river water feed solution.

Channeling a tenth of the global river water discharge (i.e., 3,730 km³/y) for PRO can potentially generate 157 GW of renewable power, or 1,370 TWh/y, after factoring in the conservative estimations on process losses and inefficiencies. This is equivalent to the electrical consumption of 520 million people, based on the average global electricity use of ~300 W/capita [35]. Producing the same amount of electricity through coal-fired power plants, which release 1 kg of CO₂ equivalent per kWh generated [36], would emit $\sim 1.37 \times 10^9$ metric tons of greenhouse gases in CO₂ equivalent. Nature's hydrological cycle offers a significant source of sustainable energy through salinity gradients. Further studies to better our understanding of the technology will enable the realization of these clean and renewable power sources towards alleviating our current climate change and energy issues.

6.6 REFERENCES

- [1] Hoffert, M. I.; Caldeira, K.; Benford, G.; Criswell, D. R.; Green, C.; Herzog, H.; Jain, A. K.; Kheshgi, H. S.; Lackner, K. S.; Lewis, J. S.; Lightfoot, H. D.; Manheimer, W.; Mankins, J. C.; Mauel, M. E.; Perkins, L. J.; Schlesinger, M. E.; Volk, T. Wigley, T. M. L., Advanced technology paths to global climate stability: Energy for a greenhouse planet. *Science* **2002**, *298* (5595), 981-987.
- [2] Pattle, R. E., Production of Electric Power by Mixing Fresh and Salt Water in the Hydroelectric Pile. *Nature* **1954**, *174* (4431), 660-660.
- [3] Ramon, G. Z.; Feinberg, B. J. Hoek, E. M. V., Membrane-based production of salinity-gradient power. *Energy & Environmental Science* **2011**, *4* (11), 4423-4434.
- [4] Dai, A. Trenberth, K. E., Estimates of freshwater discharge from continents: Latitudinal and seasonal variations. *Journal of Hydrometeorology* **2002**, *3* (6), 660-687.
- [5] La Mantia, F.; Cui, Y.; Pasta, M.; Deshazer, H. D. Logan, B. E., Batteries for Efficient Energy Extraction from a Water Salinity Difference. *Nano Letters* **2011**, *11* (4), 1810-1813.
- [6] Lacey, R. E., Energy by reverse electrodialysis. *Ocean Engineering* **1980**, *7* (1), 1-47.
- [7] Post, J. W.; Hamelers, H. V. M. Buisman, C. J. N., Energy Recovery from Controlled Mixing Salt and Fresh Water with a Reverse Electrodialysis System. *Environmental Science & Technology* **2008**, *42* (15), 5785-5790.
- [8] Loeb, S., Osmotic Power-Plants. *Science* **1975**, *189* (4203), 654-655.
- [9] Achilli, A. Childress, A. E., Pressure retarded osmosis: From the vision of Sidney Loeb to the first prototype installation - Review. *Desalination* **2010**, *261* (3), 205-211.
- [10] Yip, N. Y.; Tiraferri, A.; Phillip, W. A.; Schiffman, J. D.; Hoover, L. A.; Kim, Y. C. Elimelech, M., Thin-Film Composite Pressure Retarded Osmosis Membranes for Sustainable Power Generation from Salinity Gradients. *Environmental Science & Technology* **2011**, *45* (10), 4360-4369.
- [11] Yip, N. Y. Elimelech, M., Performance Limiting Effects in Power Generation from Salinity Gradients by Pressure Retarded Osmosis. *Environmental Science & Technology* **2011**, *45* (23), 10273-10282.
- [12] Chou, S. R.; Wang, R.; Shi, L.; She, Q. H.; Tang, C. Y. Fane, A. G., Thin-film composite hollow fiber membranes for pressure retarded osmosis (PRO) process with high power density. *Journal of Membrane Science* **2012**, *389*, 25-33.
- [13] Thorsen, T. Holt, T., The potential for power production from salinity gradients by pressure retarded osmosis. *Journal of Membrane Science* **2009**, *335* (1-2), 103-110.

-
- [14] Nijmeijer, K.; Metz, S.; Isabel, C. E. Andrea, I. S. f., Chapter 5 Salinity Gradient Energy. In *Sustainability Science and Engineering*, Elsevier: Vol. Volume 2, pp 95-139.
- [15] Smith, J. M.; Van Ness, H. C. Abbott, M. M., Introduction to chemical engineering thermodynamics. 7th ed.; McGraw-Hill, Boston, **2005**; p xviii, 817 p.
- [16] Sandler, S. I., Chemical and engineering thermodynamics. 3rd ed.; Wiley, New York, **1999**; p xx, 772 p.
- [17] Mistry, K. H.; McGovern, R. K.; Thiel, G. P.; Summers, E. K.; Zubair, S. M. Lienhard, J. H., Entropy Generation Analysis of Desalination Technologies. *Entropy* **2011**, *13* (10), 1829-1864.
- [18] Robinson, R. A. Stokes, R. H., Electrolyte solutions. 2nd rev. ed.; Dover Publications, Mineola, NY, **2002**; p xv, 571 p.
- [19] King, C. J., Separation processes. 2d ed.; McGraw-Hill, New York, **1980**; p xxvi, 850 p.
- [20] Pitzer, K. S.; Peiper, J. C. Busey, R. H., Thermodynamic Properties of Aqueous Sodium-Chloride Solutions. *Journal of Physical and Chemical Reference Data* **1984**, *13* (1), 1-102.
- [21] Semiat, R., Energy Issues in Desalination Processes. *Environmental Science & Technology* **2008**, *42* (22), 8193-8201.
- [22] Elimelech, M. Phillip, W. A., The Future of Seawater Desalination: Energy, Technology, and the Environment. *Science* **2011**, *333* (6043), 712-717.
- [23] Morel, F. Hering, J. G., Principles and applications of aquatic chemistry. Wiley, New York, **1993**; p xv, 588 p.
- [24] Kedem, O. Katchalsky, A., Thermodynamic Analysis of the Permeability of Biological Membranes to Non-Electrolytes. *Biochimica Et Biophysica Acta* **1958**, *27* (2), 229-246.
- [25] Spiegler, K. S. Kedem, O., Thermodynamics of hyperfiltration (reverse-osmosis) - criteria for efficient membranes. *Desalination* **1966**, *1* (4), 311-326.
- [26] Liu, C.; Rainwater, K. Song, L. F., Energy analysis and efficiency assessment of reverse osmosis desalination process. *Desalination* **2011**, *276* (1-3), 352-358.
- [27] Lee, K. L.; Baker, R. W. Lonsdale, H. K., Membranes for Power-Generation by Pressure-Retarded Osmosis. *Journal of Membrane Science* **1981**, *8* (2), 141-171.
- [28] Mehta, G. D. Loeb, S., Internal Polarization in the Porous Substructure of a Semipermeable Membrane under Pressure-Retarded Osmosis. *Journal of Membrane Science* **1978**, *4* (2), 261-265.

-
- [29] Baker, R. W., Membrane technology and applications. 2nd ed.; J. Wiley, Chichester ; New York, **2004**; p x, 538 p.
- [30] Mi, B. Elimelech, M., Chemical and physical aspects of organic fouling of forward osmosis membranes. *Journal of Membrane Science* **2008**, *320* (1-2), 292-302.
- [31] National Research Council, Desalination: A National Perspective. The National Academies Press, **2008**; p 312.
- [32] Fritzmann, C.; Lowenberg, J.; Wintgens, T. Melin, T., State-of-the-art of reverse osmosis desalination. *Desalination* **2007**, *216* (1-3), 1-76.
- [33] Loeb, S., Production of Energy from Concentrated Brines by Pressure-Retarded Osmosis: I. Preliminary Technical and Economic Correlations. *Journal of Membrane Science* **1976**, *1* (1), 49-63.
- [34] Greenlee, L. F.; Lawler, D. F.; Freeman, B. D.; Marrot, B. Moulin, P., Reverse osmosis desalination: Water sources, technology, and today's challenges. *Water Research* **2009**, *43* (9), 2317-2348.
- [35] EIA International Energy Data and Analysis. <http://www.eia.doe.gov/international/> (Accessed on:
- [36] Evans, A.; Strezov, V. Evans, T. J., Assessment of sustainability indicators for renewable energy technologies. *Renewable & Sustainable Energy Reviews* **2009**, *13* (5), 1082-1088.

Chapter 7:

**Influence of Natural Organic Matter
Fouling and Osmotic Backwash on
Pressure Retarded Osmosis Energy
Production from Natural Salinity
Gradients**

CHAPTER ABSTRACT

Pressure retarded osmosis (PRO) has the potential to produce clean renewable energy from natural salinity gradients. However, membrane fouling can lead to diminished water flux productivity, thus reducing the extractable energy. This study investigates organic fouling and osmotic backwash cleaning in PRO and the resulting impact on projected power generation. Fabricated thin-film composite membranes were fouled with model river water containing natural organic matter. The water permeation carried foulants from the feed river water into the membrane porous support layer and caused severe water flux decline of ~46%. Analysis of the water flux behavior revealed three phases in membrane support layer fouling. Initial foulants of the first fouling phase quickly adsorbed at the active-support layer interface and caused a significantly greater increase in hydraulic resistance than the subsequent second and third phase foulants. The water permeability of the fouled membranes was lowered by ~39%, causing ~26% decrease in projected power density. A brief, chemical-free osmotic backwash was demonstrated to be effective in removing foulants from the porous support layer, achieving ~44% recovery in projected power density. The substantial performance recovery after cleaning was attributed to the partial restoration of the membrane water permeability. This study shows that membrane fouling detrimentally impacts energy production, and highlights the potential strategies to mitigate fouling in PRO power generation with natural salinity gradients.

7.1 INTRODUCTION

The impetus to shift to a sustainable energy future has invigorated research and stimulated the development of alternative power sources [1]. Natural salinity gradients have been identified as a promising source of renewable and emission-free energy [2]. The free energy of mixing that is released when two solutions of different salt concentration are combined can be harnessed for power generation [3]. With up to 0.77 kWh (2.77 MJ) of energy produced when a cubic meter of fresh river water mixes with the ocean [4], the $\sim 37\,300\text{ km}^3$ annual global river discharge [5] represents a potentially enormous source of renewable energy that can contribute to meeting our energy challenges of today and tomorrow.

Pressure retarded osmosis (PRO) is one of the proposed technologies to harvest this sustainable energy source [2, 6-8]. In PRO salinity power generation, the river water “feed solution” is separated from the seawater “draw solution” by a semi-permeable membrane. The salt concentration difference provides the osmotic driving force for water permeation from the dilute feed solution into the concentrated draw solution, while solutes are retained by the salt-selective membrane. A hydraulic pressure lower than the osmotic pressure difference builds up on the draw solution, thereby “retarding” water flux across the membrane, and a hydroturbine extracts work from the expanding draw solution volume.

Our recent study analyzed the thermodynamics of the process and showed that PRO can convert the energy of mixing into useful work with high energy efficiency. By utilizing a tenth of the global river water discharge, 157 GW of renewable power can be potentially generated, equivalent to the electrical consumption of approximately half a

billion people [4]. In 2009, the world's first PRO pilot power plant was inaugurated in Norway, demonstrating the prospective viability of the process [7]. The venture further targets a 2 MW pilot project in Sunndalsøra to be operational in 2016 [9]. At the same time, realization of cost-effective osmotic power production was bolstered by the recent development of thin-film composite PRO membranes with transport and structural properties capable of high power densities [10-12].

Fouling is a key issue restricting the efficient performance of membrane processes [13, 14]. In conventional pressure-driven processes, such as ultrafiltration and reverse osmosis, membrane fouling has been extensively studied and shown to reduce water flux productivity, deteriorate permeate quality, increase energy consumption and treatment cost, and shorten membrane life span [13-15]. The ubiquity of foulants, such as organic matter present in natural waters, alludes that PRO will face comparable problems that impede process productivity. Fouling studies in forward osmosis, a related osmotically-driven process, and more recently in PRO found similar water flux decline and performance deterioration that supports the notion [16-22]. Because foulants are brought into the support layer of the membrane by water permeation in PRO, fouling will occur uncharacteristically *within* the membrane porous support, rather than typically *on* the membrane surface. This unique circumstance sets PRO apart from other fouling phenomena and is the focus of this current investigation.

In this study we present a systematic investigation of natural organic matter (NOM) fouling and membrane cleaning in PRO power generation. Hand-cast thin-film composite membranes were fouled with model river water containing natural organic matter. Careful characterizations were performed to examine the effects of support layer

fouling on the membrane intrinsic transport and structural parameters. The water flux behavior during fouling was analyzed and reconciled with the changes in membrane properties. Based on the experimental findings and drawing upon established membrane fouling concepts, a mechanistic account of the PRO fouling phenomenon was proposed. Osmotic backwash membrane cleaning was then carried out on the fouled membranes and the performance recovery was methodically quantified to assess the efficiency and suitability of backwashing for potential application. Finally, the power densities of the pristine, fouled, and cleaned membranes were evaluated and the implications for power generation from natural salinity gradients are discussed. This investigation aims to enhance our fundamental understanding of natural organic matter fouling in PRO, provide pertinent insights on the influence of fouling and cleaning on PRO power generation, and highlight the key considerations in the formulation of fouling mitigation strategies necessary to advance the technology.

7.2 MATERIALS AND METHODS

Materials and Chemicals. All chemicals used were analytical grade. For membrane fabrication, polysulfone (PSf) beads (M_n : 22,000 Da), 1-methyl-2-pyrrolidinone (NMP, anhydrous, 99.5%), 1,3-phenylenediamine (MPD, >99%), and 1,3,5-benzenetricarbonyl trichloride (TMC, 98%) were used as received (Sigma-Aldrich, St. Louis, MO). TMC was dissolved in Isopar-G, a proprietary non-polar organic solvent (Univar, Redmond, WA). A thin ($\sim 40 \mu\text{m}$), open structure polyester non-woven fabric (PET, Grade 3249, Ahlstrom, Helsinki, Finland) was used as a backing layer for the PSf supports.

Stock solutions of concentrated sodium chloride (NaCl, J.T. Baker, Phillipsburg, NJ), sodium bicarbonate (NaHCO₃, Sigma-Aldrich), and calcium chloride (CaCl₂, Sigma-Aldrich) were prepared by dissolving the appropriate salts in deionized (DI) water (Milli-Q, Millipore, Billerica, MA) and then filtered through a 0.45 μm membrane (cellulose acetate, Corning, Corning, NY). Appropriate volumes of the concentrated stock solutions were dosed into deionized (DI) water to achieve the required feed and draw solution composition for the membrane characterization and PRO experiments.

Suwannee river natural organic matter (SRNOM, International Humic Substances Society, St. Paul, MN), an extensively studied membrane organic foulant [23-25], was employed as the model foulant to represent natural organic matter in rivers. The characteristics of SRNOM can be found elsewhere [26, 27]. Stock solutions for SRNOM (nominally 500 mg/L) were prepared by dissolving the as-received SRNOM powder in DI water adjusted to pH 9 with sodium hydroxide, filtered through a low-binding 0.45 μm cellulose acetate membrane to remove the nondissolved fraction, and then stored at 4 °C.

Thin-film Composite Pressure Retarded Osmosis Membrane Fabrication. Hand-cast thin-film composite (TFC) PRO membranes were fabricated adapting the procedure outlined in our previous publications [10, 28, 29]. Briefly, a commercial polyester non-woven fabric (PET, Grade 3249, Ahlstrom, Helsinki, Finland) was taped on a glass plate and then wetted with NMP. Polymer dope solution, prepared by dissolving PSf beads in NMP at 12 wt%, was then drawn down the PET fabric using a casting knife (Gardco, Pompano Beach, FL) with an adjustable gate height fixed at 250 μm (~10 mils). The whole composite was immediately immersed in a DI water precipitation bath at room

temperature to initiate non-solvent induced phase separation [13]. The support membrane remained in the precipitation bath for 10 min before being transferred to a DI water bath for storage until polyamide (PA) formation.

An interfacial polymerization protocol between MPD and TMC was employed to form the highly cross-linked polyamide thin-film on top of the hand-cast PSf support layers [30]. In short, the top surface of the porous support membrane was soaked in an aqueous MPD solution (3.4 wt% in DI water) and then contacted with TMC dissolved in Isopar-G at 0.15 wt% to initiate the formation of the ultrathin selective layer. Following this reaction, the membrane was cured in DI water at 95 °C for 120 s, rinsed with a 200 ppm NaOCl aqueous solution for 120 s, then soaked in a 1000 ppm NaHSO₃ aqueous solution for 30 s, before a final wet curing step at 95 °C for 120 s. The nascent TFC membranes were rinsed thoroughly and stored in DI water at 4 °C. Prior to testing, the fabricated membranes were immersed in 25 wt% isopropanol for 30 min to wet the pores of the membrane support layer, and then rinsed thoroughly with DI water.

Membrane Characterization. The water permeability, A , salt permeability, B , coefficients of the polyamide active layers, and the structural parameter, S , of the membrane support layers were determined using a protocol adapted from our recently developed forward osmosis (FO) membrane characterization methodology [31]. Membrane characterizations were performed in a laboratory-scale experimental setup described in our previous studies [10, 28, 29]. The custom-built cell has an effective membrane area of 20.02 cm² on both sides. The feed and draw solutions were circulated in co-current crossflow at a velocity of 10.7 cm/s in closed loops. Channel spacers were not employed to avoid the possible introduction of confounding factors caused by altered

hydrodynamics. Temperature of the system was maintained at 25 ± 0.5 °C for all characterization experiments.

The hand-cast membranes were characterized in PRO configuration, i.e., porous support layer facing the feed solution and active layer facing the draw solution, without applied hydraulic pressure. Membrane characterization experiments comprised eight stages where the water and salt fluxes (J_w and J_s , respectively) were measured as the concentration difference across the membrane was varied by changing the draw and feed solution salt concentrations at each stage. PRO water and salt flux governing equations, that incorporates the performance limiting phenomena of external concentration polarization (ECP), internal concentration polarization (ICP), and reverse permeation of draw salt, were developed in our previous publication [10]:

$$J_w = A \left\{ \frac{\pi_D \exp\left(-\frac{J_w}{k}\right) - \pi_F \exp\left(\frac{J_w S}{D}\right)}{1 + \frac{B}{J_w} \left[\exp\left(\frac{J_w S}{D}\right) - \exp\left(-\frac{J_w}{k}\right) \right]} - \Delta P \right\} \quad (7.1)$$

$$J_s = B \left\{ \frac{c_D \exp\left(-\frac{J_w}{k}\right) - c_F \exp\left(\frac{J_w S}{D}\right)}{1 + \frac{B}{J_w} \left[\exp\left(\frac{J_w S}{D}\right) - \exp\left(-\frac{J_w}{k}\right) \right]} \right\} \quad (7.2)$$

where c_D and c_F are the draw and feed solution salt concentrations, respectively, π_D and π_F are the osmotic pressures of the bulk draw and feed solutions, respectively, k is the ECP boundary layer mass transfer coefficient, D is the bulk diffusion coefficient of the solute, and ΔP is the hydraulic pressure applied on the draw solution. The membrane properties were numerically determined by solving the system of water and salt flux equations, through non-linear regression of the fitting parameters A , B , and S to the

measured J_w and J_s (least-squares minimization of the residuals method). Each hand-cast membrane was characterized three times: before the fouling experiment (pristine), after SRNOM fouling in PRO (fouled), and after osmotic backwash (cleaned).

Membrane Fouling Protocol. PRO fouling experiments were carried in the same setup described in the characterization procedure with Suwannee river natural organic matter as the model organic foulant. The hand-cast TFC membranes were oriented in PRO mode (i.e., porous support layer faces feed and active layer faces draw) and no hydraulic pressure was applied. The experimental feed solution pressure (i.e., no applied hydraulic pressure) simulates actual PRO operating conditions, where the draw side is pressurized while the feed side is at ambient pressure. Initially the system was equilibrated by circulating DI water across both sides of the membrane. To initiate the fouling run, appropriate amounts of salt and foulant stock solution were dosed into the feed solution to simulate river water (0.4 mM NaCl, 0.2 mM NaHCO₃, 0.3 mM CaCl₂, and 20 mg/L (nominal) SRNOM; pH = 6.96, total ionic strength = 1.5 mM), while concentrated NaCl stock solution was added to the draw side to simulate seawater. Membrane properties determined in the earlier characterization were used with eq 7.1 to calculate the salt concentration of the model seawater draw solution required to obtain an initial water flux of 25 L m⁻²h⁻¹.

As water permeates across the membrane during the experiment, the osmotic driving force gradually declines as the model seawater draw solution is diluted by the permeated water. Baseline experiments, where the SRNOM foulant was left out of the model river water solution chemistry, were conducted before the fouling run to establish the flux decline due to the effect of draw solution dilution. Another foulant-free experiment was

repeated after osmotic backwashing (described in next subsection) to determine the recovery in water flux performance of the cleaned membrane. For each membrane, the same initial draw solution concentration was employed for the baseline, fouling, and cleaned experimental runs. The experiments were terminated when the cumulative permeate volume reaches 250 L per square meter of membrane area (~500 mL of permeate). The fouling experimental runs took around 20 h to complete, while the baseline runs lasted ~12-15 h. Due to the long duration of the experiments, the system experienced wider temperature fluctuations and was, thus, maintained at 25 ± 1.5 °C.

Osmotic Backwash. The fouled membranes were cleaned by reversing the water flux direction and utilizing the water permeation drag to remove foulants from the porous support. Osmotic backwash was performed by switching the membrane orientation such that the porous support layer faced the draw solution and active layer was towards the feed solution [32, 33]. The feed and draw streams employed in osmotic backwash were identical to those used for the baseline experiments described earlier (i.e., model river water without SRNOM foulants and NaCl solution as model seawater, respectively). Osmotic backwash was carried out for 5 L of cumulative permeate volume per square meter of membrane area (i.e., 2% of cumulative permeate volume in fouling experiment), and the system temperature was kept at 25 ± 0.5 °C.

Power Density Projection. The membrane power density, W , is defined as the power generated per unit membrane area and is equal to the rate of increase in the draw solution volume per unit membrane area (i.e., water flux across the membrane, J_w) multiplied by the hydraulic pressure applied on the draw side, ΔP :

$$W = J_w \Delta P \quad (7.3)$$

The membrane power density is a crucial factor affecting the cost-effectiveness, and hence the economical feasibility, of PRO energy production with natural salinity gradients [34, 35]. An examination of eqs 7.1 and 7.3 indicates that the power density is determined by the membrane characteristic parameters: water permeability, A , salt permeability, B , and the structural parameter, S . As such, the transport and structural properties determined in the membrane characterization can be used to project the highest power density attainable by the membrane in PRO [10, 36], and to quantify the effect of SRNOM fouling and osmotic backwash on the energy production efficiency of the process.

7.3 RESULTS AND DISCUSSION

Fabricated Membrane Transport and Structural Parameters. The FO characterization protocol presented in our recent publication [31] was adopted and modified for PRO to determine the active layer transport properties and support layer structural parameter intrinsic to the membrane. Table 7.1 presents the water permeability, A , salt permeability, B , and structural parameter, S , of duplicate hand-cast membranes (TFC-PRO #A and #B). The membrane duplicates possessed similar characteristic parameters, within experimental variations of the hand-casting fabrication technique, and are comparable to literature [29]. The water and salt fluxes predicted by the calculated membrane parameters in Table 7.1 are in excellent agreement with experimental measurements for both membrane duplicates, (coefficients of determination, R^2 , are between 0.965 and 0.999), indicating robustness of the characterization technique to accurately determine membrane properties.

Table 7.1. Characteristic transport properties and structural parameter of the fabricated membranes before the organic fouling experiment with SRNOM (i.e., pristine), after SRNOM fouling, and after osmotic backwash (i.e., cleaned).

	Water permeability, A ($L\ m^{-2}h^{-1}bar^{-1}$)	Salt (NaCl) permeability, B ($L\ m^{-2}h^{-1}$)	Structural parameter, S (μm)
TFC-PRO Membrane #A			
Pristine	1.59	0.087	479
Fouled (% change ^a)	0.96 (-39.6%)	0.066	431
Cleaned (% recovery ^b)	1.21 (+39.7%)	0.087	434
TFC-PRO Membrane #B (duplicate)			
Pristine	1.54	0.060	531
Fouled (% change ^a)	0.95 (-38.3%)	0.056	503
Cleaned (% recovery ^b)	1.19 (+40.7%)	0.069	503

^a Percentage change relative to the water permeability of the pristine membrane.

^b Percentage of the difference between cleaned and fouled water permeability, to the difference between pristine and fouled water permeability.

NOM Fouling of Membrane Support Layer Substantially Reduces Water Flux.

The PRO water flux of hand-cast membrane #A, without applied hydraulic pressure and NOM foulant, is presented in Figure 7.1 (“Baseline”, blue square symbols), as a function of the cumulative permeate volume normalized by the effective membrane area. An NaCl solution was employed as the model seawater draw solution, while a foulant-free, model river water was used as the feed solution. In the “Baseline” experimental run, the observed decline in J_w is attributed to the diminishing effective osmotic driving force as water permeating over from the feed side dilutes the seawater draw solution (effects of reverse draw salt flux and concentration of feed solution were found to be comparatively

small), resulting in reduction of the salt concentration difference across the membrane. At the end of the experiment, the water flux was $20.3 \text{ L m}^{-2}\text{h}^{-1}$, compared with $24.7 \text{ L m}^{-2}\text{h}^{-1}$ initially.

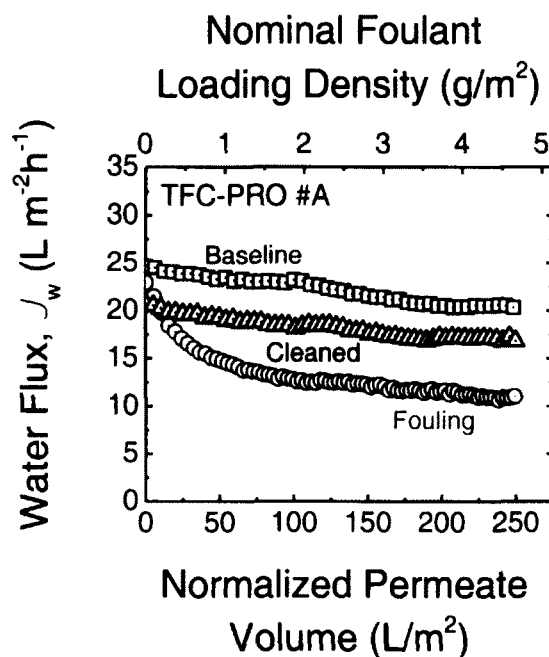


Figure 7.1. Water fluxes of hand-cast TFC-PRO membrane #A as a function of the cumulative permeate volume, normalized by the membrane area, in the baseline, fouling, and cleaned membrane experiments (blue square, red circle, and green triangle symbols, respectively). The model river water composition is 0.4 mM NaCl, 0.2 mM NaHCO₃, and 0.3 mM CaCl₂ (total ionic strength = 1.5 mM), while the model seawater is a 570 mM NaCl solution (to obtain an initial water flux of $25 \text{ L m}^{-2}\text{h}^{-1}$ in the baseline run). During the fouling experiment, 20 mg/L (nominal) SRNOM was additionally introduced to the river water as model foulant (feed solution pH = 6.98). Crossflow velocity was set at 10.7 cm/s in both membrane channels (no spacers) and the system temperature was maintained at $25 \pm 1.5 \text{ }^\circ\text{C}$. The top horizontal axis indicates the nominal foulant loading density into the membrane porous support (initial foulant concentration multiplied by permeate volume).

During PRO power generation with natural salinity gradients, water permeates from the river water feed solution into the membrane porous support, across the active layer, and into pressurized seawater draw solution (Figure 7.2). Therefore, foulants present in

the river water will be carried into the membrane support layer by the water permeation. The foulants accumulate within the porous support layer and at the active-support interface, as they are rejected by the polyamide active layer, and can lead to deterioration of PRO water flux [16, 18, 21, 22]. Fouling experiment was then performed on the membrane by using the same solution composition and operating conditions (to achieve the same initial J_w of $\sim 25 \text{ L m}^{-2}\text{h}^{-1}$), but with 20 mg/L (nominal) SRNOM present in the feed solution as the model organic foulant. A yellowish-brown tint was observed in the model river water feed solution in the presence of the organic foulants. Note that although the natural organic matter concentration of the model river water employed here is higher than typical river waters (2-10 mg/L) [37] in order to accelerate the fouling study, a recent PRO fouling study demonstrated that the effect foulant concentration is eliminated when water flux is presented as a function of the foulant loading density [21].

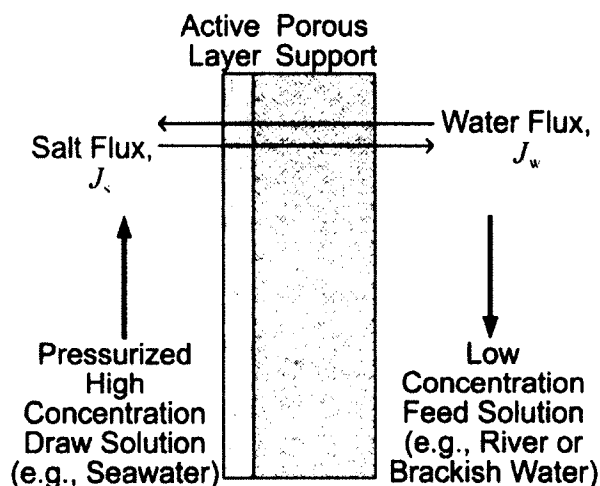


Figure 7.2. Schematic representation of the water flux, J_w , and reverse draw solute flux, J_s , across a thin-film composite membrane in PRO operating in counter-current flow. The active layer faces the pressurized high concentration draw solution (e.g., seawater), while the support layer is in contact with the low concentration feed solution (e.g., river or brackish water).

In the experimental runs presented in this study, no hydraulic pressure was applied to both the draw and feed sides. In actual PRO operation, the draw side is pressurized while the feed side is at ambient pressure. Although the experimental conditions do not fully replicate actual operating conditions, the experimental pressure on the feed side (where fouling of the membrane support layer occurs) simulates the actual feed solution pressure.

Red circle symbols in Figure 7.1 (“Fouling”) indicates J_w during the organic fouling run over the same cumulative permeate volume. The decline in water flux was substantially greater than that observed in “Baseline”. For instance, J_w at end of the fouling run was $11.0 \text{ L m}^{-2}\text{h}^{-1}$, almost half that of the water flux without fouling. This significantly larger drop in water flux is attributed to fouling of the membrane by the SRNOM brought into the porous support layer. Identical water flux trends for the baseline and fouling experimental runs were observed for duplicate membrane #B. The salt concentration of the model seawater draw solution was, likewise, adjusted to obtain an initial J_w of $\sim 25 \text{ L m}^{-2}\text{h}^{-1}$ for TFC-PRO #B. This allowed the permeation drag force on the foulant towards the membrane, an important factor in membrane fouling, to remain constant for the duplicate experiments [16]. The decrease in water flux across the NOM fouled membrane is expected to adversely affect the productivity of PRO power generation and is discussed in a later subsection.

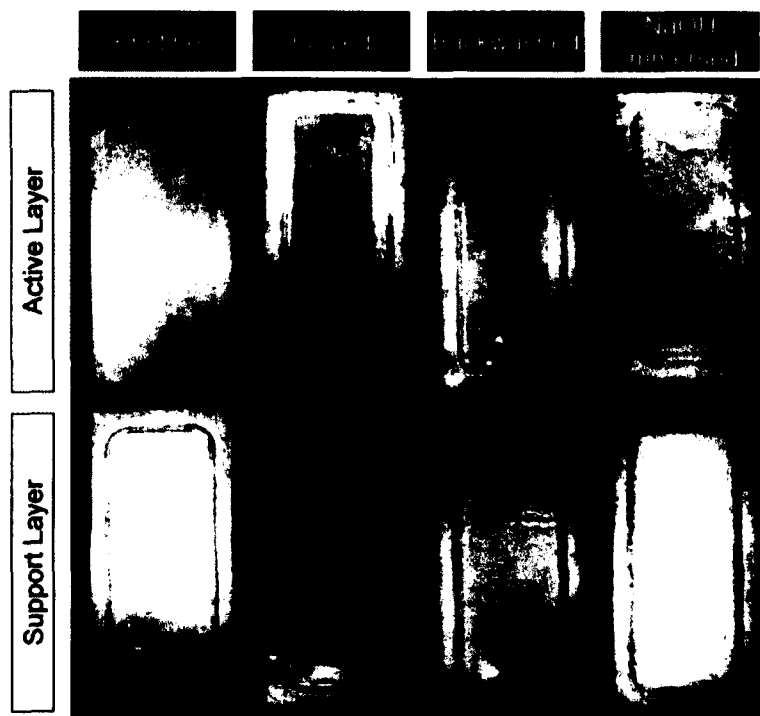


Figure 7.3. Representative images of the active and support layer of a hand-cast TFC membrane (top and bottom row, respectively) at various stages of the experimental protocol. The membrane images are for, from left to right, pristine condition (after the 1st characterization test), fouled in PRO with an NOM feed solution, after osmotic backwash cleaning, and after 48 h immersion in 0.1 M NaOH. The images were acquired from a single membrane coupon with a digital camera.

Fouling of the porous support by SRNOM can be visualized by inspecting representative images of a TFC-PRO membrane (captured with a digital camera) presented in Figure 7.3. The top and bottom rows of image show the active and support sides, respectively, of the hand-cast membrane coupon. Images of the membrane before and after fouling (“Pristine” and “Fouled”) are displayed in the first and second columns from the left, respectively. Note that the rounded rectangle around the 77 mm × 26 mm effective membrane area was imprinted by the gasket of the membrane cell. Qualitative examination of the images reveals informative visual cues that, when applied together with quantitative results, can shed light on the fouling mechanism. We observe that the

pristine, unfouled membrane appears white on both the active and support layers, while the effective area of the fouled membrane is distinctly yellowish-brown. Interestingly, the active side exhibited a notably darker hue than the support side, despite the natural organic foulants being loaded into the porous support layer of the membrane. Filtering a fouling feed solution through the porous support (i.e., no polyamide active layer) showed that the bulk of the NOM (~78 wt%) passed through and only ~22 wt% were retained by the highly porous support layer. This observation, together with the greater visual intensity of the foulants on the active side, strongly indicates that most of the SRNOM accumulated at, or very close to, the active-support layer interface.

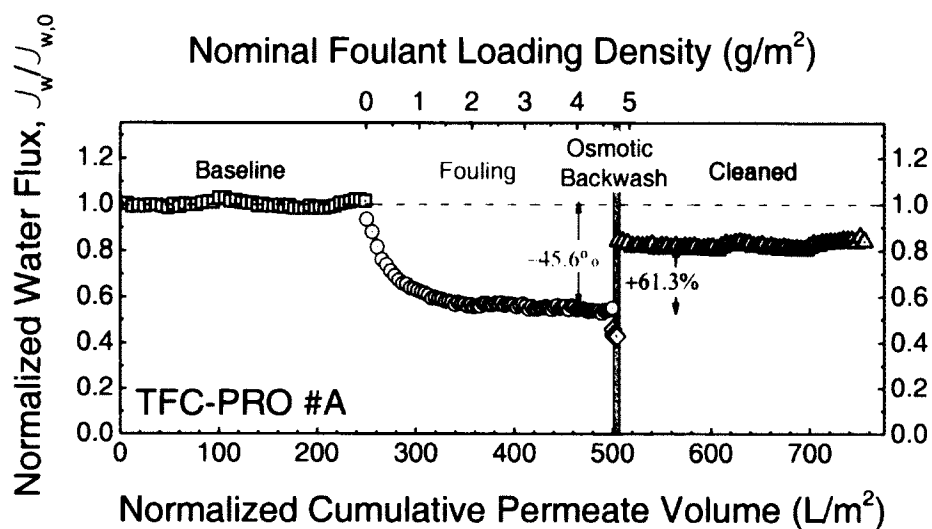


Figure 7.4. Water flux as a function of the cumulative permeate volume per unit active area of TFC-PRO membrane #A. The water flux for the baseline, fouling, osmotic backwash, and cleaned experiments (blue square, red circle, violet diamond, and green triangle symbols, respectively) is normalized with the baseline water flux, $J_{w,0}$, to account for the dilution of the draw solution. The experimental conditions are described in Figure 7.1. Osmotic backwash was performed by switching the feed and draw streams for 5 L/m² of normalized cumulative permeate volume. The top horizontal axis indicates the nominal foulant loading density into the membrane porous support (initial foulant concentration multiplied by permeate volume per unit membrane area) during fouling.

Water Flux Behavior Indicates Three Phases During Support Layer Fouling. By normalizing the water flux during the fouling run, J_w , to the baseline, $J_{w,0}$, the effect of draw solution dilution can be separated, thus allowing for the direct examination of the influence of SRNOM membrane fouling on PRO performance. The normalized water flux for hand-cast TFC-PRO membrane #A is presented in Figure 7.4 as a function of the cumulative permeate volume divided by the effective membrane area. The blue square and red circle symbols denote “Baseline” and “Fouling” experiments, respectively.

As water permeates across the membrane, foulants from the bulk feed solution are carried into the membrane porous support. Indicated on the top horizontal axis is the nominal foulant loading density during the fouling experiment, defined as the product of the cumulative permeate volume and the bulk feed solution SRNOM concentration divided by the effective membrane area. By measuring the total organic carbon (TOC) of the foulant stock solution, after filtration through a 0.45 μm membrane, with a TOC analyzer and assuming the carbon mass of natural organic matter is 50% [38], the dissolved SRNOM concentration in the model river water feed solution was determined to be 18.7 mg/L (i.e., undissolved fraction is ~ 1.3 mg/L out of the 20 mg as-received SRNOM added to a liter of DI water). Additionally, TOC measurements of the bulk feed solution before and after the fouling experiments showed that the feed foulant concentration remained practically unchanged despite the $\sim 25\%$ reduction in feed solution volume at the end of the run, validating the approximation that the foulant mass loaded into the membrane is roughly equivalent to the convective foulant transport (bulk SRNOM concentration multiplied by the cumulative permeate volume).

The water flux behavior of membrane #A during fouling in PRO is more clearly evident from Figure 7.4, and can be loosely categorized into three phases. A very steep water flux decline was observed in the initial phase of fouling, with normalized flux dropping by ~23% in the first 15 L/m² of normalized permeate volume (i.e., 250-265 L/m² on the bottom horizontal axis). Subsequently, in the second phase, normalized flux declined at a gradually reducing rate for the next 85 L/m² permeate volume (that is, 265-350 L/m² on the bottom horizontal axis). Beyond ~100 L/m² permeate volume (350-500 L/m² on the bottom horizontal axis) in the third phase, water flux attrition eased off and the normalized flux ran almost horizontal with the baseline experiment. The eventual relative decrease in PRO water flux due to SRNOM fouling of the membrane was 45.6%. Duplicate hand-cast membrane #B exhibited identical three-phase trend with almost similar water flux behavior during SRNOM fouling: ~24% water flux reduction in the initial 15 L/m² of permeation, followed by leveling out of water flux at around 100 L/m² permeate volume, and eventual reduction of -47.5% in water flux at the end of the run.

Initial Foulant Deposition at Active-Support Layer Interface Drastically Lowers Membrane Permeability. Characterization of the membranes after the fouling reveals that the SRNOM deposited in the porous support caused substantial decrease in the active layer water permeability, A (Table 7.1). The water permeability of hand-cast TFC-PRO membranes #A and #B fell by 39.6% and 38.3%, respectively, while salt permeability, B , only dropped slightly. The buildup of natural organic matter inside the membrane adds hydraulic resistance, thereby lowering the water permeability [18, 39]. The governing equation for PRO water flux (eq 7.1) indicates that J_w is directly proportional to A . Thus, the increase in hydraulic resistance of the membrane due to the SRNOM fouling is the

principal cause of the diminished water flux performance. We also note that the calculated structural parameter, S (characteristic diffusion distance of the support layer), remained practically constant within the accuracy of the characterization method. This observation indicates that the SRNOM foulants did not confer significant impedance to the diffusion of solutes in the support layer.

The immediate sharp decrease in water flux at the start of the fouling experiment followed by the gradual leveling out of the slope indicates that the initial SRNOM contributes disproportionately more to performance deterioration than subsequently loaded foulants [40]. From the top horizontal axis of Figure 7.4, the first 0.27 g/m^2 of foulants loaded into the membranes in the initial phase of fouling resulted in a steep and almost linear reduction in J_w . As the support layer, by itself, only retains a fraction of the SRNOM molecules ($\sim 22 \text{ wt\%}$), the majority of the initial foulants permeates across the entire support layer and quickly adsorbs onto the effective area of the active layer-porous support interface. We postulate that this fast sorption of foulants drastically exacerbates the hydraulic resistance and leads to a rapid decrease in A [40], accounting for the precipitous water flux decline. Subsequent SRNOM that are carried into the porous support by the water permeation are deposited on top the adsorbed foulants, forming a “cake layer” [39, 41]. In this second fouling phase, corresponding to the next 1.6 g/m^2 of foulant or $0.27\text{-}1.87 \text{ g/m}^2$ on the top horizontal axis, the gentler slope of J_w decrease suggests that the foulant cake layer does not generate as much hydraulic resistance compared to the adsorbed organic matter [40]. By now, almost all the effective area of the susceptible active-support interface possibly had already been fouled by SRNOM. Hence, for the last fouling phase, only marginal attrition in water flux was observed

despite 2.80 g/m² of foulant (that is, 1.87-4.67 g/m² on the top horizontal axis of Figure 7.4) nominally being carried into the porous support. Additionally, the high concentration of SRNOM in the membrane support layer, coupled with lesser permeation drag (i.e., lower water flux), enables greater back diffusion of the foulant molecules back into the bulk feed solution, reducing actual SRNOM deposition in the membrane.

The water permeability of the membrane can be related to the intrinsic hydraulic resistance of the polyamide active layer and the hydraulic resistance of the foulant by Darcy's law [39, 40]:

$$A = \frac{1}{\mu} \left(\frac{1}{R_m} + \frac{1}{R_f} \right) \quad (7.4)$$

where A is the membrane water permeability, μ is the dynamic viscosity of water, R_m is the hydraulic resistance of the pristine polyamide selective layer, and R_f is the hydraulic resistance of the foulant. Utilizing the A value of the pristine membranes in Table 7.1 and $R_f = 0$, R_m were calculated to be 2.26 and $2.33 \times 10^{14} \text{ m}^{-1}$ for hand-cast TFC-PRO #A and #B, respectively. Using eq 7.4 with R_m and the water permeability of the fouled membranes, R_f were determined to be 1.48 and $1.45 \times 10^{14} \text{ m}^{-1}$ for membranes #A and #B, respectively. Thus, the organic matter foulants detrimentally increased the membrane hydraulic resistance by over 60%. The foulant specific hydraulic resistance, r_f , is defined as the hydraulic resistance per unit mass of foulant ($r_f = R_f/m_f$). The average r_f for 4.67 g/m² of SRNOM nominally loaded into the membrane support layer is determined to be 3.18 and $3.10 \times 10^{13} \text{ m/g}$ for duplicate membranes #A and #B, respectively.

The same characterizations and fouling experiment was performed on a third hand-cast TFC-PRO membrane, except the fouling run was terminated earlier, after normalized

cumulative permeate volume of 15 L/m² (equivalent to 0.27 g/m² nominal foulant loading density). That is, the membrane experienced only the first phase of fouling, where SRNOM quickly adsorbs onto the effective area of the active-support interface and triggers drastic water flux decline. Water permeability of the pristine and fouled membrane, determined by membrane characterization, was 1.90 and 1.55 L m⁻² h⁻¹bar⁻¹, respectively. The calculated r_f , indicative of the adverse effect of SRNOM at the active-support interface, is 15.2×10^{13} m/g, approximately five times the average specific hydraulic resistance of $3.10\text{-}3.18 \times 10^{13}$ m/g in the complete fouling run. This quantitatively reinforces the finding that initial SRNOM foulants deposited in the membrane porous support layer cause severe escalation in membrane hydraulic resistance, thus lowering water permeability and detrimentally reducing water productivity in PRO.

Osmotic Backwash Partially Reverses Fouling. Fouling of thin-film composite membranes in PRO occurs in the membrane porous support which acts as an unstirred boundary layer. Hence, the foulants are sheltered from shear forces induced during physical cleaning (such as increasing the crossflow velocity at the membrane interface) [16], while the efficacy of chemical cleaning agents will be drastically impeded as the chemicals need to diffuse across the support layer thickness to reach foulants accumulated at active layer interface. Osmotic backwash can circumvent the shielding effect of the porous support. By swapping the feed and draw streams briefly, the direction of water permeation is momentarily reversed and membrane cleaning is initiated [32, 33]. The permeation drag that previously brought SRNOM into the porous support during fouling is now utilized to dislodge the foulants and carry the accumulated organic matter out of the support layer. After the NOM fouled membranes were

characterized, a quick osmotic backwash was conducted. The normalized cumulative volume permeated was 5 L/m^2 , corresponding to 2% of the permeate volume during the entire fouling run. During backwashing, the average nominal permeation velocity (i.e., water flux) was 2.94 and $3.03 \mu\text{m/s}$ (10.6 and $10.9 \text{ L m}^{-2}\text{h}^{-1}$) for membranes #A and #B, respectively. The water flux stabilized quickly in the first few minutes of osmotic backwash and remained fairly constant thereafter.

Foulant-free PRO experiments, with draw and feed solution compositions identical to the baseline experiment (i.e., model seawater and river water), were then carried out on the cleaned membranes to quantify the water flux recovery. Instead of achieving an initial water flux of $\sim 25 \text{ L m}^{-2}\text{h}^{-1}$ as it would if pristine, cleaned membrane #A started off with J_w of $20.7 \text{ L m}^{-2}\text{h}^{-1}$, which eventually decreased to $16.9 \text{ L m}^{-2}\text{h}^{-1}$ due draw solution dilution (Figure 7.1, green triangle symbols). The averaged normalized water flux of the cleaned membrane was 82.3% of the pristine J_w (Figure 7.4). The quick osmotic backwash achieved a partial recovery in water flux of $\sim 61.3\%$ (defined as $J_{w,\text{cleaned}} - J_{w,\text{fouled}}$ divided by $J_{w,\text{baseline}} - J_{w,\text{fouled}}$), thus demonstrating its effectiveness in reclaiming a considerable portion of the productivity lost to SRNOM fouling of the membrane porous support. Very similar water flux trends were observed for duplicate TFC-PRO membrane #B: normalized water flux of 78.7% and 55.3% recovery after cleaning.

The transport and structural parameters of the osmotic backwashed membranes were determined using the characterization protocol described in the Materials and Methods section and are presented in Table 7.1. The recovery in water flux of the cleaned membranes was attributed to a partial recuperation of the water permeability, A . The

osmotic backwash reduces the membrane hydraulic resistance by removing SRNOM foulants from the porous support, resulting in hand-cast membranes #A and #B exhibiting 39.7% and 40.7% restoration in A , respectively. Note that the structural parameters remained practically unchanged, while salt permeabilities increased slightly (~28%) relative to the fouled membranes. Visual inspection of representative images showed a distinct reduction in the yellowish-brown hue of the backwashed membrane, with the lightening of the discoloration especially pronounced for the active layer side (Figure 7.3). This change in physical appearance suggests that osmotic backwash was effective in cleaning out a substantial fraction of SRNOM foulants deposited in the membrane support layer, including foulant deposited close to the active layer. The pale yellowish-brown tint remaining on the active layer side indicates that the permeation drag induced during the backwash was insufficient to completely remove the foulants adsorbed at the active-support interface. Lastly, for comparison, the backwashed membrane was soaked in 0.1 M NaOH for 48 h to dissolve any residual SRNOM remaining in the membrane porous support. The alkaline immersed membrane appeared virtually of identical whiteness to the pristine membrane on both active and support layer sides (Figure 7.3).

From the above results, we infer that the osmotic backwash removed the majority of the foulants deposited in the support layer during the second and third phases of PRO fouling, while natural organic matter initially adsorbed at the active-support layer interface (i.e., first phase) was not entirely cleaned out by the permeation drag. Previous studies utilizing atomic force microscopy to measure foulant-membrane and foulant-foulant interactions showed that adhesion forces between natural organic matter foulant and polyamide are greater than between foulant molecules [17, 42]. As such, the

permeation drag generated by the osmotic backwash was able to remove the more loosely bound SRNOM in the foulant cake-layer. However, the foulants adsorbed at the active-support interface were cleaned to a much lesser extent. The enduring SRNOM, although small in quantity, possess relatively high specific hydraulic resistance and accounts for the incomplete reversal of fouling effects. The consistent water flux measured during the osmotic backwash (as opposed to an increasing trend) indicates that the recovery of the membrane water permeability was almost immediate. This observation further suggests that the effective cleaning occurred quickly and completely right at the onset of the backwash. The encouraging performance recovery achieved by switching the feed and draw streams for a relatively short interval demonstrates the efficiency of osmotic backwash and highlights its potential application for cleaning membrane support layers fouled in PRO.

Impact of NOM Fouling and Osmotic Backwash on Projected Membrane Power Density. Membrane power density, defined as the power produced per unit membrane area, is a key factor affecting the economic viability of PRO power generation [7, 34, 35, 43, 44]. Our previous studies showed that the peak power density attainable is determined by the membrane characteristic parameters — water permeability, A , salt permeability, B , and structural parameter, S [10, 36]. Fouling of PRO membranes by organic matter, ubiquitous in natural waters, can detrimentally alter transport parameters, while membrane cleaning can partially restore the membrane properties. Hence, SRNOM fouling and osmotic backwash of membranes is expected to impact the power density in PRO energy production. Recent studies found that operating PRO under hydraulic pressure can cause membrane deformation and alter the membrane properties

[45-47]. Hence, in actual PRO operation, the power density will be detrimentally affected by both fouling and membrane deformation. To evaluate the impact of NOM foulants on PRO performance, projected power densities were calculated assuming the membrane properties were not affected by hydraulic pressure. Peak power densities of the pristine, fouled, and cleaned membranes #A and #B were determined using eqs 7.1 and 7.3 with the model seawater draw and river water feed solutions employed in this study [36]. The results are presented in Figure 7.5 (normalized to pristine membrane values), along with the normalized water flux data discussed earlier (data from Figure 7.4).

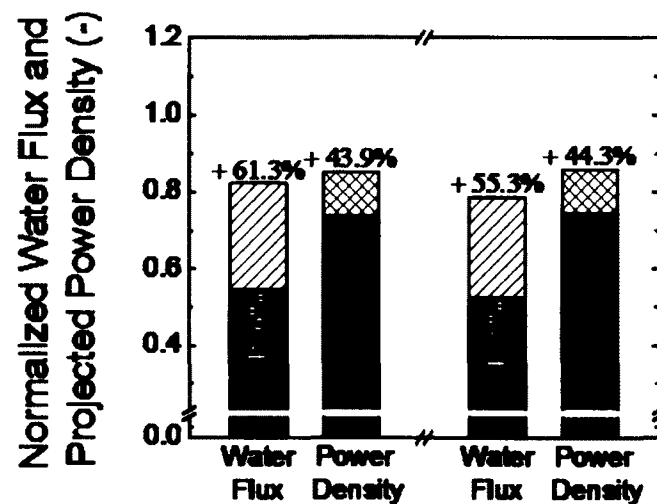


Figure 7.5. Water flux and projected membrane power density of the hand-cast TFC-PRO membranes #A and #B after SRNOM fouling and after osmotic backwash (solid and patterned columns, respectively), normalized with respect to the pristine membrane (horizontal dashed line at 1.0). Labels in the fouled membrane columns indicate the percent change relative to the pristine values, while labels above cleaned membrane columns denote the percent recovery. Experimental conditions are described in Figures 7.1 and 7.4. The projected power density of pristine membranes #A and #B are 4.64 W/m² and 4.88 W/m², respectively.

Although the transport and structural properties of the hand-cast membranes #A and #B were not tailored for high power density performance [10, 36], the absolute projected

power density values of 4.6 and 4.9 W/m², respectively, are still reasonable close to the proposed value of 5 W/m² necessary for PRO to be cost-effective [43, 44]. The initial water flux of the fouling experiments was thoughtfully selected to be ~25 L m⁻²h⁻¹ to simulate customized membranes with high power density performance in PRO energy generation with natural salinity gradients (projected ~9 W/m²) [10]. In the hand-cast TFC-PRO membranes, fouling of the porous support layer by SRNOM deleteriously increases the membrane hydraulic resistance (i.e., lower A). Hence, a greater fraction of the osmotic driving force is expended to overcome this additional friction instead of driving water flux. The rate of water permeation across the membrane is impeded and the membrane power density is consequently reduced (eq 7.3). The predicted power density of fouled TFC-PRO #A and #B decreased by 26.4% and 25.6%, respectively. Therefore, SRNOM fouling of porous support in PRO detrimentally constrains the ability of the membrane to convert salinity gradient energy into useful work.

Water permeability of the fouled membrane is partly recovered by the osmotic backwashing cleaning that removed substantial foulants from the porous support. The favorable reduction in membrane hydraulic resistance restored the projected membrane power density by 43.9% and 44.3% for TFC-PRO #A and #B, respectively. That is, after the brief backwash, the power density was approximately ~0.85 of the pristine membranes, reasonably close to the original power density. Thus, the cleaned membranes, compared to when fouled, were able to utilize a larger portion of the salinity gradient between seawater and river water for energy generation. The encouraging recovery achieved by a quick osmotic backwash underscores the potential of the

technique as an efficient and chemical-free cleaning strategy for membranes in PRO energy production with natural salinity gradients.

7.4 IMPLICATIONS FOR POWER GENERATION

In an actual seawater-river water PRO power generation plant, fouling of membrane porous support layer due to the presence of ubiquitous natural organic matter in the feed stream will diminish the power density. The adverse effects of PRO membrane fouling can be mitigated primarily through three approaches: pretreating the influent streams, using fouling-resistant membranes, and cleaning the fouled membranes. Pretreatment of the river water influent to remove natural organic matter and also microorganisms that cause biofouling can be an effective fouling prevention measure, as demonstrated in reverse osmosis desalination applications, but incurs energy and chemical costs [48]. Intermittent osmotic backwashing of fouled membranes, requiring only nominal pumping energy and posing negligible operational disruption, has the potential to achieve significant performance recovery without chemical use. This study on the efficacy of osmotic backwash showed promising results, but further investigations on a broader range of conditions, for example, the effect of larger permeation drag (i.e., water flux) produced by more concentrated draw solutions such as brine and the minimum backwash duration necessary for effective cleaning, are needed to thoroughly evaluate the suitability of the technique for application in PRO power generation.

Fouling can be alleviated by thoughtful design and/or modification of the PRO membrane to impart fouling resistant properties. Fouling studies on a broader spectrum of foulants (e.g., microorganisms, extracellular polymeric substances (EPS), and colloidal

foulants) can improve our understanding of the fouling mechanisms and provide essential insights to guide the fabrication of anti-fouling membranes. In this study, we show that power density performance deterioration is critically dictated by NOM fouling of the active-support layer interface within the porous support of thin-film composite polyamide membranes. Therefore, efforts can be targeted at reducing the fouling propensity of this susceptible interface through thoughtful modifications of the surface chemistry [42, 49, 50] or incorporation of an additional barrier layer on the back side of the support layer to prevent foulants from entering the porous support [51, 52]. A key challenge here is to achieve fouling resistance enhancements while conserving the membrane transport and structural properties necessary for high PRO power densities. An optimal fouling mitigation strategy will likely be arrived at utilizing combinations, or even all, of the three approaches, while factoring in the capital, chemical, energy, and operational costs to the overall productivity of PRO power generation with natural salinity gradients.

7.5 REFERENCES

- [1] Chu, S. Majumdar, A., Opportunities and challenges for a sustainable energy future. *Nature* **2012**, *488* (7411), 294-303.
- [2] Logan, B. E. Elimelech, M., Membrane-based processes for sustainable power generation using water. *Nature* **2012**, *488* (7411), 313-319.
- [3] Pattle, R. E., Production of Electric Power by Mixing Fresh and Salt Water in the Hydroelectric Pile. *Nature* **1954**, *174* (4431), 660-660.
- [4] Yip, N. Y. Elimelech, M., Thermodynamic and Energy Efficiency Analysis of Power Generation from Natural Salinity Gradients by Pressure Retarded Osmosis. *Environmental Science & Technology* **2012**, *46* (9), 5230-5239.
- [5] Dai, A. Trenberth, K. E., Estimates of freshwater discharge from continents: Latitudinal and seasonal variations. *Journal of Hydrometeorology* **2002**, *3* (6), 660-687.
- [6] Loeb, S., Osmotic Power-Plants. *Science* **1975**, *189* (4203), 654-655.
- [7] Achilli, A. Childress, A. E., Pressure retarded osmosis: From the vision of Sidney Loeb to the first prototype installation - Review. *Desalination* **2010**, *261* (3), 205-211.
- [8] Cath, T. Y.; Childress, A. E. Elimelech, M., Forward osmosis: Principles, applications, and recent developments. *Journal of Membrane Science* **2006**, *281* (1-2), 70-87.
- [9] GWI, *Water Desalination Report, Volume 49, Number 23, 24 June, 2013*.
- [10] Yip, N. Y.; Tiraferri, A.; Phillip, W. A.; Schiffman, J. D.; Hoover, L. A.; Kim, Y. C. Elimelech, M., Thin-Film Composite Pressure Retarded Osmosis Membranes for Sustainable Power Generation from Salinity Gradients. *Environmental Science & Technology* **2011**, *45* (10), 4360-4369.
- [11] Chou, S.; Wang, R.; Shi, L.; She, Q.; Tang, C. Fane, A. G., Thin-film composite hollow fiber membranes for pressure retarded osmosis (PRO) process with high power density. *Journal of Membrane Science* **2012**, *389*, 25-33.
- [12] Han, G.; Wang, P. Chung, T. S., Highly robust thin-film composite pressure retarded osmosis (PRO) hollow fiber membranes with high power densities for renewable salinity-gradient energy generation. *Environ Sci Technol* **2013**, *47* (14), 8070-7.
- [13] Baker, R. W., Membrane technology and applications. 2nd ed.; J. Wiley, Chichester ; New York, **2004**; p x, 538 p.
- [14] Mulder, M., Basic principles of membrane technology. 2nd ed.; Kluwer Academic, Dordrecht ; Boston, **1996**; p 564 p.
- [15] Bartels, C. R.; Wilf, M.; Andes, K. Iong, J., Design considerations for wastewater treatment by reverse osmosis. *Water science and technology : a journal of the International Association on Water Pollution Research* **2005**, *51* (6-7), 473-482.
- [16] Mi, B. Elimelech, M., Chemical and physical aspects of organic fouling of forward osmosis membranes. *Journal of Membrane Science* **2008**, *320* (1-2), 292-302.

- [17] Mi, B. X. Elimelech, M., Organic fouling of forward osmosis membranes: Fouling reversibility and cleaning without chemical reagents. *Journal of Membrane Science* **2010**, *348* (1-2), 337-345.
- [18] Tang, C. Y.; She, Q.; Lay, W. C. L.; Wang, R. Fane, A. G., Coupled effects of internal concentration polarization and fouling on flux behavior of forward osmosis membranes during humic acid filtration. *Journal of Membrane Science* **2010**, *354* (1-2), 123-133.
- [19] Lee, S.; Boo, C.; Elimelech, M. Hong, S., Comparison of fouling behavior in forward osmosis (FO) and reverse osmosis (RO). *Journal of Membrane Science* **2010**, *365* (1-2), 34-39.
- [20] Boo, C.; Elimelech, M. Hong, S., Fouling control in a forward osmosis process integrating seawater desalination and wastewater reclamation. *Journal of Membrane Science* **2013**, *444*, 148-156.
- [21] Thelin, W. R.; Sivertsen, E.; Holt, T. Brekke, G., Natural organic matter fouling in pressure retarded osmosis. *Journal of Membrane Science* **2013**, *438*, 46-56.
- [22] She, Q. H.; Wong, Y. K. W.; Zhao, S. F. Tang, C. Y. Y., Organic fouling in pressure retarded osmosis: Experiments, mechanisms and implications. *Journal of Membrane Science* **2013**, *428*, 181-189.
- [23] Lee, S. Elimelech, M., Relating organic fouling of reverse osmosis membranes to intermolecular adhesion forces. *Environmental Science & Technology* **2006**, *40* (3), 980-987.
- [24] Ang, W. S.; Tiraferri, A.; Chen, K. L. Elimelech, M., Fouling and cleaning of RO membranes fouled by mixtures of organic foulants simulating wastewater effluent. *Journal of Membrane Science* **2011**, *376* (1-2), 196-206.
- [25] Li, Q. L. Elimelech, M., Organic fouling and chemical cleaning of nanofiltration membranes: Measurements and mechanisms. *Environmental Science & Technology* **2004**, *38* (17), 4683-4693.
- [26] Averett, R. C. Geological Survey (U.S.), Humic substances in the Suwannee River, Georgia : interactions, properties, and proposed structures. U.S. G.P.O.; For sale by U.S. Geological Survey, Map Distribution, [Washington] Denver, Colo., **1994**; p ix, 224 p.
- [27] Chin, Y. P.; Aiken, G. Oloughlin, E., Molecular-Weight, Polydispersity, and Spectroscopic Properties of Aquatic Humic Substances. *Environmental Science & Technology* **1994**, *28* (11), 1853-1858.
- [28] Yip, N. Y.; Tiraferri, A.; Phillip, W. A.; Schiffman, J. D. Elimelech, M., High Performance Thin-Film Composite Forward Osmosis Membrane. *Environmental Science & Technology* **2010**, *44* (10), 3812-3818.
- [29] Tiraferri, A.; Yip, N. Y.; Phillip, W. A.; Schiffman, J. D. Elimelech, M., Relating performance of thin-film composite forward osmosis membranes to support layer formation and structure. *Journal of Membrane Science* **2011**, *367* (1-2), 340-352.
- [30] Petersen, R. J., Composite Reverse-Osmosis and Nanofiltration Membranes. *Journal of Membrane Science* **1993**, *83* (1), 81-150.
- [31] Tiraferri, A.; Yip, N. Y.; Straub, A. P.; Castrillon, S. R. V. Elimelech, M., A method for the simultaneous determination of transport and structural parameters of forward osmosis membranes. *Journal of Membrane Science* **2013**, *444*, 523-538.
- [32] Holloway, R. W.; Childress, A. E.; Dennett, K. E. Cath, T. Y., Forward osmosis for concentration of anaerobic digester centrate. *Water Research* **2007**, *41* (17), 4005-4014.
- [33] Achilli, A.; Cath, T. Y.; Marchand, E. A. Childress, A. E., The forward osmosis membrane bioreactor: A low fouling alternative to MBR processes. *Desalination* **2009**, *239* (1-3), 10-21.

- [34] Lee, K. L.; Baker, R. W. Lonsdale, H. K., Membranes for power generation by pressure-retarded osmosis. *Journal of Membrane Science* **1981**, *8* (2), 141-171.
- [35] Achilli, A.; Cath, T. Y. Childress, A. E., Power generation with pressure retarded osmosis: An experimental and theoretical investigation. *Journal of Membrane Science* **2009**, *343* (1-2), 42-52.
- [36] Yip, N. Y. Elimelech, M., Performance Limiting Effects in Power Generation from Salinity Gradients by Pressure Retarded Osmosis. *Environmental Science & Technology* **2011**, *45* (23), 10273-10282.
- [37] Morel, F. o.; Hering, J. G. Morel, F. o., Principles and applications of aquatic chemistry. Wiley, New York, **1993**; p xv, 588 p.
- [38] Perdue, E. M. Ritchie, J. D., 5.10 - Dissolved Organic Matter in Freshwaters. In *Treatise on Geochemistry*, Editors-in-Chief: Heinrich, D. H. Karl, K. T., Eds. Pergamon: Oxford, 2003; pp 273-318.
- [39] Hong, S. Elimelech, M., Chemical and physical aspects of natural organic matter (NOM) fouling of nanofiltration membranes. *Journal of Membrane Science* **1997**, *132* (2), 159-181.
- [40] Belfort, G.; Davis, R. H. Zydney, A. L., The Behavior of Suspensions and Macromolecular Solutions in Cross-Flow Microfiltration. *Journal of Membrane Science* **1994**, *96* (1-2), 1-58.
- [41] Ko, M. K. Pellegrino, J. J., Determination of osmotic pressure and fouling resistance and their effects of performance of ultrafiltration membranes. *Journal of Membrane Science* **1992**, *74* (1-2), 141-157.
- [42] Tiraferri, A.; Kang, Y.; Giannelis, E. P. Elimelech, M., Superhydrophilic Thin-Film Composite Forward Osmosis Membranes for Organic Fouling Control: Fouling Behavior and Antifouling Mechanisms. *Environmental Science & Technology* **2012**, *46* (20), 11135-11144.
- [43] Gerstandt, K.; Peinemann, K. V.; Skilhagen, S. E.; Thorsen, T. Holt, T., Membrane processes in energy supply for an osmotic power plant. *Desalination* **2008**, *224* (1-3), 64-70.
- [44] Skilhagen, S. E., Osmotic power - a new, renewable energy source. *Desalination and Water Treatment* **2010**, *15* (1-3), 271-278.
- [45] Kim, Y. C. Elimelech, M., Adverse Impact of Feed Channel Spacers on the Performance of Pressure Retarded Osmosis. *Environmental Science & Technology* **2012**, *46* (8), 4673-4681.
- [46] She, Q.; Hou, D.; Liu, J.; Tan, K. H. Tang, C. Y., Effect of feed spacer induced membrane deformation on the performance of pressure retarded osmosis (PRO): Implications for PRO process operation. *Journal of Membrane Science* **2013**, *445*, 170-182.
- [47] Coday, B. D.; Heil, D. M.; Xu, P. Cath, T. Y., Effects of Transmembrane Hydraulic Pressure on Performance of Forward Osmosis Membranes. *Environmental Science & Technology* **2013**, *47* (5), 2386-2393.
- [48] Elimelech, M. Phillip, W. A., The Future of Seawater Desalination: Energy, Technology, and the Environment. *Science* **2011**, *333* (6043), 712-717.
- [49] Park, J. Y.; Acar, M. H.; Akthakul, A.; Kuhlman, W. Mayes, A. M., Polysulfone-graft-poly(ethylene glycol) graft copolymers for surface modification of polysulfone membranes. *Biomaterials* **2006**, *27* (6), 856-865.
- [50] McCloskey, B. D.; Park, H. B.; Ju, H.; Rowe, B. W.; Miller, D. J.; Chun, B. J.; Kin, K. Freeman, B. D., Influence of polydopamine deposition conditions on pure water flux and foulant adhesion resistance of reverse osmosis, ultrafiltration, and microfiltration membranes. *Polymer* **2010**, *51* (15), 3472-3485.

[51] Wang, K. Y.; Ong, R. C. Chung, T.-S., Double-Skinned Forward Osmosis Membranes for Reducing Internal Concentration Polarization within the Porous Sublayer. *Industrial & Engineering Chemistry Research* **2010**, *49* (10), 4824-4831.

[52] Qi, S.; Qiu, C. Q.; Zhao, Y. Tang, C. Y., Double-skinned forward osmosis membranes based on layer-by-layer assembly—FO performance and fouling behavior. *Journal of Membrane Science* **2012**, *405–406*, 20-29.

Chapter 8:

**Thermodynamic, Energy Efficiency,
and Power Density Analysis of
Reverse Electrodialysis Power
Generation with Natural Salinity
Gradients**

CHAPTER ABSTRACT

Reverse electro dialysis (RED) can harness the Gibbs free energy of mixing when fresh river water flows into the sea for sustainable power generation. In this study, we carry out a thermodynamic and energy efficiency analysis of RED power generation, and assess the membrane power density. First, we present a reversible thermodynamic model for RED and verify that the theoretical maximum extractable work in a reversible RED process is identical to the Gibbs free energy of mixing. Work extraction in an irreversible process with maximized power density using a constant-resistance load is then examined to assess the energy conversion efficiency and power density. With equal volumes of seawater and river water, energy conversion efficiency of ~33-44% can be obtained in RED, while the rest is lost through dissipation in the internal resistance of the ion exchange membrane stack. We show that imperfections in the selectivity of typical ion exchange membranes (namely, co-ion transport, osmosis, and electro-osmosis) can detrimentally lower efficiency by up to 26%, with co-ion leakage being the dominant effect. Further inspection of the power density profile during RED revealed inherent ineffectiveness towards the end of the process. By judicious early discontinuation of the controlled mixing process, the overall power density performance can be considerably enhanced by up to sevenfold, without significant compromise to the energy efficiency. Additionally, membrane resistance was found to be an important factor in determining the power densities attainable. Lastly, the performance of an RED stack was examined for different membrane conductivities and intermembrane distances simulating high performance membranes and stack design. By thoughtful selection of the operating parameters, an efficiency of ~37% and an overall gross power density of 3.5 W/m²

represent the maximum performance that can potentially be achieved in a seawater-river water RED system with low-resistance ion exchange membranes ($0.5 \Omega\text{cm}^2$) at very small spacing intervals ($50 \mu\text{m}$).

8.1 INTRODUCTION

To meet current and future energy demands in a sustainable manner, alternative power sources that are clean and renewable need to be advanced [1]. Nature's hydrological cycle offers a significant source of sustainable energy through salinity gradients. When two solutions of different concentrations are combined, the Gibbs free energy of mixing that is released can be harnessed for useful work [2, 3]. The annual global river discharge of $\sim 37,300 \text{ km}^3$ represents a currently untapped, self-replenishing supply that can potentially be accessed for clean power generation. A recent study estimates that utilizing a tenth of the world's freshwater runoff can potentially generate electricity for over half a billion people with pressure retarded osmosis, a technology to convert the salinity energy to mechanical and then electrical energy [4].

Reverse electrodialysis (RED) is another emerging technology that can harvest the energy from natural salinity gradients [5, 6]. RED is the power generation analog of electrodialysis (ED) separation. Whereas energy is consumed in ED to carry out separation of ions [7], RED utilizes the permeation of counter ions across ion exchange membranes to generate a Nernst potential between two solutions of different concentration, while a redox couple at the end electrodes converts the ion flux into an electric current, thus producing energy through controlled mixing of the solutions.

Essentially, RED operates as a “salinity battery” — directly discharging stored chemical potential energy as electricity.

To advance the technology towards actual implementation, a better understanding of the potential RED process performance at a system-level is necessary. Energy efficiency and membrane power density, performance indicators critical to the potential feasibility of RED energy production, had been evaluated in previous experimental studies [6, 8-13]. However, these ad hoc investigations are restricted to laboratory-scale batch experiments. Modeling efforts to simulate actual RED power generation have limited scope, focusing piecemeal on either efficiency [14-16] or power density [16-19] optimization, with only one study concurrently examining both parameters [20]. Furthermore, to date, there are no studies that quantify the individual impact of inevitable imperfections in membrane selectivity on energy efficiency and power density performance. Without a comprehensive grasp of the potential efficiency, and power density that can be simultaneously obtained, the energy capacity available from river runoffs mixing with the ocean, and ion exchange membrane area needed to harness that energy, cannot be accurately assessed. To realize the potential of RED power generation with natural salinity gradients, it is imperative that these gaps in our current knowledge of the process be addressed.

In this study, we carry out a robust analysis of a practical reverse electrodialysis process to systematically evaluate the energy efficiency and the concurrent power density. The theoretical maximum extractable work in RED is first determined from a reversible thermodynamic model and compared to the Gibbs free energy of mixing. We then evaluate the thermodynamic efficiency of work extraction and membrane power density

in a practical RED process employing a constant-resistance external load. Membrane selectivity imperfections — co-ion transport, water osmosis, and electro-osmosis — are characterized and their influence on the RED salinity battery performance is evaluated. Lastly, energy conversion efficiency and membrane power density are quantitatively assessed with simulated technologically-available membranes. The intricate relationship between efficiency and power density is methodically examined and potential approaches to optimize the overall cost-effectiveness of the technology are discussed. Our analytical study provides insights into the intrinsic efficiency and effectiveness of RED that can guide membrane module design and inform systems operation for the advancement of sustainable energy production from natural salinity gradients.

8.2 REVERSIBLE THERMODYNAMIC MODEL OF REVERSE ELECTRODIALYSIS

Reverse electrodialysis energy production with natural salinity gradients employs an RED stack, consisting of repeating pairs of cation exchange membrane (CEM) and anion exchange membrane (AEM), with high concentration (HC) and low concentration (LC) solutions alternatively flowing through each channel between the membranes (Figure 8.1A) [5, 6, 11, 12, 21]. A repeating cell consists of, in spatial order, a CEM, an HC solution compartment, an AEM, and an LC solution compartment (which is bordered by the CEM of the next adjacent cell). The salt (or ion) concentration difference across the ion exchange membranes (IEMs) produces a Nernst potential. As the IEMs selectively allow the passage of counter ions (i.e., cations for the negatively charged CEMs and anions for the positively charged AEMs), co-ions are retained while counter ions

permeate from the HC compartment to the LC compartment. Charge neutrality in the solutions is achieved due to the simultaneous permeation of cations and anions across the CEM and AEM, respectively, sandwiching each solution compartment. A pair of electrodes caps off the stack and a reversible redox couple (e.g., $\text{Fe}^{2+}/\text{Fe}^{3+}$ or $[\text{Fe}(\text{CN})_6]^{4-}/[\text{Fe}(\text{CN})_6]^{3-}$) [22-24] is circulated between the end electrodes to convert the ionic current to an electric current. The redox couple composition is maintained constant during the RED process as oxidation at the anode is exactly offset by reduction at the cathode.

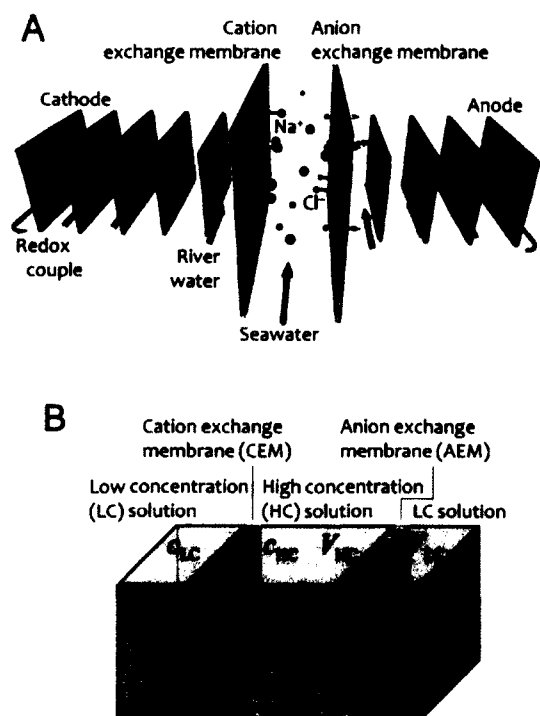


Figure 8.1. (A) Conceptual schematic of a reverse electro dialysis salinity battery. Four repeating stacks are shown and a representative membrane pair is enlarged to illustrate the ion flux. The RED battery consists of repeating cells of alternating cation exchange membrane (CEM) and anion exchange membrane (AEM). High concentration (HC) and low concentration (LC) solutions, i.e., seawater and river or brackish water, respectively, flow through the channels alternatively. The ion exchange membranes selectively allow the transport of counter ions. The concentration difference across the ion exchange

membranes produces a Nernst potential. A redox couple circulating between the end electrodes converts the ion flux to an electric current with a reversible redox reaction. (B) Schematic of one RED cell, comprising a HC solution compartment (salt concentration c_{HC} and volume V_{HC}) separated from two LC solution half-compartments (salt concentration c_{LC} and combined volume V_{LC}) by a CEM possessing fixed negative charges and an AEM having fixed positive charges.

In this section, we present a reversible thermodynamic model of RED and show the derivation of the theoretical maximum extractable work. In the following analyses, a 600 mM NaCl HC solution is used to simulate seawater of ~ 35 g/L TDS, while the salt concentrations of the LC solutions are 1.5 and 17 mM NaCl, to represent river water and brackish water of approximately 88 mg/L and 1 g/L TDS, respectively [4]. The temperature is 298 K and assumed to remain constant throughout the RED process.

Reverse Electrodialysis Model. Figure 8.1B shows one RED cell, comprising an HC solution compartment separated from two LC solution half-compartments by a pair of CEM and AEM. The potential (or electromotive force, emf) of the cell, ξ_{emf} , is the sum of the Nernst potentials across the ion exchange membrane pair due to the ion concentration difference:

$$\xi_{emf} = \xi_{\frac{1}{2}emf, \text{CEM}} + \xi_{\frac{1}{2}emf, \text{AEM}} \approx \left(\frac{\alpha_{\text{CEM}}}{z_+} + \frac{\alpha_{\text{AEM}}}{z_-} \right) \frac{R_g T}{F} \ln \frac{c_{\text{HC}}}{c_{\text{LC}}} \quad (8.1)$$

where $\xi_{\frac{1}{2}emf}$ is the half-cell potential, α is the permselectivity of the IEM, R_g is the gas constant, T is the absolute temperature, z is the ion valence (e.g., $z = 1$ for Na^+ and Cl^-), and F is the Faraday constant. The subscript of α and $\xi_{\frac{1}{2}emf}$ denotes cation or anion exchange membrane, and the subscript of z represents the cation (+) or anion (-), respectively.

Although Figure 8.1B depicts a batch process, the model can also represent a continuous flow RED stack with the solutions circulated co-currently at equal flowrates. Assuming ideal plug-flow, the solution concentrations while advancing along the axial length of the RED membrane stack corresponds to the conditions in the batch process as controlled mixing progresses (i.e., the hydraulic residence time of the stack is equivalent to the mixing duration of the batch process).

For Δn_s moles of salt that has permeated (i.e., cations across the CEM and anions across the AEM), the molar salt concentration of the HC and LC solutions are $c_{\text{HC}} = (n_{\text{s,HC}}^0 - \Delta n_s) / V_{\text{HC}}^0$ and $c_{\text{LC}} = (n_{\text{s,LC}}^0 + \Delta n_s) / V_{\text{LC}}^0$, respectively, where n_s is the moles of salt, V is the solution volume, and superscript 0 denotes the initial solution. Note that the two LC half-compartments in Figure 8.1B are considered together as one solution volume, thus preserving electroneutrality. The IEMs are assumed to be water impermeable and, hence, the solution volume remains unchanged throughout the process (the effect of water osmosis is analyzed and discussed in a later section).

Substituting the expressions for c_{HC} and c_{LC} into eq 8.1, and assuming $\alpha_{\text{CEM}} = \alpha_{\text{AEM}} = 1$ (i.e., ion exchange membranes are perfectly selective for counter ions), yield the electromotive force across the RED cell, ξ_{emf} , during the controlled mixing process. Figure 8.2A shows a representative plot of ξ_{emf} across the one-cell RED as a function of Δn_s . Using equal volumes of seawater as the HC solution and river water as the LC solution (600 mM and 1.5 mM NaCl, respectively), both z_+ and z_- are unity and the initial potential difference across the CEM and AEM pair of the RED is calculated to be 308 mV (vertical axis intercept). Actual seawater and river water contains some divalent ions (e.g., Mg^{2+} , Ca^{2+} , and SO_4^{2-}) that contribute less to the ξ_{emf} compared to monovalent ions

(as evident from the inspection of eq 8.1). For seawater and river water with 10% of salts as divalent ions, the ξ_{emf} is $\sim 7\%$ lower than the pure NaCl solutions used in this study [25].

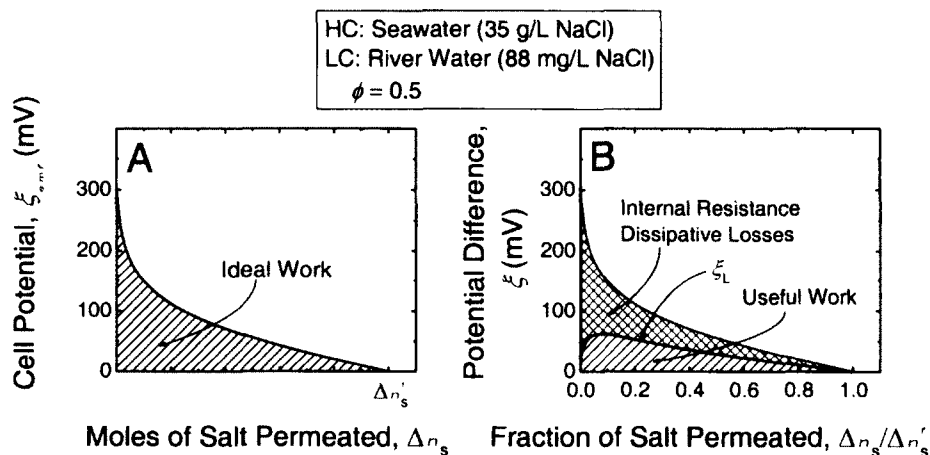


Figure 8.2. (A) Representative plot of the voltage (or electromotive force), ξ_{emf} , across the one-cell RED, as a function of the moles of salt that permeated across the ion exchange membranes, Δn_s (eq 8.1). In a reversible thermodynamic RED process, the potential difference across the external load is always exactly equal to ξ_{emf} . Multiplying the moles of salt permeated by the Faraday constant, F , and the total charge of the ions each salt molecule dissociates into (i.e., 2 for NaCl) yields the charge transported, Δq . Hence, the total amount of work extractable from the hypothetical RED process, W_{ideal} , is equal to the area under the voltage-salt permeated (or, equivalently, ξ - Δq) plot (eq 8.5). (B) Representative plot of the useful work (blue patterned region), extractable in an RED process, where maximizing the overall membrane power density is the principal objective. The region marked “Internal Resistance Losses” indicates the energy lost due to impedance caused by the RED stack resistance. In these representative plots, the HC solution is seawater (600 mM or 35 g/L NaCl), the LC solution is river water (1.5 mM or 88 mg/L NaCl), the volumetric fraction of the LC solution, ϕ , is 0.5, and temperature $T = 298$ K. The IEMs are assumed to be perfectly selective, the area specific resistance, ASR, of the membranes is $3.0 \Omega\text{cm}^2$, and the intermembrane distance, d , is $150 \mu\text{m}$.

Ion transport proceeds until the HC and LC solutions are at equilibrium and the potential across the RED cell falls to zero (horizontal axis intercept in Figure 8.2A). The

concentration of the final mixed solution, c_M^f , can be determined by applying salt mass balance:

$$c_M^f = \phi c_{LC}^0 + (1 - \phi) c_{HC}^0 \quad (8.2)$$

where ϕ is approximately the volumetric ratio of the initial LC solution to the total system volume: $\phi \cong V_{LC}^0 / (V_{LC}^0 + V_{HC}^0)$ [4]. The fraction of salt in the initial HC solution that is eventually transported across the IEMs can be calculated by solving Δn_s^f for $c_{LC} = c_{HC}$:

$$\frac{\Delta n_s^f}{n_{s,HC}^0} = \phi \left(1 - \frac{c_{LC}^0}{c_{HC}^0} \right) \quad (8.3)$$

where superscript f denotes “final”.

Reversible Thermodynamic RED Process. In a theoretical reversible thermodynamic RED process, an infinitesimal ion flux is maintained throughout the controlled mixing. This is achieved by applying an opposite external potential that is negligibly smaller in magnitude to the cell emf . A very small amount of ions is transported across the membranes because of the infinitesimal resultant potential difference. The HC solution concentration is marginally lowered due to the salt permeation, while c_{LC} increases slightly. Hence, ξ_{emf} minutely decreases such that it is now exactly equal to the external applied voltage.

The process of gradually lowering the external potential is repeated in infinite small steps to achieve a continuous decrease while keeping the external potential virtually equal to ξ_{emf} . At any point during the reversible thermodynamic process, the magnitude of the external potential can be raised slightly above the cell emf , thus flipping around the ion flux direction and causing a small amount of ions to be transported back to the HC

solution. Hence, the controlled mixing process is “reversed” and becomes a separation process (i.e., electro dialysis desalination). In actual operation, an RED process can approach reversible thermodynamics by connecting the stack to an external load of infinitely high resistance (relative to the stack) to achieve negligible ionic current.

Theoretical Maximum Extractable Work is Equal to the Gibbs Energy of Mixing. In a hypothetical reversible thermodynamic RED process, no entropy is generated [26]. The transfer of ionic charges, Δq , against the external applied voltage represents the theoretical maximum energy that can be extracted for useful work by the salinity battery. Integrating the external potential difference, which is precisely ξ_{emf} for a reversible thermodynamic RED process, across the charges transported over the entire process yields the ideal work, W_{ideal} :

$$W_{ideal} = \int \xi_{emf} d\Delta q = \nu_+ z_+ F \int_0^{\Delta n_s'} \xi_{\frac{1}{2}emf, CEM} d\Delta n_s + \nu_- z_- F \int_0^{\Delta n_s'} \xi_{\frac{1}{2}emf, AEM} d\Delta n_s \quad (8.4)$$

To account for cation transport across the CEM potential and anion flux across the AEM potential, the integral is split into the contribution from each membrane. The moles of salt permeated, Δn_s , can substitute for the variable of integration ($\Delta q_{+/-} = \nu_{+/-} z_{+/-} F \Delta n_s$).

Substituting eq 8.1 and the expressions for c_{HC} and c_{LC} into eq 8.4 gives the ideal work extractable in RED:

$$W_{ideal} = \nu R_g T \int_0^{\Delta n_s'} \ln \frac{c_{HC}}{c_{LC}} d\Delta n_s = \nu R_g T \int_0^{\Delta n_s'} \left(\ln \frac{n_{s,HC} - \Delta n_s}{V_{HC}^0} - \ln \frac{n_{s,LC} + \Delta n_s}{V_{LC}^0} \right) d\Delta n_s \quad (8.5)$$

where $\nu = \nu_+ + \nu_-$ is the number of ions each salt molecule dissociates into (e.g., ν is 2 for NaCl). Here, the IEMs were taken to be perfectly selective (i.e., $\alpha_{CEM/AEM} = 1$); the influence of co-ion leakage is examined in a later section. A graphical representation of W_{ideal} is given by area under the voltage- Δn_s plot as depicted in Figure 8.2A. The integral

can be solved using eq 8.3 for the limits of the integration to arrive at the specific ideal work, $W_{\text{ideal},V_{\text{LC}}^0}$, defined as energy per unit volume of the initial LC solution:

$$-\frac{W_{\text{ideal},V_{\text{LC}}^0}}{\nu R_g T} = \frac{c_M^f}{\phi} \ln c_M^f - c_{\text{LC}}^0 \ln c_{\text{LC}}^0 - \frac{(1-\phi)}{\phi} c_{\text{HC}}^0 \ln c_{\text{HC}}^0 = -\frac{\Delta G_{\text{mix},V_{\text{LC}}^0}}{\nu R_g T} \quad (8.6)$$

The negative sign of $W_{\text{ideal},V_{\text{LC}}^0}$ signifies that work is being done by the one-cell RED system.

The expression for $W_{\text{ideal},V_{\text{LC}}^0}$ in eq 8.6 is identical to the Gibbs free energy of mixing per unit volume of the LC solution, $\Delta G_{\text{mix},V_{\text{LC}}^0}$ [4]. This result is expected and is consistent with the principles of thermodynamics — the change in the Gibbs free energy of a system is equivalent to the work done by the system in an ideal reversible thermodynamic process [26, 27].

8.3 ENERGY EFFICIENCY OF REVERSE ELECTRODIALYSIS

Hypothetical reversible thermodynamic RED process would require infinite membrane area or unlimited time because of the infinitesimal rate of controlled mixing and is, hence, impractical to implement. Actual processes are not completely reversible due to the inevitable production of entropy [26]. Entropy production, as dictated by the second law of thermodynamics, subtracts from W_{ideal} and, thus, reduces the amount of energy accessible for conversion to useful work. In this section, we introduce operational considerations in a practical process to the RED model and analyze the power generation efficiency with natural salinity gradients.

Internal Resistances in RED Power Generation Circuit. In an actual RED salinity battery, the stack components are not ideally conductive but possess resistance that

impedes the ionic and electric current. The resistance of the stack depicted in Figure 8.1A, r_{stack} , is the sum of the stack elements in series [5, 6, 8, 28]. For the one repeating RED cell considered in Figure 8.1B, the area specific resistance, ASR_{cell} , is the product of r_{stack} and the effective cell area, A , divided by the number of membranes pairs (or repeating RED cells), N :

$$\text{ASR}_{\text{cell}} = r_{\text{cell}} A = \frac{r_{\text{stack}} A}{N} \approx \text{ASR}_{\text{AEM}} + \text{ASR}_{\text{CEM}} + \frac{1}{\Lambda} \left(\frac{d_{\text{HC}}}{c_{\text{HC}}} + \frac{d_{\text{LC}}}{c_{\text{LC}}} \right) \quad (8.7)$$

where Λ is the molar conductivity of electrolyte (NaCl) solution, d is the intermembrane distance, and c is the solution molar concentration. The product of molar conductivity and concentration yields the solution conductivity ($\kappa = \Lambda c$). For the NaCl salt concentrations considered in this study, Λ is calculated to be $0.08798 \text{ mScm}^{-1} \text{ mM}^{-1}$ from the linear regression of κ against c ($R^2 = 0.996$ for $0 < c < 1 \text{ M NaCl}$) [29]. The resistive property of the IEMs is described by the area specific resistance, ASR; dividing ASR by A yields the membrane resistance (i.e., larger membrane areas contribute less resistance to the stack).

The four terms on the right denote the contribution to resistance from AEM, CEM, HC solution compartment, and LC solution compartment, respectively, as indicated by the subscripts. For RED salinity batteries with a large number of repeating membrane pairs, the contribution of the resistance of the end electrodes and redox couple compartment to one RED cell is relatively small due to normalization by N and, thus, can be neglected [8]. The resistance of the elements is assumed to be ohmic [6, 28]. A past study reports that membrane resistance is detrimentally elevated in very dilute solutions ($< 50 \text{ mM NaCl}$) [28]. However, the final mixed solution concentration (eq 8.2) of

almost the entire range of scenarios examined here ($0 < \phi < 0.92$) is greater than 50 mM. Thus, the analysis is simplified by taking membrane resistance, ASR_{AEM} and ASR_{CEM} of eq 8.7, to be independent of the surrounding salt concentration. Additionally, concentration polarization at the boundary layer of the membrane-solution interface can detrimentally add resistance to the cell. Here, we assume adequate mixing such that the effects of concentration polarization are negligible [14, 18, 30]. The potential blocking of effective membrane area by non-conductive spacers, i.e., spacer shadow effect, is not considered. Practically, spacer shadow effects can be suppressed by using profiled membranes or very open spacers [30].

During RED, ions permeate across the membranes and c_{HC} declines while the LC solution salt concentration rises. The last two terms of eq 8.7 changes and, therefore, the area specific resistance of the cell varies as RED progresses. The ASR of the CEMs and AEMs is taken to be $3.0 \Omega\text{cm}^2$ (typical values of commercial and laboratory-fabricated IEMs reported in literature ranges between $\sim 0.7\text{-}11 \Omega\text{cm}^2$) [31, 32], while the distance between the AEM and CEM, d , is $150 \mu\text{m}$ (intermembrane distance of $\sim 60\text{-}500 \mu\text{m}$ has been investigated in previous RED studies) [6, 8, 13, 20].

The RED cell resistance over the duration of the controlled mixing process is highest at the beginning of the process due to the low initial salt concentration of the LC solution. As ions are transported into the LC solution, the compartment becomes more conductive and the overall impedance decreases correspondingly. Because the resistance of the IEMs is assumed to be constant during RED, $ASR_{AEM} + ASR_{CEM}$ gradually begin to dominate ASR_{cell} beyond a certain point when d_{LC}/Λ_{LC} becomes relatively small.

Therefore, membrane conductivity is anticipated to play an important role in RED performance.

Work Extraction with Constant-Resistance External Load. A simple electric circuit is employed to analyze the energy efficiency, where an external load of constant ohmic resistance, R_L , is connected to the RED salinity battery to perform useful work [5, 21]; the external resistor is in series with the internal cell resistance, r_{cell} . The ionic current in the RED cell is assumed to be completely converted to an electric current, I , without any losses.

Based on Ohm's law, the governing equation for current density (or equivalently, the molar ion flux multiplied by the ion valence and the Faraday constant) across the RED cell, i , is

$$i \equiv \frac{I}{A} = \frac{\xi_{emf}}{AR_L + ASR_{\text{cell}}} = \frac{\xi_{emf} - \xi_L}{ASR_{\text{cell}}} \quad (8.8)$$

where $\xi_L = R_L \xi_{emf} / (R_L + r_{\text{cell}})$ is the potential difference across the load. It is worthwhile to note that eq 8.8 takes the general form of the water flux equation in pressure retarded osmosis power generation [33, 34]. Specifically, parameters i , ASR_{cell}^{-1} , ξ_{emf} , and ξ_L are analogous to water flux, membrane water permeability, osmotic pressure difference across the PRO membrane, and the applied hydraulic pressure, respectively. As salt permeates across the membranes, the cell potential decreases according to eq 8.1 (as illustrated in Figure 8.2A) and changes in c_{HC} and c_{LC} also cause an overall reduction in r_{cell} (eq 8.7). Hence, when R_L is fixed, ξ_L varies non-linearly as RED proceeds.

The extractable work in actual RED, W , is the integral of ξ_L across the charges transported:

$$W = \int \xi_L dq = \nu R_g T \int_0^{\Delta n_s'} \frac{R_L A}{R_L A + \text{ASR}_{\text{cell}}} \ln \frac{c_{\text{HC}}}{c_{\text{LC}}} d\Delta n_s \quad (8.9)$$

Similar to the earlier integration (eq 8.4), the moles of salt permeated across the IEMs, Δn_s , can substitute for Δq . Inspection of eqs 8.5 and 8.9 reveals that the actual work is less than W_{ideal} as $R_L A / (R_L A + \text{ASR}_{\text{cell}}) < 1$. By using an external load of extremely large resistance, the fraction tends to unity and W approaches the ideal work (i.e., current is suppressed to virtually zero and the process approaches reversible thermodynamics).

Maximum Power Density in Practical RED Operation. Membrane power density, PD, defined as the power generated per unit total membrane area (i.e., both CEMs and AEMs), is a key factor in determining the economical feasibility of RED energy production with natural salinity gradients [8, 10, 14, 35]. For the one-cell RED model presented in this analysis, the instantaneous power density, PD, is

$$\text{PD} = \frac{P_L}{2A} = \frac{1}{2} \left(\frac{\xi_{emf}}{R_L A + \text{ASR}_{\text{cell}}} \right)^2 (R_L A) \quad (8.10)$$

where P_L is the useful power generated by the external load and the factor of $\frac{1}{2}$ accounts for the ion exchange membrane pair. As $P_L = I^2 R_L$ (where I is the electric current) and $\text{ASR}_{\text{cell}} = r_{\text{cell}} A$, the power density at a particular moment can be expressed as a function of the RED cell potential, ξ_{emf} , the area specific resistance of the cell, and the product of the load resistance and cell area, which is analogous to ASR. Again, as both ξ_{emf} and ASR_{cell} change during RED, the instantaneous power density has a non-linear dependence on Δn_s .

The maximum PD (or, equivalently, P_L) is obtained when the external load resistance is equal to the internal resistance. However, this would necessitate R_L to vary continuously in order to match the changing ASR_{cell} (eq 8.7) as RED proceeds. The

equivalent implementation in an actual process would require the RED stack to be divided into infinite segments. An external load having resistance specifically tailored to the local solution concentrations is connected to each segment so as to attain $R_L = ASR_{cell}/A$ at all points along the channel [20]. Such a configuration is unfeasibly complicated and, hence, a more practical approach is employed for this analysis using a single external load of constant ohmic resistance.

The net useful work divided by the entire duration of the RED process gives the average power of the load, and further normalization by the total membrane area, $2A$, yields the overall membrane power density, PD_{avg} :

$$PD_{avg} = \frac{\int_0^{\Delta q'} \xi_L d\Delta q}{2A \int_0^{\Delta q'} \frac{R_L}{\xi_L} d\Delta q} \quad (8.11)$$

where $\int \xi_L d\Delta q$ is work, W (eq 8.9). The current ($d\Delta q/dt$) during the process is ξ_L/R_L . Thus, the integral of R_L/ξ_L (inverse of current) across the charges permeated in the denominator is $\int (dt/d\Delta q)d\Delta q$ — the duration of the controlled mixing process. An inspection of eqs 8.9 and 8.11 reveals that a small load resistance will expedite the controlled mixing but produces less useful work, whereas a large R_L generates a greater W but at the expense of a longer duration (or equivalently, the residence time in a RED stack). Hence, the optimum load resistance, R_L^* , that maximizes the overall power density is obtained by solving for dPD_{avg}/dR_L equals to zero. The calculated R_L^* is then substituted into eq 8.9 to find the specific work when power density is maximized, W^* . All integrals and derivatives were analyzed numerically. In theory, RED requires infinite time for absolute completion because the rate of ion transport approaches zero as the

process nears the end (i.e., ξ_L tends to zero and $R_L/\xi_L \rightarrow \infty$). To circumvent obtaining a trivial solution for PD_{avg} , the process was terminated after 99.99% of Δn_s^f was transferred.

Energy Conversion Efficiency. The potential difference across an external load as a function of $\Delta n_s / \Delta n_s^f$, for a seawater-river water system is shown in Figure 8.2B (solid blue line). The optimal load resistance R_L^*A is $8.29 \Omega\text{cm}^2$ and $\phi = 0.5$. The work extractable with RED is represented by the area under the ξ_L curve and is obtained from eq 8.9. The energy conversion efficiency, defined as the percentage of the Gibbs free energy of mixing (or ideal work) that can be extracted in actual RED when power density is maximized ($\eta = W^*/\Delta G_{mix} \times 100\%$), can be determined using eqs 8.6 and 8.9. In this investigation, only membrane-level phenomena are considered in the determination of efficiency, while system-level inefficiencies (such as parasitic hydraulic pressure drop and overpotential at the end electrodes) [18, 22], which will further lower the overall energy conversion performance, are not incorporated.

Figure 8.3 shows the specific work (extractable energy per unit V_{LC}^0), energy efficiency, η , and overall membrane power density, PD_{avg} , as a function of the volumetric fraction of LC solution to both LC and HC solutions, ϕ . Model seawater (600 mM or 35 g/L NaCl) was employed as the HC solution and 1.5 mM or 88 mg/L NaCl was employed as the LC solution to simulate river water. The analysis assumes perfectly selective ion exchange membranes (solid blue lines) that completely exclude co-ions and water. Imperfections in membrane selectivity are discussed in a later section. The specific ideal

work (or, equivalently, the Gibbs free energy of mixing) is indicated in Figure 8.3A as the dashed black line for comparison.

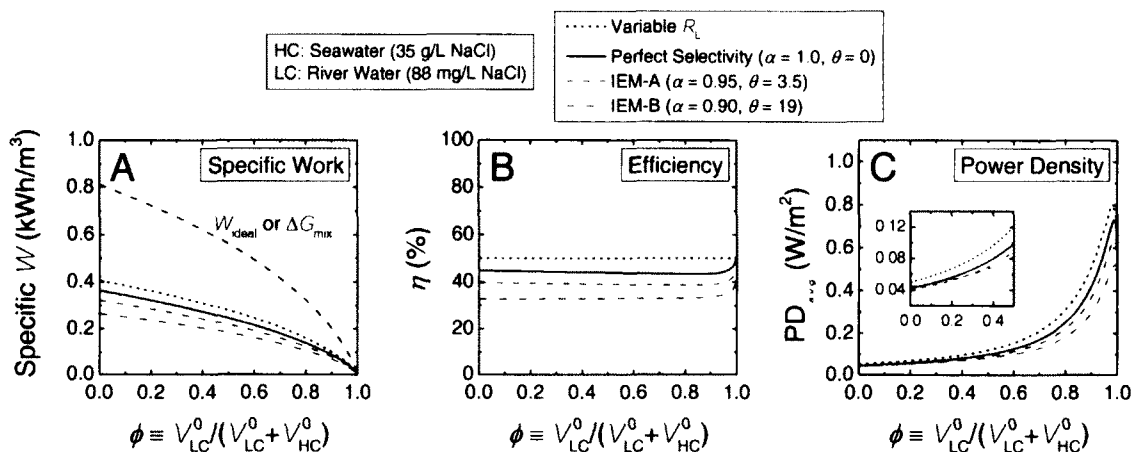


Figure 8.3. (A) Extractable work per unit volume of the LC solution, specific W^* , (B) energy conversion efficiency, η , and (C) overall membrane power density of RED energy production, PD_{avg} , as a function of ϕ . The dashed black line in (A) indicates the specific ideal work extractable in a reversible thermodynamic RED process, $W_{ideal,RED}^*$, which is equivalent to the specific Gibbs free energy of mixing, $\Delta G_{mix,RED}^*$. The solid blue lines, dashed magenta lines, and dash-dotted red lines indicate a perfectly selective membrane (i.e., $\alpha = 1$ and $\theta = 0$), IEM-A with moderately imperfect selectivity ($\alpha = 0.95$ and $\theta = 3.5$), and IEM-B with more severe selectivity imperfections ($\alpha = 0.90$ and $\theta = 19$), respectively. The dotted green lines indicate the theoretical performance achieved with perfectly selective membranes when the resistance of the external load is varied such that it always exactly matches the changing RED stack resistance (i.e., $R_L = r_{cell}$). In this hypothetical case, η is always 50% and PD is maximized. Magnified plot of (C) for $0 < \phi < 0.5$ is shown in the inset. Seawater (600 mM or 35 g/L NaCl) is employed as the HC solution, river water (1.5 mM or 88 mg/L NaCl) is used as the LC solution, and temperature $T = 298$ K. The area specific resistance, ASR, of the membranes is $3.0 \Omega\text{cm}^2$ and the intermembrane distance, d , is $150 \mu\text{m}$.

For the seawater-river water RED system with perfectly selective membranes, the amount of energy extractable per unit volume of the river water is highest at small ϕ values (specific $W^* = 0.36 \text{ kWh/m}^3$ and $\eta = 44.8\%$ when ϕ approaches zero) and W^*

diminishes to zero as ϕ increases to unity (Figure 8.3A). The dotted green lines indicate W , η , and PD_{avg} when the external load resistance varies throughout the controlled mixing process such that it exactly matches the internal resistance, to achieve the greatest possible overall power density. The resulting 50% efficiency of this hypothetical scenario (regardless of ϕ) represents the idealized η that can be achieved when PD_{avg} is maximized (Figure 8.3B).

The efficiency of RED energy conversion with constant R_L ranges between 43.3-50.7% and only changes slightly with ϕ (solid blue line in Figure 8.3B). Hence, simplifying the RED stack design by restricting the external load to a constant resistance lowers the portion of ΔG_{mix} that can be converted to useful work by up to ~7%. Similar trends were observed for RED power generation with seawater-brackish water, except with slightly better efficiency of between 47.1% and 52.2%. As discussed earlier, the batch process analyzed here also depicts a continuous flow co-current RED stack. Because greater mixing can be achieved by employing counter- or cross-current flow configurations in a membrane stack, more energy per unit volume of the low concentration river water can, therefore, be extracted [14].

Losses due to Stack Resistance. The difference between W_{ideal} and useful work is attributed to power dissipated by the internal resistance of the RED salinity battery (i.e., $I^2 r_{stack}$). During controlled mixing, ion fluxes in the RED cell are impeded by the resistance of the membranes and solution compartments. Entropy is produced when energy is expended to overcome these resistive forces. This dissipative loss (indicated in Figure 8.2B as the red pattered region) is, thus, not available for utilization by the external load to perform useful work and is analogous to the irreversible energy loss due

to entropy production in pressure retarded osmosis power generation and reverse osmosis desalination [4, 36, 37].

When RED membrane power density is maximized, slightly over half of the salinity energy is lost through internal resistance dissipation. The portion of available energy lost to entropy production (red patterned region of Figure 8.2B) is larger at the beginning of the controlled mixing process (i.e., $0 < \Delta n_s / \Delta n_s^f < 0.1$) due to mismatch of the external load resistance to r_{stack} . The energy efficiency, η , can be enhanced (e.g., >50%) by using an external load of higher resistance (eq 8.9). However, this improvement will be at the expense of a lower power density (eq 8.10), thus unfavorably raising the membrane area required [6, 14]. Detailed discussion on membrane power density performance and the relationship with η is presented in a later section.

8.4 INFLUENCE OF MEMBRANE SELECTIVITY ON ENERGY EFFICIENCY

Thus far, the analyses have assumed ideal ion exchange membranes with perfect selectivity. Specifically, the cation and anion exchange membranes completely reject co-ions and exclude water migration. In this section, we examine RED power generation for the more realistic case of imperfect membrane selectivity.

Selectivity Imperfections of Ion Exchange Membranes. Ion exchange membranes are water-swollen thin-film polymers that possess a high concentration of fixed charges (negative for CEMs and positive for AEMs) that allow the selective permeation of counter ions by Donnan exclusion of the co-ions [7, 31, 38-40]. Actual ion exchange membranes exhibit imperfections in selectivity, specifically co-ion flux across the

membranes, diffusion of water from low to high salt concentration solution due to the osmotic gradient, and electro-osmosis where water molecules are dragged along by the charged ions flux [10, 41, 42]. Here, we discuss these phenomena and evaluate the relative influence on RED energy efficiency. The cation and anion exchange membranes are assumed to have symmetrically identical selectivity.

a. Co-ion Transport. Because of Donnan exclusion, the concentration of co-ions within the charged membrane is much lower than counter ions [7, 38]. The IEMs are, therefore, preferentially selective for counter ions but still slightly permeable to co-ions. We introduce a dimensionless parameter, β , which quantifies the relative leakage of co-ions across the membranes:

$$\beta \equiv \frac{\Delta n_{s,co}}{\Delta n_{s,ct}} \quad (8.12)$$

where Δn_s denotes the moles of salt transported across the membrane, and subscripts “co” and “ct” indicates co-ions and counter ions, respectively. A perfectly selective membrane that only allows counter ion transport has β of zero, whereas $\beta = 1$ represents the transport of Na^+ and Cl^- ions in equal pairs (i.e., non-selective membrane). Membrane permselectivity, α , is related to β by [43, 44]:

$$\alpha = \frac{1 - \beta}{1 + \beta} \quad (8.13)$$

b. Osmosis. Ion exchange membranes are hydrated polymeric thin-films and, thus, are pervious to water [10, 41]. The salt concentration difference between the HC and LC solution produces an osmotic gradient across the IEMs and drives the osmosis of water. We define D^R as the ratio of water to salt (as co-ion) diffusivity:

$$D^R \equiv \frac{D_w}{D_s} = -\frac{\Delta V_{os}}{\Delta n_{s,co} \bar{V}} \quad (8.14)$$

where D_w and D_s are the effective diffusion coefficients of water and salt transported as co-ions, respectively, in the membrane matrix. For the relatively dilute solutions considered in this study, the osmotic gradient can be approximated with the salt concentration difference. Assuming co-ion and water fluxes across the IEMs are governed by Fickian diffusion [45], D^R is, thus, equal to the mole ratio of water permeated by osmosis ($\Delta V_{os}/\bar{V}$, where ΔV_{os} is the volume and \bar{V} is the molar volume of water) to salt transported as co-ions ($\Delta n_{s,co}$). Note that the negative sign indicates water osmosis is in opposite direction to salt flux. Osmosis is an uncontrolled mixing in RED and is, hence, deleterious to energy production.

c. Electro-osmosis. Charged ions permeating across a hydrated IEM exert an electrostatic field that drags along nearby polar water molecules [41, 42]. This phenomenon, termed electro-osmosis, induces a water flux in the direction of ion transport (i.e., against the osmotic gradient) and, thus, deducts from osmosis. Water migration due to electro-osmosis is proportional to the total ion flux [10, 42] by a dimensionless constant, h :

$$h = \frac{\Delta V_{eo}}{(\Delta n_{s,ct} + \Delta n_{s,co}) \bar{V}} \quad (8.15)$$

where ΔV_{eo} is the volume of water transported by electro-osmosis and $\Delta n_{s,ct} + \Delta n_{s,co}$ is the total moles of salt permeated. Unlike co-ion transport and osmosis, water migration caused by electro-osmosis is advantageous to RED power generation as it reduces the net water flux to the HC solution. In typical RED operation, the electro-osmotic flux is

lower than the osmotic flux such that there is net water transport from the LC to the HC solution [10].

Uncontrolled Mixing Decreases Extractable Work. RED extracts work from the energy of mixing through the permeation of counter ions across the Nernst potential of the ion exchange membranes. Thus, selectivity imperfections in the membrane represent uncontrolled mixing that detrimentally lowers the power output. The effect of uncontrolled mixing on extractable work and the key equations are briefly presented and discussed here.

Because of co-ion leakage and water osmosis, the fraction of salt in the initial HC solution that is transported as counter ions is lowered:

$$\frac{\Delta n_s^f}{n_{s,HC}^0} = \frac{\phi}{(1+\beta)(1+\theta\bar{V}c_M^f)} \left(1 - \frac{c_{LC}^0}{c_{HC}^0}\right) \quad (8.16)$$

where θ is the mole ratio of water to salt (both counter ions and co-ions) permeation across the IEMs. The mole ratio combines both effects of osmosis and electro-osmosis, and can be expressed as

$$\theta \equiv \frac{\Delta V}{(\Delta n_{s,ct} + \Delta n_{s,co})\bar{V}} = \frac{\beta}{1+\beta} D^R - h \quad (8.17)$$

where ΔV is the net volumetric water transport across the membranes (i.e., difference between osmotic flux and electro-osmotic flux). Note that, henceforth, Δn_s denotes the moles of salt transported as counter ions. Setting β and θ to zero in eq 8.16 recovers eq 8.3, the fraction of salt eventually transported for perfectly selective membranes.

The imperfect selectivity of the IEMs for counter ions diminishes the effective electromotive force across the one-cell RED by the membrane permselectivity factor, α

(eq 8.1). Additionally, the undesirable leakage of co-ions negates an equal charge of counter ions permeating across the CEM and AEM (Figure 8.1B), thereby lowering the net ion flux. Factoring in these deleterious effects, an external load of infinitely large resistance was employed such that ξ_L approaches ξ_{emf} and the maximum specific work (with infinitesimal ion flux and power density) was determined:

$$\begin{aligned}
 W_{\text{imp}, \nu_{\text{LC}}^0} &= zF \int_0^{\Delta n_s^f} \xi_{emf} d(1-\beta) \Delta n_s \\
 &= \alpha^2 \left\{ \Delta G_{\text{mix}, \nu_{\text{LC}}^0} - \frac{\nu R_g T}{\theta V} \left[\begin{aligned} &\frac{1-\phi}{\phi} (1+\theta \bar{V}_{\text{HC}}^0) \ln(1+\theta \bar{V}_{\text{HC}}^0) \\ &+ (1+\theta \bar{V}_{\text{LC}}^0) \ln(1+\theta \bar{V}_{\text{LC}}^0) \\ &- \frac{1}{\phi} (1+\theta \bar{V}_{\text{M}}^f) \ln(1+\theta \bar{V}_{\text{M}}^f) \end{aligned} \right] \right\} \quad (8.18)
 \end{aligned}$$

where $W_{\text{imp}, \nu_{\text{LC}}^0}$ is energy extractable in RED with imperfectly selective IEMs, per unit volume of the initial LC solution. Note that ξ_{emf} is integrated from zero to Δn_s^f (eq 8.16) that has been lowered by co-ion leakage and water transport.

It is worthwhile to note that although RED proceeded with an infinitesimal ionic/electric current in this case, it is not a reversible thermodynamic process because entropy is produced in the uncontrolled mixing of co-ion transport and water osmosis between the HC and LC solution. As $\alpha \rightarrow 1$ (i.e., β tends to zero) and $\theta \rightarrow 0$, the membranes approach perfect selectivity and the specific work (eq 8.18) reduces to the Gibbs free energy of mixing, or $W_{\text{ideal}, \nu_{\text{LC}}^0}$ (eq 8.6). Conversely, if the ion exchange membranes are completely unselective for counter ions ($\beta = 1$ and, thus, $\alpha = 0$), the net charge transfer is zero because the ions permeate across as cation-anion pairs and no work is produced.

The maximum specific work was analyzed in a seawater-river water RED salinity battery with IEM properties simulating actual commercial and laboratory-fabricated membranes [10, 31, 32]. The permselectivity, α , is 0.9 (i.e., $\beta = 0.053$) and $\theta = 19$ ($D^R = 500$ and $h = 6$). Typical α values are ~ 0.79 - 0.99 [10, 31, 32], while D^R and h ranges between 100-725 and 4.6-12, respectively [10]. To illustrate the relative migration of species, when 1 L of 600 mM NaCl HC solution and 1 L of 1.5 mM NaCl LC solution are employed in the one-cell RED depicted in Figure 8.1B, ~ 260 mmol of salt permeates the membranes as counter ions, ~ 14 mmol of NaCl diffuses across as co-ions, and ~ 93 mL of water move from the LC solution to the HC solution (i.e., osmosis minus electro-osmosis) over the entire process.

Figure 8.4 shows $W_{\text{imp}, V_{\text{LC}}^0}$ and the percentage of ΔG_{mix} lost in energy extraction, as a function of the volumetric fraction of the LC solution, ϕ , for the IEMs described above (solid red lines). The individual effect of co-ion leakage and water osmosis (indicated by dash-dotted green lines and dotted blue lines, respectively) can be further separated out by respectively setting θ to zero or $\alpha = 1$ in eq 8.18. The ideal work (or, equivalently, ΔG_{mix}) is plotted in Figure 8.4A for comparison. For the simulated imperfect selectivity membranes, co-ion leakage in RED caused a 19% decline in extractable energy, while net water permeation into the HC solution resulted in ~ 2 - 9% decrease (Figure 8.4B). This result indicates that, for the currently available ion exchange membranes, co-ion leakage has a greater impact on RED performance than water transport. The combined effects of selectivity imperfections detrimentally lowered the extractable energy by ~ 21 - 26% , with a greater loss experienced at smaller ϕ values. Co-ion and water osmosis is akin to

uncontrolled mixing of the HC and LC solutions, thus a portion of ΔG_{mix} is lost to entropy production and the process is rendered thermodynamically irreversible.

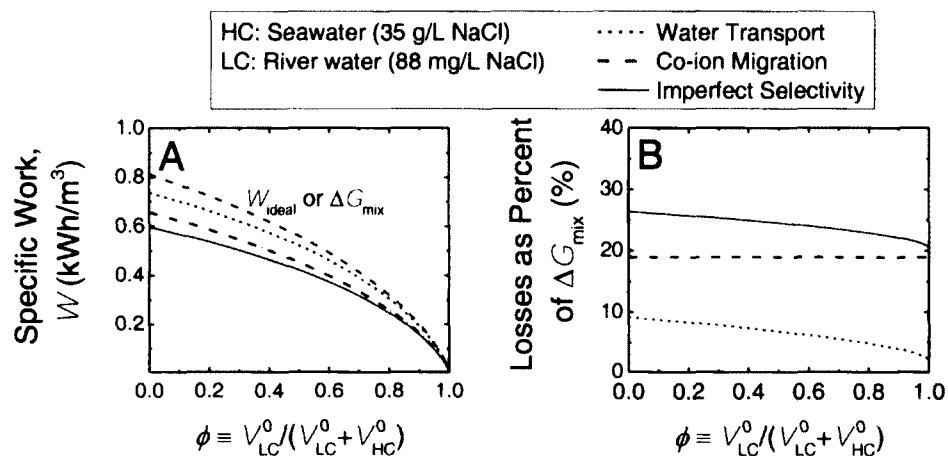


Figure 8.4. (A) Extractable work per unit volume of the LC solution, W , as a function of ϕ , where the potential difference across the external load is always exactly equal to ξ_{emf} . The dashed black line indicates $W_{\text{ideal,LC}}^0$ or $\Delta G_{\text{mix,LC}}^0$ for perfectly selective ion exchange membranes. The dotted blue line and dash-dotted green line denote W for imperfect membrane selectivity where osmosis of water ($\theta = 19$) and transport of co-ions ($\alpha = 0.9$) occurs, respectively. The specific work for non-ideal ion exchange membranes having both selectivity imperfections (i.e., $\alpha = 0.9$ and $\theta = 19$) are indicate by the solid red line. (B) The percentage of Gibbs free energy of mixing (or ideal work) that is not extractable due to selectivity imperfections in the CEM and AEM, as a function of ϕ . Lines represent the same imperfections as in (A). The temperature $T = 298$ K, the HC solution is seawater (600 mM or 35 g/L NaCl), the LC solution is river water (1.5 mM or 88 mg/L NaCl).

Imperfect Selectivity Reduces RED Power Generation Efficiency. Salinity battery performance when PD_{avg} is maximized was analyzed for two different extent of selectivity imperfection to simulate actual membranes: ion exchange membranes B (designated IEM-B) were examined earlier and presented in Figure 8.4 ($\alpha = 0.9$ and $\theta = 19$), while IEM-A represents more selective membranes with permselectivity α of 0.95 and θ of 3.5 (i.e., $\beta = 0.026$, $D^R = 300$, and $h = 4$) [10, 31, 32]. The specific work, energy

efficiency η , and overall power density as a function of ϕ are shown in Figure 8.3 for a seawater-river water system. Dashed magenta lines and dash-dotted red lines indicate membranes A and B, respectively.

Leakage of co-ions and osmosis of water across the simulated CEMs and AEMs deleteriously reduce the fraction of Gibbs free energy of mixing that can be converted to useful work with RED. Perfectly selective membranes have η of 43.3-50.7% (solid blue line), while the efficiencies of membranes A and B range between 38.7-45.6% and 32.7-40.4%, respectively, with slightly higher η achieved at larger ϕ values (Figure 8.3B). As expected, a lower selectivity (i.e., IEM-B) has a greater negative impact on RED energy production with natural salinity gradients. Therefore, imperfections in the selectivity of technologically-available membranes cause ~5-10% (absolute) of ΔG_{mix} to be lost to entropy production. Similar trends were observed when brackish water (17 mM or 1g/L NaCl) was used as the LC solution.

8.5 POWER DENSITY ANALYSIS

Membrane power density, the power generated per unit total membrane area, is critical in determining the cost-effectiveness of RED energy production with natural salinity gradients [8, 10, 14, 35]. For instance, doubling PD_{avg} would halve the membrane area requirement in a salinity battery installation and, thus, lower the capital cost. In this section, we analyze the potential membrane power density of RED salinity batteries and examine the influencing factors.

Power Density of Perfect and Imperfect Membrane Selectivity. Figures 8.3C and S8.5C show PD_{avg} for a seawater HC solution paired with river water and brackish water,

respectively, as a function of the volumetric fraction of the LC solution, ϕ . Solid blue lines indicate perfectly selective CEM and AEM, while imperfect selectivity IEM-A and IEM-B are represented by dashed magenta lines and dash-dotted red lines, respectively. Note that although only one RED cell is considered in this analysis, power density is normalized by the membrane area and, hence, the PD_{avg} values obtained are representative of a module-scale RED salinity battery with multiple membrane-pair stacks.

For the seawater-river water system with IEM-A (dashed magenta line in Figure 8.3C), PD_{avg} is lowest (0.04 W/m^2) when $\phi \rightarrow 0$ and slowly increases with ϕ before rapidly rising to a peak of 0.65 W/m^2 when ϕ is ~ 0.99 . The overall membrane power density is below 0.50 W/m^2 over a wide range of ϕ values (from 0 to ~ 0.94). As expected, PD_{avg} of the perfectly selective membranes is slightly larger (solid blue line). Less selective IEM-B has lower PD_{avg} compared to IEM-A. The power density achievable with perfectly selective membranes and a variable resistance external load, denoted by the dotted green line, signifies the maximum PD_{avg} that can be attained. The power density of this hypothetical scenario is slightly higher than the three actual scenarios with constant R_L , but otherwise displayed similar trends. When brackish water is employed as the LC solution, PD_{avg} exhibited similar behavior over ϕ , albeit at slightly lower magnitude.

Relatively higher membrane power density can be achieved by operating RED at very large ϕ values (i.e., pairing a large LC solution volume with a small amount of HC solution). For instance, in the seawater-river water system (Figure 8.3C), peak PD_{avg} of 0.65 and 0.54 W/m^2 is attained for IEM-A and IEM-B, respectively, when ϕ is ~ 0.99 (i.e.,

pairing one volume of seawater HC solution with 99 volumes of river water LC solution). The comparatively greater power density is attributed to a larger ξ_{emf} being maintained over the RED duration. However, when $\phi = 0.99$, the amount of useful work produced per unit LC solution volume, specific W^* , is 0.014 and 0.012 kWh/m³ with ion exchange membranes A and B, respectively — relatively minute compared to the specific W^* attainable at smaller ϕ values (Figures 8.3A). In power generation from natural salinity gradients, often seawater from the ocean is abundant while fresh water from estuaries is the limiting resource. As such, obtaining the most out of the available energy from the finite river water input is anticipated to be a vital performance goal. Therefore, operating RED at very large ϕ is unlikely to be feasible despite the potential for higher power density. Hereafter, the analysis will focus on performance with $\phi = 0.5$, i.e., equal volumes of HC and LC solution.

Enhancing Power Density by Energy Efficiency Tradeoff. An inspection of eqs 8.1 and 8.8 reveals that the ion flux across the IEMs rapidly diminishes towards the end of RED (i.e., $\Delta n^s \rightarrow \Delta n_s^f$). The retarding rate of ion transport unfavorably draws out the process duration and detrimentally reduces PD_{avg} (eq 8.11). Recall that, to avoid obtaining a trivial solution when numerically determining PD_{avg} , 99.99% Δn_s^f transfer was taken as the process conclusion. The protraction effect is especially evident where PD initially rises and then precipitously dwindles to a minutely low, but non-zero, level for an extended period. Useful work is still being produced by the external load, but the amount is negligibly small. Therefore, energy extraction efficiency and power density of RED fades drastically as the process approaches its finish.

Overall membrane power density performance can, hence, be improved by judiciously discontinuing the process earlier when RED is no longer adequately effective. The remaining salinity energy embedded in the unmixed HC and LC solutions is, thus, not converted to useful work by the external load. The tradeoff can be overall advantageous if the benefit from PD_{avg} enhancement outweighs the sacrifice in work extraction. Figure 8.5A shows PD_{avg} (red patterned columns, left vertical axis) and η (blue symbols, right vertical axis) after 99.99, 90, 80, 70, 60, and 50% of Δn_s^f has permeated across the membranes for $\phi = 0.5$. Model seawater and river water were employed as the HC and LC solutions, respectively, and moderately selective IEM-A ($\alpha = 0.95$ and $\theta = 3.5$) was used.

When 90% and 80% of Δn_s^f has permeated (or, alternatively, 90% and 80% of the charges are utilized), η is 39.6% and 39.0%, respectively, similar to the efficiency of 39.1% with 99.99% Δn_s^f permeation (Figure 8.5A). On the other hand, overall power density increases dramatically by 4.6 and 6.5 times to 0.42 and 0.59 W/m², respectively (compared with power density of 0.09 W/m² for 99.99% charge utilization). Hence, by forgoing the last 10-20% of Δn_s , PD_{avg} performance is substantially enhanced without significantly affecting η . When the process is ceased even earlier (i.e., 70, 60, and 50% charge utilization), η is 37.8, 35.8, and 33.2% and PD_{avg} is 0.77, 0.96, and 1.16 W/m², respectively, for $\phi = 0.5$ (Figure 8.5A). Although power density is considerably improved, the corresponding reduction in efficiency becomes noticeably substantial. Further reducing the charge utilization to 40% and 30% yields even higher power density. However, the energy efficiency is concomitantly lowered to diminished levels that could

potentially render the RED power generation process unviable. Similar trends are observed, albeit with slightly lower power densities, when brackish water is employed as the LC solution and for less selective IEM-B (results not shown).

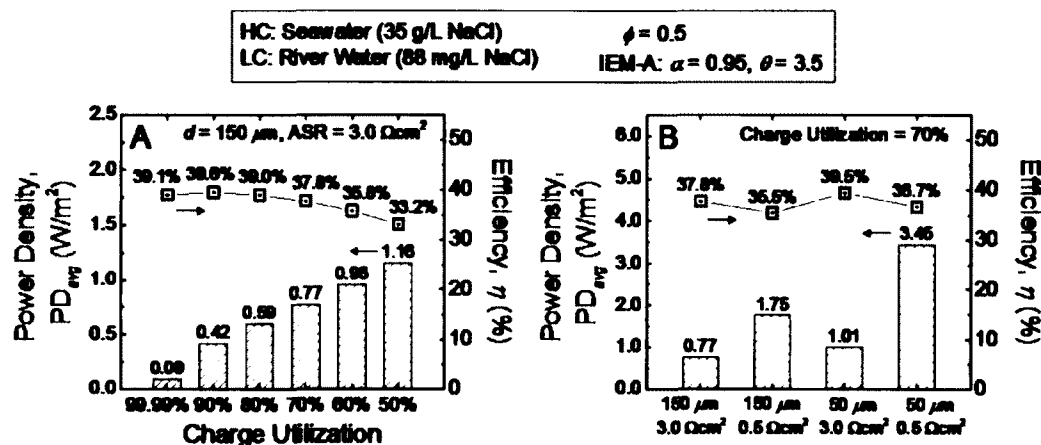


Figure 8.5. Overall membrane power density, PD_{avg} (left vertical axis), and energy conversion efficiency, η (right vertical axis), for seawater-river water RED power generation with $\phi = 0.5$. (A) The controlled mixing process is terminated prematurely, thereby utilizing only the earlier transported charges for power generation and discarding the remainder. A range of charge utilization percentages (99.99, 90, 80, 70, 60, and 50%) are evaluated. For this analysis, the intermembrane distance, d , is $150 \mu\text{m}$ and the ion exchange membrane area specific resistance, ASR, is $3.0 \Omega\text{cm}^2$. (B) Different intermembrane distance ($d = 50$ or $150 \mu\text{m}$) and membrane area specific resistance (ASR = 0.5 or $3.0 \Omega\text{cm}^2$) are employed to examine the effect on RED performance. The charge utilization is 70% for the four scenarios. In both plots, the ion exchange membranes have moderately imperfect selectivity (i.e., IEM-A with $\alpha = 0.95$ and $\theta = 3.5$). Equal volumes of seawater (600 mM or 35 g/L NaCl) and river water (1.5 mM or 88 mg/L NaCl) is used (i.e., $\phi = 0.5$), and temperature $T = 298 \text{ K}$.

Influence of Intermembrane Distance and Membrane Resistance on Power Density. The above analysis indicates that, with IEM area specific resistance of $3 \Omega\text{cm}^2$ and intermembrane distance of $150 \mu\text{m}$, the low overall membrane power density will pose a significant barrier to the cost-effective implementation of RED power generation with natural salinity gradients. An inspection of eq 8.10 indicates that reducing the

internal resistance of the repeating RED cells can improve PD_{avg} . Specifically, the CEMs and AEMs need to be more conductive and the intermembrane spacing reduced (eq 8.7). Efficiency, η , and PD_{avg} were analyzed for an additional three hypothetical scenarios: (i) the area specific resistance of the IEMs is lowered to $0.5 \Omega\text{cm}^2$, (ii) the intermembrane distance, d , is reduced to $50 \mu\text{m}$, and (iii) combining both $ASR = 0.5 \Omega\text{cm}^2$ and $d = 50 \mu\text{m}$. The results are compared to the earlier analysis where membrane $ASR = 3.0 \Omega\text{cm}^2$ and $d = 150 \mu\text{m}$, and presented in Figure 8.5B. Moderate selectivity ion exchange membranes were employed (i.e., IEM-A with $\alpha = 0.95$ and $\theta = 3.5$) and the process was discontinued after 70% of $\Delta\eta_s^f$ has permeated. Seawater was used as the HC solution, the LC solution is river water, and $\phi = 0.5$.

To simulate highly conductive CEMs and AEMs, an area specific resistance of $0.5 \Omega\text{cm}^2$ was selected (approximately the lowest reported ASR by membrane manufacturers) [31]. When membrane resistance is decreased from $3.0 \Omega\text{cm}^2$ to $0.5 \Omega\text{cm}^2$, power density was substantially enhanced 2.3 fold, from 0.77 to 1.75 W/m^2 (red patterned columns in Figure 8.5B), underscoring the importance of membrane conductivity in PD performance. The IEMs dominate the RED cell resistance for most part of the process. Employing more conductive membranes, thus, significantly reduces ASR_{cell} and enables faster ionic transport to produce greater power densities. Comparing η (blue symbols in Figure 8.5B), the more conductive membranes are slightly less efficient in extracting salinity energy (η is 35.5% and 37.8% when membrane ASR is 0.5 and $3.0 \Omega\text{cm}^2$, respectively).

The resistance of the solution compartments is directly proportional to the intermembrane distance ($ASR = d/\kappa$). Therefore, reducing the CEM-AEM spacing from

150 μm to 50 μm (approximately the lowest experimentally investigated distance) [13] trims the area specific resistance of the LC compartment, a major contributor to RED stack resistance, down by two-thirds. Compared to the case when $d = 150 \mu\text{m}$, the reduced intermembrane distance moderately enhances PD_{avg} by 1.3 times of 0.77 W/m^2 (red patterned columns in Figure 8.5B). The narrower solution compartment width suppresses ASR_{cell} and facilitates faster ion permeation across the RED cell, resulting in higher power density performance. Recall that the LC solution dominates ASR_{cell} initially and cause dissipative losses to be most pronounced at the start of the controlled mixing (Figure 8.2B). The lower d allowed better matching of constant load resistance to the early ASR_{cell} and, thereby, increase the energy extraction efficiency (blue symbols). At $\phi = 0.5$ in a seawater-river water system with 70% charge utilization, PD_{avg} is 1.01 W/m^2 and η is 39.5%.

Simultaneously decreasing IEM area specific resistance and intermembrane distance (to $0.5 \Omega\text{cm}^2$ and $50 \mu\text{m}$, respectively) enhances power density considerably by 4.5 times (red patterned columns in Figure 8.5B). Compared to the initial analysis (i.e., $3.0 \Omega\text{cm}^2$ and $150 \mu\text{m}$), the energy conversion efficiency is marginally lower (blue symbols). At $\phi = 0.5$ with 70% charge utilization, $PD_{avg} = 3.45 \text{ W/m}^2$ and $\eta = 36.7\%$ with the smaller membrane ASR and d . On the other hand, with membrane ASR of $3.0 \Omega\text{cm}^2$ and $d = 150 \mu\text{m}$, the power density and efficiency are 0.77 W/m^2 and $\eta = 37.8\%$, respectively. Note that the power density benefit acquired from the simultaneous enhancement in membrane conductivity and reduction in channel thickness is greater than the cumulative sum of each individual improvement ($4.5 > 2.3 \times 1.3$). This suggests that greater gains can be obtained by concurrently targeting the membrane and module design.

8.6 IMPLICATIONS FOR NATURAL SALINITY GRADIENT

POWER GENERATION

Energy efficiency and membrane power density will both be critical performance objectives that affect the feasibility of RED power generation with natural salinity gradients. The analysis presented in this study shows an upper bound on both the highest actual efficiency attainable and the corresponding membrane power density achievable. Additionally, the two performance parameters are inextricably linked: enhancing the power density will inevitably necessitate a sacrifice in efficiency and vice-versa. Furthermore, obtaining the most energy per unit volume of fresh water, likely to be the limiting resource, will also be a key performance target. This, together with the practical need for pretreatment of the feed streams to mitigate membrane fouling [46, 47], is anticipated to constrain the fresh water-seawater mixing proportions that can feasibly be implemented. Actual RED power generation will need to work within such practical limitation and, at the same time, balance the intricate relationships between specific work, energy conversion efficiency, and power density when fine-tuning the operating parameters to optimize the overall cost-effectiveness of the technology.

At the heart of the RED salinity battery are ion exchange membranes. Improving permselectivity and minimizing water osmosis across the membranes can curb undesired entropy production from uncontrolled mixing. The analysis here indicates that co-ion transport has a greater detrimental impact on RED power generation performance than water leakage. Feasibility studies indicate that advancement of the technology hinges on attaining higher power densities than currently available membranes [35, 48]. Our study quantitatively demonstrates that there is huge potential for power density enhancement by

developing more conductive membranes. However, recent investigations also suggest that a tradeoff relationship between ionic conductance and permselectivity exists for ion exchange membranes, where higher permselectivity is inevitably accompanied by lower membrane conductance [31, 49]. Likewise, reducing membrane resistance by fabricating thinner membranes is accompanied by greater co-ion transport and water permeation [32]. Employing novel materials or casting techniques in membrane fabrication can potentially advance CEMs and AEMs beyond the existing tradeoff relationship and improve RED performance. However, given membranes is a major component of the initial capital outlay and the current high cost of membranes [48], there is most room for improving the cost-effectiveness of the technology by developing more affordable ion exchange membranes while retaining performance.

Reducing the intermembrane distance of the RED cells lowers the stack internal resistance but poses significant engineering challenges from the concomitant increase in the parasitic pressure drop along the channel [18]. More energy is needed to push fluids through the narrower channel and, hence, the pumping cost is detrimentally raised. For a laminar flow in a rectangular channel, the pressure drop is inversely proportional to the cube of the channel height [50]. Thus, lowering the intermembrane spacing by a third, e.g., from 150 to 50 μm , will increase the head loss by a massive 27 times. Additionally, to maintain such a tiny gap between the CEMs and AEMs, channel spacers will be necessary [13]. However, such spacers further hinder flow and exacerbate the pressure drop along the channel. A previous study indicates that operating RED at a small intermembrane distance of 60 μm with spacers will negatively impact power generation because the large pumping energy consumed overwhelms the power density benefits [13].

Inventive solutions, such as profiled membranes, ion conductive spacers, and innovative channel design [20, 51, 52], are needed to overcome the resistance and hydrodynamic constraints, in order to realize RED power generation with natural salinity gradients.

8.7 REFERENCES

- [1] Chu, S. Majumdar, A., Opportunities and challenges for a sustainable energy future. *Nature* **2012**, *488* (7411), 294-303.
- [2] Pattle, R. E., Production of Electric Power by Mixing Fresh and Salt Water in the Hydroelectric Pile. *Nature* **1954**, *174* (4431), 660-660.
- [3] Logan, B. E. Elimelech, M., Membrane-based processes for sustainable power generation using water. *Nature* **2012**, *488* (7411), 313-319.
- [4] Yip, N. Y. Elimelech, M., Thermodynamic and Energy Efficiency Analysis of Power Generation from Natural Salinity Gradients by Pressure Retarded Osmosis. *Environmental Science & Technology* **2012**, *46* (9), 5230-5239.
- [5] Weinstein, J. N. Leitz, F. B., Electric-Power from Difference in Salinity - Dialytic Battery. *Science* **1976**, *191* (4227), 557-559.
- [6] Post, J. W.; Hamelers, H. V. M. Buisman, C. J. N., Energy recovery from controlled mixing salt and fresh water with a reverse electro dialysis system. *Environmental Science & Technology* **2008**, *42* (15), 5785-5790.
- [7] Baker, R. W., Membrane technology and applications. 3rd ed.; John Wiley & Sons, Chichester, West Sussex ; Hoboken, **2012**; p xiv, 575 p.
- [8] Dlugolecki, P.; Gambier, A.; Nijmeijer, K. Wessling, M., Practical Potential of Reverse Electro dialysis As Process for Sustainable Energy Generation. *Environmental Science & Technology* **2009**, *43* (17), 6888-6894.
- [9] Turek, M. Bandura, B., Renewable energy by reverse electro dialysis. *Desalination* **2007**, *205* (1-3), 67-74.
- [10] Veerman, J.; de Jong, R. M.; Saakes, M.; Metz, S. J. Harmsen, G. J., Reverse electro dialysis: Comparison of six commercial membrane pairs on the thermodynamic efficiency and power density. *Journal of Membrane Science* **2009**, *343* (1-2), 7-15.
- [11] Veerman, J.; Saakes, M.; Metz, S. J. Harmsen, G. J., Reverse electro dialysis: Performance of a stack with 50 cells on the mixing of sea and river water. *Journal of Membrane Science* **2009**, *327* (1-2), 136-144.
- [12] Veerman, J.; Saakes, M.; Metz, S. J. Harmsen, G. J., Electrical Power from Sea and River Water by Reverse Electro dialysis: A First Step from the Laboratory to a Real Power Plant. *Environmental Science & Technology* **2010**, *44* (23), 9207-9212.
- [13] Vermaas, D. A.; Saakes, M. Nijmeijer, K., Doubled Power Density from Salinity Gradients at Reduced Intermembrane Distance. *Environmental Science & Technology* **2011**, *45* (16), 7089-7095.
- [14] Vermaas, D. A.; Veerman, J.; Yip, N. Y.; Elimelech, M.; Saakes, M. Nijmeijer, K., High Efficiency in Energy Generation from Salinity Gradients with Reverse Electro dialysis. *ACS Sustainable Chemistry & Engineering* **2013**, *1* (10), 1295-1302.
- [15] Feinberg, B. J.; Ramon, G. Z. Hoek, E. M. V., Thermodynamic Analysis of Osmotic Energy Recovery at a Reverse Osmosis Desalination Plant. *Environmental Science & Technology* **2013**, *47* (6), 2982-2989.

- [16] Daniilidis, A.; Vermaas, D. A.; Herber, R. Nijmeijer, K., Experimentally obtainable energy from mixing river water, seawater or brines with reverse electro dialysis. *Renewable Energy* **2014**, *64*, 123-131.
- [17] Brauns, E., Salinity gradient power by reverse electro dialysis: effect of model parameters on electrical power output. *Desalination* **2009**, *237* (1-3), 378-391.
- [18] Vermaas, D. A.; Guler, E.; Saakes, M. Nijmeijer, K., Theoretical power density from salinity gradients using reverse electro dialysis. *Technoport 2012 - Sharing Possibilities and 2nd Renewable Energy Research Conference (RERC 2012)* **2012**, *20*, 170-184.
- [19] Tedesco, M.; Cipollina, A.; Tamburini, A.; van Baak, W. Micale, G., Modelling the Reverse Electro Dialysis process with seawater and concentrated brines. *Desalination and Water Treatment* **2012**, *49* (1-3), 404-424.
- [20] Veerman, J.; Saakes, M.; Metz, S. J. Harmsen, G. J., Reverse electro dialysis: A validated process model for design and optimization. *Chemical Engineering Journal* **2011**, *166* (1), 256-268.
- [21] Veerman, J.; Post, J. W.; Saakes, M.; Metz, S. J. Harmsen, G. J., Reducing power losses caused by ionic shortcut currents in reverse electro dialysis stacks by a validated model. *Journal of Membrane Science* **2008**, *310* (1-2), 418-430.
- [22] Veerman, J.; Saakes, M.; Metz, S. J. Harmsen, G. J., Reverse electro dialysis: evaluation of suitable electrode systems. *Journal of Applied Electrochemistry* **2010**, *40* (8), 1461-1474.
- [23] Burheim, O. S.; Seland, F.; Pharoah, J. G. Kjelstrup, S., Improved electrode systems for reverse electro-dialysis and electro-dialysis. *Desalination* **2012**, *285*, 147-152.
- [24] Scialdone, O.; Guarisco, C.; Grispo, S.; Angelo, A. D. Galia, A., Investigation of electrode material – Redox couple systems for reverse electro dialysis processes. Part I: Iron redox couples. *Journal of Electroanalytical Chemistry* **2012**, *681*, 66-75.
- [25] Vermaas, D. A.; Veerman, J.; Saakes, M. Nijmeijer, K., Influence of multivalent ions on renewable energy generation in reverse electro dialysis. *Energy & Environmental Science* **2014**, *7* (4), 1434-1445.
- [26] Smith, J. M.; Van Ness, H. C. Abbott, M. M., Introduction to chemical engineering thermodynamics. 7th ed.; McGraw-Hill, Boston, **2005**; p xviii, 817 p.
- [27] Sandler, S. I., Chemical and engineering thermodynamics. 3rd ed.; Wiley, New York, **1999**; p xx, 772 p.
- [28] Długolecki, P.; Anet, B.; Metz, S. J.; Nijmeijer, K. Wessling, M., Transport limitations in ion exchange membranes at low salt concentrations. *Journal of Membrane Science* **2010**, *346* (1), 163-171.
- [29] Robinson, R. A. Stokes, R. H., Electrolyte solutions; the measurement and interpretation of conductance, chemical potential, and diffusion in solutions of simple electrolytes. 2d ed.; Butterworths, London,, **1959**; p xv, 571 p.
- [30] Vermaas, D. A.; Saakes, M. Nijmeijer, K., Enhanced mixing in the diffusive boundary layer for energy generation in reverse electro dialysis. *Journal of Membrane Science* **2014**, *453*, 312-319.
- [31] Długolecki, P.; Nijmeijer, K.; Metz, S. Wessling, M., Current status of ion exchange membranes for power generation from salinity gradients. *Journal of Membrane Science* **2008**, *319* (1-2), 214-222.
- [32] Güler, E.; Elizen, R.; Vermaas, D. A.; Saakes, M. Nijmeijer, K., Performance-determining membrane properties in reverse electro dialysis. *Journal of Membrane Science* **2013**, *446*, 266-276.

- [33] Lee, K. L.; Baker, R. W. Lonsdale, H. K., Membranes for Power-Generation by Pressure-Retarded Osmosis. *Journal of Membrane Science* **1981**, *8* (2), 141-171.
- [34] Yip, N. Y.; Tiraferri, A.; Phillip, W. A.; Schiffman, J. D.; Hoover, L. A.; Kim, Y. C. Elimelech, M., Thin-Film Composite Pressure Retarded Osmosis Membranes for Sustainable Power Generation from Salinity Gradients. *Environmental Science & Technology* **2011**, *45* (10), 4360-4369.
- [35] Post, J. W.; Goeting, C. H.; Valk, J.; Goinga, S.; Veerman, J.; Hamelers, H. V. M. Hack, P. J. F. M., Towards implementation of reverse electrodialysis for power generation from salinity gradients. *Desalination and Water Treatment* **2010**, *16* (1-3), 182-193.
- [36] Elimelech, M. Phillip, W. A., The Future of Seawater Desalination: Energy, Technology, and the Environment. *Science* **2011**, *333* (6043), 712-717.
- [37] Liu, C.; Rainwater, K. Song, L. F., Energy analysis and efficiency assessment of reverse osmosis desalination process. *Desalination* **2011**, *276* (1-3), 352-358.
- [38] Mulder, M., Basic principles of membrane technology. 2nd ed.; Kluwer Academic, Dordrecht ; Boston, **1996**; p 564 p.
- [39] Geise, G. M.; Falcon, L. P.; Freeman, B. D. Paul, D. R., Sodium chloride sorption in sulfonated polymers for membrane applications. *Journal of Membrane Science* **2012**, *423-424*, 195-208.
- [40] Galama, A. H.; Post, J. W.; Cohen Stuart, M. A. Biesheuvel, P. M., Validity of the Boltzmann equation to describe Donnan equilibrium at the membrane-solution interface. *Journal of Membrane Science* **2013**, *442*, 131-139.
- [41] Belfort, G., Synthetic membrane processes : fundamentals and water applications. Academic Press, Orlando, Fla., **1984**; p xiii, 552 p.
- [42] Spiegler, K. S., Transport processes in ionic membranes. *Transactions of the Faraday Society* **1958**, *54*, 1408-1428.
- [43] Lakshminarayanaiah, N., Transport Phenomena in Artificial Membranes. *Chemical Reviews* **1965**, *65* (5), 491-565.
- [44] Strathmann, H., Ion-exchange membrane separation processes. 1st ed.; Elsevier, Amsterdam ; Boston, **2004**; p xi, 348 p.
- [45] Mackie, J. S. Meares, P., The Diffusion of Electrolytes in a Cation-Exchange Resin Membrane. I. Theoretical. *Proceedings of the Royal Society of London. Series A. Mathematical and Physical Sciences* **1955**, *232* (1191), 498-509.
- [46] Vermaas, D. A.; Kunteng, D.; Saakes, M. Nijmeijer, K., Fouling in reverse electrodialysis under natural conditions. *Water Research* **2013**, *47* (3), 1289-1298.
- [47] Vermaas, D. A.; Kunteng, D.; Veerman, J.; Saakes, M. Nijmeijer, K., Periodic Feedwater Reversal and Air Sparging As Antifouling Strategies in Reverse Electrodialysis. *Environmental Science & Technology* **2014**, *48* (5), 3065-3073.
- [48] Daniilidis, A.; Herber, R. Vermaas, D. A., Upscale potential and financial feasibility of a reverse electrodialysis power plant. *Applied Energy* **2014**, *119*, 257-265.
- [49] Geise, G. M.; Hickner, M. A. Logan, B. E., Ionic Resistance and Permselectivity Tradeoffs in Anion Exchange Membranes. *ACS Applied Materials & Interfaces* **2013**.

[50] Bird, R. B.; Stewart, W. E. Lightfoot, E. N., Transport phenomena. 2nd, Wiley international ed.; J. Wiley, New York, 2002; p xii, 895 p.

[51] Vermaas, D. A.; Saakes, M. Nijmeijer, K., Power generation using profiled membranes in reverse electro dialysis. *Journal of Membrane Science* 2011, 385 (1-2), 234-242.

[52] Długołęcki, P.; Dąbrowska, J.; Nijmeijer, K. Wessling, M., Ion conductive spacers for increased power generation in reverse electro dialysis. *Journal of Membrane Science* 2010, 347 (1-2), 101-107.

Chapter 9:

Comparison of Energy Efficiency and Power Density in Pressure Retarded Osmosis and Reverse Electrodialysis

CHAPTER ABSTRACT

Pressure retarded osmosis (PRO) and reverse electrodialysis (RED) are emerging membrane-based technologies that can convert chemical energy in salinity gradients to useful work. The two processes have intrinsically different working principles: controlled mixing in PRO is achieved by water permeation across salt-rejecting membranes, whereas RED is driven by ion flux across charged membranes. This study compares the energy efficiency and power density performance of PRO and RED with simulated technologically-available membranes for natural, anthropogenic, and engineered salinity gradients (seawater–river water, desalination brine–wastewater, and synthetic hypersaline solutions, respectively). The analysis shows that PRO can achieve both greater efficiencies (54–56%) and higher power densities (2.4–38 W/m²) than RED (18–38% and 0.77–1.2 W/m²). The superior efficiency is attributed to the ability of PRO membranes to more effectively utilize the salinity difference to drive water permeation and better suppress the detrimental leakage of salts. On the other hand, the low conductivity of currently available ion exchange membranes impedes RED ion flux and, thus, constrains the power density. Both technologies exhibit a tradeoff between efficiency and power density: employing more permeable but less selective membranes can enhance the power density, but undesired entropy production due to uncontrolled mixing increases and some efficiency is sacrificed. When the concentration difference is increased (i.e., natural→anthropogenic→engineered salinity gradients), PRO osmotic pressure difference rises proportionally but not so for RED Nernst potential, which has logarithmic dependence on the solution concentration. Because of this inherently different characteristic, RED is unable to take advantage of larger salinity gradients,

whereas PRO power density is considerably enhanced. Additionally, high solution concentrations suppress the Donnan exclusion effect of the charged RED membranes, severely reducing the permselectivity and diminishing the energy conversion efficiency. This study indicates that PRO is more suitable to extract energy from a range of salinity gradients, while significant advancements in ion exchange membranes are likely necessary for RED to be competitive with PRO.

9.1 INTRODUCTION

The Gibbs free energy from mixing two solutions of different concentration can be harnessed for useful work [1, 2]. The salinity gradient can be from various sources [2], such as, the mixing of fresh river water with salty seawater which occurs naturally as part of the hydrological cycle. A recent study showed that the $\sim 37,300 \text{ km}^3$ annual global river discharge represents a substantial source of clean and renewable energy that can potentially generate electricity for over half a billion people [3]. Alternatively, anthropogenic waste streams can be utilized; e.g., concentrated brine from desalination plants can be paired with wastewater effluent from treatment facilities and the power generated can partially offset the desalination energy cost. Industries discharge approximately one-third of the energy consumed as thermal losses and the worldwide $\sim 9,400 \text{ TWh/y}$ of mostly low-temperature rejected heat can be recaptured for useful work production [4]. Closed systems that hybridize energy production technologies with thermal separation methods can access this industrial waste heat, and also low-temperature geothermal energy, using engineered salinity gradients [2]. Useful work is generated from the controlled mixing of synthetic hypersaline solutions in an energy

production stage, while a solution regeneration stage thermally separates the mixture to reconstitute the salinity gradient, essentially converting thermal energy to electricity.

Several approaches have been proposed to harness salinity energy, including pressure retarded osmosis (PRO) [5, 6], reverse electrodialysis (RED) [7, 8], capacitive mixing [9, 10], osmotically-induced nanofluidic electric currents [11], and hydrogels [12]. Among the technologies, membrane-based PRO and RED have been demonstrated at pilot-scale and are considerably more advanced [6, 13]. PRO utilizes the osmotic pressure difference to drive water permeation across a salt-rejecting semipermeable membrane into a more concentrated “draw” solution. The expanding volume of the draw solution is depressurized through a hydroturbine to produce useful work. RED, on the other hand, is driven by the Nernst potential — another manifestation of the chemical potential difference. The technology employs ion exchange membrane pairs to selectively allow counter-ion permeation and the net ion flux is converted to an electric current for power generation.

PRO and RED have fundamentally different working principles as well as operating constraints and, thus, are anticipated to have different performance in salinity energy extraction. Furthermore, the permeability and selectivity of the polymeric membranes used in PRO and the ion exchange membranes employed in RED are not at equivalent technological levels [14, 15]. Therefore, it would be instructive to quantitatively analyze the strengths and weaknesses characteristic to the technologies. Evaluation of PRO and RED potential performance with current state-of-the-art membranes can shed light on the viability of harnessing energy from various salinity gradient sources, and reveal vital insights that can inform future development of the technologies. Numerous studies have

examined the energy conversion performance of the two processes separately [3, 16-20]. The few that have pitted PRO and RED in direct comparison examined either power density or efficiency [21, 22], but no study encompassed both metrics.

This study aims to identify the comparative advantages of PRO and RED and examine their practical feasibility for salinity energy extraction. Properties simulating technologically-available high performance PRO and RED membranes are employed in the analysis, and tradeoff relations governing the membrane parameters are incorporated into the evaluation. The energy efficiency and power density attainable with the simulated membranes are simultaneously assessed for three categories of salinity gradients: natural (seawater–river water), anthropogenic (desalination brine–wastewater effluent), and engineered (synthetic hypersaline solutions). The prospects and limitations intrinsic to PRO and RED are highlighted, and the working principles and primary membrane parameters affecting performance are identified and discussed. The analytical insights gleaned from this study can serve to guide membrane and process development for the advancement of PRO and RED energy production from salinity gradients.

9.2 ENERGY PRODUCTION FROM SALINITY GRADIENTS

Both PRO and RED convert the chemical energy stored in salinity gradients to useful work by the controlled mixing of two solutions of different concentrations. However, the two technologies have different working principles, operating considerations, and membrane properties and, thus, are expected to produce distinct power generation performance. In this section, the two technologies are briefly introduced and the governing transport equations are presented. Detailed description of the processes can be

found in previous studies [3, 6, 8, 23]. Here, the fundamental differences between PRO and RED are emphasized, and the different salinity gradients used in this analysis are discussed.

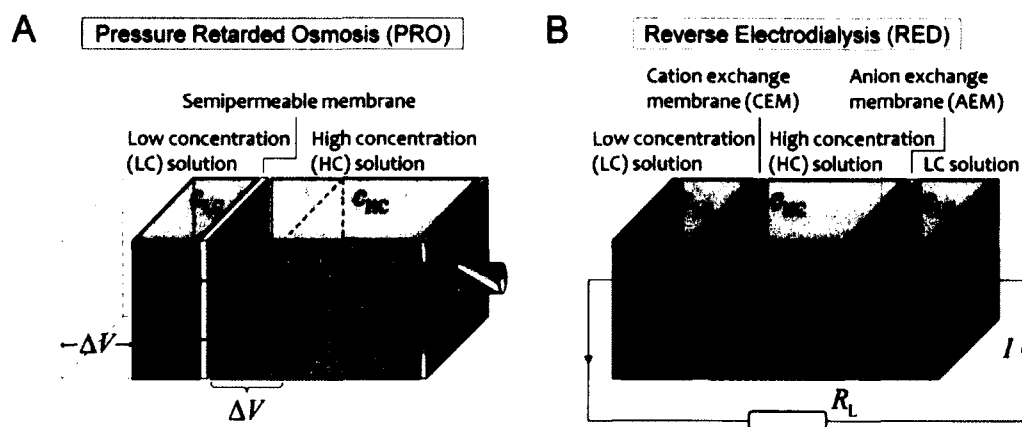


Figure 9.1. Schematic of (A) pressure retarded osmosis (PRO) and (B) reverse electrodialysis (RED). In PRO, the salinity gradient produces an osmotic driving force for water flux across the semipermeable membrane, and the increasing volume of the pressurized high concentration (HC) solution powers a hydroturbine to produce useful work. Some salt leaks from the HC solution to the low concentration (LC) solution as the membrane is not perfectly selective. In RED, the concentration difference across the ion exchange membranes produces a Nernst potential and the membranes selectively allow the transport of counter ions. The ion flux is converted to an electric current, I , with a redox couple circulating between the end electrodes and useful work is produced by the external load of resistance R_L . Water diffuses to the HC solution, while some co-ions leak across to the LC solution as the membranes are not perfectly selective. Only one RED membrane pair is shown to illustrate the process.

Pressure Retarded Osmosis. Figure 9.1A shows the schematic of a PRO process, where a semipermeable membrane separates a low concentration (LC) solution and a pressurized high concentration (HC) solution. Because of the difference in salt concentration, an osmotic pressure difference, $\Delta\pi_m$, develops across the membrane that drives water permeation from the LC solution into the more concentrated HC solution. The expanding volume of the pressurized HC solution powers a hydroturbine to produce

useful work [3]. As the semipermeable membrane is not perfectly selective, some salt diffuses from the saltier side to the more dilute LC solution (Figure 9.1). The leakage of salts across the membrane represents an uncontrolled mixing that undesirably lowers the extractable energy in PRO.

An actual PRO system would consist of membrane modules in continuous flow operation [6, 24]. Although Figure 9.1A seemingly depicts a batch process, the model is equivalent to a module operating in co-current configuration by assuming ideal plug-flow (i.e., the solution concentrations while advancing along the axial length of the module correspond to the conditions in the batch process as controlled mixing progresses). The governing equation for water flux in PRO, J_w , is [25]

$$J_w = A(\Delta\pi_m - \Delta P) = A \left\{ \frac{\pi_{\text{HC}} \exp\left(\frac{-J_w}{k}\right) - \pi_{\text{LC}} \exp\left(\frac{J_w S}{D}\right)}{1 + \frac{B}{J_w} \left[\exp\left(\frac{J_w S}{D}\right) - \exp\left(\frac{-J_w}{k}\right) \right]} - \Delta P \right\} \quad (9.1)$$

where π_{HC} and π_{LC} are the osmotic pressures of the HC and LC solutions, respectively, D is the diffusion coefficient of the salt in the LC solution, and ΔP is the hydraulic pressure applied to the HC solution. The osmotic pressure is determined by the salt concentration, c , and can be approximated using the van't Hoff equation [3]:

$$\pi \approx \nu R_g T c \quad (9.2)$$

for relatively dilute solutions (<1 M NaCl) [26]. Here, ν is the number of ions each electrolyte molecule dissociates into (i.e., 2 for NaCl), R_g is the gas constant, and T is the absolute temperature.

The water permeability coefficient, A , the salt permeability coefficient, B , and the structural parameter, S , are intrinsic properties of the PRO membrane, while k is the mass

transfer coefficient of the external concentration polarization (ECP) boundary layer at the membrane–HC solution interface. Eq 9.1 fully accounts for all three performance limiting phenomena in PRO: ECP, internal concentration polarization (ICP), and reverse salt flux. Detailed derivation of the water flux equation and discussion of the performance limiting effects can be found in our previous studies [14, 25]. Inspection of eqs 9.1 and 9.2 reveals that PRO water flux and, hence, the rate of controlled mixing is dependent on the membrane properties, A , B , and S , the hydrodynamic conditions, k , and the solution concentrations, c .

Reverse Electrodialysis. A schematic of one RED cell is shown in Figure 9.1B. The HC solution is sandwiched between a pair of cation and anion exchange membranes (CEM and AEM, respectively), which are, in turn, bordered by LC solutions. The charged ion exchange membranes (IEMs) exclude co-ions by Donnan’s principle but selectively allow the passage of counter ions. The ion concentration difference across the membranes produces a Nernst potential and an ionic current is generated from the directional permeation of ions from the HC solution to the LC solution (Figure 9.1B). The net ion flow is converted to an electric current, I , at the end electrodes with a reversible redox couple and useful work is produced by the external load of resistance, R_L [27]. The IEMs are not perfectly selective and some co-ions undesirably leak across, along with the permeation of water down the osmotic gradient. Akin to PRO, the transport of co-ions and water signifies uncontrolled mixing that subtracts from useful work production [23]. However, unlike PRO that converts salinity (chemical) energy to electrical energy via mechanical intermediary, RED directly converts salinity energy to electricity.

An actual RED stack consists of repeating cells arranged in series [23, 28], but this analysis focuses on a one-cell RED system. By appropriate normalization of the parameters, this apparent inconsistency in system scale is reconciled and the results obtained here are, thus, also applicable for RED stacks [23]. The current density, i , is defined as the current per unit effective membrane area, A_m , and can be described by Ohm's law [23]:

$$i \equiv \frac{I}{A_m} = \frac{\xi_{emf} - \xi_L}{ASR_{cell}} \quad (9.3)$$

where ξ_{emf} is the electromotive force of the RED cell, $\xi_L (=IR_L)$ is the potential difference across the external load resistor, and ASR_{cell} is the area specific resistance of the cell. Adequate mixing at the boundary layer of the membrane–solution interface is assumed such that concentration polarization effects can be neglected [29]. It is informative to note the symmetry between the PRO water flux equation (eq 9.1) and the RED current density equation (eq 9.3): J_w , A , $\Delta\pi_m$, and ΔP are analogous to i , ASR_{cell}^{-1} , ξ_{emf} , and ξ_L , respectively. Again, by assuming ideal plug flow, the batch process depicted in Figure 9.1B can similarly represent a continuous flow RED stack with co-current circulation of the solutions [23].

The electromotive force of the RED cell, ξ_{emf} , is the Nernst potential across the IEMs in Figure 9.1B. For the relatively dilute NaCl solutions assumed earlier in the PRO description [23]:

$$\xi_{emf} \approx \frac{2\alpha R_g T}{zF} \ln \left(\frac{c_{HC}}{c_{LC}} \right) \quad (9.4)$$

where z is the ion valence (i.e., 1 for NaCl), F is the Faraday constant, and the factor of 2 accounts for the CEM and AEM. The IEM permselectivity, α , describes the ability of the

membranes to selectively exclude co-ions while allowing the permeation of counter ions ($\alpha = 1$ indicates perfect selectivity). The RED cell resistance is the series sum of the four stack elements, namely AEM, CEM, the LC solution compartment, and the HC solution compartment. The membrane conductivity is assumed to be constant, while the resistance of the solution compartment is taken to be inversely proportional to the solution molar salt concentration [23]. Hence, the RED current density at any point during the controlled mixing process is determined by the membrane parameters (i.e., conductivity and permselectivity), the stack design (i.e., intermembrane distance), and also the solution properties (i.e., concentrations and resistivity).

Natural, Anthropogenic, and Engineered Salinity Gradients. To examine PRO and RED performance over a range of concentration differences, HC–LC solutions pairings of 0.6 M–1.5 mM NaCl (seawater–river water), 1.2 M–10 mM NaCl (desalination brine–wastewater), and 4.0 M–17 mM NaCl (hypersaline solution–synthetic brackish water) were employed in this study to simulate natural, anthropogenic, and engineered salinity gradients, respectively. Equal volumes of the HC and LC solutions were used. To simplify the PRO and RED analyses, molar concentration, c , was used in all calculations instead of mole fraction, and activity coefficients were assumed to be unity. Accuracy in the Nernst potential is only marginally sacrificed with this approximation (<7% difference) [30], while deviation of the initial osmotic pressure difference is more noticeable at high concentrations (approximation underpredicts $\Delta\pi$ by up to 20%) [30], but is still within tolerable threshold and does not significantly affect the general comparison between PRO and RED.

9.3 SIGNIFICANT PRO AND RED MEMBRANE PROPERTIES

Membranes are at the heart of the controlled mixing processes and, therefore, membrane properties and the design of the modules and stacks are expected to have strong bearing on PRO and RED performance. Salient parameters of the salt-selective membranes and ion exchange membranes analyzed in this study are highlighted here, and significant factors of the module and stack are briefly discussed. The parameters are selected to simulate state-of-the-art innovations and, hence, the results presented in this analysis roughly circumscribe the potential PRO and RED performance achievable with current technology.

Structural Parameter and Mass Transport Coefficient of PRO Membranes.

Internal concentration polarization (ICP) is an important performance limiting phenomenon that lowers power density in PRO by detrimentally elevating the membrane active–support layer interfacial salt concentration [14, 25, 31]. The extent of ICP is determined by the structural parameter, S , of the membrane support layer, as reflected in eq 9.1 by the term $\exp(J_w S/D)$. At the same time, pressurized PRO operation imposes mechanical strength requirements: the membrane needs to be adequately robust to withstand ΔP [32, 33]. An S value of 500 μm was selected to simulate commercially manufactured membranes with polyester woven mesh embedded in a highly porous and non-tortuous polysulfone support layer [33]. These membranes were experimentally demonstrated to possess mechanical sturdiness and substantially suppress ICP. Additionally, external concentration polarization (ECP) at the solution–active layer interface was found to be a dominant performance limiting effect at high water fluxes [14]. Mass transfer coefficient, k , of the ECP boundary layer is taken to be 27.5 $\mu\text{m/s}$ to

model PRO membrane modules with high performance channel and spacer design [33].

The parameters employed in this analysis are summarized in Table 9.1.

Table 9.1. Properties of current high performance membranes (thin-film composite polyamide membranes for PRO and ion exchange membranes for RED) analyzed in this study.

	Selectivity I	Selectivity II
PRO Membranes		
^a Water permeability, A ($L\ m^{-2}h^{-1}bar^{-1}$)	1.5	3.0
^a Salt (NaCl) permeability, B ($10^{-8}\ m/s$)	1.25	10
^b Structural parameter, S (μm)	500	500
RED Membranes		
^c Area specific resistance, ASR (Ωcm^2)	3.0	1.5
^{c,d} Permselectivity, α (-)	0.95 / 0.90 / 0.80	0.90 / 0.80 / 0.60
^d Molar water permeation ratio, θ (-)	3.5 / 11 / 26	19 / 44 / 94

^a Water and salt permeability of the PRO membranes are based on the permeability–selectivity tradeoff relationship of polyamide thin-film composite membranes [14].

^b The structural parameter is selected to simulate a membrane with woven fabric support capable of withstanding high hydraulic pressures [33].

^c Area specific resistance and permselectivity values are chosen to simulate technologically-available high performance ion exchange membranes constrained by conductivity–permselectivity tradeoff [34].

^d Permselectivity of the IEMs is assumed to deleteriously decrease with increasing salt concentration (0.6 / 1.2 / 4.0 M NaCl) of the surrounding solutions, while the molar water permeation ratio detrimentally rises [35].

PRO Membrane Selectivity–Permeability Tradeoff. An inspection of eq 9.1 reveals that water flux can be enhanced by using a membrane with large water permeability, A , and small salt permeability, B . A high A allows greater water permeation while a low B curbs the leakage of salt from the HC solution. The unfavorable buildup of leaked salt in the membrane support layer diminishes the osmotic

driving force [14, 25]. Furthermore, salt permeation across the PRO membrane constitutes uncontrolled mixing that detrimentally deducts from useful work production. However, the goals of raising A and minimizing B cannot be simultaneously achieved due to the permeability–selectivity tradeoff governing salt-rejecting polymeric membranes based on the solution diffusion mechanism of transport [36]. For example, our recent study on polyamide thin-film composite membranes indicates that doubling A would concomitantly increase B by eightfold [14].

Polyamide membranes are the state-of-the-art for reverse osmosis desalination [37, 38] and also extensively researched for PRO applications [33, 39-41]. To simulate technically-attainable polyamide membranes of different permeability–selectivity, two pairs of parameters based on the tradeoff correlation equation developed in our previous work [14] were chosen for this analysis (Table 9.1): $A = 1.5 \text{ L m}^{-2}\text{h}^{-1}\text{bar}^{-1}$, $B = 1.25 \times 10^{-8} \text{ m/s}$ and $A = 3.0 \text{ L m}^{-2}\text{h}^{-1}\text{bar}^{-1}$, $B = 10 \times 10^{-8} \text{ m/s}$ (designated I and II, respectively). Recent studies suggest that membrane properties can be altered under pressurized conditions [33, 42]. For this analysis, the spacer design of the PRO module was assumed to adequately support the membrane such that A , B , and S are constant and independent of ΔP .

RED Membrane Ionic Permselectivity–Conductivity Tradeoff. Recent studies indicate an analogous tradeoff exists for ion exchange membranes that relates permselectivity, α , and ionic conductivity [34, 43]. Specifically, an increase in α is generally accompanied by an undesired rise in the area specific resistance, ASR, of AEMs. The observed trend was attributed to fixed charge density and water content of the polymeric membranes [34, 43] and, therefore, CEMs should also exhibit similar

behavior. Our recent study showed that membrane resistance is a crucial performance factor and a low ASR is advantageous for RED [23]. On the other hand, an α close to unity is desired to maximize the Nernst potential across the RED cell, as in eqs 9.3 and 9.4, and also restrain the leakage of co-ions that represents uncontrolled mixing.

Additionally, IEMs are hydrated polymeric thin-films and are, thus, pervious to water [15]. Water permeation down the osmotic gradient, into the HC solution, constitutes uncontrolled mixing that further subtracts from useful work production. Water leakage across the membranes can be described by θ — the mole ratio of water to salt (both counter ions and co-ions) permeation [23]. In the absence of a rigorous empirical equation linking α , ASR, and θ , two sets of conductivity–permselectivity were identified from literature to reflect technologically-feasible IEMs (Table 9.1) [15, 23, 44, 45]: ASR = $3.0 \Omega\text{cm}^2$, $\alpha = 0.95$, $\theta = 3.5$ and ASR = $1.5 \Omega\text{cm}^2$, $\alpha = 0.90$, $\theta = 19$ (likewise designated I and II, respectively). The cation and anion exchange membranes are assumed to have the same conductivity and symmetrically identical selectivity. Similar to the assumptions for PRO membranes, the properties are taken to be constant during RED.

Effect of Solution Concentration and Intermembrane Distance. Ion exchange membranes utilize the Donnan exclusion principle to allow the selective permeation of counter ions while retaining co-ions. The fixed charges of IEM depress the co-ion concentration within the membrane because of charge balance, thus effectively excluding their transport across the IEM. As the ratio of counter to co-ions in the membrane matrix is approximately proportional to the square of the ratio of fixed charge density to surrounding solution concentration, the exclusion effect of the fixed charges is

diminished when the solution concentration is high [46, 47]. Hence, IEM selectivity is reduced with increasing concentration of the surrounding solution, as experimentally demonstrated in a recent study where α of commercial CEM and AEM decreased from >0.95 at c_{HC} of ~ 0.5 M NaCl, to ~ 0.80 at elevated concentrations of 4 M NaCl [35]. To simulate the deteriorating permselectivity at the high salt concentrations of anthropogenic and engineered salinity gradients, α of RED-I is reduced to 0.90 and 0.80, respectively, α of RED-II is lowered to 0.80 and 0.60, and θ is revised accordingly to reflect the greater water permeation (Table 9.1).

Apart from the IEMs, the HC and LC solutions contribute to the area specific resistance of the RED cell. As the conductivity of the solution compartment is inversely proportional to the channel height, a small intermembrane distance is advantageous to minimize ASR_{cell} and, thus, enhance PD. On the other hand, a narrow channel height exacerbates parasitic pressure drop along the channels and increases the pumping energy cost [23, 48]. To model a well-designed RED stack, an intermembrane distance of 150 μm that balances the benefits of lower cell resistance with the negative effects of pressure drop is selected [23]. Additionally, adequate mixing at the solution-membrane interface is assumed such that the effects of concentration polarization are negligible [23, 48].

9.4 SALINITY ENERGY PRODUCTION PERFORMANCE

PARAMETERS

Membrane power density, PD, and energy extraction efficiency, η , are two primary performance parameters affecting the cost-effectiveness of power generation from salinity gradients using membrane-based technologies [3, 6, 15, 23]. PD is defined as the

power produced per unit membrane area and is a measure of how quickly the membranes convert salinity energy to useful work, while η is the percent of Gibbs free energy of mixing converted to useful work and, thus, quantifies how much of the available energy is utilized by the process. In this section, the significance of the performance metrics is outlined and the practical operating conditions for PRO and RED are briefly discussed.

Membrane Power Density. Membrane is a key capital cost component for both PRO and RED [49, 50], and a high PD is desirable to reduce the membrane area required for generating a certain power. Membrane power density for PRO and RED, respectively, are

$$PD_{\text{PRO}} = J_w \Delta P \quad (9.5)$$

$$PD_{\text{RED}} = \frac{1}{2} i \zeta_L \quad (9.6)$$

Note that RED innately requires two membranes, CEM and AEM, whereas PRO requires just one salt-rejecting membrane (Figure 9.1). This difference is reflected in eq 9.6 by the factor of $\frac{1}{2}$. To simulate practical operation, this analysis considers the hydraulic pressure applied to the HC solution of the PRO membrane module and the external load of the RED circuit to be both constant throughout the controlled mixing [3, 23]. As the processes progress, which is equivalent to advancement down the PRO module or RED stack, the HC solution is diluted and c_{LC} increases, consequently changing J_w , i , and ζ_L . Therefore, the immediate power density, described by eqs 9.5 and 9.6, varies accordingly. To evaluate the overall PRO and RED performance, PD is averaged over the entire membrane module or stack to yield the net power density.

Energy Extraction Efficiency. The Gibbs free energy of mixing, ΔG_{mix} , for strong electrolyte solutions of relatively dilute concentrations [3]:

$$-\frac{\Delta G_{\text{mix}}}{\nu R_g T} \approx c_M^f \ln c_M^f - \phi_{\text{LC}} c_{\text{LC}}^0 \ln c_{\text{LC}}^0 - \phi_{\text{HC}} c_{\text{HC}}^0 \ln c_{\text{HC}}^0 \quad (7)$$

gives the theoretical maximum energy, per unit total solution volume, from the complete mixing of the HC and LC solutions. The subscript M denotes the resultant mixture, the superscripts 0 and f indicate initial and final states, and ϕ is the volume fraction ($\phi_{\text{LC}} = \phi_{\text{HC}} = 0.5$ for the equivolume analyses in this study). To fully access ΔG_{mix} for useful work would require a hypothetical reversible thermodynamic process. Practical unit operations are, however, irreversible in nature and inevitably produce entropy that reduces the efficiency, η . Due to fundamentally different working principles and dissimilar mode of practical operation, PRO and RED have inherent efficiencies that are characteristic of the processes. When comparing PRO and RED, it is, hence, instructive to examine the thermodynamic efficiency intrinsic to the technologies.

Practical Operation of PRO and RED. Key parameters and performance objectives employed in this study are briefly presented here. Our recent work indicates that, because the driving force is gradually diminished as controlled mixing progresses, judicious early discontinuation of PRO and RED can yield significantly enhanced PD with only marginal forfeit in η [23]. To model practical operation, triggers for early process termination were rationally selected (after 70% of the eventual ion permeation in RED [23] and, based on similar criteria, after 90% of the eventual water permeation in PRO). The comparisons presented here focus on RED performance when PD is maximized and PRO performance when η is maximized. All power densities and

efficiencies were analyzed numerically with temperature $T = 298$ K. Additionally, only co-current flow is considered for the simulated PRO module and RED stack unit operation; greater mixing can be achieved with counter- or cross-current configuration, thus accessing more ΔG_{mix} for energy production [17, 51]. Methodology for RED module analysis is detailed in our recent work [23] and is adapted here for evaluating PRO.

9.5 ENERGY EXTRACTION EFFICIENCY

Efficiency, Entropy Production, and Unutilized Energy. For equal volumes of HC and LC solution, the Gibbs free energy of mixing for natural, anthropogenic, and engineered salinity gradients are 0.56, 1.08, and 3.68 kWh per m^3 of LC solution volume, respectively, as determined using eq 9.7 with $\phi_{\text{LC}} = 0.5$. Alternatively, the energy can be expressed per cubic meter of the total (mixed) solution [8, 17], in which case the corresponding specific ΔG_{mix} are half of the above values as $\phi_{\text{LC}} = 0.5$. In irreversible unit operation, ΔG_{mix} is fractionated into useful work generated, entropy produced due to friction/resistance, entropy produced from uncontrolled mixing, and energy not utilized [3, 23]. The energy allotment is depicted in Figure 9.2 for natural salinity gradient, where the driving force, $\Delta\pi$ and ξ_{emf} , is plotted as a function of fraction of water permeated for PRO and salt permeated for RED. Membranes possessing properties listed in “Selectivity I” column of Table 9.1 were used in the analysis. To maximize η , ΔP in PRO is 14.2 bar while $R_{\text{LA}_m} = 9.15 \text{ } \Omega\text{cm}^2$ in RED to maximize PD.

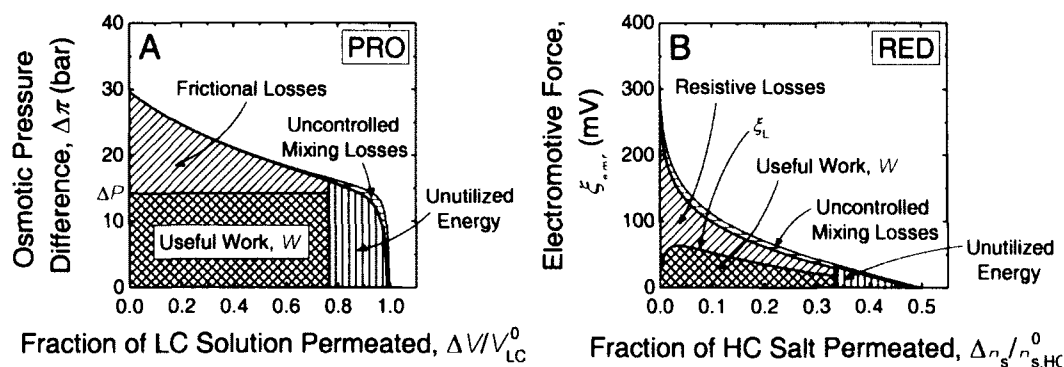


Figure 9.2. Representative plots of useful work, W (black patterned areas), frictional/resistive losses (blue patterned areas), uncontrolled mixing losses (red patterned areas), and unutilized energy (green patterned areas) for A) PRO and B) RED. The vertical axes are the driving force for water and ion flux (osmotic pressure difference, $\Delta\pi$, and electromotive force, ξ_{emf} , for PRO and RED, respectively), while the horizontal axes denote progress of the energy production process (fraction of water permeated from the low concentration (LC) solution, $\Delta V/V_{LC}^0$, and fraction of salt permeated from the high concentration (HC) solution, $\Delta n_s/n_{s,HC}^0$, respectively). For both processes, the HC solution is 0.6 M NaCl and the LC solution is 1.5 mM NaCl to simulate seawater–river water salinity gradient. Membrane properties are presented in the column “Selectivity I” of Table 9.1. To maximize η , ΔP in PRO is 14.2 bar (about half of initial $\Delta\pi$) while $R_L A_m = 9.15 \Omega\text{cm}^2$ in RED to maximize PD.

The useful work produced in constant-pressure PRO can be obtained by multiplying the applied hydraulic pressure, ΔP , and the volume of water permeated in the PRO module, i.e., area under $\Delta P - \Delta V$ (black patterned region in Figure 9.2A). Because practical PRO is not a reversible thermodynamic process, entropy is inevitably produced. Firstly, water permeating across the semipermeable membrane is impeded by water–membrane frictional forces. Energy is expended to overcome the hydraulic resistance and achieve a non-zero water flux [3]. Entropy production due to frictional losses is indicated in Figure 9.2A as the blue patterned region. Secondly, the semipermeable membranes are not perfectly selective and some salts leak across. Thus, energy is lost

from the uncontrolled mixing of the salinity gradient caused by the undesired salt flux. The red patterned region in Figure 9.2A marks the entropy production because of uncontrolled mixing. Both frictional losses and uncontrolled mixing render PRO thermodynamically irreversible. Lastly, the green patterned area denotes the portion of ΔG_{mix} that is unutilized. As PRO progresses, the net driving force gradually diminishes and water flux is eventually terminated when $\Delta\pi - \Delta P = 0$. The remaining energy still embedded in the unmixed solutions is, hence, not accessed. This characteristic is a practical limitation of constant-pressure PRO [3]. Additionally, the portion of unutilized energy is slightly augmented by the early discontinuation of PRO (discussed in previous section). Aggregating the four regions under the osmotic driving force curve yields ΔG_{mix} (Figure 9.2A).

The mixing energy can similarly be partitioned for RED, as represented by division of the area under ξ_{emf} in Figure 9.2B. Integrating the potential difference of the external load, ξ_L , across the moles of salt permeated as counter ions (equivalently, the charge transported) gives the useful work produced (black patterned region) [23]. Note that unlike constant-pressure PRO, ξ_L varies over the course of RED due to the changing solution concentrations and ξ_{emf} . Internal resistance of the RED stack, caused by the IEMs and the electrolyte solutions, dissipates energy by impeding the permeations of ions. Entropy production due to resistive energy loss in RED is indicated as the blue patterned area in Figure 9.2B, and is analogous to frictional energy loss in PRO. Similar to PRO, uncontrolled mixing in RED with real membranes also produces entropy (red patterned region): water and co-ions leaks across the IEMs as the membranes are not perfectly selective. Whereas constant ΔP in PRO restricts the complete mixing of the HC and LC

solutions, RED with constant R_L can proceed to concentration equilibrium (i.e., $c_{HC} = c_{LC}$). Therefore, a greater portion of ΔG_{mix} can be accessed by RED. The green patterned region in Figure 9.2B denotes the unutilized energy due to premature discontinuation of the process for the reason discussed in the previous section.

Higher Efficiency is Attainable in PRO than RED. Grey columns in Figure 9.3 show PRO and RED efficiency, η (defined as the percent of ΔG_{mix} converted to useful work), for natural, anthropogenic, and engineered salinity gradients. Membranes with Selectivity I (Table 9.1) were used in the analysis. With the practical operating conditions described earlier, PRO exhibits greater energy extraction efficiency (53.9, 53.9, and 56.1%) than RED (37.8, 33.1, and 18.1%) for all three salinity gradients. Note that RED can potentially attain higher η , but at the expense of drastically reduced power density, thus rendering the overall process impractical. Frictional/resistive energy losses, uncontrolled mixing losses, and unutilized energy are also presented (blue, red, and green patterned columns, respectively).

Because of the constant pressure limitation, PRO have inherently larger fractions of unutilized energy (green patterned columns) than RED. However, less entropy is produced in PRO than RED (blue and red patterned columns combined). The relatively superior selectivity of salt-rejecting membranes to the co-ion and water retention capabilities of IEMs enables PRO to better suppress uncontrolled mixing (red patterned columns). This RED disadvantage is especially pronounced at larger salinity gradients (i.e., anthropogenic and engineered), where the high concentration of the HC solution significantly suppresses the Donnan exclusion capacity of the ion exchange membranes and detrimentally diminishes the ability of RED to convert salinity energy to useful work

[35]. Even when IEM selectivity is not compromised in the natural salinity scenario, a larger portion of ΔG_{mix} is lost to entropy production due to internal stack resistance in RED than water–membrane friction in PRO (blue patterned columns). For the range of salinity gradients, the analysis indicates that PRO offers greater energy extraction efficiency advantage over RED.

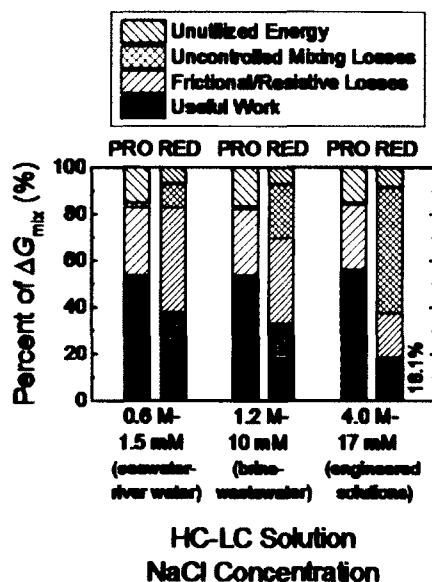


Figure 9.3. Efficiency of work extraction (grey columns), percent of energy expended to drive water or counter ion flux (blue patterned columns), percent of energy lost to uncontrolled mixing (red patterned columns), and portion of unutilized energy (green patterned columns) for PRO and RED. The HC–LC solution concentrations are 0.6 M–1.5 mM, 1.2 M–10 mM, and 4.0 M–17 mM NaCl to simulate seawater–river water, seawater desalination plant brine–wastewater, and engineered solutions, respectively. The PRO and RED membrane properties are presented in the column “Selectivity I” of Table 9.1. ΔP in PRO is 14.2, 28.6, and 96.7 bar and RED $R_L A_m$ is 9.15, 7.63, and 6.82 Ωcm^2 for the 0.6 M–1.5 mM, 1.2 M–10 mM, and 4.0 M–17 mM HC-LC solutions, respectively.

Selective Membranes Yield Greater Efficiencies. PRO and RED efficiencies with different membrane transport parameters (Selectivity I and II of Table 9.1) are presented in Figure 9.4 (unshaded and shaded symbols, respectively, and right vertical axis) for

natural, anthropogenic, and engineered salinity gradients. Both energy extraction technologies yield greater efficiencies with more selective membranes (PRO-I and RED-I) for all three salinity gradient scenarios. This result is unsurprising, as entropy production due to uncontrolled mixing is lower because less salt and co-ions leak across in PRO and RED, respectively, when membranes of higher selectivity are used. The disparity in η is most evident in RED with anthropogenic and engineered salinity gradients, as the high solution concentrations significantly suppress Donnan exclusion, thereby causing greater co-ion leakage. As discussed in the following section, despite the seeming drawback in efficiency, employing less selective membranes can be advantageous for overall productivity because of potentially greater power densities.

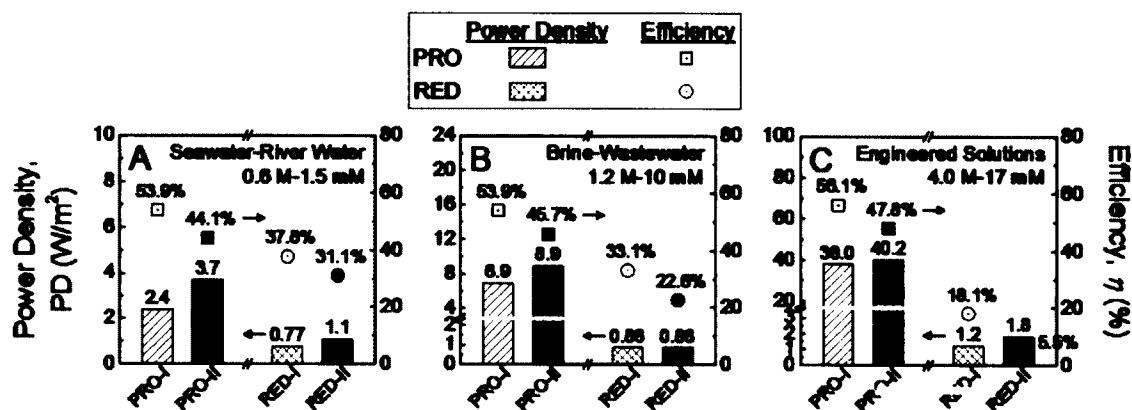


Figure 9.4. Membrane power density (columns, left vertical axis) and efficiency of work extraction (symbols, right vertical axis) for PRO and RED (blue and red data representations, respectively) at 0.6 M, 1.2 M, and 4.0 M NaCl high concentration (HC) solution concentrations. Two sets of membranes with imperfect selectivity are examined: membrane-I has moderate selectivity imperfections (unshaded columns and symbols), while membrane-II has more severe imperfection in selectivity (shaded columns and symbols). Details of the PRO and RED membrane properties can be found in Table 9.1. For Selectivity II, ΔP in PRO is 13.1, 26.3, and 88.9 bar and RED R_{L,A_m} is 6.05, 6.25, and 4.19 Ωcm^2 for the 0.6 M–1.5 mM, 1.2 M–10 mM, and 4.0 M–17 mM HC-LC solutions, respectively, while ΔP and R_{L,A_m} for Selectivity I can be found in the caption of Figure 9.3.

9.6 MEMBRANE POWER DENSITY

Higher Power Density Obtained with Less Resistive Membranes. Power density, defined as the membrane area-normalized power generation, is an important factor affecting the cost-effectiveness of PRO and RED [49, 50]. Unshaded and shaded columns of Figures 9.4A-C (left vertical axis) denote the power densities, PD, for Selectivity I and II membranes, respectively. Compared to the more selective membranes, PRO-II are twice as permeable (Table 9.1) and are able attain higher PD in the co-current operation for natural, anthropogenic, and engineered salinity gradients (2.4, 6.9, and 38.0 W/m² for PRO-I, respectively, and 3.7, 8.9, and 40.2 W/m² for PRO-II). However, this PD advantage is achieved at the expense of efficiency: η is 53.9–56.1% for PRO-I but is lower with PRO-II (44.1–47.8%) due to greater entropy production arising from more salt leakage.

The relative PD enhancement is more marked for smaller salinity gradients. For instance, by using membranes with lower hydraulic resistance, PD is augmented 54% with seawater–river water but only improved 6% with engineered hypersaline solutions. Increasing water permeability concomitantly raises salt permeability because of the permeability–selectivity tradeoff governing salt-rejecting membranes [14, 25]. As the detrimental effect of reverse salt flux coupled with internal concentration polarization is more exacerbated at higher water fluxes, PD enhancements, therefore, do not scale with the water permeability increases (eqs 9.1 and 9.5). Additionally as PRO progresses, more draw salt is accumulated in the feed solution for high c_{HC} that deleteriously reduces the effective $\Delta\pi$ across the membrane and further lowers PD. Hence, employing more selective PRO-I membranes for engineered salinity gradient can be overall more

productive as η is substantially higher (56.1%) while PD is only marginally diminished (38.0 W/m²) compared to 47.8% and 40.2 W/m² of PRO-II (Figure 9.4C).

Less resistive RED membranes exhibit a generally similar trend for the co-current stacks: PD of 0.77–1.2 W/m² is obtained with Selectivity I, while Selectivity II yields higher power densities of 0.86–1.8 W/m² (red columns of Figure 9.4). Ion exchange membranes are also bound by an analogous tradeoff [34, 43], where an increase in membrane conductivity is unavoidably accompanied by a reduction in permselectivity (Table 9.1). However, the net effect of the permselectivity–conductivity tradeoff on the resultant PD is less straightforward. A lower resistance enables greater ionic flux across the membranes and, hence, enhances PD (eqs 9.3 and 9.6) but the Nernst potential to drive ion permeation is diminished by the associated decline in permselectivity (eq 9.4). Detrimental lowering of the permselectivity by highly concentrated solutions further compounds to the complexity. The convoluted behavior is illustrated by more conductive RED-II membranes obtaining PD enhancement of 43% and 50% for natural and engineered salinity gradients, respectively, but no noticeable benefits for the brine–wastewater system.

PRO Better Utilizes Salinity Gradient to Realize Greater Power Densities.

Appreciably greater membrane power densities are attainable in PRO than RED (blue and red columns in Figure 9.4). For natural, anthropogenic, and engineered salinity gradients, respectively, PD_{PRO} is 3.1–3.4 times, 8–10 times, and 22–32 times of PD_{RED}, indicating that with the simulated state-of-the-art membrane properties, PRO requires significantly less membrane area to access the salinity energy. The PD difference between the two membrane-based energy production technologies is amplified at larger salinity gradients.

Contrary to intuition, the relatively poorer PD performance of RED in high salt concentrations conditions is not solely caused by the diminishing membrane selectivity. Using simulated RED membranes with $\alpha = 0.95$, $\theta = 3.5$, and $ASR = 3.0 \Omega\text{cm}^2$ (i.e., assuming selectivity is not compromised by solution concentration) in engineered salinity gradient yields higher η of 37.7%, but conspicuously no noticeable PD improvements (1.2 W/m^2) compared to 18.1% and 1.2 W/m^2 of RED-I.

The superior power density performance of PRO over RED at larger salinity gradients can be elucidated by examining the driving force for water and ion flux. PRO osmotic pressure difference, $\Delta\pi$, as a function of fraction of LC solution permeated, and RED electromotive force, ξ_{emf} , as a function of salt permeated (as counter-ions) per HC solution volume are presented in Figure 9.5 (inset of Figure 9.5B shows the initial ξ_{emf}). This analysis assumes ideal, perfectly selective membranes (i.e., $B = 0$, and $\alpha = 1$ and $\theta = 0$). For such ideal membranes, the area under the blue solid, green dashed, and red dotted lines is proportional to the theoretical maximum energy ΔG_{mix} (0.56, 1.08, and 3.68 kWh per m^3 of LC solution volume) for natural, anthropogenic, and engineered salinity gradients, respectively.

The Gibbs free energy of mixing is determined by the solution concentrations (eq 9.7) and is independent of the energy extraction technologies. More salinity energy is available with larger concentration differences, but PRO and RED accesses the higher ΔG_{mix} in fundamentally different ways. In PRO, the fraction of LC solution that permeates across is practically the same (horizontal axis-intercept of Figure 9.5A), but $\Delta\pi$ increases proportionally with c_{HC} (eq 9.2 and Figure 9.5A). For example, increasing c_{HC} by 6.7 times from 0.6 to 4.0 M NaCl raises $\Delta\pi$ by the same factor while taking $c_{\text{LC}} = 1.5$

mM NaCl. That is, PRO is able to fully utilize the augmented concentration difference to produce greater water flux and, hence, generate higher PDs (Figure 9.4).

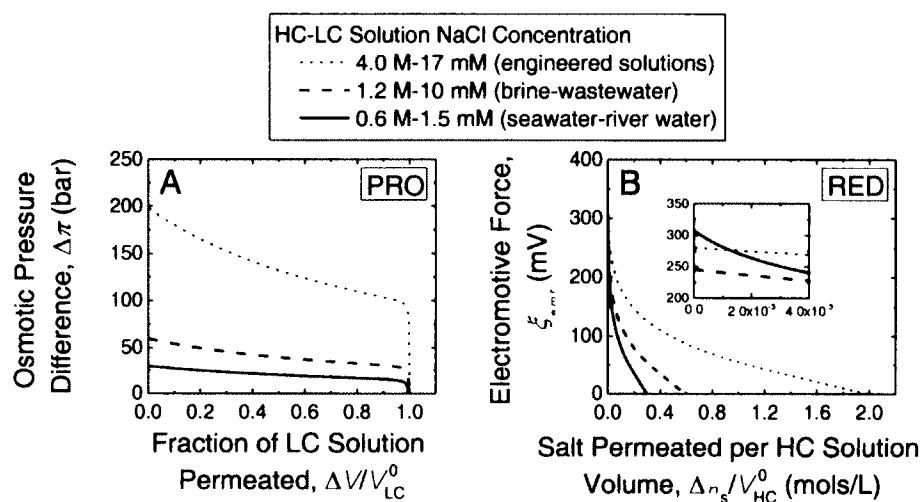


Figure 9.5. (A) Osmotic pressure difference, $\Delta\pi$ (driving force for water flux in PRO), as a function of the fraction of water permeated from the low concentration (LC) solution, $\Delta V/V_{LC}^0$. (B) Electromotive force, ζ_{emf} (driving force for ion flux in RED), as a function of the moles of salt permeated per unit volume of the high concentration (HC) solution, $\Delta n_s/V_{HC}^0$. Inset in B) shows the initial ζ_{emf} of the RED cell. Blue solid, green dashed, and red dotted lines represent natural, anthropogenic, and engineered salinity gradients, respectively. Perfectly selective PRO and RED membranes are assumed.

On the other hand, RED experiences only marginal enhancements in driving force because the Nernst potential is logarithmically dependent on solution concentrations (eq 9.4). In the previous example where c_{HC} is increased from 0.6 to 4.0 M NaCl ($\sim 6.7\times$), the Nernst potential is merely amplified $\sim 32\%$. To access the larger ΔG_{mix} of the greater salinity differences, more moles of salt permeates across as counter-ions (horizontal axis-intercept of Figure 9.5B scales directly with c_{HC}) and, hence, the controlled mixing process is undesirably protracted. In other words, while more energy is available with larger salinity gradients, RED power density is only slightly enhanced and more membrane area is needed to access the energy (Figure 9.4). While PRO is able to take

advantage of the higher c_{HC} in anthropogenic (4.0 M) and engineered (1.2 M) salinity gradients, the principle difference in energy utilization intrinsically excludes RED from exploiting the larger salinity difference to significantly improve PD, even with high permselectivity membranes.

9.7 IMPLICATIONS

Energy from salinity gradients can be extracted with PRO and RED — two membrane-based technologies with intrinsically different principles. The analysis presented here indicates that, with existing technologically-available membranes, PRO is able to achieve greater efficiency and higher power density performance for a range of salinity gradients, compared to RED. PRO is especially proficient at extracting salinity energy from large concentration differences: for equal flow rates of HC and LC solutions, significantly enhanced PDs can be attained while maintaining over 45% efficiency in a co-current flow module. The remarkable power density performance is attributed to the inherent characteristic of PRO to effectively utilize larger salinity differences for driving force augmentation. Additionally, overall PRO productivity can be optimized by suitably tuning the membrane permeability–selectivity to substantially improve power density at a small efficiency cost.

In contrast, RED is innately unable to gain appreciable power density benefits from salinity gradient increases, regardless of membrane transport properties. Furthermore, the Donnan exclusion effect, which confers selectivity to ion exchange membranes, is overwhelmed at high solution concentrations for current RED membranes, severely constraining the technology to impractically low efficiencies. These factors restrict the

feasible application of RED energy production to relatively small salinity gradients. In addition to the relatively lower PD and η , ion exchange membranes employed in RED stacks are considerably more expensive than salt-rejecting polymeric membranes used in PRO modules, further handicapping the comparative advantage of RED [2]. To advance RED beyond its current limitations, technological innovations are necessary to unhinge the conductivity–permselectivity tradeoff and develop ion exchange membranes with simultaneously greater permselectivity and higher conductivity.

Although PRO can potentially achieve excellent performance with large salinity gradients, realization of the technology can be hindered by inadequate membrane robustness. For example, to achieve the potential high PD and η for engineered salinity gradients, the polymeric thin-film composite membrane modules need to withstand hydraulic pressures >90 bar (1,300 psi) while retaining their structural and transport properties. Presently, the highest ΔP demonstration reported in literature is 48 bar (700 psi) on a coupon-sized membrane in a laboratory testing cell [33]. The large pressurization necessary for high salinity operation is likely to detrimentally alter the membrane properties and, therefore, improving the membrane mechanical robustness, together with the apt design of spacer support and membrane module, will be critical [33, 42].

The comparison presented in this study centers on membrane-level performance. Actual power generation installations would further comprise engineering components that are different for PRO and RED. For example, PRO requires pumps, pressure exchangers, and hydroturbines to convert mechanical expansion of the HC draw solution to electrical energy. RED employs a reversible redox couple at the end electrodes to

directly convert salinity energy to electricity without a mechanical intermediate, and requires pumping energy to circulate the solutions through narrow stack channels. Additionally, foulants present in natural and anthropogenic input streams (e.g., river water and wastewater effluent) can detrimentally lower PRO and RED productivity [51, 52]. Further cost-efficiency analysis of the system-level components, taking into account fouling impacts and pretreatment, are necessary to more accurately assess the practical potential of power generation from salinity gradients.

9.8 REFERENCES

- [1] Pattle, R. E., Production of Electric Power by mixing Fresh and Salt Water in the Hydroelectric Pile. *Nature* **1954**, *174* (4431), 660-660.
- [2] Logan, B. E. Elimelech, M., Membrane-based processes for sustainable power generation using water. *Nature* **2012**, *488* (7411), 313-319.
- [3] Yip, N. Y. Elimelech, M., Thermodynamic and Energy Efficiency Analysis of Power Generation from Natural Salinity Gradients by Pressure Retarded Osmosis. *Environmental Science & Technology* **2012**, *46* (9), 5230-5239.
- [4] Lin, S.; Yip, N. Y.; Cath, T. Y.; Osuji, C. O. Elimelech, M., Hybrid Pressure Retarded Osmosis–Membrane Distillation System for Power Generation from Low-Grade Heat: Thermodynamic Analysis and Energy Efficiency. *Environmental Science & Technology* **2014**, *48* (9), 5306-5313.
- [5] Loeb, S., Osmotic Power-Plants. *Science* **1975**, *189* (4203), 654-655.
- [6] Achilli, A. Childress, A. E., Pressure retarded osmosis: From the vision of Sidney Loeb to the first prototype installation - Review. *Desalination* **2010**, *261* (3), 205-211.
- [7] Weinstein, J. N. Leitz, F. B., Electric-Power from Difference in Salinity - Dialytic Battery. *Science* **1976**, *191* (4227), 557-559.
- [8] Post, J. W.; Hamelers, H. V. M. Buisman, C. J. N., Energy recovery from controlled mixing salt and fresh water with a reverse electrodialysis system. *Environmental Science & Technology* **2008**, *42* (15), 5785-5790.
- [9] Brogioli, D., Extracting Renewable Energy from a Salinity Difference Using a Capacitor. *Physical Review Letters* **2009**, *103* (5).
- [10] La Mantia, F.; Pasta, M.; Deshazer, H. D.; Logan, B. E. Cui, Y., Batteries for Efficient Energy Extraction from a Water Salinity Difference. *Nano Letters* **2011**, *11* (4), 1810-1813.
- [11] Siria, A.; Poncharal, P.; Bianco, A. L.; Fulcrand, R.; Blase, X.; Purcell, S. T. Bocquet, L., Giant osmotic energy conversion measured in a single transmembrane boron nitride nanotube. *Nature* **2013**, *494* (7438), 455-458.
- [12] Zhu, X.; Yang, W.; Hatzell, M. C. Logan, B. E., Energy Recovery from Solutions with Different Salinities Based on Swelling and Shrinking of Hydrogels. *Environmental Science & Technology* **2014**.
- [13] News Release: Progress Blue Energy generation by RED. <http://www.fujifilmmembranes.com/item/progress-blue-energy-generation-by-red> (Accessed on: June 05).
- [14] Yip, N. Y. Elimelech, M., Performance Limiting Effects in Power Generation from Salinity Gradients by Pressure Retarded Osmosis. *Environmental Science & Technology* **2011**, *45* (23), 10273-10282.
- [15] Veerman, J.; de Jong, R. M.; Saakes, M.; Metz, S. J. Harmsen, G. J., Reverse electrodialysis: Comparison of six commercial membrane pairs on the thermodynamic efficiency and power density. *Journal of Membrane Science* **2009**, *343* (1–2), 7-15.
- [16] Thorsen, T. Holt, T., The potential for power production from salinity gradients by pressure retarded osmosis. *Journal of Membrane Science* **2009**, *335* (1–2), 103-110.

- [17] Lin, S.; Straub, A. P. Elimelech, M., Thermodynamic Limits of Extractable Energy by Pressure Retarded Osmosis. *Energy & Environmental Science* **2014**.
- [18] Długołęcki, P.; Gambier, A.; Nijmeijer, K. Wessling, M., Practical Potential of Reverse Electrodialysis As Process for Sustainable Energy Generation. *Environmental Science & Technology* **2009**, *43* (17), 6888-6894.
- [19] Vermaas, D. A.; Guler, E.; Saakes, M. Nijmeijer, K., Theoretical power density from salinity gradients using reverse electrodialysis. *Energy Procedia* **2012**, *20* (0), 170-184.
- [20] Daniilidis, A.; Herber, R. Vermaas, D. A., Upscale potential and financial feasibility of a reverse electrodialysis power plant. *Applied Energy* **2014**, *119* (0), 257-265.
- [21] Feinberg, B. J.; Ramon, G. Z. Hoek, E. M. V., Thermodynamic Analysis of Osmotic Energy Recovery at a Reverse Osmosis Desalination Plant. *Environmental Science & Technology* **2013**, *47* (6), 2982-2989.
- [22] Post, J. W.; Veerman, J.; Hamelers, H. V. M.; Euverink, G. J. W.; Metz, S. J.; Nijmeijer, K. Buisman, C. J. N., Salinity-gradient power: Evaluation of pressure-retarded osmosis and reverse electrodialysis. *Journal of Membrane Science* **2007**, *288* (1-2), 218-230.
- [23] Yip, N. Y.; Vermaas, D. A.; Nijmeijer, K. Elimelech, M., Thermodynamic, Energy Efficiency, and Power Density Analysis of Reverse Electrodialysis Power Generation with Natural Salinity Gradients. *Environmental Science & Technology* **2014**, *48* (9), 4925-4936.
- [24] Cath, T. Y.; Childress, A. E. Elimelech, M., Forward osmosis: Principles, applications, and recent developments. *Journal of Membrane Science* **2006**, *281* (1-2), 70-87.
- [25] Yip, N. Y.; Tiraferri, A.; Phillip, W. A.; Schiffman, J. D.; Hoover, L. A.; Kim, Y. C. Elimelech, M., Thin-Film Composite Pressure Retarded Osmosis Membranes for Sustainable Power Generation from Salinity Gradients. *Environmental Science & Technology* **2011**, *45* (10), 4360-4369.
- [26] Robinson, R. A. Stokes, R. H., Electrolyte solutions. 2nd rev. ed.; Dover Publications, Mineola, NY, **2002**; p xv, 571 p.
- [27] Veerman, J.; Saakes, M.; Metz, S. J. Harmsen, G. J., Reverse electrodialysis: evaluation of suitable electrode systems. *Journal of Applied Electrochemistry* **2010**, *40* (8), 1461-1474.
- [28] Veerman, J.; Saakes, M.; Metz, S. J. Harmsen, G. J., Reverse electrodialysis: Performance of a stack with 50 cells on the mixing of sea and river water. *Journal of Membrane Science* **2009**, *327* (1-2), 136-144.
- [29] Vermaas, D. A.; Saakes, M. Nijmeijer, K., Enhanced mixing in the diffusive boundary layer for energy generation in reverse electrodialysis. *Journal of Membrane Science* **2014**, *453* (0), 312-319.
- [30] Pitzer, K. S.; Peiper, J. C. Busey, R. H., Thermodynamic Properties of Aqueous Sodium Chloride Solutions. *Journal of Physical and Chemical Reference Data* **1984**, *13* (1), 1-102.
- [31] Lee, K. L.; Baker, R. W. Lonsdale, H. K., Membranes for power generation by pressure-retarded osmosis. *Journal of Membrane Science* **1981**, *8* (2), 141-171.
- [32] Bui, N.-N. McCutcheon, J. R., Nanofiber Supported Thin-Film Composite Membrane for Pressure-Retarded Osmosis. *Environmental Science & Technology* **2014**, *48* (7), 4129-4136.
- [33] Straub, A. P.; Yip, N. Y. Elimelech, M., Raising the Bar: Increased Hydraulic Pressure Allows Unprecedented High Power Densities in Pressure-Retarded Osmosis. *Environmental Science & Technology Letters* **2013**, *1* (1), 55-59.

- [34] Geise, G. M.; Hickner, M. A. Logan, B. E., Ionic Resistance and Permselectivity Tradeoffs in Anion Exchange Membranes. *ACS Applied Materials & Interfaces* **2013**, *5* (20), 10294-10301.
- [35] Daniilidis, A.; Vermaas, D. A.; Herber, R. Nijmeijer, K., Experimentally obtainable energy from mixing river water, seawater or brines with reverse electrodialysis. *Renewable Energy* **2014**, *64* (0), 123-131.
- [36] Geise, G. M.; Park, H. B.; Sagle, A. C.; Freeman, B. D. McGrath, J. E., Water permeability and water/salt selectivity tradeoff in polymers for desalination. *Journal of Membrane Science* **2011**, *369* (1-2), 130-138.
- [37] Elimelech, M. Phillip, W. A., The Future of Seawater Desalination: Energy, Technology, and the Environment. *Science* **2011**, *333* (6043), 712-717.
- [38] Fritzmann, C.; Löwenberg, J.; Wintgens, T. Melin, T., State-of-the-art of reverse osmosis desalination. *Desalination* **2007**, *216* (1-3), 1-76.
- [39] Arena, J. T.; McCloskey, B.; Freeman, B. D. McCutcheon, J. R., Surface modification of thin film composite membrane support layers with polydopamine: Enabling use of reverse osmosis membranes in pressure retarded osmosis. *Journal of Membrane Science* **2011**, *375* (1-2), 55-62.
- [40] Chou, S.; Wang, R.; Shi, L.; She, Q.; Tang, C. Fane, A. G., Thin-film composite hollow fiber membranes for pressure retarded osmosis (PRO) process with high power density. *Journal of Membrane Science* **2012**, *389* (0), 25-33.
- [41] Hoover, L. A.; Schiffman, J. D. Elimelech, M., Nanofibers in thin-film composite membrane support layers: Enabling expanded application of forward and pressure retarded osmosis. *Desalination* **2013**, *308* (0), 73-81.
- [42] She, Q.; Jin, X. Tang, C. Y., Osmotic power production from salinity gradient resource by pressure retarded osmosis: Effects of operating conditions and reverse solute diffusion. *Journal of Membrane Science* **2012**, *401-402* (0), 262-273.
- [43] Guler, E.; Zhang, Y.; Saakes, M. Nijmeijer, K., Tailor-Made Anion-Exchange Membranes for Salinity Gradient Power Generation Using Reverse Electrodialysis. *ChemSusChem* **2012**, *5* (11), 2262-2270.
- [44] Długołęcki, P.; Nijmeijer, K.; Metz, S. Wessling, M., Current status of ion exchange membranes for power generation from salinity gradients. *Journal of Membrane Science* **2008**, *319* (1-2), 214-222.
- [45] Güler, E.; Elizen, R.; Vermaas, D. A.; Saakes, M. Nijmeijer, K., Performance-determining membrane properties in reverse electrodialysis. *Journal of Membrane Science* **2013**, *446* (0), 266-276.
- [46] Baker, R. W., Membrane technology and applications. 3rd ed.; John Wiley & Sons, Chichester, West Sussex ; Hoboken, **2012**; p xiv, 575 p.
- [47] Mulder, M., Basic principles of membrane technology. 2nd ed.; Kluwer Academic, Dordrecht ; Boston, **1996**; p 564 p.
- [48] Vermaas, D. A.; Saakes, M. Nijmeijer, K., Doubled Power Density from Salinity Gradients at Reduced Intermembrane Distance. *Environmental Science & Technology* **2011**, *45* (16), 7089-7095.
- [49] Skilhagen, S. E., Osmotic power — a new, renewable energy source. *Desalination and Water Treatment* **2010**, *15* (1-3), 271-278.

[50] Post, J. W.; Goeting, C. H.; Valk, J.; Goinga, S.; Veerman, J.; Hamelers, H. V. M. Hack, P. J. F. M., Towards implementation of reverse electrodialysis for power generation from salinity gradients. *Desalination and Water Treatment* **2010**, *16* (1-3), 182-193.

[51] Vermaas, D. A.; Kunteng, D.; Saakes, M. Nijmeijer, K., Fouling in reverse electrodialysis under natural conditions. *Water Research* **2013**, *47* (3), 1289-1298.

[52] Yip, N. Y. Elimelech, M., Influence of Natural Organic Matter Fouling and Osmotic Backwash on Pressure Retarded Osmosis Energy Production from Natural Salinity Gradients. *Environmental Science & Technology* **2013**, *47* (21), 12607-12616.

Chapter 10:

Conclusions

10.1 SUMMARY

The research presented in this dissertation work aims to advance emerging membrane-based technologies by addressing the critical challenges and furthering our understanding of the potentials and limitations. The thesis centered on three novel membrane processes: forward osmosis (FO), pressure retarded osmosis (PRO), and reverse electrodialysis (RED). The fabrication of thin-film composite polyamide FO and PRO membranes was demonstrated in Chapters 3 and 4, respectively. The fabricated membranes exhibited unprecedented high water flux and salt selectivity in FO, and enhanced power density performance in PRO. Methodical selection of the fabrication conditions were thoughtfully guided by the mechanistic understanding of the influence of the casting and modification parameters on membrane transport and structural properties.

Systematic analysis of the factors affecting PRO power density in Chapter 5 revealed three phenomena — external concentration polarization, internal concentration polarization, and reverse salt permeation — that determined PRO performance. The relative impact of performance limiting effects was thoroughly evaluated to elucidate the underlying influence of the membrane transport and structural properties. The study found that the permeability-selectivity of the membrane active layer needs to be balanced with respect to the structural parameter of the membrane support layer to achieve optimum power density.

Chapter 6 approached PRO energy production using thermodynamic fundamentals and determined the theoretical energy efficiency obtainable from natural salinity gradients with constant pressure operation. Inevitable entropy production, attributed to frictional losses as water permeates across the membrane, and unutilized energy, due to

inherent limitations of practical operation, were identified as the two causes of inefficiency. The thermodynamic efficiency of PRO is discussed and the global potential of energy production from the controlled mixing of river water and seawater is assessed.

Chapter 7 examined the effect of natural organic matter fouling on PRO productivity. Methodical characterization of the changes to the membrane properties ascribed the reduction in energy extraction efficiency to the detrimental increase in hydraulic permeability of the membrane selective layer. A quick osmotic backwash was used to deliver a surge of hydraulic drag into the membrane support layer and partially cleaned out the foulants to achieve substantial recovery in membrane productivity.

Chapter 8 simultaneously analyzed the membrane power density and energy conversion efficiency of RED power generation. An intrinsic tradeoff relationship between the two performance parameters was established. The studied then determined the power density and efficiency performance attainable with technologically-available ion exchange membranes and well-designed membrane stack.

The performance of module-scale PRO and RED is directly compared in Chapter 9 to identify the relative advantages and drawbacks of each technology. Simulated state-of-the-art membrane parameters were employed in the analysis to circumscribe the current potential energy efficiency and power density performance of PRO and RED. The intrinsic prospects and limitations of the processes were discussed and the most urgent areas for development in order to realize power generation from salinity gradient were highlighted.

10.2 NOVEL CONTRIBUTIONS

The **fabrication of thin-film composite polymeric membranes capable of high performance in forward osmosis represents a significant milestone** in the development of the technology [1]. Progress on realizing the numerous promising FO applications has been hindered by the lack of an suitable membrane. Conventional pressure-driven membranes yield inadequately low water fluxes, while commercial cellulose acetate-based FO membranes has a narrow stable pH range of 4-6 that severely limits their potential applications and precludes usage in ammonia-carbon dioxide systems. Additionally, the asymmetric membranes have inherently low water permeabilities. The demonstration of the high performance membranes in this thesis overcame these technical bottlenecks. Design of the hand-cast membranes was guided by **mechanistic understanding of the influence of fabrication parameters on membrane morphology and microstructure**. The casting conditions were thoughtfully selected to produce a thin, porous, and non-tortuous support layer that suppressed the detrimental effects of internal concentration polarization and maximized the osmotic driving force to achieve high water fluxes [1]. The polyamide selective layer demonstrated chemical stability, retaining the transport properties after prolonged exposure to alkaline conditions.

This work presents a mass transport model for pressure retarded osmosis that **determined the complete governing equations for water and salt flux** [2]. The model is the **first to fully incorporate the performance limiting effects of external concentration polarization, internal concentration polarization, and reverse salt permeation**. The study showed that, contrary to prevailing beliefs, the effects of reverse salt leakage, when coupled with internal concentration polarization in the membrane

support layer, can severely limit PRO productivity. Systematic investigation of a range of polyamide active layer transport properties established a **tradeoff relationship between water permeability and salt selectivity** [3]. Careful analysis revealed the intricate influence of active and support layer properties on power density and demonstrates that **power density is maximized by tailoring the water and salt permeabilities to the structural parameter**.

This knowledge was applied to build on the membrane fabrication platform, developed previously, for PRO applications. A chemical post-treatment was employed to customize the membrane transport properties and the resultant best performing **membranes were capable of attaining power densities greater than 10 W/m², twice the cost-effective benchmark of 5 W/m²** [2]. The outstanding performance was attributed to the high water permeability of the active layer, coupled with a moderate salt permeability and the ability of the support layer to suppress the undesirable accumulation of leaked salt in the porous support. The platform developed in this dissertation research can serve to **guide future membrane design and fabrication efforts for FO and PRO**.

While the Gibbs free energy of mixing from the confluence of rivers and oceans worldwide has been proposed as a clean and renewable energy source, there are no rigorous appraisals of the global capacity. The dissertation research presented here **analyzed the thermodynamic efficiency of the pressure retarded osmosis and employed the findings to arrive at a more informed assessment of the potential of sustainable energy production from natural salinity gradients with PRO** [4]. Fundamental thermodynamic principles were applied to examine work extraction in an irreversible constant-pressure PRO process and found that energy efficiencies of up to 91%

can be achieved. The study identified the causes of inefficiency inherent to PRO, and highlighted the inconsistency between the goals of achieving high power density and maximizing energy extraction. Using a conservative efficiency of 48% that reflects more practical operation, the study **estimates that a tenth of the global annual river water discharge produces enough electricity for over half a billion people** [4].

This thesis evaluated the impact of ubiquitous natural organic matter in river water on the productivity of PRO power generation and **found membrane fouling to be a crucial phenomenon that diminishes performance** [5]. The pioneering study on organic fouling of the membrane support layer revealed that the **foulant accumulation detrimentally elevates the hydraulic resistance but did not increase the support layer structural parameter**. Because of the reduced membrane permeability, PRO water flux and power density consequently decreased and the fouled membranes were less efficient in converting salinity energy into useful work. A **novel osmotic backwash technique demonstrated substantial recovery in performance** [5]. The brief, chemical-free cleaning method inventively reversed the osmotic gradient between the seawater and river water and utilized the permeate drag to flush out the organic foulants. Insights on the fouling phenomenon acquired in this systematic study will serve to guide the formulation of effectual fouling mitigation strategies.

Besides PRO, salinity energy can be extracted with other methods, with reverse electrodialysis being comparatively the most mature and competitive. The **RED energy conversion efficiency and membrane power density were simultaneously analyzed** in a seawater-river water system [6]. Using parameters that simulate state-of-the-art ion exchange membranes and stack design, the study determined that **efficiencies of ~33-44%**

can be obtained. However, a **tradeoff effect was observed between efficiency and power density**; higher power densities are generally achieved at the expense of lower efficiencies. By judicious control of the extent of mixing in RED, the power density can be significantly enhanced with only marginal sacrifice in energy efficiency. The study, **for the first time, quantified the relative impact of membrane selectivity imperfections on RED energy production performance** and found the leakage of co-ions across the membranes to be dominant [6]. The findings of the study can **inform membrane development and guide stack design** to advance RED power generation towards realization.

The **pioneering comparison on the energy efficiency and power density performance of PRO and RED** offer several insights that can shape the discussion on salinity gradient power generation [7]. The study indicates that, with existing technologically-available membranes, **greater efficiencies (54–56%) and higher power densities (2.4–38 W/m²) can be obtained with PRO** than RED (18–38% and 0.77–1.2 W/m²) for a range of salinity gradients. Furthermore, by thoughtful tuning of the membrane properties within the bounds of the permeability–selectivity tradeoff, the **power density can be considerably enhanced with only a minor penalty to the efficiency**. The analysis further revealed a limitation in the working principles of RED: **the process is inherently unable to take advantage of a larger concentration difference to enhance performance**. On the other hand, PRO does not possess this characteristic and, hence, **is advantageous for employment in energy extraction from large salinity gradients**.

The following publications are associated with work presented in this dissertation thesis:

- 1) Yip, N.Y., Tiraferri, A., Phillip, W.A., Schiffman, J.D., and Elimelech, M., "High Performance Thin-Film Composite Forward Osmosis Membrane", *Environmental Science & Technology*, Volume 44, May 2010, pages 3812–3818.
- 2) Yip, N.Y., Tiraferri, A., Phillip, W.A., Schiffman, J.D., Hoover, L.A., Kim, Y.C., and Elimelech, M. "Thin-Film Composite Pressure Retarded Osmosis Membranes for Sustainable Power Generation from Salinity Gradients", *Environmental Science & Technology*, Volume 45, May 2011, pages 4360–4369.
- 3) Yip, N.Y. and Elimelech, M. "Performance Limiting Effects in Power Generation from Salinity Gradients by Pressure Retarded Osmosis", *Environmental Science & Technology*, Volume 45, December 2011, pages 10273–10282.
- 4) Yip, N.Y. and Elimelech, M. "Thermodynamic and Energy Efficiency Analysis of Power Generation from Natural Salinity Gradients by Pressure Retarded Osmosis", *Environmental Science & Technology*, Volume 46, May 2012, pages 5230–5239.
- 5) Yip, N.Y. and Elimelech, M. "Influence of Natural Organic Matter Fouling and Osmotic Backwash on Pressure Retarded Osmosis Energy Production from Natural Salinity Gradients", *Environmental Science & Technology*, Volume 47, November 2013, pages 12607–12616.
- 6) Yip, N.Y., Vermaas, D.A., Nijmeijer, K., Elimelech, M. "Thermodynamic, Energy Efficiency, and Power Density Analysis of Reverse Electrodialysis Power Generation with Natural Salinity Gradients." *Environmental Science & Technology*, Volume 48, May 2014, pages 4925–4936.
- 7) Yip, N.Y. and Elimelech, M. "Comparison of Energy Efficiency and Power Density in Pressure Retarded Osmosis and Reverse Electrodialysis" *Environmental Science & Technology*, 2014, Submitted.

10.3 IMPLICATIONS AND FUTURE DIRECTIONS

The fabrication of thin-film composite membranes capable of attaining high performance overcame a significant technical hurdle in FO. Crucially, the membranes were cast using fabrication techniques that can be readily scaled up. Since the demonstration of the membranes in this dissertation work, and also from other research groups [8, 9], thin-film composite polyamide FO membranes have been manufactured commercially and are beginning to find their way to applications. Membrane fouling is anticipated to be a dominant phenomenon in FO applications [10-13]. Hence, future membrane

development efforts focusing on fouling resistant membranes or formulation of expedient cleaning techniques will reap the greatest benefits in advancing FO [14-16]. Such endeavors will need to take heed of the dominant foulant types specific to the application and tailor the anti-fouling or cleaning approaches accordingly.

Likewise in PRO power generation, fouling will be a critical phenomenon. The theoretical maximum energy, i.e., the Gibbs free energy of mixing, that can be extracted from equal volumes of seawater and river water is ~ 0.28 kWh per cubic meter of both the seawater and river water. Pretreatment of the input streams to remove foulants would incur significant chemical and energy expenditure. Presently, due to the lack of operational data, there are no firm figures on such cost. However, using the seawater pretreatment cost in reverse osmosis desalination of $\sim 0.1-0.2$ kWh/m³ as a ballpark estimate, extensive pretreatment of the PRO input streams as a fouling control tactic will likely be unfeasible. Hence, the alternative approaches of fouling-resistant membranes and cost-effective cleaning methods will need to be pursued.

This work showed that, unlike FO fouling that occurs on the membrane active layer, fouling in PRO takes place in the membrane porous support layer due to the membrane orientation with respect to the water flux direction. This unique fouling mechanism poses non-trivial challenges to both conferring of fouling resistant properties to the membranes and cleaning of the fouled membranes, because the membrane porous support acts as a sheltering boundary layer. Successful fouling mitigation strategies will likely require an optimized blend of a three-pronged approach: nominal pretreatment of the seawater and river water streams, developing fouling resistant membranes, and expedient cleaning techniques.

Alternatively, PRO can be employed in closed-loop systems such as the pressure retarded osmosis-membrane distillation osmotic heat engine that converts low-temperature heat sources into useful work [17]. Because the engineered solutions utilized can be very clean, membrane fouling can be almost eliminated. Our studies showed that PRO is more advantageous, compared to RED, for accessing the salinity energy from large concentration gradients [7]. However, to fully exploit of the advantages of the engineered high concentration draw solutions, an extremely high hydraulic pressure will need to be applied to the membrane. Here, the challenge is to develop mechanically robust membranes that retain their transport and structural properties when highly pressurized [18].

Another critical effect that limits the power density and, hence, the cost-effectiveness of PRO energy production, is external concentration polarization (ECP) at the membrane active layer. The magnitude of ECP is exponentially magnified and becomes dominant at high water fluxes. Therefore, while membrane advances can increase water permeability, minimize salt leakage, and suppress internal concentration polarization, innovative membrane channel and module design will be necessary to keep the detrimental impact of ECP in check. More in-depth cost analysis that incorporates the pumping expenses associated with reducing ECP, the pretreatment requirements, and the productivity during membrane cleaning will shed light on the cost-effective operation of PRO energy production with natural and engineered salinity gradients.

The study on the polyamide transport properties showed a tradeoff behavior between water permeability and salt selectivity. This tradeoff relation is in agreement with the solution-diffusion mechanism proposed for polymeric salt-rejecting membranes [19-21].

Currently, polyamide is the gold standard material for salt selective membrane applications and is widely employed in seawater and brackish water desalination. The permeability-selective tradeoff plot can be used to compare the performance of alternative membrane materials [22-24] with polyamide. Achieving membranes that surpass polyamide would represent a momentous breakthrough for nanofiltration, reverse osmosis, forward osmosis, and pressure retarded osmosis.

Analysis of RED power generation with natural salinity gradients yielded energy efficiencies and power densities lower than PRO. The primary factors limiting RED performance are the low conductivity of currently available ion exchange membranes and the high resistance associated with the dilute stream. Raising RED power density performance to levels comparable with PRO would necessitate the increasing the membrane conductivity by approximately an order of magnitude, a daunting but not insurmountable task. On the other hand, reducing the resistance of the dilute stream channel is less straightforward. A low salt concentration gives a higher energy of mixing greater but is deleterious to power density because of the greater resistive energy losses. Inventive solutions will be needed to concurrently achieve both goals and enhance the prospects of energy production with reverse electrodialysis.

10.4 REFERENCES

- [1] Yip, N. Y.; Tiraferri, A.; Phillip, W. A.; Schiffman, J. D. Elimelech, M., High Performance Thin-Film Composite Forward Osmosis Membrane. *Environmental Science & Technology* **2010**, *44* (10), 3812-3818.
- [2] Yip, N. Y.; Tiraferri, A.; Phillip, W. A.; Schiffman, J. D.; Hoover, L. A.; Kim, Y. C. Elimelech, M., Thin-Film Composite Pressure Retarded Osmosis Membranes for Sustainable Power Generation from Salinity Gradients. *Environmental Science & Technology* **2011**, *45* (10), 4360-4369.
- [3] Yip, N. Y. Elimelech, M., Performance Limiting Effects in Power Generation from Salinity Gradients by Pressure Retarded Osmosis. *Environmental Science & Technology* **2011**, *45* (23), 10273-10282.
- [4] Yip, N. Y. Elimelech, M., Thermodynamic and Energy Efficiency Analysis of Power Generation from Natural Salinity Gradients by Pressure Retarded Osmosis. *Environmental Science & Technology* **2012**, *46* (9), 5230-5239.
- [5] Yip, N. Y. Elimelech, M., Influence of Natural Organic Matter Fouling and Osmotic Backwash on Pressure Retarded Osmosis Energy Production from Natural Salinity Gradients. *Environmental Science & Technology* **2013**, *47* (21), 12607-12616.
- [6] Yip, N. Y.; Vermaas, D. A.; Nijmeijer, K. Elimelech, M., Thermodynamic, energy efficiency, and power density analysis of reverse electrodialysis power generation with natural salinity gradients. *Environ Sci Technol* **2014**, *48* (9), 4925-36.
- [7] Yip, N. Y. Elimelech, M., Comparison of Energy Efficiency and Power Density in Pressure Retarded Osmosis and Reverse Electrodialysis. *Environmental Science & Technology* **2014**, *Submitted*.
- [8] Wang, R.; Shi, L.; Tang, C. Y.; Chou, S.; Qiu, C. Fane, A. G., Characterization of novel forward osmosis hollow fiber membranes. *Journal of Membrane Science* **2010**, *355* (1-2), 158-167.
- [9] Wang, K. Y.; Chung, T.-S. Amy, G., Developing thin-film-composite forward osmosis membranes on the PES/SPSf substrate through interfacial polymerization. *AIChE Journal* **2012**, *58* (3), 770-781.
- [10] Boo, C.; Lee, S.; Elimelech, M.; Meng, Z. Hong, S., Colloidal fouling in forward osmosis: Role of reverse salt diffusion. *Journal of Membrane Science* **2012**, *390-391* (0), 277-284.
- [11] Mi, B. Elimelech, M., Chemical and physical aspects of organic fouling of forward osmosis membranes. *Journal of Membrane Science* **2008**, *320* (1-2), 292-302.
- [12] Mi, B. Elimelech, M., Organic fouling of forward osmosis membranes: Fouling reversibility and cleaning without chemical reagents. *Journal of Membrane Science* **2010**, *348* (1-2), 337-345.
- [13] Tang, C. Y.; She, Q.; Lay, W. C. L.; Wang, R. Fane, A. G., Coupled effects of internal concentration polarization and fouling on flux behavior of forward osmosis membranes during humic acid filtration. *Journal of Membrane Science* **2010**, *354* (1-2), 123-133.
- [14] Lu, X.; Romero-Vargas Castrillón, S.; Shaffer, D. L.; Ma, J. Elimelech, M., In Situ Surface Chemical Modification of Thin-Film Composite Forward Osmosis Membranes for Enhanced Organic Fouling Resistance. *Environmental Science & Technology* **2013**, *47* (21), 12219-12228.
- [15] Qi, S.; Qiu, C. Q.; Zhao, Y. Tang, C. Y., Double-skinned forward osmosis membranes based on layer-by-layer assembly—FO performance and fouling behavior. *Journal of Membrane Science* **2012**, *405-406* (0), 20-29.

-
- [16] Tiraferri, A.; Kang, Y.; Giannelis, E. P. Elimelech, M., Superhydrophilic Thin-Film Composite Forward Osmosis Membranes for Organic Fouling Control: Fouling Behavior and Antifouling Mechanisms. *Environmental Science & Technology* **2012**, *46* (20), 11135-11144.
- [17] Lin, S.; Yip, N. Y.; Cath, T. Y.; Osuji, C. O. Elimelech, M., Hybrid Pressure Retarded Osmosis–Membrane Distillation System for Power Generation from Low-Grade Heat: Thermodynamic Analysis and Energy Efficiency. *Environmental Science & Technology* **2014**.
- [18] Straub, A. P.; Yip, N. Y. Elimelech, M., Raising the Bar: Increased Hydraulic Pressure Allows Unprecedented High Power Densities in Pressure-Retarded Osmosis. *Environmental Science & Technology Letters* **2013**, *1* (1), 55-59.
- [19] Paul, D. R., Reformulation of the solution-diffusion theory of reverse osmosis. *Journal of Membrane Science* **2004**, *241* (2), 371-386.
- [20] Wijmans, J. G. Baker, R. W., The solution-diffusion model: a review. *Journal of Membrane Science* **1995**, *107* (1–2), 1-21.
- [21] Geise, G. M.; Park, H. B.; Sagle, A. C.; Freeman, B. D. McGrath, J. E., Water permeability and water/salt selectivity tradeoff in polymers for desalination. *Journal of Membrane Science* **2011**, *369* (1–2), 130-138.
- [22] Li, X.; Wang, R.; Wicaksana, F.; Tang, C.; Torres, J. Fane, A. G., Preparation of high performance nanofiltration (NF) membranes incorporated with aquaporin Z. *Journal of Membrane Science* **2014**, *450* (0), 181-188.
- [23] Lind, M. L.; Eumine Suk, D.; Nguyen, T.-V. Hoek, E. M. V., Tailoring the Structure of Thin Film Nanocomposite Membranes to Achieve Seawater RO Membrane Performance. *Environmental Science & Technology* **2010**, *44* (21), 8230-8235.
- [24] Zhao, L. Ho, W. S. W., Novel reverse osmosis membranes incorporated with a hydrophilic additive for seawater desalination. *Journal of Membrane Science* **2014**, *455* (0), 44-54.